



9<sup>th</sup> European Workshop on  
**PHYSICAL PROCESSES  
IN NATURAL WATERS**

4-6 SEPTEMBER 2005  
LANCASTER UNIVERSITY  
UNITED KINGDOM

Edited by  
Andrew Folkard<sup>1</sup> and Ian Jones<sup>2</sup>

<sup>1</sup>Department of Geography, Lancaster University, U.K.

<sup>2</sup>Centre for Ecology and Hydrology, Lancaster, U.K.



## Preface

The series of European workshops on "Physical Processes in Natural Waters" began in Kastenienbaum, Switzerland in 1996, inspired by an earlier meeting in Australia organized by the Centre for Water Research at the University of Western Australia. Since then, meetings have been held annually or bi-annually around Europe and have been attended by researchers from throughout Europe and the rest of the world. The intention of the workshops is to provide a forum for scientists to exchange ideas and discuss ongoing research on topics related to physical processes in inland and coastal waters.

This publication includes papers detailing the presentations from the ninth in this series of workshops, which is being held in the United Kingdom for the first time, at the University of Lancaster. The papers cover a wide range of topics related to lakes, reservoirs, rivers, wetlands, estuaries, coastal waters and semi-enclosed seas and feature in particular mixing processes, internal waves, interactions with the atmosphere, eco-hydrodynamics and influences on biogeochemistry.

Andrew Folkard  
Lancaster, August 2005

# European Workshop Series on Physical Processes in Natural Waters

## International Organising Committee

Alfred Wuest	(Switzerland, Chair)
Adolf Stips	(Italy)
Bertram Boehringer	(Germany)
Andrew Folkard	(UK)
Arkady Terzhevskiy	(Russia)
Madis-Jaak Lilover	(Estonia)
Sergei Semovsky	(Russia)
Xavier Casamitjana	(Spain)
Lars Bengtsson	(Sweden)
Erich Baeuerle	(Germany)
Nikolai Filatov	(Russia)

## Local Organising Committee

Andrew Folkard  
Ian Jones  
Helen Miller

## Workshop Presentations

### SUNDAY, SEPTEMBER 4<sup>TH</sup>

#### **ORAL SESSION: INTERNAL WAVES AND MIXING I**

- Invited Talk:** Shear, stratification and mixing in the North Sea 9  
*H van Haren*

- Inter-basin exchange and mixing in the hypolimnion of a large lake: the role of internal waves 17  
*L Umlauf and U Lemmin*

- Dynamics of high-frequency internal waves in the littoral zone of a large lake 19  
*A Lorke, F Peeters and J Thorwartz*

- Wave-induced resuspension in the littoral zone of Lake Constance 21  
*H Hofmann, A Lorke and F Peeters*

#### **ORAL SESSION: INTERNAL WAVES AND MIXING II** 23

- Invited Talk:** Vertical Mixing in seasonally stratified continental shelf seas 25  
*T Rippeth*

- Numerical simulations of shoaling internal waves in a tilting tank experiment 31  
*K Lamb*

- Observations and modelling of nonlinear internal waves in Lake Onega 39  
*V Vlasenko, N Filatov, M Petrov, A Terzhevik, R Zdrovennov, and N Stashchuk*

- Birth, rapid development and sudden death of a distinct double-diffusive staircase in Lake Nyos, Cameroon 47  
*A Wuest, M Schmid and B Muller*

- Observations of Multilayer Structure in a Small Lake 53  
*J Ilmberger, K Wunderle and C von Roden*

- Observations of a cyclonic gyre produced by an internal surge in a small deep lake 61  
*G Kirillin, C Engelhardt and S Golosov*

#### **POSTER SESSION I** 69

- Some new statistical estimates for functions of distribution for spacing of Langmuir circulation 71  
*S Ryazhin, N Kochkov and L Karlin.*

- FLake – A Lake Model for Environmental Applications 73  
*D Mironov, S Golosov, E Heise, E Kourzeneva, B Ritter, N Schneider and A Terzhevik*

Bathymetric map definition and water balance of the shallow Poopo Lake, Bolivia <i>R Pillco and L Bengtsson</i>	75
Water budget of the Caspian Sea and its sensitivity to external forcing <i>R Ibrayev and E Ozsoy</i>	83
Anomalous rainfall and associated atmospheric circulation in the NE Spanish Mediterranean area and its relationship to sediment fluidization events in a lake <i>M Soler, T Serra, J Colomer and R Romero</i>	91
Direct numerical simulations of baroclinic wave processes in a stratified tank (with application to lake dynamics) <i>N Stashchuk, V Vlasenko and K Hutter</i>	99

### MONDAY, SEPTEMBER 5<sup>TH</sup>

<b>ORAL SESSION: RIVERINE AND SHALLOW WATERS</b>	<b>107</b>
<b>Invited Talk:</b> Vertical transport in and above submerged canopies <i>H Nepf</i>	109
Modelling hydrodynamics in flexible vegetation <i>J Dijkstra and R Uittenbogaard</i>	117
Hydrodynamic measurements in a shallow lagoon <i>C Nasello, G Ciraolo and G La Loggia</i>	125
Physical processes control the variability in phytoplankton populations in both temperate and tropical Australian rivers <i>M Bormans and P Ford</i>	135
Evolution of Estuaries – Past and Future <i>D Prandle</i>	143
<b>ORAL SESSION: ATMOSPHERIC INFLUENCES</b>	<b>145</b>
The influence of lake size on the value of transfer coefficients <i>I Jones</i>	147
Influence of weather on lake temperature and thermal stratification: a case study by model simulation from 1953–2004 on the Danish lake Esrum Sø <i>R M Closter</i>	155
Studies of Physical Processes in Lake Erie <i>Y Rao</i>	163
Wind profile restructuring due to the roughness reduction in land-water transition <i>M De Marchis, J Jozsa, B Milici and E Napoli</i>	171

**POSTER SESSION II**

SYMPOSIUM ON LAKE ECOLOGY AND MANAGEMENT

**179**

- Temperature variations within and outside reed stands causing horizontal mixing 181  
*C Lovstedt*

- The vertical distribution of soluble reactive phosphorus in the water column of Esthwaite Water and the effect of physical variables 183  
*H Miller, I Jones, A Folkard and S Maberley*

- Dynamics of phytoplankton in response to rapid events of physical forcing in three temperate lakes 191  
*A Pannard, M Bormans and Y Lagadeuc*

- On the influence of flexible vegetation on flow fields in shallow water: a flume experiment 195  
*A Maltese, A Folkard, G Ciraolo, E Cox and G Ferreri*

**TUESDAY, SEPTEMBER 6<sup>TH</sup>****ORAL SESSION: BIOGEOCHEMICAL-PHYSICAL INTERACTIONS** **203**

- Invited Talk:** Turbulence, Internal Waves and Intrusions: Implications for Biogeochemistry 203  
*S MacIntyre*

- Modelling the physical structure and the succession of algae in two basins of Lake Malaren, Sweden, with emphasis on mixing depth 205  
*I Persson and H Markensten*

- Evidence of the role of horizontal advection and surface vertical mixing in the phytoplankton distribution in a stratified reservoir 207  
*T Serra, J Vidal, J Colomer, X Casamitjana and M Soler*

- A synoptic view of carbon and oxygen dynamics in European regional seas: an approach coupling hydrodynamical and biogeochemical modelling and satellite datasets 213  
*L Deydier-Stephan, A Stips, M Dowell and W Schrimpf*

- Hypolimnetic oxygenation with bubble plume diffusers: modelling oxygen transfer and plume dynamics 221  
*V Singleton and J Little*

- Physical background of oxygen depletion development in ice-covered lakes 229  
*S Golosov, E Schipunova, A Terzhevsk, O Maher, and G Zdorovenanova*

**ORAL SESSION: MIXING AND COLD WATER**

Warm discharges into cold lakes <i>A Kay</i>	241
Cold-water events in the mixed layer of Lake Geneva <i>B Ozen, S Thorpe, U Lemmin and T Osborn</i>	249
Vertical slice tomography experiments in Lake Geneva: observing the winter cooling <i>X Falourd</i>	257
Effect of hydropower operation on downstream riverine particle transport and density intrusions into a peri-alpine lake – a case study <i>D Finger, A Wuest and M Schmid</i>	265
Convective dynamics above the upper interface of a warm fluidised bed located at the bottom of a lake <i>X Sanchez and E Roget</i>	273
Mixing processes in Lake Van (Turkey) <i>H Kaden, F Peeters, A Lorke and R Kipfer</i>	281
Suspended sediment controlling the path of the Mulde flood waters through Lake Goitsche <i>B Boehrer and M Schultze</i>	287

# INTERNAL WAVES & MIXING I



# Shear, stratification and mixing in the North Sea

by Hans van Haren

(NIOZ, P.O. Box 59, 1790 AB Den Burg, The Netherlands, [hansvh@nioz.nl](mailto:hansvh@nioz.nl))

*Shelf seas at moderate latitudes like the North Sea are a very dynamic environment with high biological productivity. This high productivity is governed by typical shallow seas physical processes, which induce transport and mixing of nutrients and suspended matter between different water masses. Oscillatory motions like tides dominate turbulent mixing, firstly near the bottom but also in the interior varying on the larger, seasonal scale. Seasonal variations in convective and wind mixing near the sea surface allow the development of stable vertical stratification in density in summer. Such stratification is thought to hamper vertical exchange between nutrient-rich near-bottom waters and the photic zone. Here, observations and some modeling will be presented that evidence de-stabilization of stratification by oscillatory current differences, which become enhanced across layers of strongest stratification. Occasional breaking of small-scale internal waves cause vertical transport even in high summer. The crucial importance of the rotation of the Earth will be stressed also for marine biology.*

## 1. Introduction

Motions in shelf seas (<200 m water depth) show quite some similarity with those in the deep-ocean: large-scale (low-frequency) currents are more energetic than small-scale (~turbulent) motions with exception of energy peaking at intermediate tidal and inertial frequencies. Motions at the latter frequencies (near-inertial motions) are mainly generated following sudden changes in wind (Millot and Crépon, 1981), but only when (part) of the water column is vertically stably stratified in density, density variations in the ocean being mainly induced by variations in temperature and salinity. At least two main differences are distinguished between the deep-ocean and shelf seas: 1) external frictional stresses near the surface and bottom are important for the dynamics in large parts of shelf seas, whilst negligible in most of the ocean, 2) vertical stratification due to temperature gradients is variable in time also on a seasonal scale in large parts of shelf seas. As a result, only when surface-bottom turbulent boundary layers do not overlap inertial motions can be generated in shelf seas, the energy of which thus varies seasonally there (van Haren, 2004). Here we neglect stratification of a more permanent character that occurs for example near river outflows and in sufficiently deep 'shelf' seas, e.g. at the transition between the North Sea and the Atlantic Ocean.

Stratification inhibits vertical turbulent exchange because it suppresses the vertical scale of turbulence. However, stratification also supports internal waves. Such waves are characterized by propagation in all three dimensions. Via non-linear interaction they redistribute energy across various scales, so that through straining locally enhanced stratified layers alternate with layers of weaker stratification. As a result, interior turbulent mixing following Kelvin-Helmholtz shear-

instabilities can be generated via vertical current ( $u$ ,  $v$ ) shear  $\mathbf{S} = (\partial u / \partial z, \partial v / \partial z)$  associated with (large-scale) internal waves, through the breaking of (short-scale) internal waves.

In frequency ( $\sigma$ ), free internal gravity can exist between  $f < \sigma < N$ ,  $N \gg f$ , with  $f = 2\Omega \sin \phi$  the Coriolis parameter (i.e. the local planetary inertial frequency,  $\Omega$  the Earth's rotational vector and  $\phi$  the latitude) and  $N = (-g \cdot d\ln p/dz)^{1/2}$  the buoyancy frequency computed over 'some' vertical interval  $dz$ , with  $g$  denoting the acceleration of gravity and  $p$  denoting density. For most latitudes, semidiurnal tidal harmonic frequencies, mainly  $M_2$ ,  $S_2$ ,  $N_2$ , (their band is named ' $D_2$ '), lie within the internal wave band. In general, the larger internal wave scales reside near  $f$ , the shorter scales near  $N$ . Most energy is found near  $f$  and  $D_2$ , so that atmospheric and tidal forcing dominate internal wave generation. Thus, one expects largest shear near  $f$  (and  $D_2$ ). However, this depends also on the vertical length scale, given the definition of shear. In theory, this length scale is infinitively small for internal wave motions at  $f$ , at which frequency they propagate exclusively horizontally. Thus,  $f$ -shear induced by internal waves may be relatively more important than internal tidal shear.

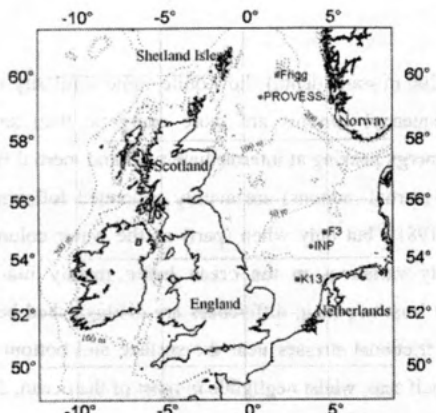


**Figure 1.** Map of the North Sea showing northern site of PROVESS and INP, together with some oil rigs at which meteorological data were collected (from: van Haren and Howarth, 2004).

Observations on the (varying) relation between N, |S| at f and D<sub>2</sub> and their effects on the biology (phytoplankton blooms) were made during several multi-disciplinary projects between 1992-1996 and 1998-2001, focusing on the central North Sea (H~50 m water depth; 'INP', van Haren et al., 1997) and the northern North Sea (H~100 m; EC-MAST-III 'PROVESS', Howarth et al., 2002), respectively (Fig. 1). Both sites are characterized by a seasonal strong thermal stratification, with surface-bottom homogeneous waters in winter and >10°C vertical temperature difference in summer. Tidal currents are typically 0.1-0.2 m s<sup>-1</sup>, yielding a bottom boundary layer of 20-30 m. Principal means of investigation were moored instrumentation consisting of acoustic Doppler current profilers (ADCP), current meters, temperature sensors, in-situ nutrient samplers

(that worked only occasionally), light meters, transmissometers and in-situ fluorometers. With the addition of shipborne sampling a comprehensive data-set was collected, yearlong for INP and during the autumn for PROVESS.

### 2.a. Effect of stratification on large-scale motions

In the open ocean, shear is predominantly induced via large-scale internal wave (baroclinic; vertically non-uniform) flows. In contrast, in the stratified North Sea tidal is observed in isotherm displacements, but they are not due to internal tides (van Haren and Maas, 1987; Howarth, 1998). Instead, they are primarily a result of externally forced, barotropic (surface pressure gradient driven), viscous flows and variations therein due to the stratification (Maas and van Haren, 1987; van Haren, 2000). This is due to the dominant effects of Earth rotation and boundary friction, which combine in 'Ekman dynamics'. The two major large-scale sources (Fig. 2) are tidal shear generated at the bottom, and inertial shear generated at the surface and via a coastal boundary (Millot and Crépon, 1981).

In the central North Sea, tidal and inertial motions are quite differently polarized: nearly rectilinear and circular, respectively. In winter the tidal motions show a smooth vertical profile. However, in summer this profile is distorted by the stratification and its shear vector is circularly polarized like that of inertial shear. This is direct evidence of the dominance of Ekman dynamics, as the Earth rotation causes an asymmetry in frictional properties of (anti)-clockwise circular motions, into which any oscillatory ellipsoidal motions in a rotating frame of reference can be decomposed (Prandle, 1982). The stratification only affects the vertical momentum flux of the least hampered (clockwise) current component. It is this component which is (theoretically) the only one which is forced at f.

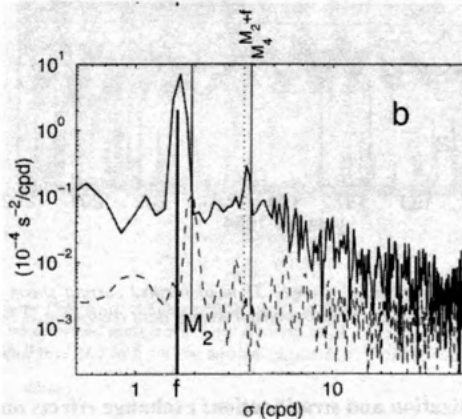


**Figure 2.** INP shear spectra observed in summer at 13 m (solid) and 40 m (dashed) (from: van Haren et al., 1999).

As a result, in summer the familiar spring-neap cycle may not be always observed in strongly stratified waters and, instead, a 3-4 days cycle representing the inertial-tidal cycle is observed predominantly (van Haren et al., 1999). Furthermore, as inertial and tidal shear *magnitude* are both a slow function of time, much slower varying than at a inertial or tidal period, the destabilization of stratification adopts a ‘~constant’ value (Fig. 3; van Haren, 2000). A separation in shear layer was observed ‘coming from above’ ( $f$ -shear) and ‘from below’ ( $D_2$ -shear), although the reason for this strict separation was not well understood.

## 2.b. Effect of stratification on small-scale motions

A measurable relationship between stable  $N$  and destabilizing  $|S|$  referring to small-scale mixing is the gradient Richardson number  $Ri = N^2/|S|^2$ . For  $Ri < 0.25$ , linear analysis suggests that a transition to turbulence will occur (Miles, 1961; Howard, 1961). However, under a strongly non-linear internal wave regime, a turbulent-transition value of  $Ri \approx 1$  has been suggested (Abarbanel et al., 1984). Thus, when  $Ri > 1$  vertical turbulent exchange is definitely hampered, whilst when  $Ri < 0.25$  turbulent mixing will homogenize the water column. In case of the former situation, previously considered typical for a stratified shelf sea, well-mixed near-bottom and near-surface layers will demonstrate a different biological regime.

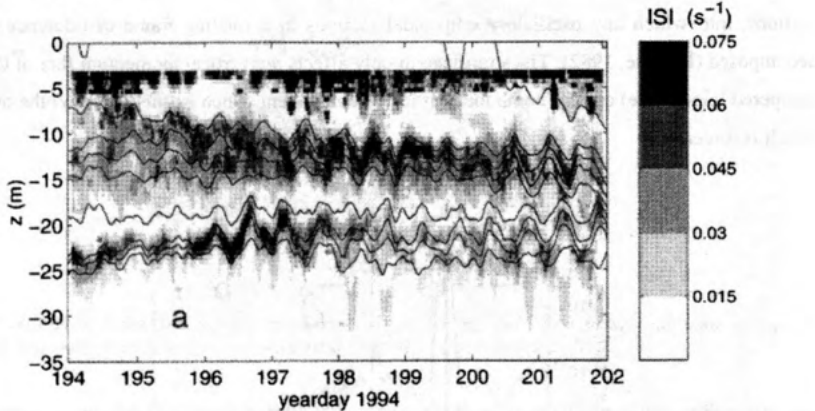


**Figure 3.** Mid-summer INP observations of upper 35 m of vertical current shear magnitude from ADCP data (grey scale) and stratification from thermistor string data (represented by isotherms every 1 °C) (from: van Haren, 2000).

## 3. Large-scale destabilization and stratification: exchange effects on phytoplankton

The canonical view of physical conditions for a phytoplankton bloom to occur (Sverdrup, 1953) was that stratification is a prerequisite prior to the onset of the spring bloom, because otherwise plankton would sink out of the photic zone. After the onset of stratification the photic zone would

become depleted of nutrients, causing a halt to the spring bloom, which could also not further develop below the main stratification because of light limitation. The idea was also that the late-summer or autumn phytoplankton bloom could not occur before the complete autumnal destruction of the stratification. The present North Sea observations proved otherwise, as the spring bloom occurred before the onset of stratification and the late summer bloom well before the autumnal destruction, but after the absolute minimum found in mid-summer (Fig. 4).

A minimum level of turbulence was required for the onset of the phytoplankton bloom in the central North Sea (van Haren et al., 1998). As this bloom consisted mainly of heavy diatoms, they needed turbulence to be transported into the shallow photic zone, briefly. As soon as (short spells of) stratification occurred, the bloom sank out of the photic zone. In the turbulent near-bottom layer however, this stock remained relatively fresh, because onset of stratification also caused sediment to sink out of the photic zone, allowing light to penetrate the bottom boundary layer.

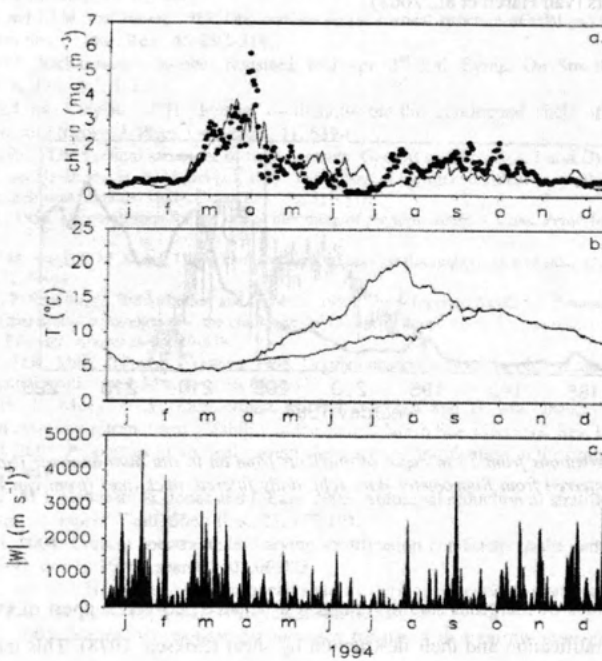


**Figure 4.** Some of yearlong INP data. **a.** Chlorophyll at 13 m from fluorometer data (dots; daily filtered) compared with numerical model data (solid line; Ruardij et al., 1997). **b.** Temperature measured at 2 m from the surface (solid) and at 2 m from the bottom (dashed). **c.** Wind speed cubed (from: van Haren et al., 1997).

Occasionally in summer, f-shear layer was less than 1 m vertically separated from a tidal shear layer. Also, shear was found maximum ( $180^\circ$  phase difference in current components), and implying slowly varying shear amplitude, across layers of largest N. These layers, of which two were found during high summer in the central North Sea, measured ~5 m in the vertical across

which a temperature difference of 5°C was found. In autumn in the northern North Sea similar stratified layers were observed thinning to ~1 m, so that N increased locally, but not following wind induced mixing due to an autumn storm, but after the sudden shut-down of inertial motion and, thus, inertial shear (van Haren and Howarth, 2004). Both sets of observations implied a necessary liaison between N and  $|S|$  so that the gradient Richardson number  $Ri = N^2/|S|^2$  is small, occasionally  $Ri < 0.25$ , mean  $Ri \approx 0.5$  at the depth of largest N. Thus, large stratification was found marginally stable with associated non-zero diapycnal transport (van Haren et al., 1999).

As a consequence, the late-summer phytoplankton bloom, mainly consisting of dinoflagellates, was observed well before the autumnal homogenization from surface-bottom: about nine days after an observed impulse of nutrients into the surface mixed layer, a peak was found in near-surface fluorescence in the central North Sea (Fig. 5). Likewise observations were made in the northern North Sea, although later in the year due to the larger distance between well-mixed near-bottom and near-surface layers (van Haren et al., 2003).

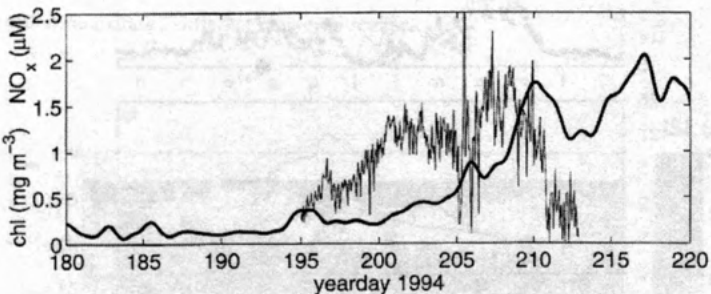


**Figure 5.** Hourly observations from 13 m depth of nutrients from an in situ auto-analyzer ( $No_x$ , thin line) and chlorophyll inferred from fluorometer data (chl, daily filtered, thick line) (from van Haren et al., 1999).

The observed values of marginal stability suggest a balance between support of (small-scale) internal waves by stratification and their destruction by shear (Eriksen, 1978). This internal wave breaking balance also implies that simple models can be used to estimate vertical exchange. Gargett (1984) inferred from microstructure measurements that vertical turbulent diffusivity  $K_v$  scales with  $N^{-1}$  and thus with  $|S|^{-1}$ , following  $\sim$ constant  $Ri$ . Assuming that internal wave breaking dominates diapycnal exchange and given that N varies between  $10^{-3} \text{ s}^{-1}$  (in winter under strong mixing conditions) and  $10^{-1} \text{ s}^{-1}$  (under summer stratification of  $5 \text{ }^\circ\text{C m}^{-1}$ ),  $K_v \approx 10^{-3} - 10^{-5} \text{ m}^2 \text{ s}^{-1}$ , as observed in the North Sea (van Haren et al., 1999; 2003). Even though interior diapycnal exchange rates are weak in summer, they are nevertheless O(100) times larger than molecular diffusion and

they are sufficient to maintain the steady increase of near-bottom temperature by some 6-8°C between April-October without the necessity of invoking lateral horizontal advection.

The lower end of these turbulent diffusivity values are also observed in the open ocean and they are considered typical for internal wave breaking. Although the North Sea is different from the ocean, some results obtained on f and D<sub>2</sub> shear in such shallow sea are also useful for understanding open ocean mixing, which is also primarily governed by inertial and tidal motions.

## References:

- Abarbanel, H.D.I., D.D. Holm, J.E. Marsden and T. Ratiu, 1984. Richardson number criterion for the non linear stability of three-dimensional stratified flow. *Phys. Rev. Lett.*, 52, 2352-2355.
- Eriksen, C.C., 1978. Measurements and models of fine structure, internal gravity waves, and wave breaking in the deep ocean. *J. Geophys. Res.*, 83, 2989-3009.
- Gargett, A.E., 1984. Vertical eddy diffusivity in the ocean interior. *J. Mar. Res.*, 42, 359-393.
- Howard, L.N., 1961. Note on a paper of John W. Miles. *J. Fluid Mech.*, 10, 509-512.
- Howarth, M.J., 1998. The effect of stratification on tidal current profiles. *Cont. Shelf Res.*, 18, 1235-1254.
- Howarth, M.J., J.H. Simpson, J. Sündermann and H. van Haren, 2002. Processes of Vertical Exchange in Shelf Seas (PROVESS). *J. Sea Res.*, 47, 199-208.
- Maas, L.R.M. and J.J.M. van Haren, 1987. Observations on the vertical structure of tidal and inertial currents in the central North Sea. *J. Mar. Res.*, 45, 293-318.
- Miles, J., 1987. Richardson's number revisited, in *Prepr. 3<sup>rd</sup> Intl. Symp. On Stratified Flows*, CalTech, Pasadena, CA, Feb. 3-5, 1-7.
- Millot, C. and M. Crépon, 1981. Inertial oscillations on the continental shelf of the Gulf of Lions- Observations and theory. *J. Phys. Oceanogr.*, 11, 639-657.
- Prandtl, D., 1982. The vertical structure of tidal currents, *Geophys. Astrophys. Fluid Dyn.*, 22, 29-49.
- Ruardij, P., H. van Haren and H. Ridderinkhof, 1997. The impact of thermal stratification on phytoplankton and nutrient dynamics in shelf seas: a model study. *J. Sea Res.*, 38, 311-331.
- Sverdrup, H.U., 1953. On conditions for the vernal blooming of phytoplankton. *J. Cons. Perm. Int. Explor. Mer.*, 18, 353-414.
- Van Haren, J.J.M. and L.R.M. Maas, 1987. Temperature and current fluctuations due to tidal advection of a front. *Neth. J. Sea Res.*, 21, 79-94.
- Van Haren, H., P. Ruardij, H. Ridderinkhof and D. Mills, 1997. The Integrated North Sea Programme (INP). In J.H. Stel et al. (eds) *Operational oceanography, the challenge for European cooperation*. Proceedings of the first Intl. Conf. On EuroGOOS, Elsevier, Amsterdam, 529-538.
- Van Haren, H., D.K. Mills, L.P.M.J. Wetsteijn, 1998. Detailed observations of the phytoplankton spring bloom in the straitifying central North Sea. *J. Mar. Res.*, 56, 655-680.
- Van Haren, H., L. Maas, J.T.F. Zimmerman, H. Ridderinkhof and H. Malschaert, 1999. Strong inertial currents and marginal internal wave stability in the central North Sea. *Geophys. Res. Lett.*, 26, 2993-2996.
- Van Haren, H. 2000. Properties of vertical current shear across stratification in the central North Sea. *J. Mar. Res.*, 58, 465-491.
- Van Haren, H., M.J. Howarth, K. Jones and I. Ezzi, 2003. Autumnal reduction of stratification in the northern North Sea and its impact. *Cont. Shelf Res.*, 23, 177-191.
- Van Haren, H. 2004. Current spectra under varying stratification conditions in the central North Sea. *J. Sea Res.*, 51, 77-91, doi:10.1016/j.seares.2003.06.003.
- van Haren, H. and M.J. Howarth. 2004. Enhanced stability during reduction of stratification in the North Sea. *Cont. Shelf Res.*, 24, 805-819, doi:10.1016/j.csr.2004.01.008.
- van Haren, H. 2005. Internal waves near the buoyancy frequency in a narrow wave-guide. *J. Sea Res.*, 53, 121-129.

the first time in history that the majority of the world's population has been born into a state of poverty. This is a state of affairs that must be changed.

It is also important to understand that the world's population is not evenly distributed. There are vast differences in the number of people living in different parts of the world. Some countries have very large populations, while others have very small ones. This is a fact that must be taken into account when considering the issue of world population control.

Another important factor to consider is the fact that the world's population is growing rapidly. This is a trend that must be reversed if we are to avoid a future of overpopulation and environmental degradation. We must take steps now to ensure that our planet can support a sustainable population in the future.

In conclusion, the issue of world population control is a complex one that requires a multi-faceted approach. It is a topic that must be addressed by governments, individuals, and organizations around the world. By working together, we can find solutions that will help to ensure a better future for all.

The world's population is currently estimated at approximately 7.8 billion people. This is a number that is projected to continue to grow in the coming years. While there are many factors that contribute to this growth, one of the most significant is the lack of access to education and healthcare. In many parts of the world, people do not have the opportunity to receive a good education or to access basic medical services. This lack of access leads to higher rates of poverty, disease, and death. It also leads to lower birth rates, which is a key factor in population growth. In addition to these social factors, there are also economic and environmental factors that contribute to population growth. For example, as economies develop and become more industrialized, they often experience a shift in their labor force from agriculture to manufacturing and services. This shift can lead to a decrease in agricultural land and a increase in urbanization, both of which can contribute to population growth. Additionally, as the world's climate changes due to global warming, it may become increasingly difficult for some populations to sustain themselves in their current locations. This could lead to migration and further population growth in other areas.

There are many different approaches to addressing the issue of world population control. One approach is to focus on improving access to education and healthcare. This can help to reduce poverty and improve overall health outcomes, which can lead to lower birth rates. Another approach is to promote family planning and responsible parenthood. This can help to ensure that families have the resources and support they need to make informed decisions about their reproductive choices. Additionally, there are efforts to address the underlying causes of population growth, such as economic development and environmental degradation. These efforts can help to create a more sustainable future for everyone.

In conclusion, the issue of world population control is a complex and multifaceted one. It requires a coordinated effort from governments, individuals, and organizations around the world. By working together, we can find solutions that will help to ensure a better future for all. It is important to remember that every person on this planet deserves to live a healthy, safe, and fulfilling life. Let us work towards creating a world where everyone can实现这个目标。

## Inter-basin exchange and mixing in the hypolimnion of a large lake: The role of long internal waves

Lars Umlauf<sup>1</sup> and Ulrich Lemmin<sup>2</sup>

<sup>1</sup> Baltic Sea Research Institute, Seestrasse 15, D-18119 Rostock, Germany.

<sup>2</sup> Laboratoire d'Hydraulique Environnementale, Faculté ENAC, EPFL, CH-1015 Lausanne, Switzerland.

We conducted a combined field and numerical study of the effects of episodic internal Kelvin-type waves on bottom boundary turbulence, and the exchange of a passive tracer between the main basin and the side basin of a large lake (Lake Geneva). High-resolution measurements of the vertical current structure near the entrance of the 25 km long and 70 m deep side basin revealed that hypolimnetic current speeds frequently exceed  $0.2 \text{ m s}^{-1}$ , leading to a turbulent bottom boundary layer several meters thick with logarithmic current profiles, and to a region of strong shear across the thermocline. The time series and vertical structure of the currents were reproduced by a three-dimensional numerical model of the lake. It was demonstrated that after episodes of strong winds from NE and SW, exchange flows due to internal Kelvin waves were able to temporarily half or double the hypolimnetic volume of the side basin, leading to an irreversible exchange of up to 40 percent of the hypolimnetic water in the side basin of Lake Geneva within only a few wave cycles. With the help of the numerical model, it was shown that the key mechanisms of exchange are horizontal dispersion by resolved scales and, to a small extent, shear dispersion in the bottom boundary layer. It is suggested that bottom boundary layer turbulence and the inter-basin exchange can explain the structural differences in the oxygen profiles observed in the side basin and the main basin, respectively.



## Dynamics of high-frequency internal waves in the littoral zone of a large lake

A. Lorke, F. Peeters, and J. Thorwart

*Limnological Institute, University of Konstanz, D-78464 Konstanz, Germany*

The dynamics of internal waves was studied in Lake Konstanz (Germany) by combining off-shore measurements of thermal stratification and isotherm displacement with high-frequency near-shore current velocity measurements within the littoral zone. The continuous observations covered the seasonal cycle from strong stratification in summer to deep convective mixing during winter. High-frequency internal waves were a persistent, but not continuous feature of the stratified part of the water column at both stations. The high-frequency limit of these waves followed the seasonal change of the buoyancy frequency. The most important result of the statistical analysis of the internal wave dynamics, however, was the strong correlation, found between the observation of high-frequency internal waves in the littoral zone and the passage of the basin-scale Kelvin wave at the off-shore station. The passage of the Kelvin wave, which had a period of about four days, was not detectable in the near-shore temperature and current velocity measurements directly, but only by the occurrence of strong high-frequency internal wave activity around the maximum buoyancy frequency. The measurements demonstrate the generation of internal waves by basin-scale motions in the pelagic and the subsequent radiation and dissipation of energy into the boundary regions of the lake.



## WAVE-INDUCED RESUSPENSION IN THE LITTORAL ZONE OF LAKE CONSTANCE

**Hofmann, H.**, Lorke, A. and Peeters, F.

Environmental Physics Group, Limnological Institute, University of Konstanz, Konstanz, Germany, [hilmar.hofmann@uni-konstanz.de](mailto:hilmar.hofmann@uni-konstanz.de)

The disturbance of the littoral zone by surface waves causes wide ranged consequences for the habitat, e.g. resuspension, transport and reallocation of sediment or abrasion of benthic organisms. The wave field and suspended sediment concentrations in the littoral zone of Lake Constance were monitored continuously using pressure sensors, a variety of acoustic current sensors as well as optical and acoustical backscatter measurements. The analysis of the wave field showed that the study site is mainly affected by waves from public cruising ship traffic. Wind-induced waves can have a strong impact on resuspension. However, wind events of sufficient intensity were infrequent during the observation period. Ship waves, in contrast, occurred regularly throughout the day which provided the opportunity to study numerous resuspension events. The investigation revealed how the interrelationship between individual wave groups, resuspension and sedimentation of particles varies with water depth and wave height. The continuous disturbances keep the sediment in motion, and thus prevent consolidation. Hence, sediment transport and reallocation by background currents can occur permanently.

the first time in 1993, and 2000. The following year, 2001, saw the first major breakthrough in the field of quantum computing.

Quantum computing is a relatively new field of research, and it has already made significant progress. In this article, we will explore the basic principles of quantum computing and its potential applications.

Quantum computing is based on the principles of quantum mechanics, which describe the behavior of matter and energy at the smallest scales. In classical computing, data is represented by bits, which can have a value of either 0 or 1. In quantum computing, data is represented by qubits, which can have a value of 0, 1, or both simultaneously. This allows quantum computers to perform many calculations at once, making them potentially much faster than classical computers. One of the most promising applications of quantum computing is in the field of cryptography. Quantum computers can break many of the encryption methods used today, such as RSA, which rely on the difficulty of factoring large numbers. They can also generate secure keys for encryption, making them a valuable tool for protecting sensitive information. Another potential application is in the field of simulation, such as simulating complex chemical reactions or predicting the behavior of subatomic particles. Quantum computers could also revolutionize fields like medicine, finance, and materials science by enabling us to solve problems that were previously impossible or impractical to solve with classical computers.

In conclusion, quantum computing is a rapidly advancing field with many exciting possibilities. As researchers continue to develop new technologies and algorithms, we can expect to see even more remarkable breakthroughs in the future.

INTERNAL WAVES & MIXING II

18 AUGUST 1944 120000Z

## VERTICAL MIXING IN SEASONALLY STRATIFIED CONTINENTAL SHELF SEAS.

Tom P Rippeth

University of Wales Bangor, School of Ocean Sciences, Askew Street, Menai Bridge,  
Anglesey, LL59 5AB, UK.

e-mail: [t.p.rippeth@bangor.ac.uk](mailto:t.p.rippeth@bangor.ac.uk)

### ***Abstract***

Over the past 2 decades measurements of turbulence in the marine environment have led to a more fundamental understanding of the continental shelf sea environment. In particular the new measurements have led to a more fundamental test of the turbulence closure schemes which are used to drive vertical exchange in state-of-the-art numerical models of continental shelf seas. In this contribution we will focus on the identification of and attempts to parameterise the key mechanisms and processes which drive mixing across the thermocline in seasonally stratified continental shelf seas.

### ***1. Introduction***

Coastal or continental shelf seas have an importance which is out of proportion to the relatively small fraction of the surface area of the global ocean which they occupy (~7%). They are areas of intense physical and biological activity. Flow in shelf seas is dominated by the barotropic tide involving strong tidal current streams – which are equivalent to daily hurricane force winds in the atmosphere. Overall shelf seas account for 60-70% of the global tidal energy dissipation (Egbert & Ray, 2000).

As a consequence of both high inputs of nutrients and their efficient use it is estimated that continental shelf seas account for 15-30% of the total oceanic primary production (Muller-Karger, 2005). They thus play a key role in the global carbon cycle, linking the terrestrial, oceanic and atmospheric carbon pools. Recent observations suggest that continental shelf seas export sufficient CO<sub>2</sub> to account for between 20 and 50% of the open ocean CO<sub>2</sub> storage through processes collectively known as the 'shelf sea pump'. These processes are only effective in removing CO<sub>2</sub> when they take place in the seasonally stratified areas (Thomas et al., 2004).

Key components of the shelf sea pump are the residual circulation and the levels of seasonal stratification and vertical mixing. Before stratification and circulation can be modelled realistically, and the response of the shelf sea system to climate change accurately predicted, the climatology of mixing must be established and the major mixing processes identified and parameterised. In this paper we shall look at the progress to date in the identification and representation of vertical mixing processes in numerical models of continental shelf seas with specific reference to the seasonally stratified regions.

### ***2. The Water Column Structure and Seasonal Cycle of Stratification***

The first order paradigm of water column structure and vertical mixing in the summer in shelf seas is well established; the water column structure is determined by the balance between surface heating – which acts to stratify the water column – and shear generated turbulence generated close to the sea bed, by the barotropic tide, and the sea surface by wind stress (Simpson & Hunter, 1974). This simple energetics model is closed by using an empirically determined mixing efficiency to relate the large scale circulation to the large scale stratification. The success of this model in correctly predicting the water column structure and the position of tidal mixing front (fig. 1), which separate the well mixed parts

of the water column from the stratified regions, provides two important results: (i) to a first order, seasonal changes in the water column structure in shelf seas are determined predominantly by vertical processes. (ii) That the boundary mixing, driven by tidal shear stresses and wind stress, are inefficient in mixing the water column. Ie. 0.37% of the energy loss to bottom drag by the barotropic tides is actually used in increasing the water column potential energy through mixing.

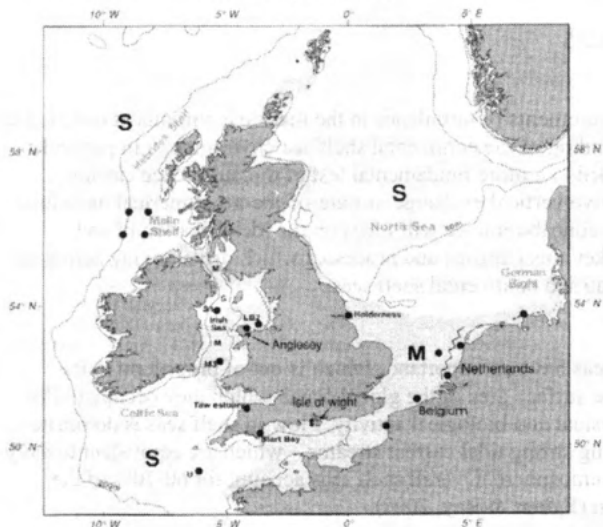


**Figure 1:** North West European Shelf. Lightly shaded areas remain well mixed all year round, whilst white areas stratify in the summer. Site S1 is marked.

The seasonal cycle of water column structure (fig. 2) shows a warm surface layer developing from early May and persisting until the autumnal breakdown of stratification, which occurs towards the end of October. In the intervening period the temperature of the bottom layer gradually increases, which may indicate the mixing of warmer surface water into the deep layer. Efforts to model the seasonal cycle of stratification at a number of locations in the North West European Shelf Seas have exposed the deficiencies of the boundary mixing model. The models use a turbulence closure scheme to simulate vertical exchange. The scheme basically consists of a diffusion equation;

$$\frac{\partial C}{\partial t} = \frac{\partial}{\partial z} \left( K_c \frac{\partial C}{\partial z} \right)$$

in which the diffusion coefficient provides closure between the water column structure and circulation, eg.;

$$K_c = func\left(\frac{N^2}{S^2}\right) + v_p$$

Where the  $func(N^2/S^2)$  is a function which uses stability criteria to determine the contribution to mixing from unstable flow and  $v_p$  is a background diffusivity.

In order to model correctly the observed seasonal cycle, values of  $v_p$ , which are several orders of magnitude larger than the molecular viscosity of heat, are required. When temperature is treated as a prognostic quantity, the values of  $v_p$  required vary significantly in both time and space (Elliott and Li, 1995; Pohlmann, 1996). The magnitude and variability of  $v_p$  suggest that the 'background' value is necessary to compensate for the lack of a spatially and/or temporally varying physical process(es) in the model.

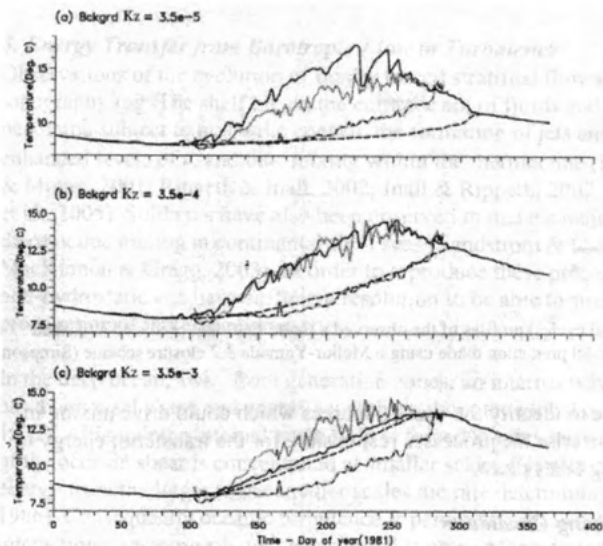


**Figure 2:** 1-D simulations of the seasonal cycle of thermal stratification at Irish Sea station S1. The lighter lines represent the surface (solid) and 100 m (broken) temperatures. The darker lines represent the model simulations. The results demonstrate the sensitivity of the model to the value of the background  $v_p$  selected.

$$a) v_p = 0.35 \text{ cm}^2 \text{s}^{-1}$$

$$b) v_p = 3.5 \text{ cm}^2 \text{s}^{-1}$$

$$c) v_p = 35 \text{ cm}^2 \text{s}^{-1}$$

### 3. The Vertical Structure of the Rate of Dissipation of Turbulent Kinetic Energy, $\varepsilon$

A more fundamental test of the vertical exchange schemes used in the numerical models is through direct comparison of observed and simulated profiles of a turbulence parameter. Over the past decade we have been making direct estimates of  $\varepsilon$ , the rate of dissipation of turbulent kinetic energy, from velocity microstructure using a loosely tethered profiler (Rippeth et al., 2003). Observations at well mixed locations (ie. Where the bottom boundary layer extends to the surface) in the Irish Sea and Georges Bank are easily reproduced using standard turbulence closure models (Simpson et al., 1996; Burgett et al., 2000). However, this is not the case for thermally stratified shelf sea locations.

The tidal mean profile of  $\varepsilon$  for a station in the stratified portion of the Western Irish Sea (S1, figure 1) shows nearly all of the dissipation is taking place in the bottom boundary layer, where there is a quarter diurnal variation with maxima of  $\varepsilon \sim 10^{-3} \text{ Wm}^{-3}$  corresponding to the maximum flood and ebb tidal currents. The bottom boundary layer, in this case, is about 35m thick. Above this layer is a diffuse thermocline, where  $\varepsilon \sim 10^{-5} \text{ Wm}^{-3}$ . In simulations of  $\varepsilon$  made using a model with realistic forcing and a Mellor-Yamada 2.2a turbulence closure scheme (in which a local equilibrium between TKE production and dissipation and work against buoyancy forces is modified by the vertical diffusion of TKE) there is good qualitative and quantitative agreement with the observations from the well mixed bottom boundary layer (fig. 3), but  $\varepsilon$  is underestimated by 4 orders of magnitude in the thermocline region (Simpson et al., 1996). The implication is again a missing source of turbulent kinetic energy within the thermocline. In order to force the model to reproduce the correct mid-water dissipation a (tuned) lower limit for turbulent kinetic energy ( $q^2$ ) is set (Burchard et al., 1998). This limitation in  $q^2$  can be interpreted as a crude parameterisation of internal wave breaking within the thermocline.

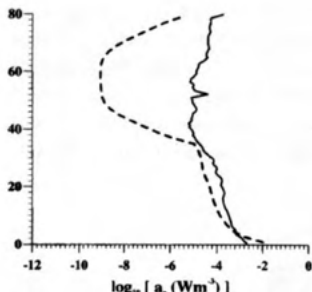


**Figure 3:** Mean (averaged of 2 tidal cycles) profiles of the observed  $\varepsilon$  (solid line) and predicted  $\varepsilon$  (dashed line) from Irish Sea station, S1. Model prediction made using a Mellor-Yamada 2.2 closure scheme (Simpson et al., 1996).

Clear challenges are therefore to identify the energy sources which could drive mixing in the thermocline and to parameterise the processes responsible for the transfer of energy to the scales at which the mixing takes place.

#### 4. Potential Thermocline Mixing Candidates

Two candidate mechanisms have been identified as potentially contributing to mixing within the shelf sea thermocline; internal tides generated when the barotropic tide forces stratified flow over rough topography, and inertial oscillations generated by abrupt changes in the wind direction or sea breezes (van Haren et al., 1999; Rippeth et al., 2002). These mechanisms are thought to be considerably more effective at driving mixing within the thermocline because they inject energy into the regions of strong gradient (Stigebrandt & Aure, 1989, estimate a mixing efficiency of  $\sim 6\%$  for an internal tide in fjords).

The potential of the internal tide in powering pelagic mixing has been demonstrated for a number of continental shelf seas. Rippeth et al. (2005) show that although the internal tide generated at the shelf break to the west of the UK only contributes  $\sim 0.2\%$  to the total tidal energy budget of the NW European Shelf Seas, its contribution to increasing the water column potential energy is potentially comparable to that of the barotropic tide in the seasonally stratified shelf region to the west of the UK. Energy dissipation rate estimates of  $10^{-3} - 10^{-2} \text{ W m}^{-3}$  have been made, based on the divergence of the internal tide across a number of continental shelves (Holloway et al., 2001; Sherwin, 1988; Largier, 1994; Sharples et al., 2001). Similarly inertial oscillations have been shown to be potentially important mechanisms for mixing across the thermocline (Sherwin, 1987; van Haren et al., 1999).

Direct measurements of  $\varepsilon$  show thermocline dissipation rates  $\sim 10^{-4} - 10^{-2} \text{ W m}^{-2}$  at various mid-shelf locations (Simpson et al., 1996; Rippeth & Inall, 2002; MacKinnon & Gregg, 2003; Rippeth et al., 2005). Diffusion coefficients inferred from these measurements ( $K_p = 0.2\varepsilon/N^2$ ; Osborn, 1980) have values of order  $1 \text{ cm}^2 \text{s}^{-1}$  (ie. Similar to the values of  $v_p$  required for the correct prediction of the seasonal cycle of stratification in section 2).

The results from this and the previous two sections provide significant quantitative evidence to suggest that the enhanced levels of  $\varepsilon$ , and thus mixing, within the seasonally stratified continental shelf sea thermocline, result from the damping of externally forced internal oscillations. In terms of the development of models to simulate mixing within seasonally stratified shelf seas an important question arises: do the models fail to reproduce the thermocline mixing because they are not correctly forced, or is it because the physics within the model does not correctly represent the energy transfer mechanisms, or both?

### **5. Energy Transfer from Barotropic Flow to Turbulence**

Observations of the evolution of tidally forced stratified flow and  $\varepsilon$  close to rough topography (eg. The shelf break, the entrance sill of fjords and shelf banks) show flow becoming subject to hydraulic control, the formation of jets and lee waves and very much enhanced levels of  $\varepsilon$ , and thus mixing within the thermocline (Holloway et al., 2001; Nash & Moum, 2001; Rippeth & Inall, 2002; Inall & Rippeth, 2002; Arneborg et al., 2004, Inall et al., 2005). Solibores have also been observed to make a major contribution to thermocline mixing in continental shelf seas (Sandstrom & Oakey, 1995; Inall et al., 2000; MacKinnon & Gregg, 2003). In order to reproduce these processes the models should be non-hydrostatic and have sufficient resolution to be able to simulate the structure and propagation of these phenomena.

In the deep ocean, away from generation zones, an internal wave spectrum exists which has a universal shape and energy level throughout the global ocean (Garrett & Munk, 1972). Although the internal wave field is forced at tidal and near inertial frequencies, most of the oceanic shear is concentrated at smaller scales (Gargett et al., 1981) with the flux of energy from the larger to the smaller scales the rate determining process (Heneyey et al., 1986). Consequently oceanic turbulence is parameterised in terms of wave-wave interactions, an approach which has bought some success in reproducing turbulence observations in the weakly stratified oceanic thermocline (eg. Polzin et al., 1995). However, such parameterisations fail when applied to shelf seas locations (MacKinnon & Gregg, 2005).

In contrast, the continental shelf sea thermocline is marginally stable with Richardson number  $\sim 1$  (van Haren et al., 1999; Rippeth et al., 2005) suggesting mixing may be controlled by instabilities of the large-scale wave modes as their velocity becomes comparable to their phase speed. D'Asaro & Lien (2000) estimate that for typical shelf sea depths and stratification the transition between stratified turbulence and wave turbulence corresponds to  $\varepsilon_{\text{trans}} \sim 10^{-4} \text{ W m}^{-3}$  (a value of the same order as those observed in the seasonally stratified shelf sea thermocline; Rippeth et al., 2005). Whilst turbulence closure schemes include the correct physics to be able to simulate stratified turbulence (providing they are correctly forced), when  $\varepsilon$  falls below the transfer threshold they will fail to correctly simulate the energy transfer through the internal wave spectrum.

### **6. Summary**

It has recently been suggested that the shelf seas play a significant role in the oceanic draw down of CO<sub>2</sub>. As CO<sub>2</sub> drawdown only takes place in the stratified portions of the continental shelf seas, the intensity of thermocline mixing in these areas will be an important parameter in determining the magnitude of the shelf sea pump. Attempts to simulate (i) the seasonal cycle of thermal stratification and (ii)  $\varepsilon$  have clearly demonstrated that the models lack the necessary physical processes to be able to simulate this mixing correctly. Incorporation of realistic simulations of internal tides, inertial oscillations, solibores and lee wave formation over bumps into models thus presents a clear challenge for the shelf sea modelling community.

### **7. Reference List**

- Arneborg, L, CD Janzen, B Liljebladh, TP Rippeth, JH Simpson & A Stigebrandt (2004). *J. Phys. Oceanogr.*, **34**, 1697-1691.
- Burchard, H, O Peterson, TP Rippeth (1998). *J. Geophys Res.*, **103**(C5), 10543-10554.
- Burgess RL, D Hebert & NS Oakey (2001). Vertical Structure of the southern flank of Georges bank. *J. Geophys. Res.*, **106**, 22545-22558.
- D'Asaro, E, R-C Lien (2000). *J. Phys. Oceanogr.*, **30**, 1669-1678.

- Egbert, GD & RD Ray (2000). *Nature*, **405**, 775-778.
- Elliott, AJ and Z Li (1995). *Cont. Shelf Res.*, **40**, 265-280.
- Gargett, AJ, PJ Hendricks, TB Sanford, TR Osborn & AJ Williams (1981). *J. Phys Oceanogr*, **11**, 1258-1271.
- Garrett, CJR & WH Munk (1975). *Annu. Rev. Fluid Mech.*, **11**, 339-369.
- Holloway, P., PG Chatwin & P Craig (2001). *J. Phys. Oceanogr.*, **31**, 1182-1199.
- Heney, F, J Wright & SM Flatté (1986). *J. Geophys. Res.*, **91**, 8487-8495.
- Inall, ME & TP Rippeth (2002). *Environmental Fluid Mech*, **2**, 219-240.
- Inall, ME, TP Rippeth, C Griffiths and P Wiles (2005). *Geophys Res Lett*, **32**, L08607, doi:10.1029/2004GL022289.
- Inall, ME, TP Rippeth & TJ Sherwin (2000). *J. Geophys. Res.*, **105**, 8687-8705.
- Largier, J (1994). *J. Geophys. Res.*, **99**, 10023-10034.
- MacKinnon, J, & MC Gregg (2003). *J Phys Oceanogr.*, **33**, 1476-1492.
- MacKinnon, J, & MC Gregg (2005). *J Phys Oceanogr. (In Press)*
- Muller-Karger et al. (2005). *Geophys. Res. Lett*, **32**, L01602, doi:10.1029/2004GL021346.
- Osborn, T (1980). *J Phys Oceanogr.*, **10**, 83-89.
- Pohlmann, T (1996). *Cont. Shelf Res.*, **16**, 147-161.
- Rippeth, TP & ME Inall (2002). *J. Geophys. Res.*, **107(C4)**, doi:10.1029/2000JC00761.
- Rippeth, TP, M Palmer, JH Simpson, NR Fisher & J Sharples (2005). *Geophys Res Lett*, **32**, L05602, doi:10.1029/2004GL022104
- Rippeth, TP, JH Simpson, R Player, M Garcia (2002). *Cont. Shelf Res.*, **22**, 247-265.
- Rippeth, TP, JH Simpson, E Williams & ME Inall (2003). *J. Phys. Oceanogr.*, **33**, 1889-1901.
- Simpson JH, WR Crawford, TP Rippeth, A Campbell & JVS Cheok (1996). *J. Phys. Oceanogr.*, **26**, 1579-1590.
- Sandstrom, H & NS Oakey (1995). *J. Phys. Oceanogr.*, **25**, 604-614.
- Sharples, J, CM Moore & E Abrahams (2001). *J. Geophys. Res.*, **106**, 14069-14081.
- Sherwin, TJ (1987). *Cont. Shelf Res.*, **7**, 292-213.
- Sherwin, TJ (1988). *J. Phys. Oceanogr.*, **18**, 1035-1050.
- Simpson JH and J Hunter (1974). *Nature*, **250**, 404-406.
- Stigbrandt, A & J Aure (1989). *J. Phys. Oceanogr.*, **39**, 917-926.
- Thomas, H, Y Bozac, K Elkalay, HJW Baar (2004). *Science*, **304**, 1005-1008.
- Van Haren, H, L Mass, JTF Zimmerman, H Ridderinkhof & H Malschaert (1999). *Geophys. Res. Lett*, **26**, 2993-2996.

## Numerical simulations of shoaling internal solitary waves in tilting tank experiments

Kevin G. Lamb<sup>1</sup>, Leon Boegman<sup>2</sup>, Greg Ivey<sup>3</sup>

<sup>1</sup>*University of Waterloo, Waterloo, Ontario, Canada*

<sup>2</sup>*Queen's University, Kingston, Ontario, Canada*

<sup>3</sup>*University of Western Australia, Crawley, Australia*

### 1. Introduction

Internal solitary wave (ISW) trains have been observed in many lakes (e.g., Farmer 1978. See also references in Boegman *et al.* 2005 and Vlasenko & Hutter 2002). They are indirectly generated by winds which blow warm surface water to the lee of the lake creating a tilted thermocline. When the wind dies down basin scale internal waves start propagating. Nonlinearity and dispersion results in the formation of the ISW trains. An important problem in physical limnology is understanding the energy content of these high-frequency waves and the consequences of their breaking when they reach the shore. These waves are inherently non-hydrostatic and of short wave length making them difficult to simulate in lake-scale numerical models. The high resolutions and large domains required to simulate the formation, run-up and breaking of solitary wave makes the use of a two-dimensional model highly desirable. Two-dimensional models are currently the norm in such simulations (Fringer & Street 2003, Vlasenko & Hutter 2002). This presents problems if one of the objectives is to predict the amount of mixing associated with breaking ISWs, an inherently three-dimensional process.

In order to elucidate the breaking of shoaling ISWs Boegman *et al.* (2005) did a series of laboratory experiments using a tilting tank. In this paper some preliminary results of two-dimensional non-hydrostatic simulations of one of these experiments are presented. Comparisons of the amount of mixing predicted by the simulations with that in the laboratory experiments is made.

### 2. Experiments

The experiments were carried out in a sealed acrylic tank 6 m long, 0.3 m wide and 0.29 m deep. The tank was filled with a two-layer stratification using fresh and saline water. A sloping bottom with a slope of 0.1 or 0.15 was placed at one end of the tank. After filling with water the tank was rotated by a small angle and the fluid was allowed to come to rest. Then, the tank was rapidly rotated to the horizontal. This resulted in an initial state with a sloping pycnocline. The adjustment of this

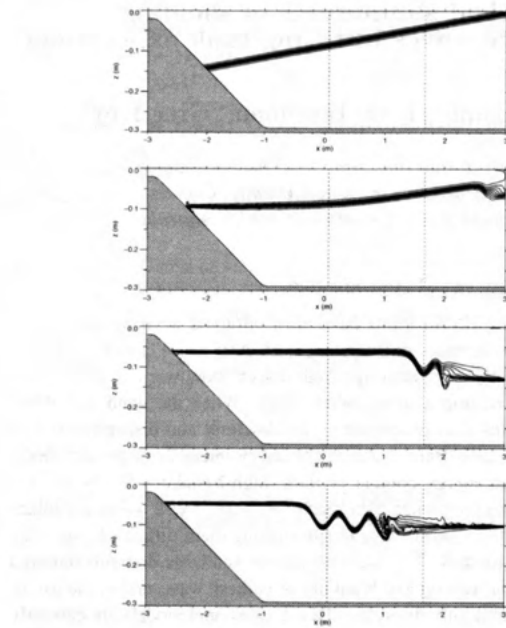


Figure 1: Density contours for simulation of experiment 14.09.04 at  $t = 0, 20, 40$  and  $60$  s. Vertical lines indicate positions of wave guages. Case 11.

state was measured with three ultrasonic wave guages (Michallet & Berthélémy 1997) and using a digital camera (Boegman *et al.* 2005).

### 3. The numerical model

The numerical model used in this study is a modified version of the non-hydrostatic model described in Lamb (1994), which uses the Boussinesq approximation. The model uses a rigid lid with the surface at  $z = 0$ . The rotation of the Earth is ignored due to the short length and time scales considered. The effects of rotation of the tank about the horizontal  $y$  axis are included because the fluid in the tank rotates relative to the tank as the tank is brought to the horizontal at the

beginning of the experiment. The model equations are

$$\frac{D\vec{U}}{Dt} + 2\frac{d\theta}{dt}(w, -u) = -\vec{\nabla}p - \rho\vec{g}(\sin\theta, \cos\theta) - \frac{d^2\theta}{dt^2}(z, -x) + \vec{F}_u \quad (1)$$

$$\frac{D\rho}{Dt} = F_\rho, \quad (2)$$

$$\vec{\nabla} \cdot \vec{U} = 0, \quad (3)$$

where  $\vec{U} = (u, w)$  is the velocity vector in a reference frame fixed with the tank,  $u$  and  $w$  being the horizontal ( $x$ ) and vertical ( $z$ ) components.

The scaled density and pressure  $\rho$  and  $p$  are related to the fluid density and pressure  $\rho^*$  and  $p^*$  via  $\rho^* = \rho_o(1 + \rho)$  and  $p^* = \rho_o(-gz + p)$  where  $\rho_o$  is the reference density. The angle made by the along-tank  $x$  axis from the horizontal is  $\theta(t)$  is measured counterclockwise about the negative  $y$ -axis. The centripetal acceleration  $\vec{\Omega} \times (\vec{\Omega} \times \vec{x})$ , where  $\vec{\Omega} = (0, -d\theta/dt, 0)$ , which has the form of a gradient, has been absorbed into the pressure. The viscous and diffusive terms have the form

$$\vec{F}_u = \left(K_u \vec{U}_z\right)_z + Kh_u \vec{U}_{xx} \quad (4)$$

$$\vec{F}_\rho = \left(K_\rho \rho_z\right)_z + Kh_\rho \rho_{xx} \quad (5)$$

Terrain following (sigma) coordinates are used and  $\chi$  is the horizontal terrain-following coordinate. No-slip boundary conditions are used for the velocity field along the bottom and top boundaries (the tank is completely filled with fluid) and along the end walls. No-flux boundary conditions are used for the density.

Because terrain following coordinates are used the fluid depth cannot be reduced to zero at the left end of the tank as in the laboratory situation. The bottom of the tank is at

$$z = -0.02 - 0.5m \left( \operatorname{itanh}(x, x_1, d) - \operatorname{itanh}(x, x_2, d) \right), \quad (6)$$

where

$$\operatorname{itanh}(x_k, a, s) = \int_{-\infty}^{x_k} 1 + \tanh\left(\frac{x'_k - a}{s}\right) dx'_k,$$

is a function which smoothly changes from 0 to a constant slope of 2 at  $x = a$  over a characteristic distance  $s$ . For these simulations

$$x_1 = 0.02/m, \quad (7)$$

$$x_2 = x_1 + 0.27/m, \quad (8)$$

$$d = 0.05, \quad (9)$$

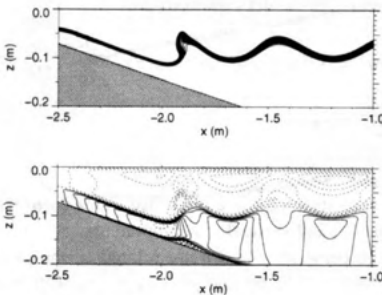


**Figure 2:** Onset of first breaking event at  $t = 84$ . Upper panel shows the density field, lower panel is the horizontal velocity field with solid/dashed contours indicating positive/negative velocities. Case 11.

where the slope of the sloping part of the bottom is

$$m = \frac{0.29}{l}, \quad (10)$$

where  $l = 2$  or  $3$  m is the length of the sloping bottom in the laboratory experiment. All terms in these expressions have units of meters.

The initial stratification has the form

$$\rho = \frac{\delta\rho}{2} \tanh \frac{z - \gamma x - z_{pyc}}{d_{pyc}}. \quad (11)$$

Here  $\delta\rho$  is the density jump across the pycnocline, scaled by the reference density  $\rho_o$ ,  $d_{pyc}$  gives the thickness of the pycnocline and  $\gamma$  is the initial slope of the pycnocline relative to the along-tank axis.

The laboratory experiments begin with the tank, initially inclined at an angle  $\theta_o$  to the vertical, being rapidly brought to the horizontal. Because the tank is brought to the horizontal in a few seconds baroclinic generation of vorticity is negligible and hence the fluid, which is initially irrotational, remains irrotational outside of the viscous boundary layers adjacent to the tank boundaries. As a consequence, the fluid in the tank rotates relative to the tank as the tank is brought to the horizontal as if the density is constant. The movement of the fluid in the tank can be estimated on this basis. For an angle  $\theta_o = 1.56^\circ = 0.0274$  rad corresponding to experiment 14\_09\_04 which is discussed below, the fluid moves about 0.75 cm along the upper and lower boundaries except within about 30 cm (tank depth) of the end walls, and it moves about 0.5 cm along the end walls at the mid-depth.

case	<i>I</i>	<i>J</i>	max $\Delta t$ (s)	$K_u$ ( $10^{-6}$ m s $^{-1}$ )	$K_\rho$ ( $10^{-6}$ m s $^{-1}$ )	$K_{h\rho}$ ( $10^{-6}$ m s $^{-1}$ )
5	2400	160	0.015625	2.0	0.1	2.0
10	2400	160	0.015625	2.0	0.01	2.0
11	4000	200	0.015625	2.0	0.01	2.0
15	2400	160	0.00390625	2.0	0.01	2.0
16	2400	160	0.0078125	2.0	0.01	2.0
17	2400	160	0.0078125	2.0	0.01	0.01

Table 1: Subsample of some of the simulations of experiment 14\_09\_04.  $I$  and  $J$  are the number of grid points in the horizontal and vertical,  $\Delta t$  is the maximum time step allowed,  $K_u$  and  $K_\rho$  are the vertical viscosity and diffusivity,  $K_{h\rho}$  is the horizontal diffusivity. The horizontal viscosity was equal to the vertical viscosity in all of these runs.

### 3. Results: Experiment Exp14\_09\_04

This experiment begins with downwelling over the slope. The initial density field has the form (13) with  $\delta\rho = 0.0203$ ,  $\gamma = 0.0274$ ,  $z_{pyc} = -0.0871$  m and  $d_{pyc} = 0.0079$  m. The tank lies between  $x = -3$  m and  $x = 3$  m with the surface at  $z = 0$ . For the runs discussed here the tank was not rotated, i.e.,  $\theta = 0$  in equation (1), as the effects of rotating the tank were found to be negligible.

Figure 1 shows a sequence of density contour plots from 0 to 60 s illustrating the formation of a solitary wave train. The vertical dashed lines in the figures indicate the location of two of the wave gauges which were used to measure the height of the pycnocline in the laboratory experiments. In the left half of the tank the pycnocline thins as it rises. At the right end of the tank the pycnocline thickens. This is largely due to the flow in the corner: an inviscid simulation gave a similar result. Figure 2 shows the onset of the first breaking event at time  $t = 84$  s. The density field is shown in the upper panel while the horizontal velocity field is shown in the lower panel. A small separation bubble along the bottom boundary can be seen immediately below the breaking wave.

A large number of model runs have been done with different resolutions, time steps, viscosities and diffusivities. Details of six of these are presented in table 1. The time evolution of the background potential energy (BPE) for these cases is shown in figure 3. The BPE is obtained by sorting the density field to obtain a horizontally uniform background density  $\rho_r(z)$  and computing the potential energy of the sorted density field. The increasing BPE corresponds to a permanent thickening of the pycnocline. In the figure it can be seen that the BPE increases very slowly for

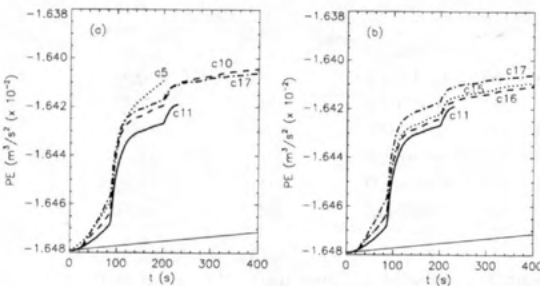


Figure 3: Time evolution of the BPE for six different simulations of experiment 14\_09\_04. The straight line indicates the expected time evolution of the BPE for a fluid at rest with a diffusivity of  $10^{-7} \text{ m}^2 \text{ s}^{-1}$ .

the first 20–40 s. For comparison a line indicating the theoretical increase in BPE for a rest state, assuming a flat bottom, is shown for a diffusivity of  $10^{-7} \text{ m}^2 \text{ s}^{-1}$ . This is approximately 10 times larger than the diffusivity of salt. Thereafter the growth rate increases until  $t \approx 90$  s after which it grows very rapidly. This rapid growth corresponds to the first breaking event during which several solitary wave break on the slope. A second, weaker, breaking event occurs at about  $t = 200$  s. The only difference between cases 5 and 10 is in the vertical diffusivity. Lowering the diffusivity from  $10^{-7}$  to  $10^{-8} \text{ m}^2 \text{ s}^{-1}$  significantly lowers the increase in BPE in the first breaking event. Comparing cases 10 and 11, which differ only in the resolution, shows that increasing the resolution also decreases the amount mixing in the first breaking event and that case 10 is under resolved. Case 11 took about one week to run making longer or higher resolutions runs difficult. Cases 10, 15 and 16 differ only in the time step. The latter two cases, with the smaller time steps are similar. Cases 17 and 10 differ in the horizontal diffusivity  $Kh_\rho$ , with  $Kh_\rho$  being 200 times larger in case 10. Comparison of these two cases indicates that the results are not very sensitive to  $Kh_\rho$ .

Figure 4 compares the density profiles measured before and after the laboratory experiment with the sorted density profiles  $\rho_r(z)$  from the numerical simulations. The initial experimental and numerical profiles are slightly different. Results from two cases (11 and 17) are shown. Both indicate that the final pycnocline is a bit thicker than in the experimental results, particularly as the experimental measurement was taken after the water in the tank was at rest. Note, however, that for case 17 the density profiles at  $t = 300$  and 400 s are very similar. Little further thickening can be expected.

# ADVECTION AND THICKENING OF A PYCNOCLINE WATER IN LAB TANKS

John D. Marshall, Michael J. McGuinness, Michael C. Mackay,  
Mark R. Wilson and Michael J. Stastna

37

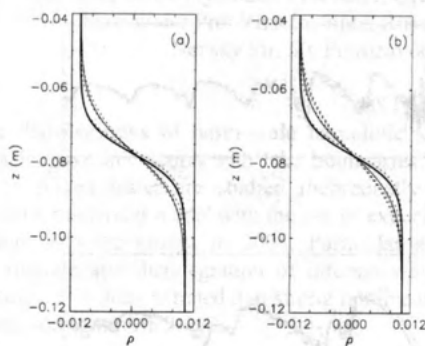


Figure 4: Comparison of density profiles for experiment 14.09.04. Only a portion of the water column is shown. Solid curves are lab measurements taken before and after the experiment. Dotted curves are numerical results every 100 s starting at  $t = 0$ . (a) Case 11, numerical results at  $t = 0, 100$  and  $200$  s. (b) Case 17, numerical results at  $t = 0, 100, 200, 300$  and  $400$  s.

Figure 5 compares the interface displacement (relative to the undisturbed location of the pycnocline when the tank is level) measured in the laboratory (solid) and in the numerical experiments (dotted) at two different locations. Panels (a) and (b) show the results at  $x = 0.07$  m for cases 11 and 17 respectively. Panels (c) and (d) are the results at  $x = 1.67$  m. Case 17, which ran for 400 s, shows that the general decay of the basin scale wave is captured very well in the simulations. One noticeable difference is that the amplitudes of the solitary waves are larger in the numerical simulations and, at  $x = 1.67$ , there are more of them in the first group ( $t = 50$ –75 s). Another difference is that at  $x = 1.67$  the interface in the numerical simulations is above that in the laboratory experiments between about  $t = 55$  and  $t = 140$  s. This may be in part due to the difference in how the interface height is computed: in the simulations the interface height is given by the zero density contour (centre of the pycnocline), in the laboratory experiments it is measured by an ultrasonic probe which measures the travel time of an acoustic pulse.

## 4. Summary

The numerical model simulates several aspects of the tilting tank experiments quite well. The overall energy decay is simulated very well however the thickening of the pycnocline is overestimated. In addition, the amplitudes of the solitary waves may be over-predicted in the model simulations, however this could be due in part to measurement differences. Further model tests are being done to see if the use of

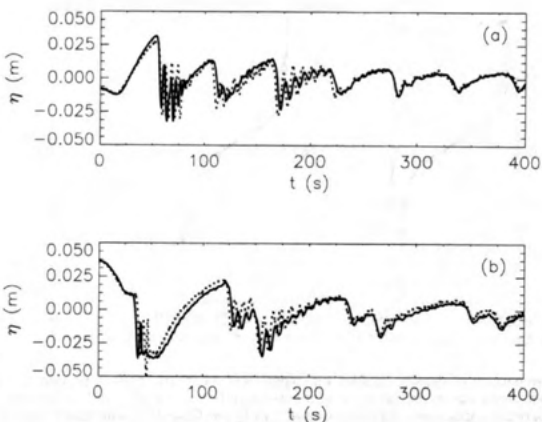


Figure 5: Comparison of interface heights for experiment 14.09.04. Solid curves are lab measurements, dotted curves are results from numerical simulations (case 17). (a)  $x = 0.07$ . (b)  $x = 1.67$ .

additional terms (e.g., Rayleigh damping) in the momentum equations or a subgrid turbulence model (e.g., a Smagorinsky model) can lead to improvements.

Model runs with 600 grid points in the horizontal had significant non-monotonic BPE, indicating that the numerical error is too large. Simulations with 1200 grid points had almost monotonic BPE, however there were small oscillations during the first strongest breaking event.

#### References

- Beogman, L., Ivey, G. N., & Imberger, J. 2005. The degeneration of internal waves in lakes with sloping topography. *Limnol. Oceanogr.* In Press.
- Farmer, D. M. 1978. Observations of long nonlinear waves in a lake. *J. Phys. Oceanogr.* 8:63–73.
- Fringer, O. B., Street, R. L. 2003. The dynamics of breaking progressive interfacial waves. *J. Fluid Mech.* 494, 319–353.
- Lamb, K. G. 1994. Numerical experiments of internal wave generation by strong tidal flow across a finite amplitude bank edge. *J. Geophys. Res.*, 99, 843–864.
- Vlasenko, V. II, & Hutter, K. 2002. Transformation and disintegration of strongly nonlinear internal wave by topography in stratified lakes. *Ann. Geophys.* 20, 2087–2103.

## OBSERVATIONS AND MODELLING OF NONLINEAR INTERNAL WAVES IN LAKE ONEGA

Vasiliy Vlasenko<sup>a</sup>, Nikolay Filatov<sup>b</sup>, Mikhail Petrov<sup>b</sup>, Arkady Terzhevsk<sup>b</sup>,  
Roman Zdrovennov<sup>b</sup>, and Nataliya Stashchuk<sup>a</sup>

<sup>a</sup>School of Earth, Ocean and Environmental Sciences, Plymouth University, Drake Circus, PSQ A504 Plymouth, PL4 8AA, UK. E-mail: vvlasenko@plymouth.ac.uk

<sup>b</sup>Northern Water Problems Institute, Russian Academy of Sciences, Alexander Nevsky Str. 50, Petrozavodsk, 185003, Russia

### ABSTRACT

The degenerations of basin-scale baroclinic seiche into short-period internal waves, their successive interaction with lake boundaries, as well as breaking with generation of spots of mixed water are studied theoretically on the basis of a fully non-linear non-hydrostatic numerical model with the use of experimental data obtained during the summer campaign in Lake Onega in 2004. Particular attention was paid to the processes of transformation and disintegration of internal waves during their shoaling near the lake boundaries. It is demonstrated that strong nonlinear wave-topography interaction can affect the background stratification.

### INTRODUCTION

After storms, internal waves in lakes may take the form of an internal surge or packets of internal solitons, generated by the nonlinear steepening of a basin-scale finite-amplitude wave (Thorpe, 1977; Farmer, 1978; Wiegand and Carmack, 1986). Since these solitons are much shorter in length than the wind-induced initial large-scale thermocline displacements, their generation results in a transfer of energy within the internal wave field from large to small scales. As a confirmation of such an energy sink, field observations show that wind-forced basin-scale waves decay at a rate far greater than can be accounted for simply by internal dissipation (Imberger, 1994; Stevens et al., 1996).

An additional evidence of this pathway for energy from large to small scales was reported recently by Horn et al. (2001). In this paper the authors concluded that one of the more probable scenarios of the basin-scale wave disintegration in long narrow lake is its nonlinear steepening and fission into series of solitary waves. These waves further must inevitably encounter lake boundaries where they eventually destroy (Vlasenko and Hutter, 2002). During the breaking event, water stratification is changed in the place of wave breaking. In the present study, we apply the mathematical model to examine the effect of the bottom topography and nonlinearity on energy cascading from the basin-scale internal waves to short-period internal waves and farther – to turbulence and mixing. The model is applied to the conditions of Lake Onega where during the summer campaign in 2004 some experimental data on the baroclinic response of lake to the wind forcing were collected.

### 2. FIELD MEASUREMENTS

The field campaign was performed in Lake Onega, Karelia, Russia, on 18–28 July 2004. Lake Onega (Fig. 1a) is the second largest lake in Europe after Lake Ladoga. The area of the lake is 9800 km<sup>2</sup>, the volume 291.2 km<sup>3</sup>, with maximum and mean depths of 127 and 30 m, respectively. To register the vertical thermal structure during a probable shoaling of nonlinear internal waves, the following equipment was installed along the line with depths from 10 to 32 meters in the Bolshoe Onego Bay (Fig. 1b): Thermistor chains with sampling interval 5 min were installed at stations 1, 3 and 5; Currents were measured by current meters with time interval of 10 and 5 min at stations 4 and 5, respectively; Free

falling CTD profiler was used for every 20-min temperature profile measurements at station 4.

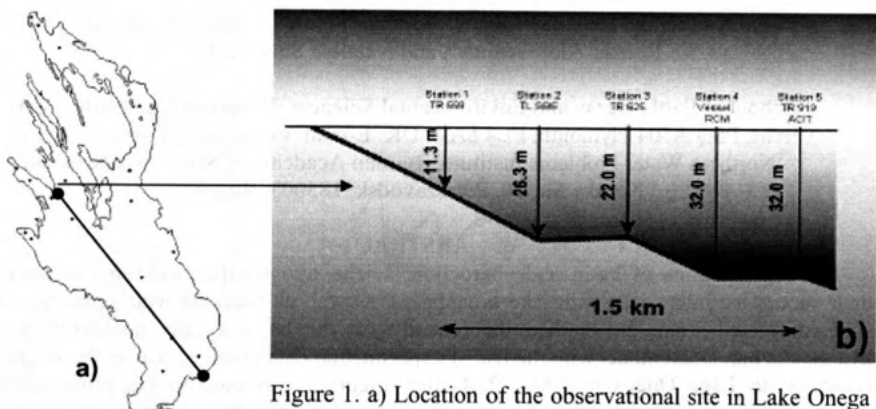


Figure 1. a) Location of the observational site in Lake Onega in July 2004. b) Positions of stations with respect to the shore.

Weather conditions during the period of field measurements were close to calm. Average wind velocity was about  $3 \text{ m}\cdot\text{s}^{-1}$ , with maximum up to  $5\text{-}6 \text{ m}\cdot\text{s}^{-1}$ . The initial state of the thermal structure can be characterised as summer stratification. The upper mixed layer was 5-m thick, and its temperature was about  $18^\circ\text{C}$ . The water temperature in bottom layers ( $\sim 30 \text{ m}$ ) was close to  $5\text{-}6^\circ\text{C}$  (see Fig. 2).

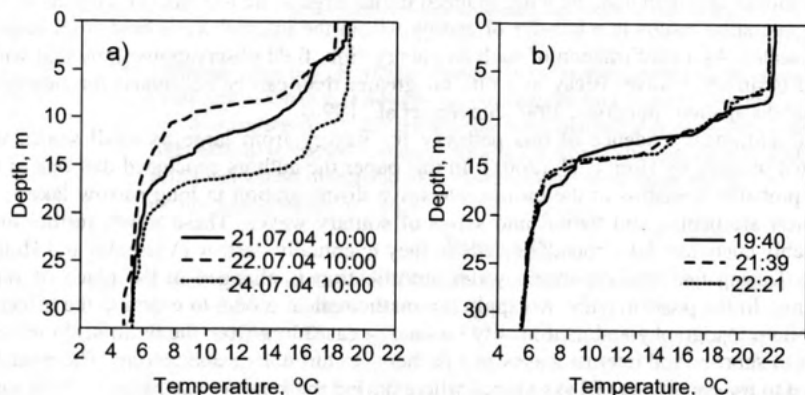


Figure 2. Vertical temperature profiles at station 4. a) Profiles 21.07, 10:00 present the situation before the upwelling, 22.07, 10:00 during the upwelling event, 24.07, 10:00 after the upwelling relaxation, respectively. b) Profiles done on 25 July.

Dynamical processes registered during the experiment in the Bolshoe Onego Bay during the experiment can be described in terms of the time series presented in Fig. 3. Evolution of temperature at the depth of 10 m reveals a very weak water activity during the time span 18-20 July. But then on 21-st and 22-nd July, sudden decrease of temperature took place, which could be the consequence of the near-shore upwelling developed in the north-west part of Lake Onega. Cold water remained near the free surface for about one day, and after that the thermocline slowly returned back to its undisturbed position (from the analysis of the thermistor chains data not presented here). This descending was accompanied by the

vertical oscillations of metalimnion with periods from several hours to one day. The more high-frequency oscillations with periods 10-20 min can also be identified in the time series of the thermistor chains (see, for instance, positions 1-5 in Fig. 3).

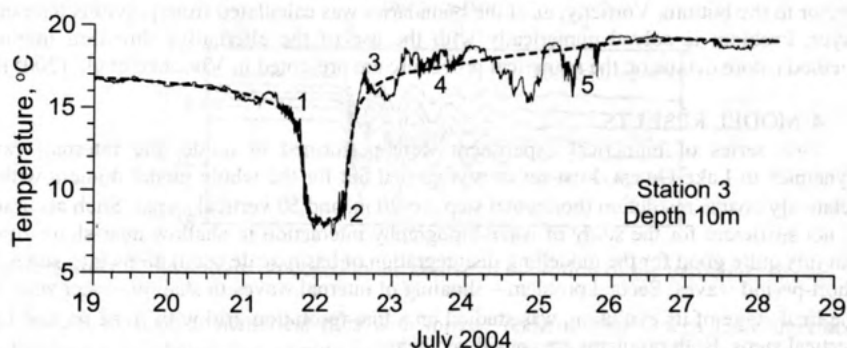


Figure 3. Evolution of water temperature at Station 3 (depth 10m) during the experiment.

The comparative analysis of the whole data set obtained by all devices during the experiment allows one to assume the following probable scenario of the registered event. The initial elevation of pycnocline (up to 15 m) registered in the Bolshoe Onego Bay on 21-22 July was the manifestation of the local upwelling caused by either basin-scale baroclinic seiche, or any other type of more short baroclinic wave motion (we have got no data to prove or reject the idea). The long-period disturbance was followed by more short-period baroclinic oscillations with a period from several hours to one day. These oscillations, in turn, were accompanied by even more short-period disturbances with time-scales in the range between 10 and 20 min. The curve in Fig. 3 represents this fission process, which can be an evidence of the energy cascading from basin-scale baroclinic motions to short-period waves and mixing. To check this hypothesis, a numerical model was developed and applied to the conditions of Lake Onega.

### 3. MODEL

Baroclinic wave motions developing in lakes with complex bottom topography and shoreline possess complex three-dimensional structure. However, if we are not interested in a detailed description of any particular basin (Lake Onega in present case), but only in the mechanisms of the energy transform, we can restrict our analysis to a 2-D case bearing in mind that we describe not the detailed structure, but mechanisms and tendencies. With such a stipulation, the two-dimensional system of the Reynolds equations in the Boussinesq approximation, written in Cartesian ( $x, z$ ) coordinates in which the  $x$  and  $y$ -axis lie on the undisturbed free surface and the  $z$ -axis points upwards (opposite to the direction of gravity), takes the form

$$\begin{cases} \omega_t + J(\omega, \psi) = g\rho_x / \rho_a + (a_h\psi_{xz})_{xz} + (a_h\psi_{xx})_{xx} + (a_v\psi_{zz})_{zz} + (a_v\psi_{xz})_{xz}, \\ \rho_t + J(\rho, \psi) = (k_h\rho_x)_x + (k_v\rho_z)_z, \end{cases}$$

Here  $\psi$  ( $u=\psi_x$ ,  $w=-\psi_z$ ) is the stream function, where  $u$ ,  $w$  are the horizontal and vertical velocity components, and  $\omega=\psi_{xx}+\psi_{zz}$  is the vorticity;  $\rho$  is the water density;  $k_v$  and  $k_h$  are the coefficients of vertical and horizontal turbulent diffusion,  $a_v$  and  $a_h$  are the coefficients of vertical and horizontal turbulent viscosity;  $J(a,b)=a_zb_z - a_zb_x$  is the Jacobian operator. Richardson number dependences (Packanowski and Philander, 1981) were used for parameterization of the coefficients of vertical turbulent exchange  $a_v$  and  $k_v$ . For the coefficients of horizontal turbulent exchange  $a_h$  and  $k_h$ , the gradient dependent parameterization by Stacey and Zedel (1986) was used.

We are only interested in baroclinic motions, and thus use the “rigid lid” conditions at  $z=0$ . The bottom line  $z=-H(x)$ , is a streamline at which the “non-slip” condition and zero mass flux across the boundary is used, viz.  $\psi=\rho_n=\psi_x=\psi_z=0$ , where  $n$  is the unit normal vector to the bottom. Vorticity,  $\omega$ , at the boundaries was calculated from previous temporal layer. Problem is solved numerically with the use of the alternative direction implicit method (more details on the numerical procedure are presented in Vlasenko et al., (2005)).

#### 4. MODEL RESULTS

Two series of numerical experiment were performed to model the internal wave dynamics in Lake Onega. First series was carried out for the whole model domain with a relatively coarse resolution (horizontal step  $\Delta x=20$  m, and 50 vertical steps). Such accuracy is not sufficient for the study of wave-topography interaction in shallow near-shore zone, but it is quite good for the modelling disintegration of basin-scale oscillations into series of short-period waves. Second problem – shoaling of internal waves in shallow-water zone on the final stage of its evolution, was studied on a fine-resolution grid with  $\Delta x=2$  m, and 150 vertical steps. Both problems are considered below.

##### 4.1 NONLINEAR DISINTEGRATION OF BAROCLINIC SEICHE

Water stratification was taken close to those presented in Fig. 2 b. A smoothed profile of the bottom topography along the lake’s longest axis (Fig. 1a) was taken from the bathymetry map. It was assumed that the wave motions are generated by the initially tilted interface. Vertical deflection of the density jump from its initially undisturbed position at both sides of lake comprises 5 m. This value is assumed to be typical for Lake Onega.

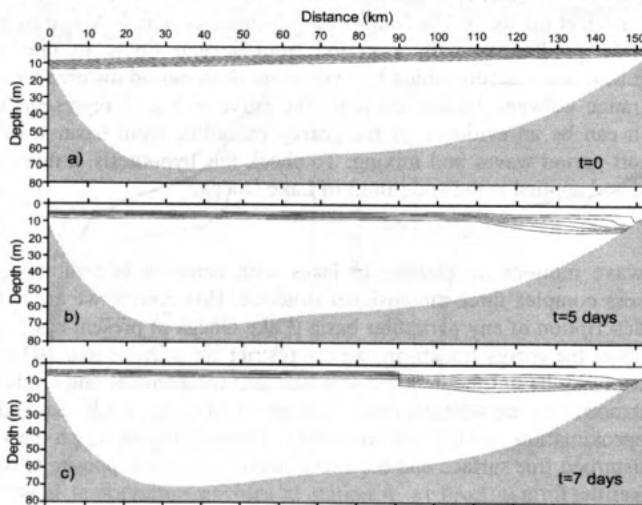


Figure 4. Model predicted nonlinear evolution of basin-scale internal wave. Formation of baroclinic bore is clearly seen after 7 days of the model time.

As it can be inferred from the analysis of model results, initially tilted interface being released slowly returns to the undisturbed horizontal position. It is almost horizontal by day 5 (see Fig. 4b). However, the topography of the interface is not symmetrical with respect to the basin’s centre. Due to the nonlinear steepening, the formation of a progressive baroclinic bore at the right hand side of the basin takes place. By day 7, this bore is fully developed (see Fig. 4c). In the course of propagation, the undulating bore gradually transforms into series of short-period internal wave presenting in Fig. 5. At the

final stage of its evolution, the baroclinic bore is disintegrated into series of solitary waves propagating to the shore. The maximum amplitude of the leading wave in the present case is about 7 m.

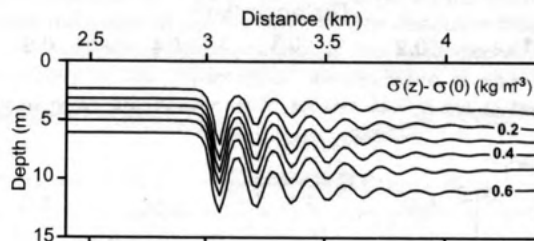


Figure 5. Internal wave train produced in the course of evolution of the baroclinic seiche.

The results from other numerical runs with initial "realistic" for Onega Lake interface inclinations have shown that amplitudes of internal solitary waves (ISW) can lie in the range between 5 and 15 m. As a result, one can assume that baroclinic response of the Bolshoe Onego Bay observed in the experiment was probably caused by one or several such incoming waves propagating from the deep part to the shore. Their interaction with shallow water zone is considered below.

#### 4.2 SHOALING OF INTERNAL WAVES

Numerical experiments on shoaling of solitary internal waves in the area of the Bolshoe Onego Bay were performed for several incoming waves with amplitudes varying in the range between 5 and 15 m. Generally, the experiment site is very interesting from the viewpoint of internal wave shoaling, because it includes the "turning point" where the incoming solitary waves can change their polarity and transform from the wave of depression into the wave of elevation. In terms of weakly nonlinear theory this takes place when density jump is located just in the middle between free surface and bottom (see Fig. 2), so that the coefficient of the quadratic nonlinearity in the Kortevég-de Vries equation turns to zero. Analyzing Figs. 1b and Fig. 2, one can conclude that the turning point is located somewhere between Stations 1 and 5.

The process of wave decomposition near the "turning point" can also take a form of dispersive disintegration of incoming waves into a secondary wave train. Finally, the more striking scenario of wave evolution over inclined bottom is wave breaking in case its amplitude becomes comparable with the total water depth. The breaking event leads to the formation of turbulent pulsating jet and spots of mixed water. As it was found from the analysis of the model results, all these scenarios are very probable for the area under study.

Figure 6 represents the shoaling of ISW over the inclined bottom with the inclination angle of  $1.3^\circ$ . This value is close to the average one taken from the bathymetry map. In the deep part of a basin with depth of 70 m, the amplitude of ISW was 10 m (Fig. 6a). At the first stage of evolution over inclined bottom the incoming ISW becomes asymmetric (Fig. 6b) and further gradually transforms into a packet of short-period internal waves (Figs. 6c and 6d). Wave breaking does not take place at this stage because the steepening of the rear face of the wave over the slowly varying bottom (Fig. 6b) is compensated by the permanent leakage of the wave energy into the dispersive wave tail (Fig. 6c). However, several leading waves eventually are destroyed when this balance is violated by stronger nonlinearity in the more shallow part of the basin (see Fig. 6e). The breaking occurs between Stations 4 and 5, so that the resulting reconstruction of the vertical water stratification must be observed in the experiment, if the breaking events really took place.

As it is seen from Fig. 1b, the bottom profile in the experimental site is not monotonous. It includes several sections with greater and lesser inclinations than it was considered in the

discussed above experiment. To check sensitivity of the model results to the bottom inclination, several additional runs were performed.

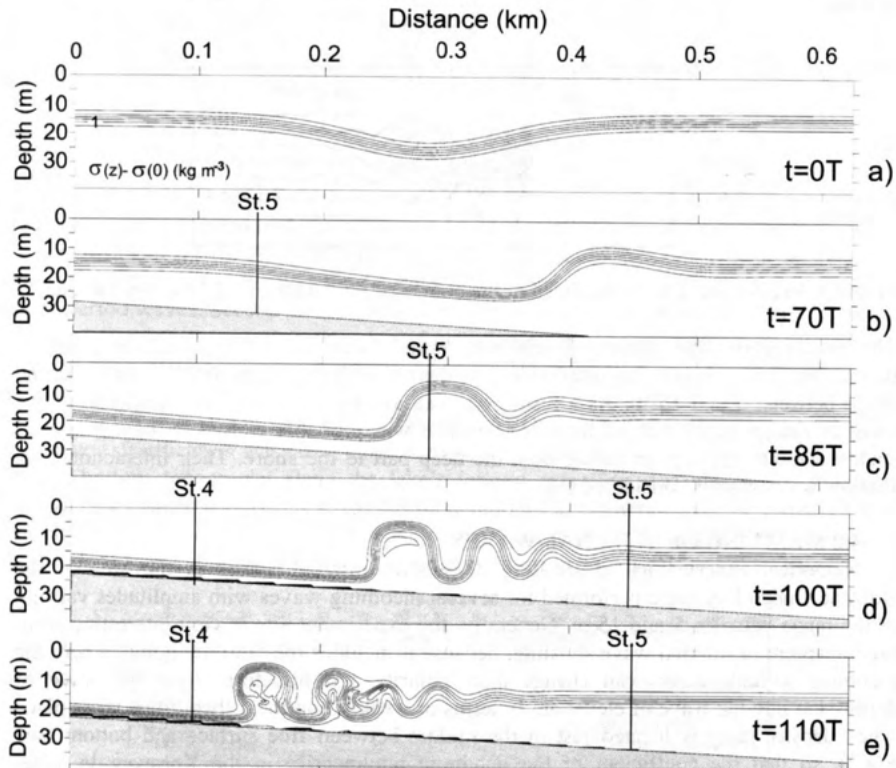


Figure 6. Model predicted evolution of internal solitary wave with initial amplitude of 10m over the inclined bottom. Inclination angle equals  $1.3^\circ$ , time scale  $T=75$  sec.

Figure 7 represents the breaking regime of the wave evolution. It occurs when the inclination angle equals  $2.3^\circ$ . The initial stage of the breaking event is not shown in Fig. 7; it is similar to those described in Vlasenko and Hutter (2002). An important result from this run is that wave breaking is able to change dramatically the background stratification.

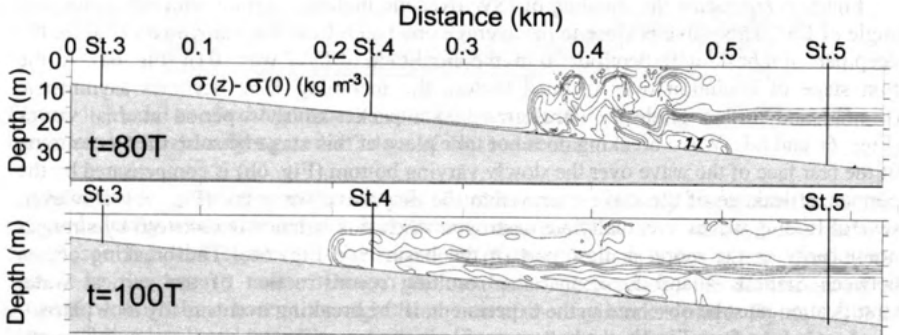


Figure 7. Density field showing the result of internal wave breaking over relatively steep bottom topography (inclination angle equals  $2.3^\circ$ ; Initial amplitude equals 10m,  $T=75$  sec).

Quite a different scenario of wave evolution is expected for relatively gently sloping bottom profiles with inclination angles less than  $1^\circ$ . The dispersive fission of the incoming ISW into series of short-period internal waves is the basic mechanism controlling the evolution. An example of the “dispersive” disintegration is shown in Fig. 8. The cumulative effect of nonlinear steepening in present case is not as fast as the dispersive disintegration.

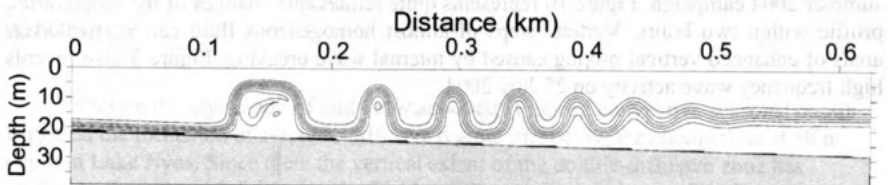


Figure 8. Density field showing the result of dispersive disintegration of ISW with initial amplitude of 10m over the gently sloping topography (inclination angle equals  $0.6^\circ$ )

The above results concern the evolution of a relatively large wave. Similar effects of breaking and dispersive fission also took place for all other considered waves, although for small-amplitude ISW they are not so pronounced. Figure 9 represents the evolution of 5 m amplitude ISW propagating over the bottom topography with inclination angle of  $1.3^\circ$ . Dispersive disintegration, which is predominant at the first stage (upper panel), is changed into breaking and formation of the horizontal intrusion (middle panel). Note that the breaking process is not so pronounced as it is for large-amplitude waves. Instead of the turbulent pulsating jet, the upstream propagating wave of elevation (or “bolus”, in term of the experimental work by Helffrich (1992)) is produced in the breaking area.

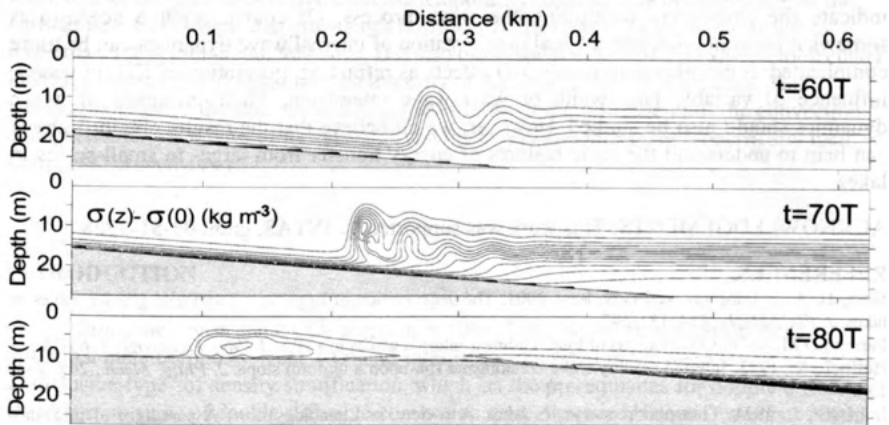


Figure 9. Evolution of 5 m amplitude solitary internal wave over the bottom topography. Inclination angle equals  $1.3^\circ$ , time scale  $T=144$  sec.

## 5. DISCUSSION AND CONCLUSIONS

The results presented in this paper indicate possible important scenarios of wave energy sink from the large-scale motions to smaller scales and further to turbulence. At the first stage of evolution, the basin-scale baroclinic seiche gradually transforms into series of solitary internal waves. It occurs due to the nonlinear steepening and dispersive

disintegration of the propagating baroclinic bore. The second important stage of the energy cascading is wave-topography interaction when propagating internal waves interact with lake's boundaries. Depending on the wave amplitude, stratification and the bottom profile, the process of wave-topography interaction can take a form of strong overturning and breaking, as it shown in Figs. 6e and 7, or more "soft" dispersive disintegration, as it is presented in Fig. 8. In the case of wave breaking (even local as in Fig. 9) the background stratification can change dramatically during a quite short time span. It is very likely, that such a reconstruction of the vertical stratification was observed in Lake Onega during the summer 2004 campaign. Figure 10 represents quite remarkable changes of the temperature profile within two hours. Vertical steps of almost homogeneous fluid can be treated as areas of enhanced vertical mixing caused by internal wave breaking. Figure 3 also reveals high frequency wave activity on 25 July 2004.

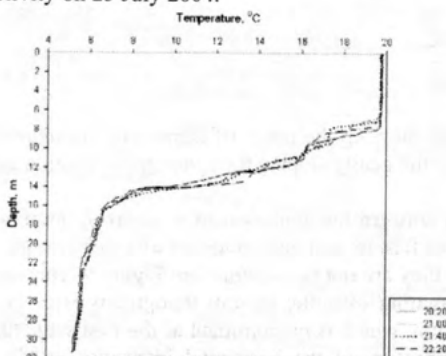


Figure 10. Profiles of temperature measured at station 4 on 25 July 2004.

We highlighted only one possible scenario of wave evolution in lake and tried to indicate the parameters controlling the wave process. Of course, such a scenario is somewhat conventional, and the real manifestation of internal wave dynamics can be more complicated. It can also incorporate 3-D effects as refraction, generation of Kelvin waves, influence of variable lake width or wave-wave interaction. Their influence on wave dynamics should also be studied. However, we do believe that the results obtained above can help to understand the basic features of energy transfer from large- to small-scales in lakes.

**ACKNOWLEDGEMENTS:** This work was supported by INTAS, grant 03-51-3728.

#### REFERENCES:

- Horn, D. A., J. Imberger, and G.N. Ivey, 2001: The degeneration of large-scale interfacial gravity waves in lakes. *J. Fluid Mech.*, 434, 181-207.
- Farmer, D.M., 1978: Observations of long nonlinear internal waves in a lake. *J. Phys. Oceanogr.*, 8, 63-73.
- Helfrich, K., 1992: Internal solitary wave breaking and run-up on a uniform slope. *J. Fluid. Mech.*, 243, 133-154.
- Imberger, J., 1994: Transport processes in lakes: A review. in Limnology now: A paradigm of planetary problems. Ed. R. Margalef. Elsevier.
- Stevens, C., C. Lawrence, P. Hamblin, and J. Imberger, 1996: Wind forcing of internal waves in a long stratified lake. *Dyn. Atmos. Oceans*, 24, 41-50.
- Thorpe, S.A., 1977: Turbulence and mixing in a Scottish loch. *Phil. Trans. R. Soc. Lond.*, A 286, 125-181.
- Vlasenko, V., and K. Hutter, 2002: Transformation and disintegration of strongly nonlinear internal waves by topography in stratified lakes. *Annales Geophysicae*, 20, 2087.
- Vlasenko, V.I., N.M. Stashchuk, and K. Hutter, 2005: Baroclinic tides: theoretical modelling and observational evidence. *Cambridge University Press*, 350p.
- Wiegand, R. C., and E. Carmack, 1986: The climatology of internal waves in a deep temperature lake. *J. Geoph. Res.*, 91, 3951-3958.

# Birth, rapid development and sudden death of a distinct double-diffusive staircase in Lake Nyos (Cameroon)

A. Wüest, M. Schmid and B. Müller

EAWAG, Limnological Research Institute, Seestrasse 79, CH-6047 Kastanienbaum,  
alfred.wuest@eawag.ch, Tel +41 41 349 21 81, Fax +41 41 349 21 62.

## ABSTRACT

During the dry season of mid February 2002 (Figure), convective seasonal cooling triggered the formation of a double-diffusive regime just below the chemocline at 50 m depth in Lake Nyos. Since then, the vertical extent of the double-diffusive zone has continuously increased, following the Fickian diffusion model proposed by Turner and Huppert (1981). In summer 2004 the double diffusive zone embraced about a 40 m vertical section and the base reached to about 92 m depth. The input of turbulent energy from wind or surface convection below the chemocline is very weak (in terms of horizontal currents as well as baroclinic oscillations) and not sufficient to disturb the development of the double-diffusive staircase. The lake represents thus a perfect natural laboratory to study the development and the horizontal variability of a double-diffusive staircase at a much larger scale than in laboratory experiments.

Rapidly after the initiation of the phenomenon (probably after a few weeks), the number of perfectly-mixed layers reach 27 (uncertainty ~1 to 2). Since then, the number remained constant, although new layers were continuously formed at the expanding (lower) base of the double-diffusive zone. This fact implies that the layer merging rate was identical to the formation rate, which we found at approximately 1 per month. The formation of the double-diffusive staircase temporarily leads to a local divergence of the vertical heat flux, which also propagates downwards. The layer thickness increased to more than 1.3 m after about 900 days. But also the vertical extent of the (almost molecular) interface increased and weakened the intensity of the double diffusive process. This weakening reduced the salt, gas and heat fluxes through the staircase until the convection collapsed after ~900 days of its existence and the layers and interfaces (specifically their sharpness) eroded away.

## INTRODUCTION

Since the catastrophic CO<sub>2</sub> eruption in 1986, Lake Nyos' stratification went through a metamorphosis. Heat, CO<sub>2</sub> and salinity accumulated in the deep layers and let to a "diffusive-type" of density stratification, which set the prerequisites for double diffusion. However, no signs of double-diffusive convection were observed before December 2002, when a set of 26 well-mixed layers with thicknesses of 0.2–2.1m and sharp interfaces in between were discovered at 53–74m depth.

A temperature time series measured at 62 m depth indicates that the double-diffusive convection started in the second half of March 2002 at that particular depth range (figure 1). The trigger, caused by relatively strong seasonal convective cooling at the top of this double-diffusive layer, occurred however slightly before (early February 2002). The reason for this temporal structure is due to the vertical expansion of the double-diffusive layer as a function of time.

The double-diffusive upward heat flux is more effective than the purely (turbulent) diffusive flux, active already before the onset of the double diffusion. This observation is a key element of the temporal development of the DD. Firstly, the onset of DD was triggered by the increasing strength of the temperature gradient as a result of the heat accumulated in the stratified water column. Secondly, due to the DD-enhanced heat fluxes at the upper end of the DD zone, the temperature gradient became even stronger and generated new layer formation at the lower end (Figure 1) of the DD zone. After about 30 months, the expansion had reached such a vertical extent, that the temperature gradient started to wane. The content of this talk is to discuss the mechanisms defining the birth, the rapid expansion and the death of the DD layering phenomenon observed in Lake Nyos.

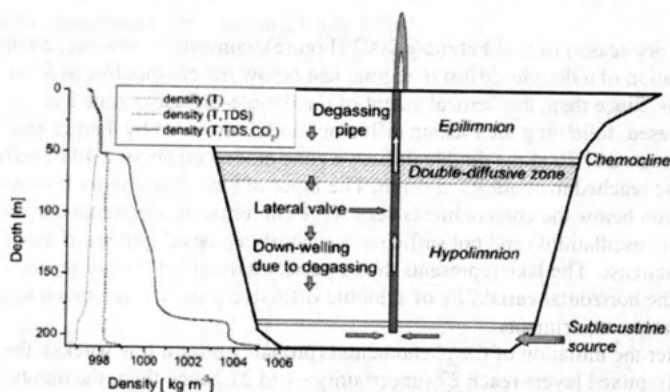


**Figure 1:** Schematics of the vertical structure of Lake Nyos. Left: the contributions of temperature, TDS and CO<sub>2</sub> to the density stratification. The vertical position of the DD zone is indicated. The pipe self-siphoning causes down-welling of 1–3 m/yr. Figure from: Schmid, M.; Lörke, A.; Dinkel, C.; Tanyileke, G. & Wüest, A. 2004. Deep Sea Research Part I 51 (2004) 1097–1111.

## DATA BASE

The data material consists of approximately two dozens of CTD profiles taken on the following occasions: 3 November 2001, March 2002, July 2002, 8 December 2002, July 2003, March 2004 and March 2005. The CTD profiles were collected, using a Sea-Bird SBE-19. The device was lowered slowly, with a resulting average vertical measurement resolution of several cm (the best-resolved ~4 cm; worst-resolved ~15 cm). In addition we had temperature sensors moored for continuous readings at about 10 to 15 minutes.

## OBSERVATIONS

The observations made can be summarized as follows:

- Lake Nyos is a special case of double diffusion, as the antagonists of DD are mainly temperature and CO<sub>2</sub>.
- The number of layers remained constant at 27±2.

## New Layer Formation

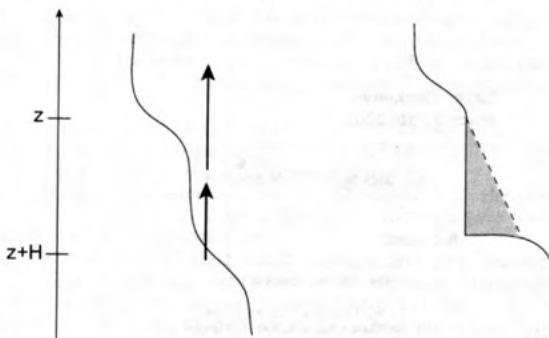


**Figure 2:** Schematics for the explanation of the formation of new DD-layers. Due to the divergence of the heat flux (see arrows) the cooling is faster at depth  $z$  compared to depth  $z+H$ . Under certain conditions, the cooler water on top becomes heavier and can lead to local instabilities forming the initiation of a new layer. The vertical expansion of layers follows a diffusion process, as does the entire extent of the zone (Figure 3).

- The zone of layering expanded downward from 51 to 92 m depth (in 25 months).
- The thickness of the DD zone expanded to ~40 m within ~900 days (Figure 3) of DD dominance.
- The thickness of the DD layers has grown to ~1.36 m within ~900 days (Figure 4).
- The steady-state layers thickness is close to the predictions by Kelly (1984).
- Also the interface thickness seems to grow; at least within 15 months the interfaces expanded from 16 to 33 cm vertical extent.
- The upward heat flux, average:  $0.27 \text{ W m}^{-2}$  was found in perfect agreement with the predictions of Kelly and Turner.
- Temperature within the DD zone decreased by heat flux divergence.
- Temperature of layers increased due to downward migration of layers by  $\sim 0.15^\circ\text{C}$ :
- The temperature gradient decreased within the DD zone as an effect of the DD.

### Lake Nyos DD Zone Thickness since 3 February 2002

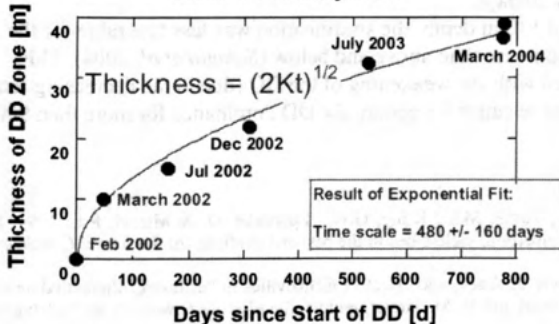


**Figure 3:** Thickness of the DD zone relative to the initiation on 3 February 2002. The red line shows the expansion according to Fickian diffusion.

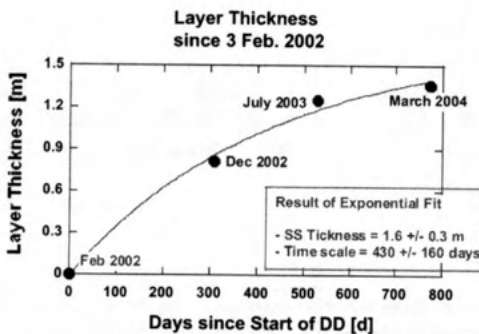


**Figure 4:** Average layer thickness within the DD zone relative to the initiation on 3 February 2002. The red line shows an exponential curve with a time scale of 430 days.

## CONCLUSIONS

The formation of a double-diffusive staircase has been triggered in Lake Nyos by convective cooling during the dry season in February 2002. The initiation occurred on 15 February 2002 ( $\pm 1$  week uncertainty) at the top of the chemocline. Since then, the double-diffusive staircase has been continuously expanding downwards for more than 900 days (the exact end has still to be determined) with an average speed of about 1.4 m per month. Within the double-diffusive zone, the heat transport is dominated by the double-diffusive convection, and about one order of magnitude larger than it was before the onset of double diffusion. The increased upwards heat flux leads to a local divergence of heat and consequently a reduction of temperature near the front of the developing staircase.

The average thickness of the observed mixed layers has increased from about 80 cm in December 2002 to 1.5 m in March 2004. The number of observed layers remained almost constant at  $27 \pm 2$ , which implies that for every newly formed layer at the front of the staircase, two layers must have merged. The new layers formed between 85 and 90 m depth were around 80 cm thick. Consequently, the formation of a new layer at the front takes on average about 20 days.

Between 95 and 130 m depth, the stratification was less favorable for the formation of a double-diffusive staircase than above and below (Schmid *et al.*, 2004). This circumstance, combined with the weakening of the DD (due to the decreasing temperature gradient) was the probable cause for ending the DD dominance for more than 900 days.

## REFERENCES

- Evans, W.C.; White, L.D.; Tuttle, M.L.; Kling, G.W.; Tanyileke, G. & Michel, R.L. 1994. Six years of change at Lake Nyos, Cameroon, yield clues to the past and cautions for the future. *Geochemical Journal* 28(3):139-162.
- Fedorov, K. N. (1988). Layer thickness and effective diffusivities in "diffusive" thermohaline convection in the ocean. In J. C. J. Nihoul and B. M. Jamart, editors, *Small-scale turbulence and mixing in the ocean*, pages 471-479. Elsevier.
- Halbwachs, M. 2002. Degassing Lake Nyos project: <http://perso.wanadoo.fr/mhalb/nyos/nyos.htm>.
- Halbwachs, M. & Sabroux, J.C. 2001. Removing CO<sub>2</sub> from Lake Nyos in Cameroon. *Science* 292(5516):438-438.

- Hoare, R.A. 1966. Problem of heat transfer in Lake Vanda, a density stratified arctic lake. *Nature* 210:787-789.
- Huppert, H.E. & Turner, J.S. 1972. Double-diffusive convection and its implications for the temperature and salinity structure of the ocean and Lake Vanda. *Journal of Physical Oceanography* 2:456-461.
- Huppert, H. E. (1971). On the stability of a series of double diffusive layers. *Deep-Sea Res.*, **18**, 1005-1022.
- Huppert, H. E. and Linden, P. (1979). On heating a stable salinity gradient from below. *J. Fluid Mech.*, **95**, 431-464.
- Huppert, H. E. and Turner, J. S. (1981). Double-diffusive convection. *J. Fluid Mech.*, **106**, 299-329.
- Kelley, D.E.; Fernando, H.J.S.; Gargett, A.E.; Tanny, J. & Oezsoy, E. 2003. The diffusive regime of double-diffusive convection. *Progress in Oceanography* 56:461-481.
- Kling, G.W.; Clark, M.A.; Compton, H.R.; Devine, J.D.; Evans, W.C.; Humphrey, A.M.; Koenigsberg, E.J.; Lockwood, J.P.; Tuttle, M.L. & Wagner, G.N. 1987. The 1986 Lake Nyos gas disaster in Cameroon, West-Africa. *Science* 236(4798):169-175.
- Kusakabe, M.; Tanyileke, G.Z.; McCord, S.A. & Schladow, S.G. 2000. Recent pH and CO<sub>2</sub> profiles at Lakes Nyos and Monoun, Cameroon: implications for the degassing strategy and its numerical simulation. *Journal of Volcanology and Geothermal Research* 97(1-4):241-260.
- Lorke, A.; Tietze, K.; Halbwachs, M. & Wüest, A. 2004. Response of Lake Kivu stratification to lava inflow and climate warming. *Limnology and Oceanography* 49(3).
- Newman, F.C. 1976. Temperature steps in Lake Kivu: a bottom heated saline lake. *Journal of Physical Oceanography* 6:157-163.
- Nojiri, Y.; Kusakabe, M.; Tietze, K.; Hirabayashi, J.; Sato, H.; Sano, Y.; Shinohara, H.; Njine, T. & Tanyileke, G. 1993. An estimate of CO<sub>2</sub> flux in Lake Nyos, Cameroon. *Limnology and Oceanography* 38(4):739-752.
- Osborn, T.R. 1973. Temperature microstructure in Powell Lake. *Journal of Physical Oceanography* 3:302-307.
- Schmid, M.; Lorke, A.; Dinkel, C.; Tanyileke, G. & Wüest, A. 2004. Double-diffusive convection in Lake Nyos, Cameroon. *Deep Sea Research Part I* 51 (2004) 1097-1111.
- Schmid, M.; Lorke, A.; Wüest, A.; Halbwachs, M. & Tanyileke, G. 2003. Development and sensitivity analysis of a model for assessing stratification and safety of Lake Nyos during artificial degassing. *Ocean Dynamics* 53:288-301.
- Sigvaldason, G.E. 1989. International Conference on Lake Nyos Disaster, Yaounde, Cameroon 16-20 March, 1987 - Conclusions and Recommendations. *Journal of Volcanology and Geothermal Research* 39(2-3):97-107.
- Spigel, R.H. & Priscu, J.C. 1998. Physical limnology of the McMurdo Dry Valleys lakes. In: J.C. Priscu (Ed.) *Ecosystem Dynamics in a Polar Desert*. Washington, D.C.: AGU.
- Turner, J.S. 1973. *Buoyancy Effects in Fluids*. Cambridge: Cambridge University Press.



## Observation of Multilayer Structures in a Small Lake

J. Ilmberger, K. Wunderle and C. von Rohden

Institut für Umweltphysik, Universität Heidelberg

Mail: Johann.Ilmberger@iup.uni-heidelberg.de

### Abstract:

In a small gravel mining lake near Ludwigshafen/Rhein time series of current profiles were measured with a bottom mounted 1200 kHz-Acoustic Doppler Current Profiler (ADCP). Additional information was obtained by high resolution CTD-profiles and temperature time series with moored sensors.

Typical current speeds in Lake Willersinnweiher are very low, in the range of several mm/s (especially in the hypolimnion). During wind incidents currents in the upper layer (~1m) reach a few dm/s and some cm/s in deeper strata. Long term Fourier transform does not show significant peaks in the spectra, whereas Short Time Fourier Transform (STFT) reveals transient internal waves with a period of a few hours. There is no indication of a first mode internal wave, which should have a period of about 1h.

In summer, with a strong temperature dominated stratification, current measurements display in the vertical patterns of opposing velocity directions during wind incidents. These layers occur in depth regions with large density gradients. The analysis of correlation of the horizontal currents at different depths reveals a typical layer thickness in the range of 1m. This length scale as well as the localisation of the structures in the stratified region resemble the higher modes eigen functions of a rectangular basin. Assuming a cross lake standing wave, the observed and calculated periods are in accordance.

### Introduction

Internal seiches play an important role in a wide range of physical, chemical and biological processes in lakes. Therefore seiching in lakes and reservoirs has been extensively discussed. Mostly the vertical one and horizontal one or higher ( $V1H_n$ ) modes have been observed and investigated. In many cases, very good agreements of the observed and calculated seiche periods were found using the two layer approximation. A short overview is given by Wüest and Lorke (2003).

There are also some reports about the vertical second ( $V2H_1$ ) mode (Wiegand and Chamberlein 1987, Münnich et al. 1992, Roget et al. 1997, Antenucci et al. 2000).

Observations of higher than second vertical modes of water currents in lakes are rare. There are only a few reports, for example LaZerte (1980), who claimed having seen up to the 10<sup>th</sup> vertical mode in a small lake from temperature time series. Antenucci et al (2000) measured water currents and temperature time series finding a 3<sup>rd</sup> mode structure. Pérez-Losada et al. (2003) reported from a reservoir and identified the 3<sup>rd</sup> vertical mode via correlation of temperature time series at different depths.

Our multilayer findings are mainly based upon ADCP measurements of profiles of water currents at a time intervall of 5 min.

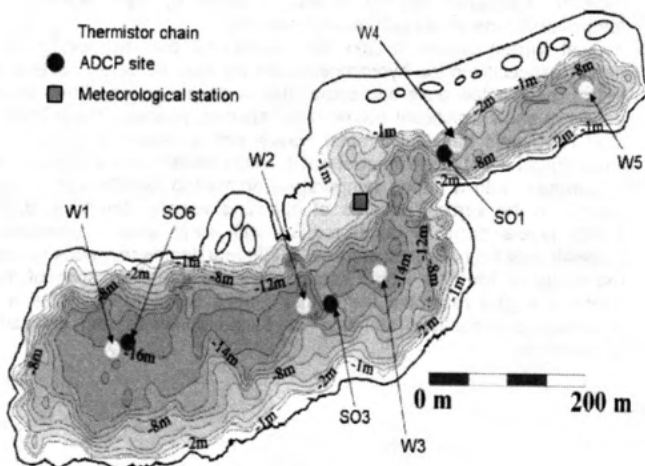
## Site

The study site is a gravel mining lake (Lake Willersinnweiher) near Ludwigshafen/Rhein, Germany.

It is a small lake with a size of about 17 ha and a maximal depth of ~19 m. It develops a temperature dominated strong summer stratification with an anaerobic hypolimnion. During the cold season we find complete mixing.

There is no surface in- or outflow. Thus the water budget is mainly determined by groundwater.

Fig. 1: The map of lake Willersinnweiher. Light grey circles indicate the locations, where temperature measurements were performed and the dark ones mark the positions of ADCP measurements.



## Measurements

Temperature time series were acquired at location w1, w3 and w5 (see fig. 1) using temperature recorders at different water depths. The sampling interval was 5 minutes and the resolutions are 0.012 and 0.035°C.

CTD-profiles (conductivity-temperature-depth) were taken about weekly at five measurement sites (fig. 1) using an automatic Idronaut Ocean Seven 319 probe. The vertical resolution is 2 cm. The resolution of the temperature and conductivity sensor is 0.001°C and 0.1 mS/cm, respectively.

Current measurements were made at different locations (fig. 1) with a bottom mounted 1200kHz ADCP (Acoustic Current Profiler, RD Instruments). Typically 800 pings were averaged and recorded every 5 minutes. The vertical resolution (bin size) was chosen as 0.4/0.5 m. The ADCP was powered through a cable from ashore using a low cost rechargeable 60 V battery pack. The cable was also used to check the operation and download the stored data once a week using a laptop computer. To minimize projection effects of horizontal into vertical velocities when the ADCP is inclined, the ADCP was mounted in a cardanic suspension to keep the inclination angles below 2°. From April to the end of 2004 velocity measurements were carried out at different sites (SO1, SO3 and SO6) for periods of a few weeks at each location.

## Results

Typical current speeds in Lake Willersinnweiher are very low in the range of several mm/s (especially in the hypolimnion), occasionally reaching a few cm/s during wind incidents.

### Noise reduction

In order to extract the current velocities from noise, the data have to be filtered. To reduce the noise we used smoothing in the vertical and temporal. The smoothing in the space domain was done over three adjacent bins. A time window of 40 minutes, i.e. a moving average of 8 consecutive data points was used (fig. 2). This window in the time domain corresponds to a frequency of  $1.6 \text{ h}^{-1}$ . That value is the frequency which separates the noise from the data in the Fourier spectra of the velocity measurements (fig. 3).

### Fourier transform

Long term Fourier transform, performed on the velocity data, does not show significant peaks. This indicates that there are no dominant eigenfrequencies excited. Exemplary some of the calculated spectra are shown in figure 4.

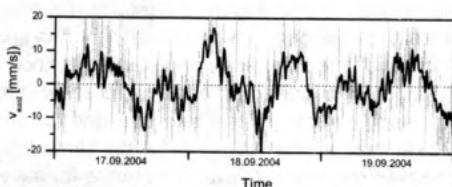


Fig. 2: Time series of the east-west component of the water current at a depth of 6.4 m (location SO1). Grey: original data. Black: smoothed data.

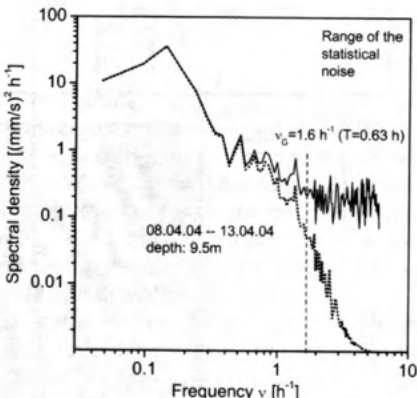


Fig. 3: Spectra of the east-west component of the water velocity at location SO1, calculated from the original (solid line) and the smoothed (dotted) time series.

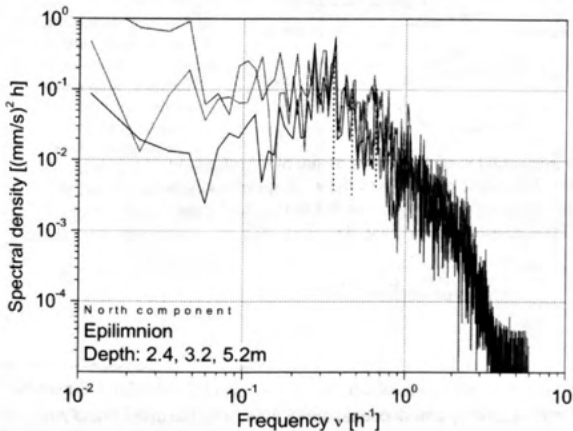


Fig. 4: Spectra of the north-south component of the water velocity at location SO1, calculated from time series of 1024 5-min values beginning at Aug. 7 at different water depths.

In contrast to this finding is the regular pattern of current velocity which can be seen in the measurements. Figure 5 shows a plot of the north component of the water current velocity profile during a two days period in summer with a strong stratification. In this figure two time segments, one starting at noon of the 7<sup>th</sup> and the second at 2 pm of the 8<sup>th</sup> can be recognised. The top panel shows the wind velocity (with rather poor quality), measured directly at the lake site and for comparison meteo station measurements (30 km afar at the IUP (Institut für Umweltphysik)). The left panel gives the Brunt-Väisälä-Frequency<sup>a</sup>  $N^2$  as a measure for the stratification.  $N^2$  is calculated from CTD-casts performed the 3<sup>rd</sup> of August at station w1.

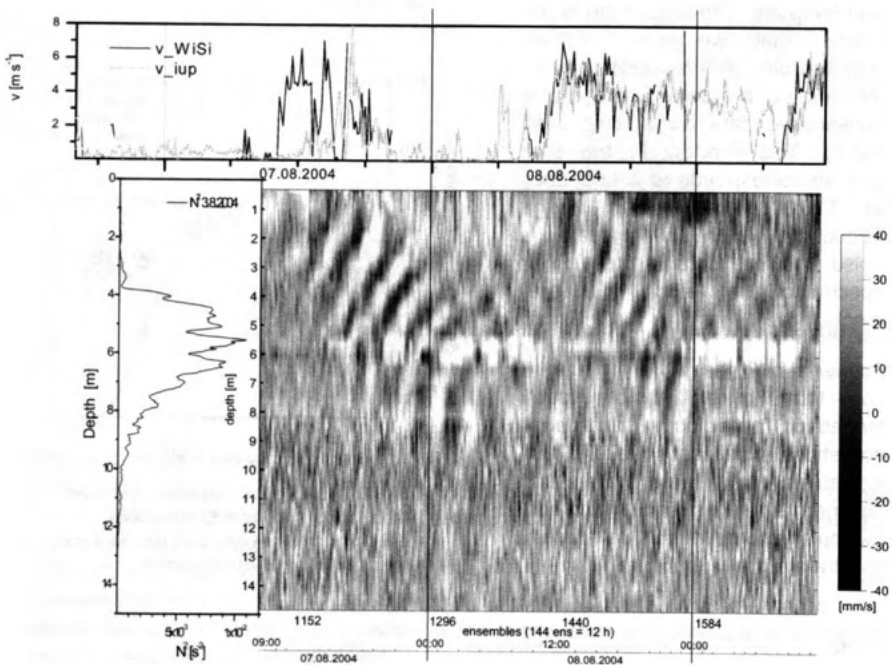


Fig. 5: North component of the horizontal current velocity at site SO6 (see fig. 1), section Aug. 07 – Aug. 11, 2004. The upper panel shows the wind speed measured at the lake side and for comparison the record of a meteo station 30 km afar. Left panel: Stability  $N^2$  calculated from CTD-measurements at Aug. 03.

<sup>a</sup>  $N^2$  is defined as:  $N^2 = -g/\rho \frac{dp}{dz}$ , where  $g$  is the gravitational acceleration,  $\rho$  is the density and  $z$  the vertical coordinate

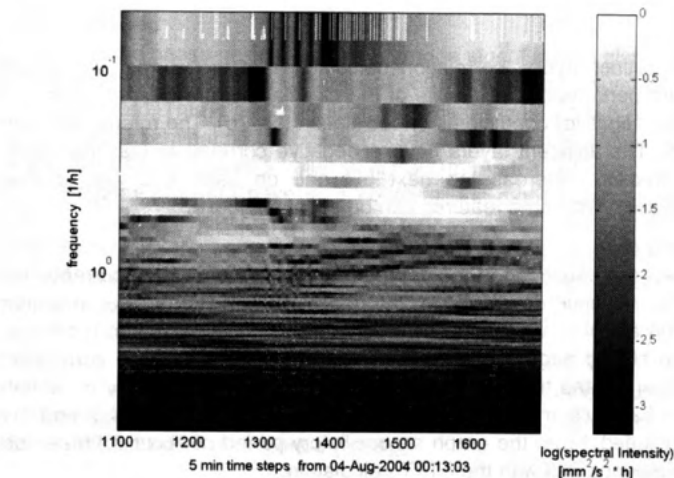


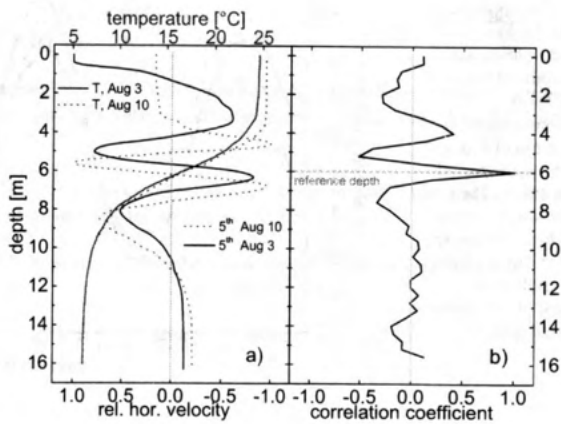
Fig. 6: Short Time Fourier Transform of the north component of the horizontal current velocity at a depth of 4 m (data of fig 5, same time interval) with a dominant frequency at  $\sim 3.5$  h.

#### Short Time Fourier Transform

Using Short Time Fourier Transform (STFT), spectra of the current velocity are calculated. The contour plot (fig. 6) shows the transient character of these oscillations and explains the missing peaks at the 'long term' spectra (fig. 4). The spectra show a distinct peak at about  $0.3 \text{ h}^{-1}$ . This peak is highest about 5 h after the onset of the wind (see fig. 5, upper panel). After a few hours, when the wind ceased, the peak decreases and is slightly shifted towards higher frequencies ( $0.4 \text{ h}^{-1}$  or  $2.5$  h period). A new wind incident started at noon of August 8, 2004 maintaining the intensity of the peak at about the reduced level with a broadening towards higher frequencies.

Estimating the first mode vertical and horizontal oscillation period from the Merian formula<sup>b</sup> gives a value of about 1 h which we do not see in the data. The reason might be an inhomogeneous exciting at the lake surface (The more sophisticated calculations of the resonant period via the eigenfunction's equivalent height gives similar results).

Fig. 7:  
 a) 5<sup>th</sup> vertical mode of horizontal currents, calculated for a rectangular basin and two measured temperature profiles  
 b) Vertical correlation of hor. currents (Aug 07, 09:08 – Aug 08, 01:48). The vertical length scale is about 1 m and 5 layers can be distinguished.



<sup>b</sup> Merian formula:  $T = 2 \cdot L / v_{ph}$ , where  $L$  is the length of the basin and  $v_{ph}$  the phase velocity  $v_{ph}^2 = g \cdot \Delta \rho / \rho \cdot H_1 \cdot H_2 / (H_1 + H_2)$ , with  $g$ : gravitational acceleration  $\rho$ : density,  $\Delta \rho$ : density difference,  $H_1$ : height of the epilimnion and  $H_2$ : the hypolimnion.

### *Correlation*

In order to detect distinct layers, correlation calculations of the current velocity at different depths were performed. The results of the calculations are local maxima and minima (positive and negative) coefficients of correlation (fig. 7b). The reference depth was chosen as 6 m. The adjacent layers have a negative correlation, that means an opposite current direction, whereas the next but one on each side are positive correlated (are in phase). The same features can be seen in figure 8.

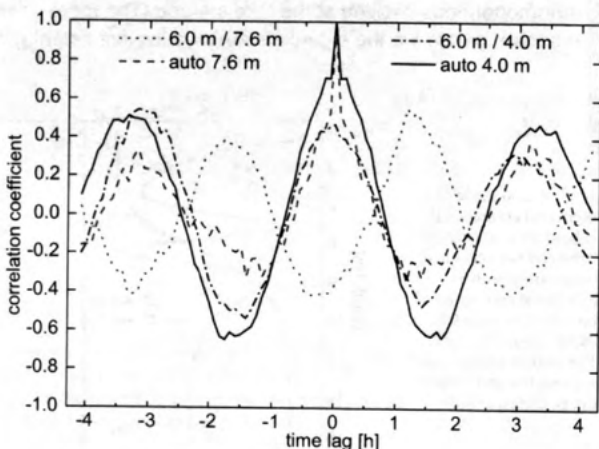
### *Time shift, autocorrelation*

In order to investigate the phase lag at the depths of the highly correlated currents, we chose from fig. 7 the reference depth of 6 m, the depth of 7.6 m with a local minimum (negative) correlation and 4 m, where the correlation has a local maximum (positive). The time series are shifted and the correlation is calculated. In fig. 8 the correlation coefficients are drawn vs. the time shift. The 6 m - 4 m correlation is nicely in phase, while the 7.6 m - 6 m has a clear shift of 180°. The autocorrelations of the 4 m and the 7.6 m signals are included. From the graph an oscillatory period of about 3.1 h can be read off, which corresponds well with the STFT calculation.

### *Vertical eigenfunction*

The observed multilayer structures (exemplary in fig. 7b)) occur in depth regions with strong density gradients (metalimnion). In fig. 7a the temperature profiles from the 3<sup>rd</sup> and 10<sup>th</sup> of August are drawn. The same panel shows the 5<sup>th</sup> mode vertical eigenfunction of the horizontal velocity of a rectangular basin with a flat bottom. This was calculated using the density profiles derived from the CDT-measurements. The two eigenfunctions are rather different concerning the depths of the maximum and minimum values, but the length scale is about 1 m, which is the same what we find calculating the correlation of the velocity signal of different depths (fig. 7b).

Fig. 8: Correlation coefficients derived from the 5 min - north velocity data at depths of 6 m, 4 m and 7.6 m. Autocorrelation at the depth of 4 m and 7.6 m (same period as in fig. 7). The direction of current at 7.6 m is opposite and at 4 m in phase. An oscillation period of ~3.1 h can be read off.



### Resonant period

Calculating the phase velocity<sup>c</sup> of the 5<sup>th</sup> mode eigenfunction gives a value of 3.2 cm/s. Together with the cross lake distance of 180 m this leads to a value of about 3 h for the resonant period. This is in accordance with the findings of the STFT and the correlation calculations. Examining the Rossby Radius<sup>d</sup>  $r_R$ , which is a measure of the influence of the Coriolis force, gives a value of  $r_R \sim 300$  m. As this is considerably larger than the cross length, we do not have to account for the modification caused by the Coriolis force.

When calculating the vertical eigenfunction and the resonant period, we have to keep in mind, that the lake has neither a flat bottom nor straight walls and therefore these considerations can only be an estimation.

The typical layer thickness in the range of 1 m as well as the localisation of the structures in the stratified region resembles the higher modes of a rectangular basin (fig. 7a)). Correlation functions of the data with a time lag of  $\pm 4$  h document obvious phase shifts and oscillation period (fig. 8)).

### References

- Antenucci JP, Imberger J, Saggio A. 2000. Seasonal evolution of the basin-scale internal wave field in a large stratified lake. *Limnol. Oceanogr.* 45:1621–38.
- LaZerte BD. 1980. The dominating higher order vertical modes of the internal seiche in a small lake. *Limnol. Oceanogr.* 25:846–54
- Münnich, M., A. Wüst and D.M. Imboden 1992. Observations of the second vertical mode of the internal seiche in an alpine lake. *Limnol. Oceanogr.* 37: 1705–1719.
- Pérez-Losada, J, Roget, E. and Casamitjana, X., (2003) Evidence of high vertical wave-number behaviour in a continuously stratified reservoir: Boadella, Spain. Journal of hydraulic engineering Vol. 129 Num. 9 pp. 734-737
- Roget E, Salvade G, Zamboni F. 1997. Internal seiche climatology in a small lake where transversal and second vertical modes are usually observed. *Limnol. Oceanogr.* 42: 663–73
- Wiegand RC, Chamberlain V. 1987. Internal waves of the second vertical mode in a stratified lake. *Limnol. Oceanogr.* 32:29–42
- Wüst A. and Lorke A. 2003. Small-Scale Hydrodynamics in Lakes. *Annu. Rev. Fluid Mech.* 35: 373–412.

<sup>c</sup> Phase velocity:  $v_{ph} = (g H_e)^{1/2}$ , with g gravitational acceleration and  $H_e$  the equivalent height.

<sup>d</sup> Rossby Radius:  $r_R = v_{ph}/f$ , f: Coriolis parameter ( $1.08 \times 10^{-4} \text{ s}^{-1}$ )



## OBSERVATION OF A CYCLONIC GYRE PRODUCED BY INTERNAL SURGE IN A SMALL DEEP LAKE

Georgiy Kirillin, Christof Engelhardt and Sergey Golosov

Institute for Water Ecology and Inland Fisheries, Berlin

Corresponding address: Müggelseedamm 310, 12587 Berlin, Germany.

email: kirillin@igb-berlin.de

### Abstract

Mesoscale eddies are known to be an important mechanism of the energy transport in the atmosphere and in the ocean. Small lakes, with horizontal dimensions less than Rossby deformation radius are conveniently assumed to be free from large eddy structures as long as the Coriolis force is of minor importance here and strong, fast-moving horizontal density fronts are unlikely. Nevertheless, a recent field experiment on Lake Stechlin, Germany has allowed us to uncover a lake-specific mechanism of vortex formation. A gyre with a radius of about 100m was discovered using satellite-tracked drifters deployed in the lake for one day in November 2004. The vorticity in the gyre was close to that of solid-body rotation thus allowing estimation of the gyre's movement velocity and reconstruction of its path across the lake. Combined with data from thermal chains, this information disclosed the genesis of the gyre: flushing of the cold hypolimnion water into shallower near-shore areas driven by strong internal seiches propagating along the deep autumn thermocline. We present kinematic characteristics of the gyre and discuss possible importance of the mechanism for basin-scale lake mixing and boundary processes.

## 1 Study site description and observation techniques

**Lake Stechlin characteristics.** Lake Stechlin, located in North-East Germany, has the area of 4.5 km<sup>2</sup> and the maximum depth about 68m. Relatively high depths, very clear water, and small horizontal dimensions result here in strong stratification from May to the end of November (see Fig. 1). During the entire stratified period internal seiches dominate the lake dynamics, whose characteristics are perplexed by irregular lake shape and bottom topography. The lake shape represents three virtually isolated sidearms (northern, southern and western basins) of nearly the same area (Fig. 2) giving rise to a number of different horizontal seiche modes. Higher vertical modes also present in the seiche dynamics and the 2nd vertical mode even prevails during the mid-summer being in resonance with diurnal wind oscillations over the lake.

**Field experiments with satellite-tracked drifters.** Among monitoring of various dynamical characteristics by moored instruments and hydrodynamical modeling, the investigation program on circulation in Lake Stechlin includes registration of lagrangian current characteristics by submerged drifters of zero buoyancy. A drifter consists of the water-filled cylindrical balloon of 0.5m height and 30l volume. The balloon has slightly negative buoyancy and is tethered to a small surface buoy with a GPS receiver. Up to 10 drifters are deployed simultaneously at depths 4 to 10 meters. The deployment time is limited by the receiver batteries capacity and is about 18-30 hours depending on batteries type and sampling frequency. Series of drifters experiments with various configurations has been performed during the years 2004 and 2005. Their detailed description and analysis is to be presented elsewhere, and the present contribution is dedicated to a single dataset from the experiment, performed on the 06 November 2004. Four drifters were deployed at the 5m depth for about 12 hours and the resulting trajectories clearly demonstrate that all drifters were captured by a slowly moving vortex-like structure with the diameter of about 200m (Fig. 2). Kinematic properties of the observed eddy and mechanisms of its possible generation are discussed below.

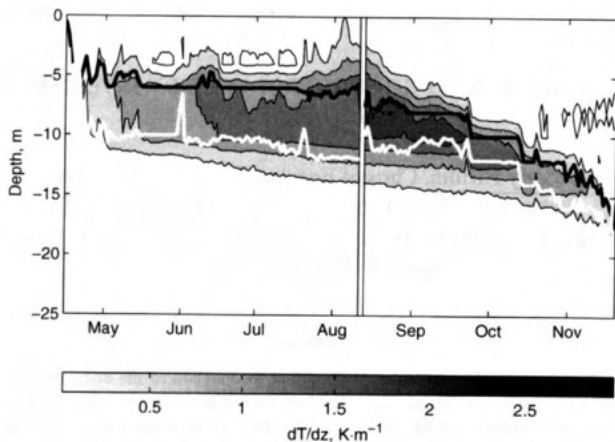


Figure 1: Seasonal evolution of the vertical temperature gradient in Lake Stechlin, 2004. Black and white thick solid lines are depths of the upper and the lower boundaries of the thermocline, defined as  $z(\max[\partial T/\partial z])$  and  $z(\max[\partial^2 T/\partial z^2])$  correspondingly.

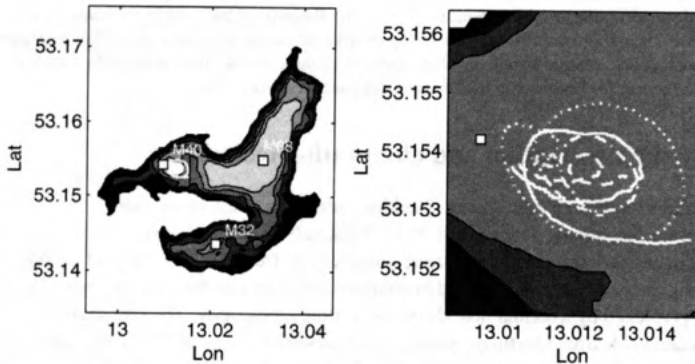


Figure 2: Bathymetric map of Lake Stechlin (10,20,30 and 40m isobathes) with trajectories of the 4 drifters deployed on 06 Nov 2004 (white lines) and location of the 2 thermal chains (squares). Right panel shows the increased view of the eddy area.

## 2 Observation of the eddy structure

**Kinematic eddy characteristics.** In order to determine kinematic properties of the rotational flow, the observed lagrangian velocities can be decomposed into three components (Okubo and Ebbesmeyer, 1976):

$$\vec{U} = \vec{U}_0 + \vec{u} + \vec{u}', \quad (1)$$

where:

$\vec{U}_0$  is the velocity of the eddy's drift,

$\vec{u}$  is the rotational velocity,

$\vec{u}'$  is the residual velocity, including turbulent fluctuations.

If we further suppose a solid body rotation with constant angular velocity  $\omega$ , ( $\vec{u} = \vec{\omega} \times \vec{r}$ , where  $\vec{r}$  is the distance from the eddy center), and assume the eddy drift be also nearly constant ( $d\vec{U}_0/dt = 0$ ), the problem of velocity components determination is diminished to the solution of the system of linear algebraic equations:

$$\begin{aligned} X &= X_0 + U_x t \\ Y &= Y_0 + U_y t, \end{aligned} \quad (2)$$

where  $X, Y$  are matrices of the observed drifter positions and  $U_x, U_y$  are components of the horizontal velocity vector  $\vec{U}$  as they given by (1). The resulting equation system achieved by substitution of (1) into (2) and rearranging with respect to unknown variables can be found in (Sanderson, 1995).

Figure 3 shows the velocity components for the four drifters, decomposed using the analysis described above. According to the analysis, the eddy moves along the main axis of the western

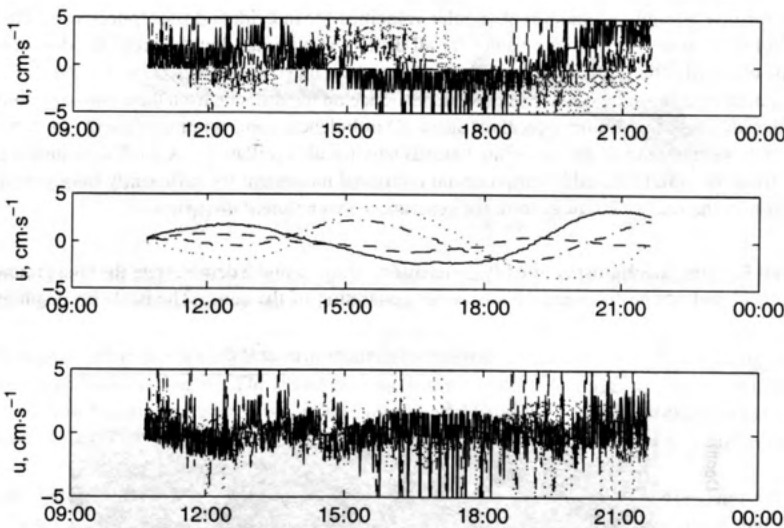


Figure 3: Drifter velocities (top), and their decomposition into rotating (middle) and residual (bottom) components

basin towards the lake center with the velocity of 320 m/day. Drifter trajectories with the eddy drift removed are shown in Fig. 4 (left panel). The eddy has an ellipsoidal shape with the major axis of 250m coinciding with the direction of the eddy drift, and the minor axis of about 200m. Other kinematic properties are summarized in the table below:

Divergence $\partial u / \partial x + \partial v / \partial y$	Vorticity $\partial v / \partial x - \partial u / \partial y$	Stretching $\partial u / \partial x - \partial v / \partial y$	Shear $\partial v / \partial x + \partial u / \partial y$
$0.5 \cdot 10^{-4} \text{ s}^{-1}$	$4.5 \cdot 10^{-4} \text{ s}^{-1}$	$-1.2 \cdot 10^{-4} \text{ s}^{-1}$	$-1.2 \cdot 10^{-4} \text{ s}^{-1}$

One of the background assumptions of the analysis is that of constant angular velocity within the eddy, which is half the vorticity in this case, that is  $2.25 \cdot 10^{-4} \text{ rad/s}$  or about 3 cpd. The assumption

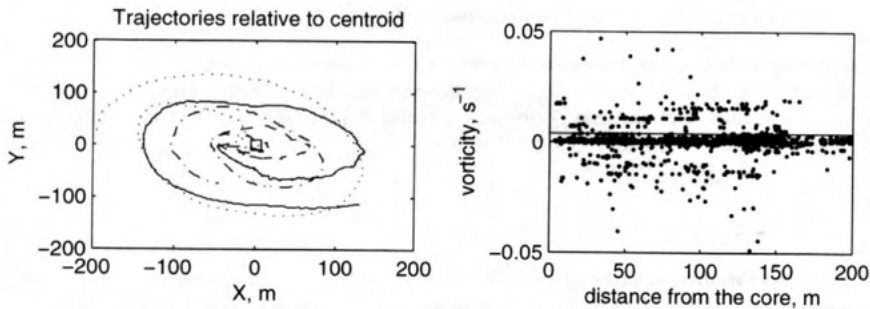


Figure 4: Drifter trajectories relative to centroid (left) and relative vorticity for all observations from all drifters against their distance from the eddy's centroid.

can be verified through calculation of angular velocities for individual drifter trajectories. The right panel in Fig. 4 shows the vorticity values for all drifters at all times drawn against the distance from the eddy centroid. The values tend to aggregate around the line  $\partial v / \partial x - \partial u / \partial y = 4.5 \cdot 10^{-4} \text{ s}^{-1}$  with larger scatter near the eddy center; no other dependence on the distance from the centroid is observed. Thus, the eddy reveals features typical for quasi-2D turbulence: concentration of energy in large-scale coherent motion instead of cascading towards small-scale oscillations. A crude conclusion can be drawn from the result: the eddy can maintain rotational movement for sufficiently long periods and can transport the energy far away from the generation area before it dissipates.

**External forcing, mechanisms of eddy generation** Figs. 5 and 6 demonstrate the background meteorological and seiche forcing responsible for generation of the eddy. The isotherm displacement

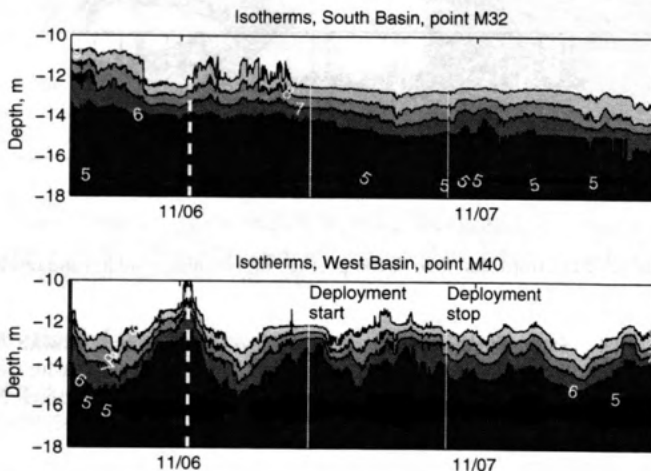


Figure 5: Isotherm displacements in the southern and western basins of Lake Stechlin (points M32 and M40 in Fig. 2, correspondingly). Dashed line indicates seiche-driven surge in the western basin. Solid lines designate start and stop times of drifter observations.

shown in Fig. 5 reveal an internal seiche of high amplitude passing the western basin a day before

the drifters deployment. The seiche is weakly pronounced in the southern basin and expresses itself mostly in generation of high-frequency small-amplitude internal waves, which result apparently from the seiche breaking. The development of the seiche can be traced back in time using the low-resolution

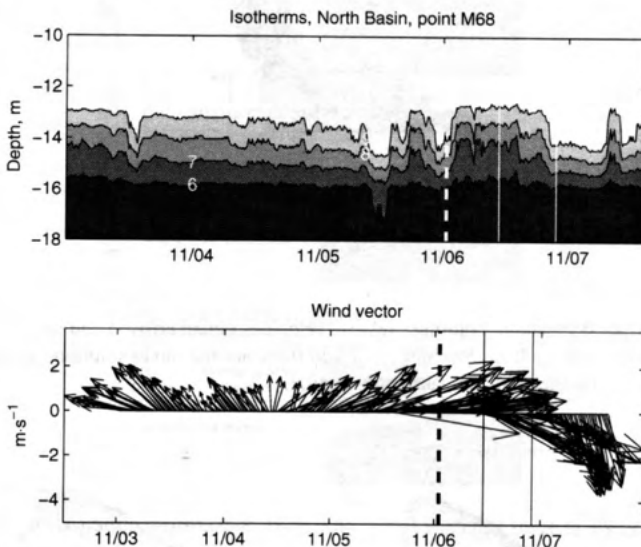


Figure 6: Isotherm displacements in the northern basin, point M68 (top) and wind vector (bottom) during the 4-day period preceding the eddy observation.

temperature readings made with a thermal chain in the northern basin and wind data from the nearby meteorological station (Fig. 6). The initial thermocline rise in the northern basin (and concurrent fall in the western basin) was formed before 04 November by the east component of the wind vector. Seiching started on 05 November, after the wind direction had changed to south-east, and continued for two whole seiche periods.

Horizontal distribution of the seiche characteristics was estimated using two-layered normal mode calculations on finite-element grid approximating the lake shape. The interface slope and seiche currents distribution for the slowest uninodal seiche ("first" mode) is shown in Fig. 7. The 1st mode of the model is pronounced mostly in the western and the northern basins that agrees with characteristics of the observed seiche (cf. isotherm displacements in Figs. 5 and 6).

The fact that the northern basin is sufficiently deeper than the western one explains the increase of the seiche amplitude in the western basin up to 6m. The important effect of this high-amplitude oscillation is the internal surge – flushing of the dense metalimnion water into littoral areas, shallower than the mixed layer depth. Examination of the lake bathymetry shows that the shallow sidearm on the end of the western basin is almost completely filled with the metalimnion water by the seiche's crest (see the shadowed area in Fig. 8). Such an upwelling of the cold dense water suggests formation of a horizontal density front in the lateral zone (Fig. 9A). The resulting strong density gradients in couple with horizontal currents generated by subsequent outflow can lead to the baroclinic instability and give rise to initial vorticity (Fig. 9B).

The situation is similar to this resulting in formation of atmospheric cyclones, where the density front is formed by cold air outbreak (e.g. from Greenland) to the warm air masses (formed by Gulf Stream, in this case) or oceanic eddies, such as lenses of dense Mediterranean water bursting into North Atlantic.

The vorticity of the eddy is four times larger than the planetary vorticity at the lake's latitude and

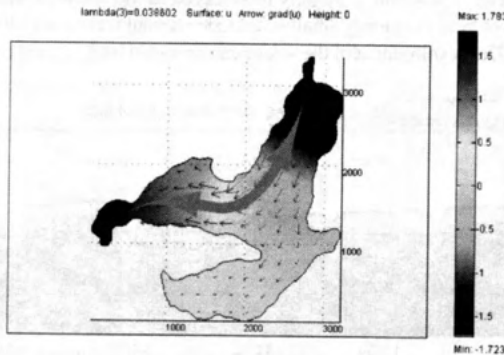


Figure 7: Interface declination (coloring), relative velocities (small arrows) and main axis of the first horizontal seiche mode in Lake Stechlin calculated from normal mode solution of the two-layered flat-bottom inviscid model with real lake configuration.

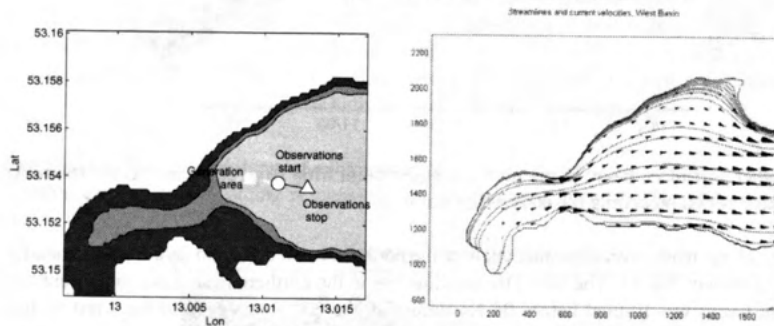


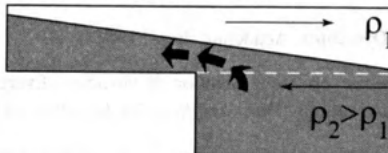
Figure 8: **Left:** the internal surge in sidearm of the western basin shaded area between 6m and 12m isotherms filled by metalimnion water during the seiche on November, 06. Also shown is the eddy drift during the measurements on November, 07 and supposed eddy location during the surge. **Right:** Streamlines and relative current velocity vectors in the upper layer calculated from the two-layered model. The flow convergence and intensification can be clearly distinguished in the sidearm's outlet.

the Burger number based on the eddy dimensions is about  $10^{-2} \div 10^{-1}$ , i.e. the dimensions are smaller than but comparable to the internal Rossby radius. The strong increase of vorticity can be attributed to the local flow characteristics (Fig. 9C). One important factor here is the narrow outlet connecting the sidearm with the rest of the western basin (Fig. 8). As a result, the flow convergence should give rise to the cyclonic vorticity here and corresponding flow intensification impose the eastward velocity to the eddy. Another mechanism of the increase of the vertical component of vorticity can consist in stretching of the vortex line by thermocline sinking driven by the seiche. Assuming the eddy to occupy the entire mixed layer, conservation of potential vorticity for a shallow homogeneous layer can be written as (Gill, 1982),

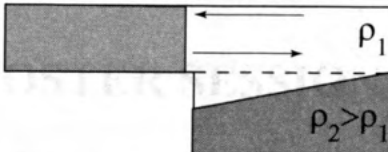
$$\zeta - f\eta/H = \text{const.}$$

where,  $\zeta$  and  $f$  are the relative and planetary vorticity, correspondingly,  $\eta$  is the thermocline declination and  $H$  is the layer depth. Using the values  $H = 13\text{m}$ ,  $f = 1 \cdot 10^{-4}\text{s}^{-1}$ ,  $\zeta_M = 4.5 \cdot 10^{-4}\text{s}^{-1}$ ,

A. Internal surge (coast left)



B. Formation of horizontal front



C. Vortex intensification

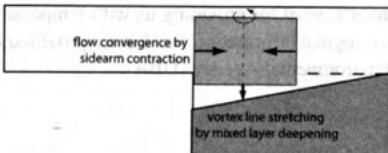


Figure 9: Sketch illustrating formation of the density front by internal surge in a sidearm.  $\rho_1$  is the density of the mixed layer,  $\rho_2$  is the metalimnion density

$\eta_m = 4\text{m}$  (subscript m means the values at the moment of drift measurements) and defining  $\zeta_0 = \zeta|_{\eta=0}$  one arrives at

$$\Delta\zeta \equiv \zeta_m - \zeta_0 = f\eta_m/H = 0.3 \cdot 10^{-4} \text{ s}^{-1},$$

or the thermocline deepening results in vorticity increase only of 6%. It is also unlikely that the remaining vorticity was produced by the flow convergence. Apparently, other mechanisms participated in the vortex formation, particularly the inverse cascading of the turbulence energy from small-scale to large-scale motions, characteristic for 2-D turbulence (Provenzale, 1999). Our data did not allow resolving of spectral characteristics of the eddy current in order to verify the hypothesis about inverse cascading of energy.

It is probable that the observed eddy represents rather accidental phenomenon specific only for Lake Stechlin in very special conditions. However, the following considerations force us to draw attention to this observation:

- Internal surge is a common phenomenon, especially in stratified lakes with indented shoreline. Hence, the formation of instable density fronts can be also expected in other lakes.
- there are little, if any, reports on mesoscale coherent structures in small lakes. The present observation indicates that processes responsible for mesoscale eddies formation in the Atmosphere and in the Ocean can be also important in lakes. Lake eddies, if appearing regularly, provide a great opportunity for investigation with many useful analogies in other geophysical flows.
- in situations when eddies similar to this appear in a lake, their impact on the lake mixing should be undoubtedly taken into account, especially when considering exchange processes in the lateral zone.

## References

- A. Gill. *Atmosphere–Ocean Dynamics*. Academic Press, 1982.
- A. Okubo and Curtis C. Ebbesmeyer. Determination of vorticity, divergence and deformation rates from analysis of drogue observations. *Deep-Sea Res.*, 23:349–352, 1976.
- A. Provenzale. Transport by coherent barotropic vortices. *Annu. Rev. Fluid Mech.*, 31:55–93, 1999.
- Brian G. Sanderson. Structure of an eddy measured with drifters. *J. Geophys. Res.*, 100(C4):6761–6776, 1995.

## Acknowledgements

This work is part of the research project KI-853/2 "Circulation in Lake Stechlin" supported by German Science Foundation (DFG). Dr. Peter Casper contributed strongly to the experimental part of the study. We thank Prof. Dr. Rainer Koschel for providing us with temperature profiles from the deepest point of Lake Stechlin. Meteorological information was kindly provided by the measurements station Neuglobsow of the German Environmental Agency (UBA).

## **POSTER SESSION I**

EDWARD TELLER

# Some new statistical estimates functions of distribution for spacing of Langmuir circulation (LC)

Sergey V. Ryanzhin<sup>1,2)</sup>, Nikolay V. Kochkov<sup>1)</sup>, Lev N. Karlin<sup>3)</sup>

1) Institute of Limnology, Russian Academy of Sciences, Sevastyanova Str. 9, St Petersburg, 196105, RF,  
Phone/Fax +7 812 3878020/3887327, E-mail: [ryanzhin@peterlink.ru](mailto:ryanzhin@peterlink.ru),

2) contact author;

3) Russian State Hydrometeorologic University, Maloohktinskii pr. 98, St Petersburg, 195196, RF,  
Ph/Fax +7 812 4444163/6090; E-mail: [Klara@rshu.ru](mailto:Klara@rshu.ru)

Vast field measurements of characteristics of Langmuir circulation (LC) were carried out at the Gulf of Finland, Black Sea, Lake Ladoga and Punnus-Jarvi. Particulate attention was paid to obtain the sets of LC spacing – the most reliably and easily measured LC value. 62 sets of LC spacing were obtained under various hydrometeorological (wind speed, wind-wave parameters, mixed layer depth, buoyancy flux at the air-water surface etc.) and bathymetric (water depth) conditions (Ryanzhin 1982, 1995; Ryanzhin et al. 2003, 2004; Ryanzhin and Chu 2003). 28 histograms obtained under the sea and lake conditions and published in world literature (Faller and Woodcock 1964; Williams 1965; McLeish 1968; Myer 1969, 1970; Kenney 1977; Thorpe and Hall 1982; Ichijo et al. 1985; Zedel and Farmer 1991; Osborn et al. 1992; Farmer and Li 1995; Gemmrich and Farmer 1999) were also approached for analyses. Approximating statistical function of distribution was calculated for each of 90 sets of LC spacing obtained by the authors and taken from literature. Using routine  $\chi^2$ -test at 0,95-confidence level each histogram was tested to fit exponential, gamma-, lognormal, Maxwell-, Raleigh- and Weibull- distribution. Although gamma-, Raleigh-, Weibull- and Maxwell- distribution occurred (27, 8, 6 and 1 cases respectively) prevailing of lognormal distribution was found (49 cases). Further analyses and discussion of the results obtained are given.



## FLake - A Lake Model for Environmental Applications

*Dmitrii Mironov<sup>1</sup>, Sergey Golosov<sup>2</sup>, Erdmann Heise<sup>1</sup>, Ekaterina Kourzeneva<sup>3</sup>,  
Bodo Ritter<sup>1</sup>, Natalia Schneider<sup>4</sup> and Arkady Terzhev<sup>5</sup>*

<sup>1</sup> German Weather Service, Offenbach am Main, Germany

<sup>2</sup> Institute of Limnology, St. Petersburg, Russia

<sup>3</sup> Russian State Hydrometeorological University, St. Petersburg, Russia

<sup>4</sup> University of Kiel, Kiel, Germany

<sup>5</sup> Northern Water Problems Institute, Petrozavodsk, Russia

### Abstract

A lake model for environmental applications is developed. The model, termed Flake (<http://nwpi.krc.karelia.ru/ake/index.htm>), is capable of predicting the vertical temperature structure and mixing conditions in lakes of various depth on time scales from a few hours to a year. It is based on a two-layer parametric representation of the evolving temperature profile and on the integral budgets of heat and kinetic energy for the layers in question. The structure of the stratified layer between the upper mixed layer and the basin bottom, the lake thermocline, is described using the concept of self-similarity (assumed shape) of the temperature-depth curve. The same concept is used to describe the temperature structure of the thermally active upper layer of bottom sediments and of the ice and snow cover. The result is a computationally efficient bulk model that incorporates much of the essential physics. Empirical constants and parameters of Flake are estimated, using independent empirical and numerical data. They should not be reevaluated when the model is applied to a particular lake (there are, of course, lake-specific external parameters, such as depth to the bottom and optical properties of water, but these are not part of the model physics). In this way, FLake does not require re-tuning, a procedure that may improve an agreement of model results with a limited amount of data but should generally be avoided as it greatly reduces the predictive capacity of a physical model. In order to compute fluxes of momentum and of sensible and latent heat at the lake surface, a parameterization scheme is developed that accounts for specific features of the surface air layer over lakes. The new lake model and the new surface-layer parameterization scheme are favourably tested against observational data through single-column numerical experiments.

Various applications of the new lake model are discussed. As a lake parameterization module, FLake is implemented (Mironov et al. 2005) into the limited-area numerical weather prediction system LM run operationally at the German Weather Service, Offenbach am Main, Germany. It is also implemented into the regional climate modelling systems CLM, run at GKSS Research Centre, Geesthacht, Germany, and RCA, run at Swedish Meteorological and Hydrological Institute, Norrkoping, Sweden. As a single-column lake model, FLake is used to assess the response of shallow lakes to climate variability (Kirillin 2003). It is also used as a physical module in models of lake ecosystems (Golosov et al. 2004, Maher et al. 2004) and as an educational tool (Braslavski 2004).



## Bathymetric map definition and water balance of the shallow Poopó Lake, Bolivia

Ramiro Pillco Zolá\* & Lars Bengtsson

Department Water Resources Engineering, Lund University, Sweden

Institute of Hydraulic & Hydrology, San Andres Mayor University, Bolivia

### Abstract

The bathymetry of the shallow Lake Poopó in the Bolivian Altiplano has been determined through depth sounding and using satellite images. The hypsographic curve found was correlated with a water balance calculation. The maximum depth of the lake is less than 3.5 m; the maximum surface area is around 2800 km<sup>2</sup>. Much of the lake is less than 25 cm deep.

**Keywords:** Bathymetry; Hypsographic curve; Morphology; Depth sounding; Satellite images; Water balance.

### Introduction

Mapping lake bathymetry principally allows estimates to be made of morphometric and hydrologic parameters. The hypsographic curve in respect to the first issue also is to be determined, which allow knowing the water depth sensitive in respect to the hydrological input and output variables changes, implementing aquatic habitat management and lake dynamic predicting.

The popular method in determining the lake hypsographic curve (HC) is using a bathymetric map and by plotting the graph of different surface areas against its depths values, although is necessary to have the lake leveling data. The HC may be obtained through water balance computation in respect to the depths but the method could be limited for lakes where the water level does not drop too much. Last time, satellite image Thematic Map™ have been used for mapping the bathymetry although this kind of data can not be used as the primary source (Bullard, 1983; Pirazolli, 1985).

The bathymetric studies are available since 1906. The first lake's observations was done by D' Orbigny (1830s). The last study was done in 1977 by Boulange. However several years later in 1986, marked by high rainy season, the lake had overflowed through its outlet river to the big salt field Coipasa and Uyuni. This event according Iltis (1993) defined two bathymetric maps and different HC probably; one before of 1986 and other after this year.

Based on water levels data of Lake Titicaca, available since 1920, from which the Poopó Lake is very dependent, was predicted long-term water level variation of Poopó Lake (Pillco & Bengtsson, 2004), this information shows that the water depths in Poopó Lake had never reached its maximum in 52 years, except in 1986. The maximum depth in 2001 year was measured at 2.5 m; echo sounding was applied unsuccessfully this year.

Two methods were selected in defining the HC; based on the bathymetric map, which was constructed from lake leveling data, performed by depth sounding, the missing depths were filled from Landsat Thematic Map™; the second method is based on water balance model (WB) computation, for which was used hydrologic data of 2001 year, also images in determining the water surfaces; during the WB computation the storage water in the small Uru-Uru Lake, in upstream of Lake Poopó, was considered. The comparison of the results by both methods is discussed. Other objective is to confirm the lake morphologic changes.

### Geographic description

The modern saline Poopó Lake, remained from the paleolakes, is located in the central part of Bolivian Altiplano between 18 °C 30' – 19 °C 15' of SL and 66 °C 30' – 67 °C 15' of

WL coordinates, at 3700 m above the sea level (Fig. 1). Since 2002 is considered as a wetland and included on the list of *Ramsar Convention on Wetlands, Iran of 1971* (Olivo O. et al., 2002) because several times during the last decades the lake almost has dried.

The actual functioning of hydrographic system is configured by the serial lakes connected through the mean Desaguadero River (DR). The Poopó Lake in the upstream through the right branches of DR is connected to Uru-Uru Lake, with 0.75 m of maximum depth and with area of 350 km<sup>2</sup>, also to Titicaca Lake; downstream, by Laka-Jawuira River is connected to the salt fields mentioned. The Uru-Uru Lake was formed in 1950s because the DR was divided in two branches.

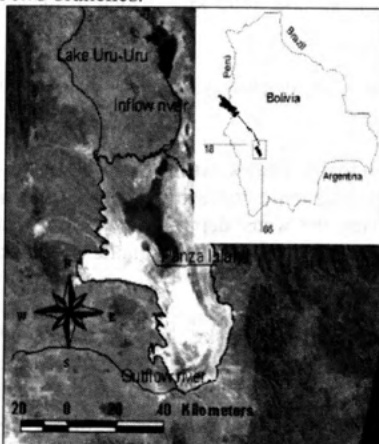


Fig. 1: Poopó Lake location in the central Altiplano (Bolivia).

Topographically the surrounding area of Poopó Lake is completely uniform although the drainage mountain type area of 12488 km<sup>2</sup> varies between 3750 and 4800 m. The lake bottom is flat and the habitual deepness is less than 1.5 and close to the shoreline varies between 10 and 25 cm of depth. The large ephemeral area changes between 3 and 5 km of extension. The deepest part of lake is located at the right cost of Island Panza (figure 1). Three small islands also are spread along the lake but are not visible at all on the images.

The temporal discharge in the sub basins is typical, due the seasonal austral summer rainfall, where over than 70 % of the 350 mm of annual rainfall is concentrated (Aceituno et al., 1993). The mean annual discharge in the regional rivers is 10 m<sup>3</sup>s<sup>-1</sup>; in the mean river is 66 m<sup>3</sup>s<sup>-1</sup> (Pillco and Bengtsson, 2004). The mean temperature is 10 °C. The sediments are carried out by 23 rivers; according by Iltis, the water transparency varies greatly but mostly turbid during the wet period; the mean river has <1m of turbidity. Temporal images data also show high turbidity in the lake. The wind in the zone could be over 18 ms<sup>-1</sup>, especially a strong nightly wind with south-east direction could be the responsible for little farther of water surface advances (Allen, 1940).

The water storage regime in the small Uru-Uru Lake is not easy to estimate because the water inflow from DR through two branches is unpredictable, but satellite images and the hydrologic lake parameters can help in determining approximately.

#### **Previous lake leveling**

The old morphometric parameters are different. In a temporal analyzing, they are not in a tendency. In term of lake large, according to the last bathymetric map available (Boulange,

1977) it has 90 km of longitude and 53 km of width. The shoreline defined after 1986 gives 95 km of longitude and 58 km of width. In detail the old morphometric parameters values are shown in table 1.

Table 1. Morphometric parameters of Lake Poopó since 1905.

Authors	$A$ $\text{km}^2$	$h_{\max}$ $m$	$\bar{h}$ $m$	$\bar{h} / h_{\max}$ -	$V$ $\text{km}^3$	$D_L$ -
Naveu-Lemaire (1906)	2530	2.50	1.40	0.56	3.542	
B. Boulange (1977)	2650	2.20	0.97	0.44	2.569	1.69
Iltis (1986)	3000	3.00				

In 2005, after the rainy season, was made lake leveling through the depth sounding in five transects, three transects are shown in figure 2. The total depth data are 144, and for each point was fixed XY-data using handled *Global Positioning System* (GPS). The sections don not describe the whole lake because the water level was below of its shoreline. The location of these transects will show later. The maximum water depth this time was found at 1.20 m.

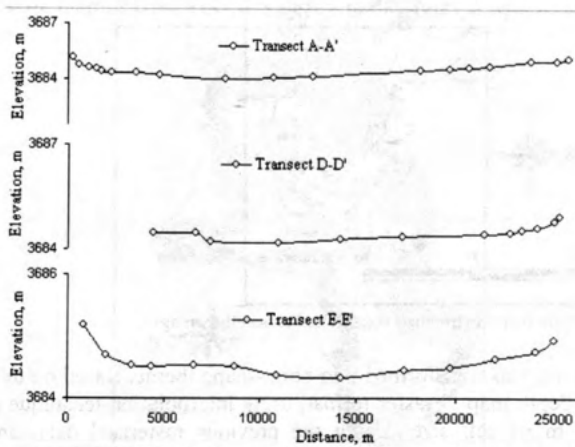


Fig. 2. Lake sections determined after rainy season of 2005.

In the figure 1 is shown the largest water surface area taken place in 1986. Several satellite images show the water level marks in the Poopó depression because the lake is saline between 5 and 80  $\text{g L}^{-1}$  of concentration, and during the resection time the water level marks are leave.

#### Depth contour map construction

The water level marks seeing on the satellite images were used to generate the depth contour map with Arc View (AV). The water level references or polygons were defined by digitalizing, particularly using TM images corresponding to Mach 30/1986, to July 15/1992 and to October 20/1995 (this one plotted in fig.1). On the first image is seen the shoreline of the lake, it allows to define the maximum contour line; on the third image are seen three marks, including a minimum surface area; and on the second was found the second contour line, after the shoreline. During the same procedure was defined the Panza Island shape. After this the polygons were converted into line-shape theme with XY-data.

For the line-shape theme was defined the Z-data. Firstly was defined the shoreline elevation by topographical leveling *in situ* and knowing the BM. Simultaneously, by

sounding was found the maximum depth at 1.20 m, by other hand between the shoreline mark and the actual water level was determined the height difference by topographical leveling. The more real height was found in the island side; only in 54 m of distance was found 2.27 m of difference. Now by adding these values the maximum depth results 3.47 m. Then the Z-data for the smallest contour line in the figure 3 was defined subtracting the maximum depth from the shoreline elevation. The elevations for other contour lines were determined by linear interpolation.

The different contour lines considered and mentioned above was joined in unique line-shape theme using *merge* of AV. The depth contour map with its elevation is shown in the figure 3 at 1: 30000 scales, where the elevation of shoreline is at 3687.50 m and the deepest zone of lake is at 3684.03 m.

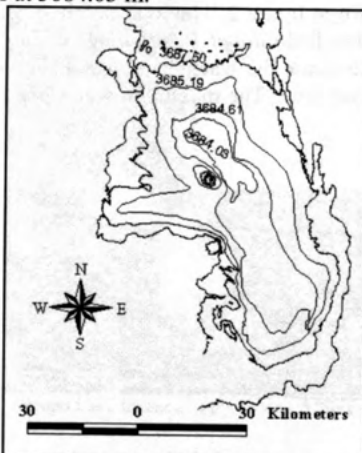


Fig. 3. Approximate bathymetric map constructed on satellite images.

The line-shape theme, above, was transformed into point-shape theme. Based on this data, was constructed a digital depth map in raster format, using interpolation-technique (IDW) available in AV at 300 m of cell size. Using the previous rasterised data, and just considering some depth data points, were performed the section in the same transects where were made depth measurements, exposed in above chapter. The location of these sections is exposed in the figure 4.



Fig. 4. Water depth transects and contour lines defined on the images.

The comparisons of the sections gotten by two approaches were made, and generally they show good agreement. The maximum difference of height found between these sections is at 35 cm, for example for the transect C-C'.

### Mapping the lake bathymetry

The sections compared above are quite similar, then were performed the full sections filling missing depth data from contour map constructed on the TM. Behind to the first five sections mentioned above, based on the TM data (figure 4), were performed others five sections on different transects showed in the same figure. Now the depth points are 246.

Based on the last depth points was constructed again the depth map on GIS following the same process which was applied in the previous chapter; finally also was got the rasterised theme of the depth map again for 300 m of cell size. Is necessary to clarify that for this mapping was considered the XYZ-data of shoreline, the nearest topographic curve and the contour lines describing the Panza Island. On the rastered theme was created the contour lines map with 25 cm of height variation, considering the above limit of 3687.50 m. The bathymetric map of Lake Poopó is shown in the figure 5 with its contour line elevations.



Fig. 5. Bathymetric map of Poopó Lake after 1986 year.

The different surfaces areas and its volumes between below and above water depths were calculated automatically with *Area and Volume statistics* option of AV, which are shown in table 2 (columns 1, 2 and 3), the rest of the morphometric parameters were calculated with standard equations showed in the same table. The maximum depth ( $H_{max}$ ) is 3.47 m at 3687.50 m elevation and the bottom is at 3684.03 m. The volume capacity of the lake is  $5.512 \text{ km}^3$  corresponding to the maximum water surface area of  $2727.31 \text{ km}^2 (A_o)$ , framed between 95 km ( $L$ ) and 58.55 km of width ( $B_{max}$ ). The perimeter for the maximum shoreline is 348.80 km ( $P$ ) and Development of shore lines is 1.88 ( $D_L$ ).

Table 2. Morphometric parameters of Poopó Lake after 1986 year.

Elevations m	H m	$A_o$ km <sup>2</sup>	V km <sup>3</sup>	L km	$B_{max}$ km	b km	Mean depth m	Relative depth -	P km	$D_L$ -
1	2	3	4	5	6	7	8	9	10	11
3687.50	3.47	2727.31	5.512	95.99	58.55	35.85	2.02	0.58	348.80	1.88
3687.00	3.00	2433.73	4.222							
3686.50	2.50	2147.56	3.076							
3686.00	2.00	1856.08	2.075							
3685.50	1.50	1557.12	1.222							
3685.00	1.00	1133.38	0.536							
3684.50	0.50	542.12	0.103							
3684.03	0.00	153.82	0.000							

Taken the different values of depth ( $H$ ), surface areas ( $A_o$ ) and volumes ( $V$ ) from the table 2, were plotted the hypsographic curves (graph of volume-depth and area-depth) to find the equations of relationships. The best fit relationship volume-depth describes this one

$$V = 0.028h + 0.5759h^2 - 0.0365h^3 \quad (1)$$

The relation equation of area-depth should be described with this equation

$$A = a + 2bh + 3ch^2 \quad (2)$$

Replacing the values of a (0.028), b (0.5759) and c (0.0365) from the (1) on the (2) equation and modifying its units, the relationship equation between areas and depths describes this

$$A = 28 + 151.8h - 109.5h^2 \quad (3)$$

### Water balance computation

The WB model was applied for the hypsographic curves of Poopó Lake. Considering the inflow and outflow of the lake during 2001, the equation defined and which was computed in respect to depth variation at month scale is this

$$\partial h / \partial t = (Q_{Des} + Q_{reg} + (P - E_{lake}) A_{lake} - V_{ur}) / A_{lake} \quad (4)$$

$Q_{Des}$  represents the discharge of Desaguadero River;  $Q_{reg}$  is the total discharge from 22 regional rivers;  $P$  is the precipitation on the lake;  $V_{ur}$  is the storage water in the small Uru-Uru Lake;  $(E_{lake})$  is the water evaporative losses from the lake;  $(A_{lake})$  is the water surface changes in the lake. Outflow is not considered because during this year the lake did not spillway.

The discharge of  $Q_{Des}$  comes from hydrological measurements. The discharge in the regional rivers was defined throughout the specific discharge ( $q$ ); in several rivers were measured the couple parameters  $H-Q$  and have been obtained the discharge curves; several values of  $q$  in different rivers were compared; the  $q$  values were quite similar; then  $q$  value of Sevaruyo River, was applied for the whole catchment of Poopó Basin because it has not missing data. The  $P$  value was calculated as the arithmetic average on the five rain gauge stations. The  $E_{lake}$ , which is not available for 2001, was considered the standard monthly values from corrected observation on pan of six stations between 1990-1995. The different water surface areas of both lakes have defined on the images, collected during 2001 from

*Conae-Argentina and from Gateway to Astronaut Photography of the Earth, Nasa-Johnson Space Center.* The most important variable is the water inflow in the DR, continued by the runoff in the small rivers, the minimum part of inflow belongs to the rainfall.

The WB computation was made in respect to  $h_{t+1}$ , being the depth at the end of month; for the start month depth  $h_t$  was considered the water surface area in December of 2000. The small water volume accumulated in the Uru-Uru Lake, was estimated for each month knowing a relation depth-area ( $h_{ur} = A/370$ ) and knowing the water surfaces areas determined on the images, the different volumes for each month have been subtracted during the computation of WB.

### Comparison of the results

The hypsographic curves (HC) defined through two methods, are plotted in the figure 6. The volume-depth curve (a), generally, shows a good agreement between those methods. Although two points from WB method did not fitted very well; these points are affected by the discharges of DR in January and February, by the time has been exhibited a maximum discharges and producing a flooding upstream of Uru-Uru Lake, which is difficult to estimate. The February discharge in DR only could be compared with discharge of 1986 by the time the Poopó Lake had exhibited spillover. The area-depth (figure 6-b) curve also shows a good agreement between the methods

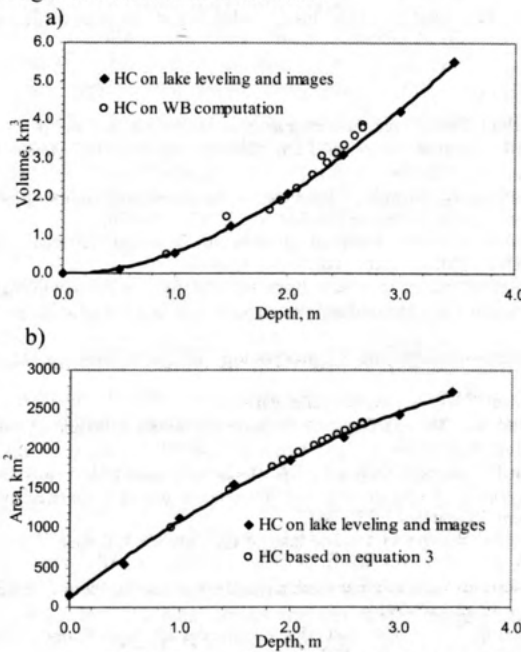


Fig. 7. Volume-depth curve (a) and Area-depth curve (b).

Based on the absolute HC (figure 6-b) and relative area-depth curve, has been analyzed the actual lake shape. Then 20 percent of the area found at greater 45 percent of the maximum depth, it means that Poopó Lake belongs to group of convex lakes. After the WB computation, for 2001, confirms that littoral zone is very unstable, characterized with fast water dynamic; for example, during this year the water surface area changed from 1000 until 2500 km<sup>2</sup>. Considering the inflow of 2001 the lake needs 1.02 year of time to be filled.

The morphology of lake by two HCs comparison, exhibits changes between the old and the actual curve, the morphometric parameters resulted different. The old HC has almost concave type and the actual is on a tendency of convex type. The form changes also could be seen by the comparison between old and actual lake sections; the first one show a bottom deeper than the actual; also the shoreline is more irregular than the before one which is explained by ( $D_L$ ). The morphometric parameters are different in respect to the before morphometric parameters.

### **Conclusions**

The bathymetric map and HC found, considering the maximum shoreline taken place in 1986, reflect the morphologic lake changes, and according the comparison at least of two HCs, the Poopó Lake is on a tendency of convex type. In circumstances, like during 2001 year, the WB method could be useful for HC construction when the lake level falls until very shallow.

The shoreline moves with the wind so bathymetry is difficult to determine, but the hypsographic curve does not change while its shoreline recover.

### **Acknowledgements**

We would like to thank to Sida-Sarec (Sweden) for the financial supporting, also to assistant researcher from IHH-UMSA (La Paz), who were involved during the lake leveling mission.

### **References**

- Aceituno, P., Montecinos, A., 1993. Circulation anomalies associated with dry and wet periods in the South American Altiplano. Proc. Fourth Int. Conf. On Southern Hemisphere Meteorology, Hobart, Australia, Amer. Meteor. Soc., 330-331.
- Allen, G., O., 1940. IX. Charophyta. In: Reports of the Percy Sladen Trust Expedition to Lake Titicaca in 1937. Transactions of the Linnean Society of London, ser. 3, 1(2), 155-160.
- Boulange, B., Rodrigo, L., Vargas, C., 1978. Morphology formation et aspects sedimentologiques du lac Poopó, Bolivia. Cah. ORSTOM, ser. Geol., vol. X, No 1, 69-78.
- Bullard, R. K., 1983. Detection of marine contours from Landsat film and tape. In Remote Sensing Application in Marines Science and Thecnology, edited by A. P. Cracknell (Dordrecht: D. Reidel) pp. 373-381.
- Clapperton, C., 1993. Quaternary Geology and Geomorphology of South America, Elsevier, Science Publisher, 779 p.
- D'Orbigny, A., 1835. Voyage dans l'Amérique Méridionale. Paris.
- Fornari, M., Risacher, F., Feraud, G., 2001. Dating paleolakes in the central Altiplano of Bolivia. Elsevier Science B.V., Paleo. 172, 269-282.
- Fritz SC, Baker PA, Lowenstein TK, Seltzer GO, Rigsby CA, Dwyer GS, Tapia PM, Arnolds KK, Ku TL, Luo SD, 2004. Hydrologic variation during the last 170 000 years in the southern hemisphere tropics of South America. Quaternary Research 47, 235-248.
- Iltis, A., 1993. Recent limnological changes in a saline lake of the Bolivian Altiplano, Lake Poopó. Int. J. Salt Lakes. 2 (1), 17-19.
- Naveau-Lemaire M., 1906. El Titicaca y el Poopó: contribucion al estudio de los lagos altiplanos, Rev. Min. De Colon y Agric. No 16, 17 18, 568-591 p.
- Olivo, R., O., 2002. Diagnóstico de los recursos naturales y culturales los lagos Poopó y Uru-Uru, El trato-Bolivia, Convención Ramsar, WCS, La Paz, Bolivia
- Pilleo, R., Bengtsson, L., 2004. Long-term and extreme water level variation of the shallow Poopó Lake, Bolivia. (In publication).
- Pirazzoli, P.A., 1978. Bathymetry mapping of coral reefs and atolls from satellite. Proceeding of the 5<sup>th</sup> International Coral Reef Congress, Taiti, 6: 539-545.
- Risacher F., Fritz B., 2000. Bromine geochemistry of Salar de Uyuni and deeper salt crusts, Central Altiplano, Bolivia, Chemical Geology, 167, 373-392.
- Servant, M., Fontes, J., 1978. Les lacs quaternaires des hauts plateaux des Andes boliviennes. Premières interprétations paleoclimatiques. Cahiers ORSTOM, ser. Geol. 10 (1), 9-23.

## WATER BUDGET OF THE CASPIAN SEA AND ITS SENSITIVITY TO EXTERNAL FORCING

Rashit A. Ibrayev<sup>a</sup>, Emin Özsoy<sup>b</sup>

<sup>a</sup>*Institute of Numerical Mathematics, Russian Academy of Sciences, Moscow, Russia,  
ibrayev@inm.ras.ru*

<sup>b</sup>*Institute of Marine Sciences, Middle East Technical University, Erdemli, Mersin, Turkey,  
ozsoy@ims.metu.edu.tr*

### ABSTRACT

A three-dimensional primitive equation model including sea ice thermodynamics and air-sea interaction is used to study seasonal circulation and water mass variability in the Caspian Sea under the influence of realistic mass, momentum and heat fluxes. River discharges, precipitation, radiation and wind stress are seasonally specified in the model, based on available data sets. The evaporation rate, sensible and latent heat fluxes at the sea surface are computed interactively through an atmospheric boundary layer sub-model, using the ERA15 atmospheric data and model generated sea surface temperature. The model successfully simulates sea-level changes and baroclinic circulation / mixing features with forcing specified for a selected year. Simulation of sea surface topography yields verifiable results in terms of sea level. Model successfully reproduces sea level variability for four coastal points, where the observed data are available. Analyses of heat and water budgets confirm climatologic estimates of heat and moisture fluxes at the sea surface. Experiments performed with variations in external forcing suggest a sensitive response of the circulation and the water budget to atmospheric and river forcing.

### **1. Introduction**

The Caspian Sea is the largest totally enclosed water body on Earth, constituting 44 % of the global volume of lacustrine waters. Compared to other semi-enclosed and enclosed seas of the world, little is known of the Caspian Sea variability. The most urgent, yet unresolved questions relating to the Caspian Sea is: Through which climatic and dynamic mechanisms is the sea level variability controlled? The phenomenological evidence is too ambiguous or insufficient to give satisfactory answers to these questions.

The water budget of the landlocked Caspian Sea is extremely sensitive to climatic variability in the surrounding areas. The water budget depends on climate, but anthropogenic effects such as water regulation schemes also had significant effects, leading to inter-annual, inter-decadal and longer term variations in sea level throughout the history of the Caspian Sea (Kosarev *et al.*, 1994; Rodionov, 1994). Rapid sea level change occurred in 20<sup>th</sup> century. Superposed on these inter-decadal changes, the sea level displays a clear seasonal cycle, as a function of the net water budget (rainfall + river inflow - rainfall). The sea level reaches its lowest seasonal value in winter and increases in the May – July period, following the spring floods. The climatological mean seasonal range of sea level is about 30 cm (Baidin *et al.*, 1986).

Earlier models of sea level variability (*e.g.* Radionov, 1994) generally considered the problem from a stochastic point of view. While stochastic models had a certain level of success, a more fundamental understanding can only be based on controls by hydrological as well as oceanic processes. The total water fluxes across the ocean surface and river mouths determine the mean sea level in an enclosed water body such as the Caspian Sea. Surface fluxes of momentum, water and heat are coupled together, and can strongly be

modified by the surface temperature and circulation of the sea. These fluxes are also the basic elements of the regional hydrological cycle coupled to the global climate.

The basic features of the Caspian Sea seasonal cycle were studied in *Ibrayev et al., 2002*. The Model of Enclosed Sea Hydrodynamics (MESH), *Ibrayev, 2001*, which was used in the study, is 3-D circulation model with variable water mass in the basin, including air-sea interaction and sea ice thermodynamics sub-models.

## 2. Model Description

In the study we use free-surface, primitive equation, z-level numerical Model for Enclosed Sea Hydrodynamics (MESH), described by *Ibrayev* (2001), employing Boussinesq and hydrostatic approximations. Formulation of free-surface condition in the model allows propagation of surface gravity waves and mean sea surface elevation changes in response to non-zero water balance. An essential for the model formulation is capability to simulate variability of total water mass in the basin. We use kinematic equation at the sea surface, which make it possible to introduce time-varying thickness of the upper layer in correspondence with the continuity equation. An important issue concerning the formulation of boundary conditions arise from the fact that fresh water income and outflow plays an important role in the sea dynamics. Thus the estimates show that the hydrological turnover time for the Sea is of the order of 200 years and for the shallow NCB of the order of 1 year. As was discussed by *Beron-Vera, Ochoa & Ripa* (1999), use of ad hoc surface boundary conditions for salt balance, such as salt relaxation or "virtual" salt flux conditions are unphysical in nature because they create or destroy salt mass. The correct boundary conditions should include the fact that the vast majority of the salt particles remain in the sea during evaporation, and that the precipitated water is essentially pure freshwater. In formulation of boundary conditions for salt, heat and momentum fluxes we follow the approach of *Beron-Vera et al.* (1999), and of *Roulett & Madec* (2000) and add to the usual formulation of air-sea fluxes the terms responsible for freshwater influence.

The heat fluxes at the sea and ice upper boundaries are the sum of long-wave backward radiation, sensible and latent heat fluxes at the sea surface. The momentum, sensible heat and evaporation fluxes are calculated through the air-sea interaction sub-model based on the Monin-Obukhov similarity theory. Whenever thermal conditions are favourable to form ice, air-sea fluxes are modified to account for the effects of sea-ice, based on the thermodynamic sea-ice sub-model of *Schrum & Backhaus* (1999).

The subsurface profile for solar radiation is computed using the two-band approximation of *Paulson & Simpson* (1977). The attenuation length for short wave band of solar radiation strongly depends on turbidity and differs between coastal and offshore regions. For the Caspian Sea its value is estimated to be about 10-15 m in the central parts of the MCB and SCB, and about 1-5 m in the NCB (*Terziev et al., 1992*). We parameterise the short wave attenuation length depending on local depth.

The grid resolution of the model is  $(1/12)^\circ$  in latitude and  $(1/9)^\circ$  in longitude, which gives a grid size of about 9. km. There are 20 vertical model levels. The model is initialized from a state of rest corresponding to the climatologic sea state in November.

## 3. External forcing

The model forcing is based on the ERA15 monthly averaged atmospheric data (wind velocity at 10 m height, air and dew point temperatures at 2 m height, incoming solar radiation and thermal back radiation). The evaporation rate, wind stress, sensible and latent heat fluxes at the sea surface are computed interactively through an atmospheric boundary layer sub-model. Precipitation and radiation fluxes are also based on ERA15 data. River discharges are specified in the model, based on available monthly mean data sets. The validity of ERA15 data for the Caspian Sea was analysed using available

climatologic data. Monthly mean river runoff data were obtained from routine hydrometeorological observations.

#### 4. Air-sea fluxes of heat and mass

We focus our attention on the seasonal air-sea fluxes of heat and moisture at the air-sea interface. Estimation of surface heat flux from bulk formulae using monthly mean values of surface wind speed, humidity, air and sea surface temperature, has been shown to differ by less than 10% from computations using all samples by *Esbensen & Reynolds (1981)*, and has been confirmed to have a ratio of 1.02-1.09 for different parts of the Caspian Sea by *Panin (1987)*. We thus employ a correction factor of 1.09 for sensible and latent heat fluxes computed from monthly fields.

##### 4.1. Evaporation

In winter, a region of high evaporation in the eastern part of MCB (*Fig. 1a*) results from the combined effects of (i) cold and dry air intrusions from the eastern coast and (ii) warm water from the SCB advected along the eastern coast. The summer evaporation pattern is the opposite (*Fig. 1b*): the cold water along the eastern shelf of MCB produces very little evaporation. Evaporation in summer has an increasing trend from north to south, except in the shallow NCB where evaporation is increased to almost twice the deep basin values. Analyses of monthly mean evaporation in the Caspian Sea made on the basis of 150,000 observations (*Panin, 1987*) are in good agreement with the simulated evaporation both in terms of distribution and magnitude.

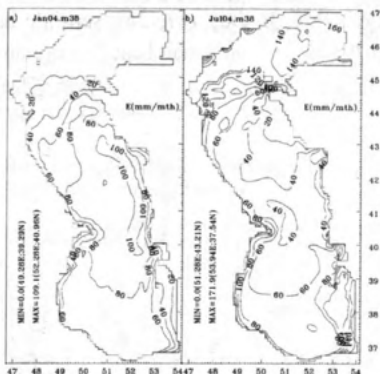


**Figure 1.** Evaporation (mm/month) in (a) January and (b) July.

##### 4.2. Sensible and latent heat fluxes

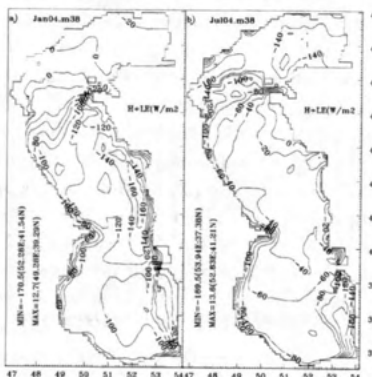
Monthly and annual mean heat budget components are given *Table 1*. The seasonal cycle of latent heat flux follows that of evaporation. In summer the sensible heat flux almost vanishes as a result of the small difference between SST and air temperature. SST is higher than the air temperature in the NCB and SCB (*Panin, 1987*), while in the MCB, SST is usually lower than the air temperature as a consequence of upwelling. Sensible heat flux becomes relatively more significant in the heat budget in the autumn and winter seasons, when it is close to the net radiative heat flux.

**Table 1.** Monthly mean heat flux components ( $W/m^2$ ) at the sea surface.

$Q_s$  = incoming solar radiation,  $Q_b$  = (long wave) thermal radiation,  $Q_s + Q_b$  = total radiative heat flux,  
 $H$  = sensible heat flux,  $LE$  = latent heat flux,  $Q$  = total heat flux.

Month	$Q_s$	$Q_b$	$Q_s + Q_b$	$H$	$LE$	$Q$
1	65.1	-79.2	-14.0	-22.6	-59.2	-95.8
2	94.4	-76.5	17.9	-23.2	-57.3	-62.7
3	146.3	-72.9	73.5	-4.9	-38.3	30.3
4	208.3	-68.0	140.3	4.3	-25.7	118.8
5	247.9	-73.5	174.4	-2.3	-43.5	128.6
6	269.5	-84.7	184.8	-0.3	-63.1	121.4
7	257.1	-84.4	172.7	0.9	-76.0	97.5
8	228.9	-91.7	137.2	-1.8	-109.9	25.5
9	175.7	-90.5	85.2	-7.4	-109.6	-31.9
10	108.7	-79.7	29.0	-21.6	-109.9	-102.4
11	65.9	-73.4	-7.6	-27.5	-90.2	-125.2
12	57.0	-82.6	-25.6	-18.6	-56.7	-100.8
Annual mean	160.4	-79.8	80.6	-10.4	-69.9	0.3
Std. deviation	77.5	7.0	84.5	10.9	27.9	94.4

In winter, the turbulent heat flux (sum of sensible and latent heat fluxes) at the sea surface (**Fig.2**) has a maximum along the east coast of the MCB, produced by the interaction of the warm water tongue with overlying cold air. In this area both terms of the turbulent heat flux are of the same order ( $-250 W/m^2$  for latent and  $-150 W/m^2$  for sensible heat flux), whereas in other parts of the sea, latent heat flux is often 2-5 times larger than the sensible heat flux. In July (**Fig.2b**), sensible heat flux in the same area decreases to about  $(-10) + (+20) W/m^2$  and latent heat flux dominates in total flux.

**Figure 2.** The sum of sensible and latent heat fluxes in ( $W/m^2$ ) in a) January and b) July.

## 5. Sea level variability and water budget

### 5.1. Mean sea level variability

Time series of model simulated and observed sea level anomaly at four Caspian Sea stations are shown in **Fig.3** for the year 1982. Common features of the sea level time series at all four stations are the minimum in September-October, the rising trend from autumn to spring, followed by the fall in summer. There is a net rise in sea level at the end of the presented one year period because the sea level is on a rising trend in the longer term.

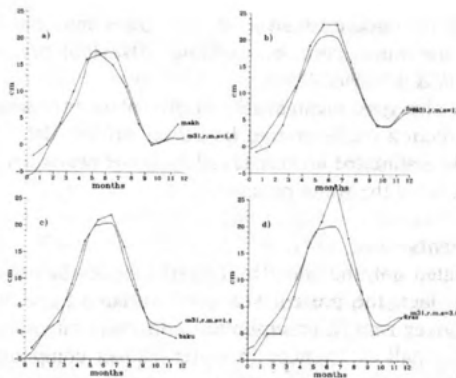


**Figure 3.** Sea level anomaly (cm) in 1982 at different locations around the Caspian Sea: a) Makhachkala; b) Fort-Shevchenko; c) Baku and d) Krasnovodsk. Smooth curves show model results and the broken lines correspond to observations.

### 5.2. Water budget

Estimates of Caspian Sea water balance terms based on various sources (**Table 2**) do not differ significantly from each other. The model simulated evaporation rate, of 86.5 cm/yr, is close to the estimate of *Bortnik & Nikonova* (1992) for the period 1978-1990 and to the climatologic estimate of 96.3 cm/yr of *Panin* (1987).

The river runoff in 1982 was significantly lower than the other years, amounting to only 73 % of mean runoff value for the 1978-1990 period. It should be noted that inter-annual variability of river runoff is extremely high. For example, the difference between maximum and minimum yearly runoff in the last century is about 260 km<sup>3</sup>/yr or more than 100 cm/yr in terms of sea level rise (*Bortnik et al.*, 1992).

**Table 2.** Water budget of the Caspian Sea. Water fluxes are given in cm/yr, expressed in units of mean sea level change.

Period and source	River Runoff	Underground Inflow	Precipitation	Evaporation	Outflow into Kara-Bogaz-Gol	Sea level increment
1970-1977 (Bortnik & Nikonova, 1992)	66.7	1.1	24.3	-103.9	2.0	-13.8
1978-1982 (Baidin & Kosarev, 1986)	85.8	-	25.7	-97.9	0.7	14.0
1978-1990 (Bortnik & Nikonova, 1992)	81.9	1.1	23.0	-91.8	0.5	13.7
1982 (model)	59.5	0	34.0	-86.5	0	7.0
1982 (ECMWF data & observations)	59.5 (observed)	0	34.0 (ECMWF)	-95.7 (ECMWF)	0	-2.2

Low river runoff in 1982 is compensated by high precipitation. The ECMWF reanalysis data for 1982 gives a value 28% higher than the estimates of *Bortnik et al.* (1992) for the 1970-1977 and 1978-1990 periods. Precipitation in ECMWF reanalysis

actually could have been underestimated, if one takes into account similar estimates elsewhere at around the same latitude, yielding 20% less precipitation compared to observations (Betts, Ball & Viterbo, 1999).

In **Table 2**, we also give mean sea level increment estimated from observed river runoff data and precipitation / evaporation based on ERA15 data. The difference of 9.2 cm/yr between ECMWF estimated and observed sea level change gives a measure of error of the modern estimations of the water balance.

## 6. Sensitivity experiments

As already pointed out, the water budget of Caspian Sea is extremely sensitive to climatic variability. In fact, the present sea level variations are much smaller than the contributing terms of river runoff, precipitation and evaporation, which tend to balance each other. Therefore, small differences in water budget components can lead to large changes in sea level. It is a widespread opinion that inter-annual variability of sea level is controlled by river runoff while anomalies of precipitation and evaporation have less impact on the range of sea level fluctuations (Radionov, 1994).

A set of experiments was performed to ascertain the sensitivity of the circulation and sea level change to external forcing and model parameters. We refer to the above experiment with the parameters and forcing given earlier, as the control run (CR). In the following experiments, we have run the model with further variations in model parameters and of external forcing, using the beginning of the fourth year of the CR as initial conditions. In most of these sensitivity experiments we have implemented external forcing, which varied from the central run comparable with the observed inter-annual variability in them. Seasonal sea level changes derived from the sensitivity experiments are shown in **Fig.4**.

*Experiment 1: 50% increase in river runoff.* We increase the runoff of all rivers by 50%. The reaction of the water budget and of sea level is quite expected and is almost linear. Mean sea level compared to the CR is increased by 28.3 cm/yr, corresponding to a value less than the 29.8 cm/yr that would be obtained by linear extrapolation. The small non-linear response of the water budget is related to increased stability of the water column followed by an increase of SST, which leads to excessive evaporation compared to the CR. The main consequence of increased runoff on circulation is the extension of western coastal current towards the south.

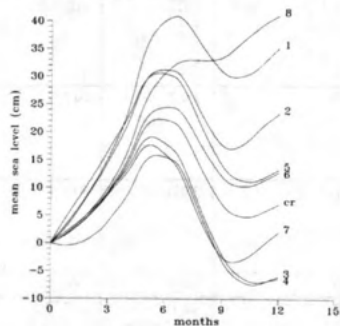


**Figure 4.** Mean sea level seasonal cycle obtained from sensitivity experiments.

*Experiment 2: 50% increase in precipitation.* Based on linear extrapolation we expect an increase of 17 cm/yr in sea level when precipitation is increased by 50% (**Table 2**), while the model gives an increase of 16.4 cm/yr. As in the first experiment, we have more stable water column especially in the SCB, due to excessive precipitation.

*Experiment 3: 50% increase in wind speed.* Much stronger non-linear reaction occurs in the case of increased wind speed. Based on linear extrapolation, the sea level would be expected to drop by 43.2 cm/yr, amounting to 50% increase in annual evaporation (**Table 2**). Because mixing is enhanced by increased wind stress, both the sensible and latent heat fluxes are affected, thus considerably modifying the expected reaction. As cooling is increased, SST decreases by 1-2°C compared to the CR, decreasing the surface humidity yielding a smaller specific humidity difference at the sea surface and at 10m height ( $q_{surface} - q_{10m}$ ). The increased wind stress also changes the circulation. The overall decrease of mean sea level produced by the model is 13.0 cm/yr, which is about 3.3 times smaller than expected from a proportional linear calculation.

*Experiment 4: 5°C warmer air temperature.* When air temperature is warmer and the dew point temperature is the same as that used in CR, the obvious reaction of the model is an increase of SST (up to 2°C in summer) and corresponding increase of specific humidity at the sea surface, resulting in more unstable atmospheric boundary layer with an increased Danton number  $C_E$  by a factor of 1.2-1.3. More intensive evaporation, as a result of larger difference  $C_E(q_{surface} - q_{10m})$ , results in a sea level drop of 13.4 cm/yr as compared to CR.

*Experiment 5: Warmer and more humid air.* An increase of the dew point temperature by 5°C compared to Experiment 4 affects the water balance in the opposite direction. Higher specific humidity of air prohibits the excessive evaporation observed in the previous experiment, leading to 6.2 cm/yr higher rise of sea level compared to the CR and of 19.6 cm/yr as compared to Experiment 4. As a result of the restricted latent heat flux, the surface waters are warmer by 2°C compared to Experiment 4.

*Experiment 6: Solar radiation without correction.* In the CR we have used ECMWF solar radiation heat flux with a correction factor of 1.05 to ensure better correspondence to climatologic estimates. The primary influence of correction of solar radiation is on the SST. In the experiment without correction we have 1°C lower SST compared to climatology, though the seasonal cycle of currents and of upper mixed layer show very little change. In response to the lower SST in the model we have lower evaporation, with an annual budget giving 5.7 cm/yr higher rise of sea level as compared to CR.

*Experiment 7: Absorption of solar radiation at the sea surface.* In this experiment we have checked the sensitivity of the seasonal cycle of sea level to parameterization of solar penetration into the sea. We put attenuation length for the short fraction of the solar radiation equal to 0.033 m, such that all the solar radiation is absorbed in the first model layer. Compared to the CR, SST starts to increase much faster in the spring to produce a sharper thermocline and a shallower upper mixed layer. As a result, we have higher values of SST and of evaporation in the period from January till September. On the other hand, the balance between sensible and latent heat release from the sea is modified such that relatively larger part of the heat flux is accounted by sensible heat flux. In May, the sensible and latent heat fluxes are equal to (-10.8; -65.2) W/m<sup>2</sup> compared to (-2.3; -43.5) W/m<sup>2</sup> in the CR, which means that the heat formerly released through evaporation or stored in the upper mixed layer is now released through sensible heat. In the period from September till December, the balance between sensible and latent heat fluxes is changed. In November we have (-19.0; -73.6) W/m<sup>2</sup> for sensible and latent heat fluxes as compared to (-27.5; -90.2) W/m<sup>2</sup> in the CR. The reduced penetration of heat into the sea results in

stronger surface currents and more pronounced influence of baroclinicity on the circulation pattern.

*Experiment 8: Constant vertical mixing coefficients.* This experiment is designed to explore how the specification of mixing coefficients modifies the circulation. We take constant values of  $K_m$  and  $K_h$ , equal to the maximum values of  $(50, 10) \cdot 10^{-4} m^2 s^{-1}$  used in the CR. The reaction of the sea circulation is dramatic, sea currents become almost barotropic. The major effect of increased vertical mixing is a lowering of the SST by about  $11^\circ C$  in August and a corresponding decrease of evaporation from the sea surface as compared to the CR. Annual sea level rise is increased by  $34.1 \text{ cm/yr}$  compared to the CR. The fall of sea level in August-October typical of the seasonal cycle in the CR is now absent, due to insufficient heat stored in the summer.

## 7. Summary and conclusions

A coupled sea hydrodynamics – air/sea interaction – sea ice thermodynamics model has been developed to simulate intra-annual variability of the Caspian Sea circulation and sea level. An important part of the work is the simulation of sea surface topography, yielding verifiable results in terms of sea level. Analyses of heat and water budgets confirm climatologic estimates of heat and moisture fluxes at the sea surface. Experiments performed with variations in external forcing suggest a sensitive response of the circulation and the water budget to atmospheric and river forcing, comparable with the inter-annual variability observed in these fields.

*Acknowledgments.* This study has been supported by NATO Science for Peace Programme, Grant#981063. The research of R. A. Ibrayev was supported by Russian Foundation for Basic Research, grant #05-05-64842.

## 8. References

- Baidin, S.S., & Kosarev, A.N. (1986). *Kaspiskoe more. Gidrologiya a Gidrohimija*. Moscow: Nauka (in Russian).
- Beron-Vera, F.J., Ochao, J., & Ripa, P. (1999). A note on boundary conditions for salt and freshwater balances. *Ocean Modelling*, 1, 111-118.
- Betts, A.K., Ball, J.H., & Viterbo, P. (1999). Basin-scale surface water and energy budgets for the Mississippi from the ECMWF reanalysis. *J. Geophys. Res.*, 104, D16, 19293-19306.
- Bortnik, V.N., & Nikanova, R.E. (1992). Vodnyi balans. In F.S. Terziev, A.N. Kosarev, & A.A. Kerimov, *Gidrometeorologiya i Gidrohimija Morey. Vol.6: Kaspiskoe more. Iss.1: Gidrometeorologicheskie usloviya* (pp. 211-221). St.Petersburg: Hydrometeoizdat.
- Esbensen, S.K., & Reynolds, R.W. (1981). Estimating monthly averaged air-sea transfers of heat and momentum using bulk aerodynamic method. *J. Phys. Ocean.*, 11, 457-465.
- Ibrayev, R.A., E. Ozsoy and C. Schrum (2002). Seasonal variability of the Caspian Sea circulation and sea level: analysis of model results and observed data. *Caspian Floating University Research Bulletin No. 3*. CaspNIRKH Publ., Astrakhan, Russia, pp. 8-19. (in Russian)
- Ibrayev, R.A. (2001). Model of enclosed and semi-enclosed sea hydrodynamics. *Russ. J. Numer. Anal. Math. Modelling*, 16(4), 291-304.
- Kosarev, A.N., & Yablonskaya, E.A. (1994). *The Caspian Sea*. SPB Academic Publishing.
- Panin, G.N. (1987). *Isparenie i teploobmen Kaspiskogo morya*. Moscow: Nauka. (in Russian)
- Paulson, E.A., & Simpson, J.J. (1977). Irradiance measurements in the upper ocean, *J. Phys. Oceanogr.*, 7, 952-956.
- Radionov, S.N. (1994). *Global and regional climate interaction: The Caspian Sea experience*. Ser. Water and Technology Library, vol. 11, Kluwer Academic Publishers.
- Roulett, G., & Madec, G. (2000). Salt conservation, free surface, and varying levels: a new formulation for ocean general circulation models. *J. Geophys. Res.*, 105(C10), 23927-23942.
- Schrum, C., & Backhaus, J.O. (1999). Sensitivity of atmosphere-ocean heat exchange and heat content in North Sea and Baltic Sea. A comparative Assessment. *Tellus* 51A, 526-249.
- Terziev, F. S., Kosarev, A. N., & Kerimov, A.A. (1992). *Gidrometeorologiya i Gidrohimija Morey. Vol.6: Kaspiskoe more. Iss.1: Gidrometeorologicheskie usloviya*. St.Petersburg: Hydrometeoizdat. (in Russian)

## ANOMALOUS RAINFALL AND ASSOCIATED ATMOSPHERIC CIRCULATION IN THE NORTH-EAST SPANISH MEDITERRANEAN AREA AND ITS RELATIONSHIP TO SEDIMENT FLUIDIZATION EVENTS IN A LAKE

*Marianna Soler, Teresa Serra and Jordi Colomer*

Group of Environmental Physics, Physics Department, University of Girona, 17071  
Girona, Spain. [teresa.serra@udg.es](mailto:teresa.serra@udg.es)

*Romualdo Romero*

Meteorology Group, Physics Department, University of the Balearic Islands, 07122 Palma  
de Mallorca, Spain

This study investigates the sediment fluidizations of confined bed-sediments in the last nineteen years (1986-2004) in the basins of Lake Banyoles, located in the north-east of Spain, where water enters mainly through subterranean springs. The sediment fluidization events are studied in basin B2 where fluctuations in the vertical migration of sediment present episodic behavior as a result of episodic rainfall in the area. The initiation of the fluidization events takes place when the monthly rainfall is ~ 2.7 times greater than the mean monthly rainfall of the雨iest months in the area, especially in spring (April and May), in the months of autumn and in December. Results show that the sediment fluidization in B2 remained in suspension in the 39.9% of the whole historical record. The rainfall, in turn, is associated with six main atmospheric circulation patterns among the 19 fundamental circulations that emerged in an earlier study focused on significant rainfall days in Mediterranean Spain. They comprise a wide variety of flows over the Iberian peninsula, with marked seasonal distributions and a clear distinction between Atlantic and western Mediterranean disturbances. In this study an analogue procedure is used to classify each of the 1970-2002 daily atmospheric states, as represented by the ECMWF reanalysis data, within the 19 circulation types or as insignificant (not rainy) days. The results are then used to construct some statistics aimed at comparing the occurrence of the circulation types during the fluidization periods with their occurrence in the monthly climatology: the Atlantic types AP3, AP4 and AP9, and the Mediterranean types AP8, AP14 and AP19 are identified as the most frequent during the sediment fluidization events and represent 64% of the days with significant rainfall in the months of initiation of the fluidization events.

The Spanish Mediterranean area (Figure 1) possesses a rather complex topography. It is influenced by both Atlantic low pressure systems (notably west and north of the area) and by Mediterranean disturbances (in the eastern part), and it is subject to extreme seasonal contrasts as a result of its latitude (36-44°N). All these factors yield daily rainfalls of considerable spatial and temporal variability (Romero et al. 1998). Among the studies related to the Spanish Mediterranean, Summer et al. (1995) associate the distribution of significant rainfalls over the island of Mallorca with recognized dominant surface circulation types. However, the effects of defined synoptic types on hydrology, although they have been conceptually recognized for a long time and have become apparent through numerous case studies (notably of heavy precipitations in eastern Spain), have been poorly studied for Mediterranean Spain.

Lake Banyoles (42°07'N, 2°45'E), in the eastern Catalan pre-Pyrenees, is a small multi-basin lake (surface area of 1.12 km<sup>2</sup>) of mixed tectonic-karstic origin (Canals et al. 1990) composed of six main basins (B1-B6). One of the most important aspects of the hydrological environment of Lake Banyoles is the fact that basin B1 (the largest basin) supplies around the 85% of the total incoming water by subterranean springs (at approximately 75 m of depth) and the rest is supplied by river flows entering the lake from

the southeast. The tectonic constraint of the lake forces the vertical discharge of ground water flow through the bottom of the basins. In addition, the subterranean springs mix the sediments above them up to a fairly sharp interface known hereafter as the lutocline (Figures 2a and 2b). The sediment in basin B2 usually remains consolidated at the bottom, with the lutocline at a depth of approximately 44 m (Casamitjana and Roget 1993, Colomer et al. 1998). Eventually, the subterranean springs in B2 supply water to the lake at a rate comparable to B1 (in the order of  $0.5 \text{ m}^3/\text{s}$ ). This is possible for high precipitation periods that recharge the aquifer which in turn increase the pressure enough for incoming water to resuspend the confined and consolidated sediment at the bottom of B2. In this case sediment migrates upward and initiates the fluidization of the confined bed sediments.

We chose then to examine the dynamics of the sediment fluidization in Lake Banyoles associated with meteorological conditions for two main reasons. First, the time evolution of sediment fluidizations in basins B1 and B2 has been recorded over the past 19 years; records show that the sediment fluidization in B1 is permanent (chronic fluidization) while in basin B2 it develops episodically (episodic fluidization). Second, the sediment fluidizations are of great limnological interest because convection occurs above the lutocline interface (Colomer et al. 2001, Colomer et al. 2003).

#### *Classification of daily atmospheric circulation patterns*

The climatological counterpart of this study is underpinned by earlier research, which derived 19 characteristic atmospheric patterns (Aps) responsible for significant rainfall in Mediterranean Spain (Romero et al. 1999b). Specifically, atmospheric states of all days in the period 1984-93 in which at least 5% of the 410 rain gauge stations shown in Figure 1 registered more than 5 mm (1275 days) were classified into 19 classes using principal components analysis and cluster analysis (see the details in Romero et al. 1999b). The classification was based on the flow patterns at 925 and 500 hPa over the region shown in Figure 5, using the gridded meteorological analyses of the European Centre for Medium-Range Weather Forecasts (ECMWF) as input data. In fact, the synoptic classification was also attempted based on grid analyses of temperature, relative humidity, horizontal wind components and other composite fields, but the most satisfactory results in terms of the relationship between the resulting atmospheric patterns and certain daily rainfall spatial distributions known for the region (Romero et al. 1999a) were obtained from a combination of the geopotential height fields at 500 and 925 hPa.

#### *Historical observations of sediment fluidizations in basin B2*

The fluidization events (F1, F2, etc) were detected by measuring the depth of the lutocline  $Z_L$  in basin B2. The lutocline level was well detected by seismic profiles (Figure 2a and 2b), echo sounding profiles or continuous water temperature measurements. In the third case, measurements of water temperature in the water column of B2 showed that the temperature at and below the lutocline in B2 changed from around  $17.5^\circ\text{C}$  at the beginning of the fluidization process to  $19.1^\circ\text{C}$  in the fluidized state. For all registered values at the lutocline depth an inverse temperature gradient of  $2-8^\circ\text{C}/\text{m}$  was found. The mean sediment concentration below the lutocline in both B1 and B2 depends on the state of fluidization, and varied between 100 and 280 g/l, therefore in both the seismic and echo sounding profiles the lutocline appeared in the plots as a flat line (Figure 2). As shown in the south to north seismic transect in Figure 2, B1 presented an active fluidization with the lutocline located at a depth of 24 m while the sediment in B2 was confined at the bottom (non-fluidized state) with the lutocline located at a depth of 44 m.

In the last nineteen years (1986-2004), while the sediments in B1 were found to be always in suspension (termed here as chronic fluidization), the sediments in B2 presented high temporal variability depending on the fluidization events (Figure 3). Two sparse cases (F1

and F2) in 1976-1977 and cases from F3 to F11 in the period of continuous measurements (1986-2004) have been detected out of 11 vertical migrations of the lutocline in basin B2. The strength of a fluidization event was quantified by the maximum vertical migration of the lutocline. Based on this, the largest migration was detected during the F7 event in 1996-1997, when the lutocline in B2 migrated to a depth of about 20.5 m. (The maximum vertical migration of the lutocline from the historical record is about 24 m.) Of remarkable interest is the fact that the major fluidization events may last more than one year, especially because some events are coupled: F3-F4, F5-F6, F7-F8 and F10-F11. This behavior can be explained by taking into account that a second fluidization is quite possible after one fluidization although the inflow of water is not so high. Also, the fluidization in B2 does not happen each year, so it has not been related to seasonal dynamics. The fluidizations, therefore, happened eventually or episodically without following any periodic evolution. For all of the above reasons, the fluidization events in B2 have been termed as episodic.

#### *Sediment fluidization events related to local rainfall*

The initiation of the fluidization usually coincides with the maximum mean monthly rainfall, which was about 250-350 mm (F2, F3, F7, F9 and F10). For the fluidizations following a previous one (F4, F6, F8 and F11), a monthly local rainfall of about 200 mm is enough to drive the next event in B2. The anomaly of rainfall defined as the difference between the local monthly and the mean local monthly rainfall (for the whole period of available data) divided by the last one present the largest values (of about 100-300 %) during the fluidization events. A value of 200% means that the value of the local monthly rainfall is three times the mean monthly rainfall. The mean anomalies of rainfall in the area of aquifer recharge and in Lake Banyoles, for the months of the initiation of the fluidization events, are 167 and 151 %, respectively. Then, the local monthly rainfalls are 2.67 and 2.51 times the mean monthly rainfall, respectively.

It is worth noting that the extent and duration of a fluidization event not only depends on the local monthly rainfall of a particular month but on the cumulative monthly rainfall in the months proceeding and after the initiation of the process. Fluidization F9 presents an extreme behavior, in that the maximum local monthly precipitation value ever recorded in the area of aquifer recharge (April 2002) drove this fluidization, although with a weak vertical extent and duration, of about 6 m and 4 months, respectively (Figure 3). This fluidization was preceded by a very dry period on the whole, and therefore the sediment could not be maintained in suspension and lutocline migrated down. On the contrary, F6 lasted for about 16 months (June 1992 to October 1993) as a result of large sustained precipitation in the area of aquifer recharge. Based on this interpretation, another variable comes into question as a possibly useful empirical determinant of the extent of a fluidization event: the accumulated monthly rainfall in the months preceding the event. Thus, we can make the assumption that the extent and duration of a fluidization event is associated with monthly rainfall accumulated over some fixed period of time; i.e. that the vertical migration of the lutocline is correlated with the monthly anomalies of local rainfall

in the area of aquifer recharge,  $P_{j,N}$ , defined in discrete form as  $P_{j,N} = \frac{1}{N} \sum_{j=J-N+1}^{J=N} P_{j,N}$  where

the location parameter J is the month of the year on which the fluidization process begins, the integrating parameter N is the number of preceding months over which the sum is performed, and  $P_{j,N}$  is the monthly rainfall in month j. The best linear relationship between the vertical depth of the lutocline and  $P_{j,N}$  is then obtained by finding the values of N that maximize  $r^2$ , the proportion of variance explained (Livingstone 1997, Livingstone 1999). Values of  $r^2$  were computed at monthly intervals of  $3 \leq N \leq 12$ , which included seasonal and annual accumulated rainfall. The maximum explained variance ( $r^2 = 50.6\%$ ) was obtained with the monthly rainfall accumulated for the previous 10 months.

It is interesting to remark that the maximum distance the lutocline migrated was about 24-22 m. This maximum excursion is limited by the fact that vertical velocity of incoming water diminishes from the inflow at the basin entry (at 85 m of depth) up to the lutocline depth (because of increasing transversal area), and at this depth the downward settling vertical velocity of the sediment suspension equals the upward vertical velocity of water (Colomer et al. 2001). Another possible explanation of the limited maximum excursion of lutocline is the fact that the sediment suspension flowed out the basin because at the south of Basin B2 the depth is about 20-22 m; this process would only take place during the major fluidization events F6, F7, F8 and F11. Finally, for the coupled fluidizations, the input of water in the aquifer increased its pressure and, as a result, the water entering into an already fluidized bed could produce a secondary migration of the lutocline that reached upper distances, i.e. less depth if counting from the water surface, as in the F3-F4 and F10-F11 cases.

Out of the 11 fluidization processes, 7 took place in the expected seasons of maximum rainfall: spring and autumn, 3 cases: F5, F7 and F8 took place in winter, as a direct result of the local monthly rainfall of December, and only F6 initiated a fluidization in the warm season of summer (June 1992). All in all, in the period 1986-2004, the sediment bed in B2 remained in suspension in 39.9% of the whole historical record, defining its episodic behavior.

Based on the above timing of initiation and duration of fluidizations, a major limnological implication comes into question: fluidizations F1, F3, F5, F7, F8, F10 and F11 in Lake Banyoles either initiated or initially developed when the water column of the lake was mixed; the mixing period of the lake was established between the end of October and mid-April and the rest of time the water column of the lake was stratified. In addition, Colomer et al. (2001) found the lutocline to be warmer (because water entry at the bottom of the basins is 19.1 °C, as mentioned previously) than the water above the lutocline. The difference in temperature between the suspension zone and the water above induces the development of a turbulent convective plume above the lutocline. As a major characteristic of convection from an isolated source, the plume entrains particles from the lutocline and carries upward a suspension of clay and silt particles with particle volume concentrations of ~ 5-10 µl L<sup>-1</sup>. Because of the temperature inversion at the lutocline, the plume is negatively buoyant. As a result, it develops upward and in the absence of a thermal stratification background or in the presence of a weak one (as it is in the mixed lake period) it is expected to reach the surface waters after which it spreads laterally, with the consequent change of water quality in terms of an increase of the suspended particle concentration. It can be expected, then, that the suspended particles change the clarity of the water, which might imply a habitat constraint for fishes as limiting their feeding opportunities and other visual activities. Not only this, as Casamitjana and Roget (1990) found, but whenever the water column in B2 is stratified and the sediment compacted at the bottom of the basin (no inflow), at the top (22 m of depth) of the basin, a secondary, stationary thermocline develops; it is only destroyed in the cold months of January and February. Then, during the major fluidizations events, as lutocline migrates upward, the secondary thermocline is eroded and finally vanishes, and as a result the lake hypolimnion warms up not only because of the heat released by the lutocline in B1 but because of the lutocline in B2, which is in the order of ~ 50 to 200 Wm<sup>-2</sup> each (Casamitjana et al. 1988).

#### *Sediment fluidization events related to Atmospheric Patterns*

The classification of daily atmospheric circulations for the period 1970-2002 described in the previous section allowed the daily rainfalls in the area of study to be associated with

one of the 19 emergent Aps. The Aps may be compared with each other in terms of both 500 and 925 hPa circulation dissimilarities within the considered geographical window. In some cases, the structures at 500 hPa, which are smoother, are relatively similar but the surface circulations exhibit substantial differences. In other cases, both levels show very similar aspects in some areas, but in other areas important differences in the position, orientation, size or depth of the disturbance appear (Romero et al. 1999b). In this section, though, only the most frequent atmospheric patterns during the months of onset of the fluidization events (comprising a total of 525 days) are studied in detail. Here we consider an atmospheric pattern to be relevant if its frequency is larger than 5%. Accordingly, the atmospheric patterns AP3, AP4, AP8, AP9, AP14 and AP19 were identified as the most frequent at the time of initiation of the fluidization events (Figure 4): AP8 (18%), AP19 (12%), AP14 (11%), AP3 (9%), AP4 (7%) and AP9 (7%) account for a total of 64% of all days. These atmospheric patterns are shown in Figure 5 and will be discussed in detail.

Also, for the whole 1970-2002(August) data set, the monthly incidence of the derived atmospheric patterns (AP1 to AP19) is quantified by introducing the so-called month-frequency ratio ( $AP_{ij\text{month-frequency}}$ ). It is defined, for each month and AP, as the ratio between the number of days with the selected AP to the total number of days presenting any AP, using the whole period of data (Figure 11) without considering the non rainy days

$$\text{(with } AP = 0\text{), as follows } AP_{ij\text{month-frequency}} = \frac{N(AP_{ij})}{\sum_{i=1}^{19} N(AP_i)} \text{ where } N(AP_{ij}) \text{ is the number of}$$

days with an AP in the month  $j$ . This index is useful to assess the monthly AP climatology in the Spanish Mediterranean area for the 33-year period, i.e. to determine to which degree each AP is expected in any given month on rainy days.

Pattern AP3 (Figure 5) is characterized by deep depressions centered to the northwest of the Iberian Peninsula. At upper levels, the nearly meridionally oriented transverse axis implies a general southwesterly flux and advection of positive vorticity over the whole of the Mediterranean region of Spain. In the eastern part of the region, there is warm and humid advection from the south-southeast, favoring rainfall development over the exposed areas of eastern Spain, including Catalonia. Pattern AP3, comparatively frequent during fluidization episodes (9%), exhibits its maximum occurrence during autumn, especially in October (10.6%) and November (10.8%). These values are above the values during spring and winter. Pattern AP3 mainly developed in fluidizations F3 and F5. Circulation AP4 (Figure 5) presents a frequency of 7 % during fluidization periods and represents southwesterly flows at all levels associated with low pressure systems to the northwest of Spain. Characteristically, the geopotential fields indicate the presence of weak cold fronts moving into the Iberian Peninsula from the west. Apart from the Atlantic rainfall patterns that affect the west of Catalonia, rainfall in the area of study is also favored. This circulation presents almost equal month-frequencies in August, October and December, and seasonally it presents the highest frequency in winter and autumn. It showed high occurrence in fluidization F1, F7 and F8.

The most persistent circulation during the onset of the fluidization events, AP8 (Figure 5, 18%), presents occasions when short baroclinic waves occur over the Iberian Peninsula. The general circulation is characterized by deep troughs in the westerlies at upper levels lying over western Spain, but no appreciable tilting. At the surface, the northwesterly winds are associated with the passage of cold fronts. Rainfalls in Catalonia are largely activated by this pattern since that area is affected by maximum positive vorticity advection at 500 hPa. In addition, moisture from the Mediterranean is available ahead of the cold front. AP8 tends to appear in summer (June and July), followed in frequency by

spring (April and May). It developed mainly during fluidizations F6, F9 and episodically in F5 (December 1991). However, this atmospheric pattern is not considered frequent for that month of the year. The AP9 composite (Figure 5) basically represents west to northwesterly winds at all levels following the passage of cold fronts from the Atlantic to the Mediterranean. This appears to be an ideal situation for the development of orographically enhanced rainfalls in the South Mediterranean. The northeastern regions (Catalonia and the Balearic Islands) are close to the cold front and this is reflected in the typical rainfalls of winter and spring, where it presents large month-frequencies. It showed high occurrence in fluidization F2. AP14 (Figure 5), with an 11% frequency during the months of the initiation of the fluidizations, is characterized at 500 hPa by an accentuated trough with a positively tilted axis which is restricted to the central part of the Iberian Peninsula. The area with maximum advection of vorticity is the southeast and east, which also benefits from rainfall generated by the warm and humid Mediterranean flows induced by the surface pressure distribution. Rainfalls in the interior of Andalusia, which is the nearest zone to the  $\square$ trati of the disturbance and receives favorable northwesterly surface winds, are also produced. Rainfall also occurs in the exposed Pyrenees. This circulation pattern exhibits its maximum month-frequency in the months of summer and spring, and the 925 hPa geopotential fields indicates relatively low pressure areas over the Iberian and African plateau, a signature of warm-season thermal lows. This circulation was episodically present in fluidizations F2, F4 and F9. It should be remarked that in April 2002, in the area of aquifer recharge, it rained 324.5 mm (the largest value registered for the whole period of analysis), and is therefore associated with the F9 event. Finally, cluster AP19 (Figure 5) comprises 500 hPa lows over the Gulf of Lyon with associated low-level cyclone to the east of the Balearic Islands, which may drive strong rainfall in the north-east of Catalonia. This circulation pattern exhibits high frequency during fluidization periods (12%) and is more frequent in the months of spring and winter than in autumn. It showed high occurrence in fluidizations F2 and F5.

**Acknowledgments:** Precipitation data were provided by the 'Instituto Nacional de Meteorología', stations of Jafre, Les Planes d'Hostoles and Castelló d'Empúries. We also would like to thank the people in charge of the meteorological stations of Darnius and Banyoles. The authors are grateful to captain Joan Corominas for the outstanding help and support in the field campaigns in Lake Banyoles. Also to Josep Pasqual (meteorological station of L'Estartit) for providing some of the temperature data in basin B2. The funds for this research were provided by the 'Ministerio de Ciencia y Tecnología' (MCYT) projects REN2001-2239/HID and CGL 2004-02027.

## References

- Canals, M., Got, H., Julia, R., and J. Serra, 1990: Solution-collapse depressions and suspensates in the limnogenic lake of Banyoles (NE Spain). *Earth Surf. Proc. Land.* **15:** 243-254.
- Casamitjana, X., Roget, E., Jou, D., and J.E. Llebot, 1988: Effect of suspended sediment on the heating of lake Banyoles. *Journal of Geophysical Research* **93 (C8):** 9332-9336.
- Casamitjana, X., and E. Roget, 1990: The thermal structure of Lake Banyoles. *Verh. Internat. Verein. Limnol.* **24:** 88-91.
- Casamitjana, X., and E. Roget, 1993: Resuspension of sediment by focused groundwater in Lake Banyoles. *Limnology and Oceanography* **38(3):** 643-656.
- Colomer, J., Ross, J.A. and X. Casamitjana, 1998: Sediment entrainment in karst basins. *Aquat. Sci.* **60:** 338-358.
- Colomer, J., Serra, T., Piera, J., Roget, E., and X. Casamitjana, 2001: Observations of a hydrothermal plume in a karstic lake. *Limnol Oceanogr.* **46:** 197-203.

- Colomer, J., Serra, T., Soler, M., and X. Casamitjana, 2003: Hydrothermal plumes trapped by thermal stratification. *Geophys. Res. Lett.* **30**, 21, 2092, [doi:10.1029/2003GL018131]

Livingstone, D.M., 1997: Break-up dates of Alpine lakes as proxy data for local and regional mean surface air temperatures. *Climate Change* **37**: 407-439.

Livingstone, D.M., 1999: Ice break-up on southern Lake Baikal and its relationship to local and regional air temperatures in Siberia and to North Atlantic Oscillation. *Limnology and Oceanography* **44 (6)**: 1486-1497.

Romero, R., Guijarro, J.A., Ramis, C., and S. Alonso, 1998: A 30 year (1964-1993) daily rainfall data base for the Spanish Mediterranean regions: first exploratory study. *International Journal of Climatology* **18**: 541-560.

Romero, R., Ramis, C., and J.A. Guijarro, 1999a: Daily rainfall patterns in the Spanish Mediterranean area: an objective classification. *International Journal of Climatology* **19**: 95-112.

Romero, R., Summer, G., Ramis, C., and A. Genovés, 1999b: A classification of the atmospheric circulation patterns producing significant daily rainfall in the Spanish Mediterranean area. *International Journal of Climatology* **19**: 765-785.

Summer, G.N., Romero, R., Homar, V., Ramis, C., Alonso, S., and E. Zorita, 1995: An estimate of the effects of climate change on the rainfall of Mediterranean Spain by the late twenty first century. *Climate Dynamics* **20**: 789-805.

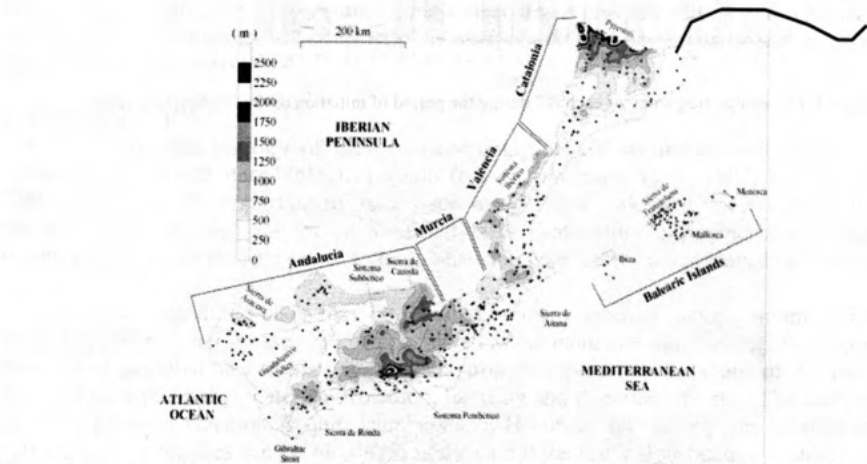


**Figure 1.** The Spanish Mediterranean area, which comprises the regions of Catalonia, Valencia, Murcia, Andalusia, and Balearic Islands. It includes a smoothed version of its orography, the position of the rain gauge stations (410 in total), and some geographical references mentioned in the text.

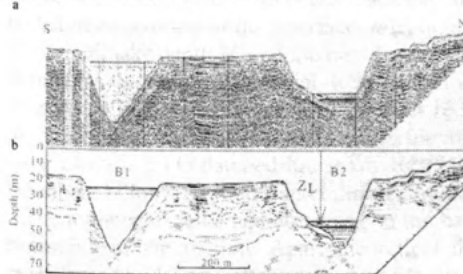


**Figure 2.** (a) South-North seismic transect and (b) schematic interpretation of the section from B2 to B1 (Canals et al. 1990); the lutocline is well detected by the seismic profile and is located at a depth  $Z_L$  from the surface.

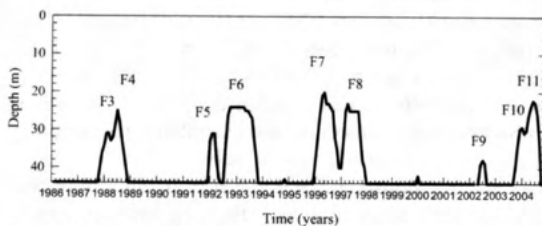


**Figure 3.** Lutocline depth, at B2 (as shown in 3b) during the period 1986-2004, where fluidization events are identified (from F3 to F11).

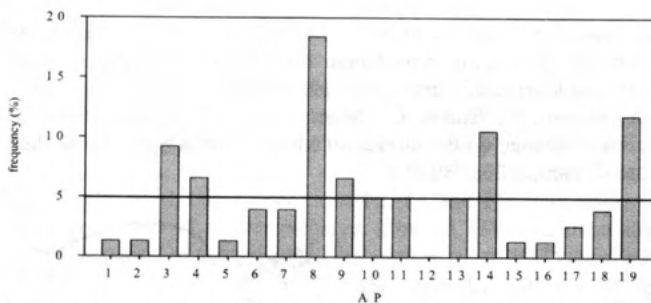


**Figure 4.** Percentage frequency of each AP during the period of initiation of the fluidization events.

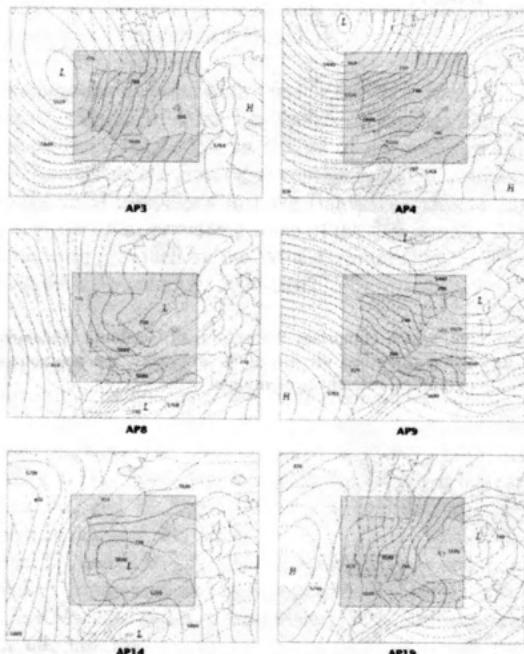


**Figure 5.** Composites of the 6 most frequent Aps during fluidization events. The continuous lines represent the geopotential height field at 925 hPa (contour interval, 10 m), and the dashed line represents it at 500 hPa (contour interval, 20 m). The interior rectangle represents the geographical window used for the pattern classification.

## NUMERICAL MODELLING OF BAROCLINIC WAVE PROCESSES IN STRATIFIED TANK (WITH APPLICATION TO LAKE DYNAMICS)

Nataliya Stashchuk<sup>a</sup>, Vasiliy Vlasenko<sup>a</sup> and Kolumban Hutter<sup>b</sup>

<sup>a</sup>School of Earth, Ocean and Environmental Sciences, Plymouth University, Drake Circus, PSQ A504 Plymouth, PL4 8AA, UK. E-mail: vvlasenko@plymouth.ac.uk

<sup>b</sup>Institute of Mechanics, Darmstadt University of Technology, Hochschulstr. 1, 64289, Darmstadt, Germany. E-mail: hutter@mechanik.tu-darmstadt.de

### ABSTRACT

Internal waves in a long stratified tank are studied numerically on the basis of the Navier-Stokes equations. External impact in a system is introduced by initially tilted interface. Being released, stratified fluid starts to oscillate with eigen frequency inherent to basin-scale baroclinic gravitational seiche. Laboratory experiments performed by D.A. Horn, J. Imberger and G.N. Ivey (JFM, 2001) reproduced several regimes of the degeneration of basin-scale internal waves into packets of solitary waves, shear instability, billow and spots of mixed water. The developed numerical model reproduces all types of flows, some of which were not observed with the experimental set-up. In particular, model results have shown that in the conditions of low dissipation, the regimes of baroclinic bores, Kelvin-Helmholtz billows and supercritical flows may transform into a solitary wave regime. Obtained results can help in interpretation of numerous observations of mixing processes in real lakes.

### 1. INTRODUCTION

Water quality and ecology of most lakes strongly depend on the vertical mixing of nutrients, oxygen and other biological agents (e.g. Mortimer and Horn, 1982; Vinni et al., 2000). So, it is very important to understand the physical processes which control the mechanisms of induced mixing in stratified lakes. Laboratory experiments and field observations suggest that the major role in enhancing lake turbulence is played by internal waves.

Oscillations in stratified lakes may be initiated by many external factors, among which the nonstationary wind stresses can be considered as the more probable forcing. Baroclinic response of stratified lake to the wind impact strongly depends on the shape of the shore line, bottom topography, water stratification, intensity and direction of wind. The analysis of every concrete situation is quite cumbersome. However, the description of different baroclinic wave regimes can be simplified in the case if the water stratification is close to a two-layer system and lakes configuration resembles a two-dimensional tank. Exactly such a situation was studied by Horn et al. (2001). They found that the baroclinic wave regime in the long narrow tank depends basically upon two non-dimensional parameters: the undisturbed position of the interface,  $h/H$ , defined as the ratio of the pycnocline depth  $h$  to the overall lake depth  $H$ , and the non-dimensional amplitude of the initial basin-scale wave defined as the ratio of the initial deflection of the pycnocline,  $\eta$ , to its undisturbed depth  $h$  (Fig.1a). With the help of simple two-layer rectangular model five different wave regimes of the disintegration of the initial basin-scale internal seiche into small-scale internal waves were identified: (1) damped linear waves; (2) solitons; (3) supercritical flow; (4) Kelvin-Helmholtz billows; (5) bores and billows (Fig.1b).

The regimes were named according to the basic phenomenon which predominates at the beginning of the motion. Apart theoretical description, regimes 1, 2 and 4 were also investigated by laboratory modelling in 6 m long, 0.29 m deep and 0.3 m wide rectangular tank filled with two-layer fluid. The density interface was initially tilted and motion of the fluid was investigated with the use of PIV camera.

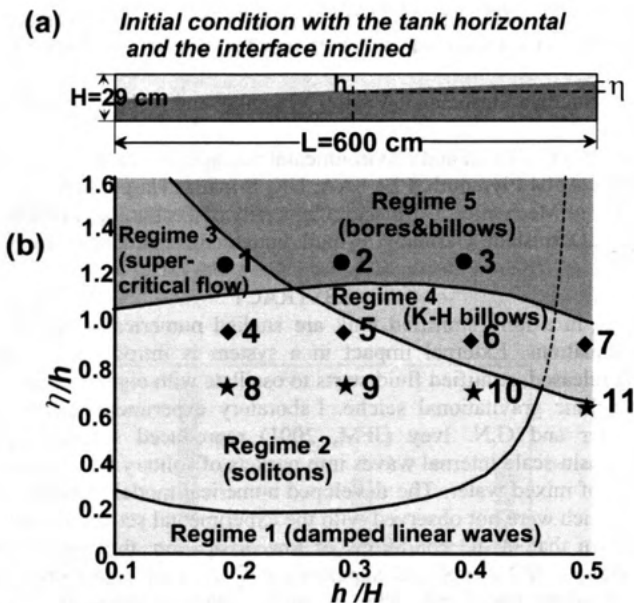


Figure 1. (a) Initial set-up and (b) schematic diagram showing the regime boundaries for the laboratory and numerical experiments plotted in terms of  $h/H$  and  $\eta/h$  (adopted from Horn et al., 2001, Figure 2). The numerical experiments are shown by symbols.

In the present study an attempt is made with the help of mathematical modelling to reproduce all the regimes of basin-scale wave disintegration, including those not considered in the laboratory experiments. We apply the fine resolution numerical model developed on the basis of the Navier-Stokes equations in the Boussinesq approximation to examine the influence of the steep topography and nonlinearity of a wave process on the mechanism of the energy transfer from the large to small scale motions (to turbulence and mixing, as an extreme situation).

## 2. MODEL

The two-dimensional system of equations, written in Cartesian ( $x, z$ ) coordinates in which the  $x$ -axis lie on the undisturbed free surface and the  $z$ -axis points upwards (opposite to the direction of gravity), reads

$$\begin{cases} \omega_t + J(\omega, \psi) = g\rho_x / \rho_a + v(\omega_{xx} + \omega_{zz}), \\ \rho_t + J(\rho, \psi) = k(\rho_{xx} + \rho_{zz}), \end{cases}$$

Here  $\psi$  ( $u=\psi_z$ ,  $w=-\psi_x$ ) denotes the stream function, where  $u$ ,  $w$  are the horizontal and vertical velocity components;  $\omega=\psi_{xx}+\psi_{zz}$  is the vorticity;  $\rho$  is the density;  $v$  and  $k$  are the coefficients of kinematic viscosity and molecular diffusivity, respectively;  $J(a,b)=a_x b_z - a_z b_x$  is the Jacobian operator. The rigid lid conditions are used at the model top,  $z=0$ , and at the bottom  $z=-H$ , viz.  $\psi=\rho_z=0$ . Absence of horizontal fluxes is used at the lateral boundaries:  $\psi=\rho_x=0$ . Vorticity,  $\omega$ , at the boundaries was calculated from previous temporal layer.

Problem is solved numerically with the help of the alternation direction implicit method (more details on the numerical procedure are presented in Vlasenko et al., 2005). The numerical runs were carried with the molecular values of viscosity and diffusivity:  $v$  and  $k$  were equal to  $10^{-6} \text{ m}^2 \text{s}^{-1}$ . The spatial resolution was  $2.4 \cdot 10^{-4} \text{ m}$ . The stability of the model scheme was achieved by taking  $10^{-2} \text{ s}$ .

### 3 SCENARIOS OF SEICHE EVOLUTION

The experimental results of Horn et al. (2001) were used as a basis for the modelling, i.e. all parameters of the model were similar to those in the laboratory set up:  $L=6\text{ m}$ ,  $H=0.29\text{ m}$  (see Fig. 1a), and density difference between layers equals  $20\text{ kg m}^{-3}$ . Numerical experiments were carried out in a wide range of the input parameters  $h$  and  $\eta$  (see Fig. 1b). It was found that numerical model reproduces all the regimes presented in Fig. 1: viscous damping, formation of solitary waves, supercritical flow or generation of bores and billows (we use the terminology introduced by Horn et al., 2001).

#### 3.1 REGIME: VISCOUS ATTENUATION

Viscous attenuation is the more trivial scenario of the wave evolution. As was observed in numerical runs, the basin-scale wave slowly attenuates with time when the amplitude  $\eta$  is too small to produce remarkable nonlinear steepening. Weak nonlinearity was normally compensated by viscous dissipation. In this scenario the nonlinearity due to small amplitude plays a secondary role in comparison with viscosity.

#### 3.2 REGIME: SOLITONS

More strong effects take place when the initial amplitude is large enough to generate solitary waves. Figure 2 presents the evolution of seiche oscillation when  $h/H=0.3$ ,  $\eta/h=0.9$  (hereafter  $T$  is the time scale, viz.  $T=2L/C_p$  is the period of an internal seiche, where  $C_p$  is the linear long-wave phase speed). Being inclined "due to the wind action" the interface begins to return to its equilibrium position. At the first stage the horizontal motion of fluid is accompanied by vertical motion at the ends of the tank. Upwelling of the water near the left wall leads to formation of internal surge, which is clearly seen at the time moment  $t=0.35T$ . Propagating to the right this surge eventually evolves into a packet of solitary wa-

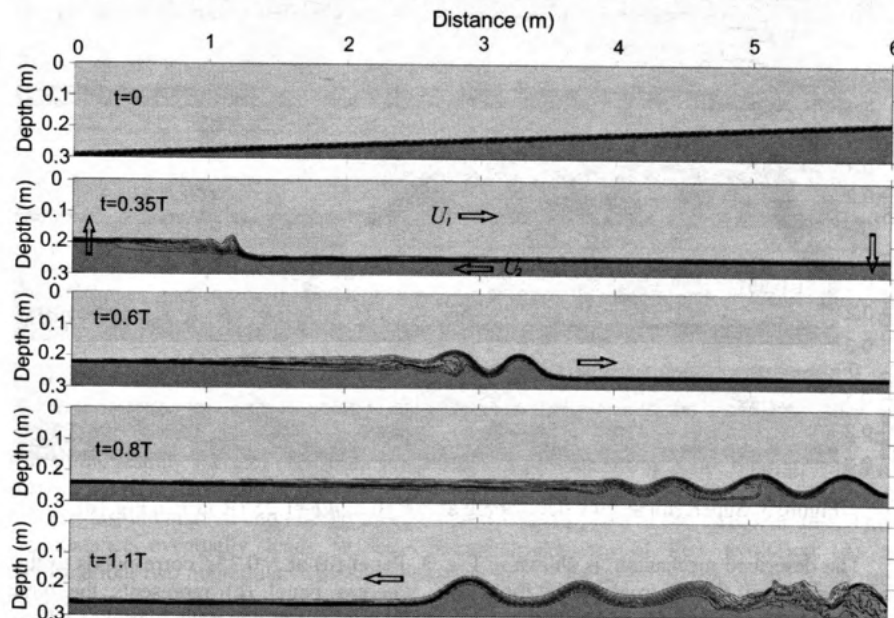


Figure 2. Numerical series showing the evolution of the initial basin-scale internal wave into a packet of solitary waves (Run 5 in Fig. 1b).

ves. Initial stage of this process is shown at  $t=0.6T$ . An addition effect, which can take place here is the generation of turbulence and water mixing during the reflection of internal waves from the basin boundary. The result of strong wave-wall interaction is clearly seen in the tail of the reflected wave packet at  $t=1.1T$ . The "Solitons"-scenario covers a substantial part of the parameter space in Fig. 1b. Thus the nonlinear internal waves are expected to be "ordinary" phenomena in the energy cascading from large to small scales.

### 3.3 REGIME: SUPERCRITICAL FLOW

SUPERCRITICAL regime takes place when local Froude number becomes large than unity. In the case of two-layer fluid the Froude number can be introduced as:  $F=(F_1^2+F_2^2)^{1/2}$ , where  $F_1^2 = U_1^2/g'h$ ,  $F_2^2 = U_2^2/g'(H-h)$ ,  $g'$  is the reduced gravity acceleration,  $U_1$  and  $U_2$  are the velocities in upper and lower layers, respectively (see Fig. 2). Standing seiche oscillations have maximum velocities in the centre of the basin and zero at the ends. If the amplitude  $\eta$  is sufficiently large, it may lead to the supercritical conditions ( $F>1$ ) in the middle of the basin but subcritical ( $F<1$ ) at the ends where standing wave has maximum of vertical displacements. Under supercritical conditions solitary internal waves, which effectively evolved from the propagating internal surge in the regime "Solitons" (see Fig. 2), are not released from the baroclinic bore because it propagates faster generating turbulence and water mixing in the area of interface.

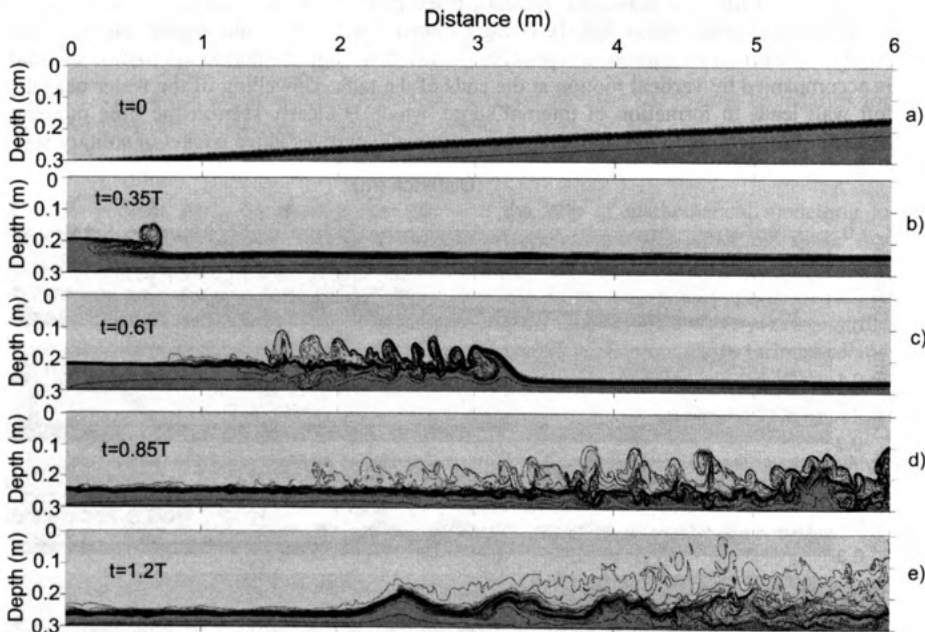


Figure 3. Supercritical flow developing at  $h/H=0.2$ ,  $\eta/h=1.25$  (Run 1 in Fig. 1b).

The described mechanism is shown in Fig. 3. Panel (b) at  $t=0.35T$  corresponds to the initial stage of the internal surge formation, whereas panel (c) represents the well developed supercritical flow. Moving rightward, internal surge generates vortexes which mix water near the interface. Eventually, as the propagating bore loses its energy due to the generation of turbulence at the interface (including also strong interaction with wall, see panel (d)) and friction, it evolves into series of solitary internal waves (Fig. 3e).

### 3.4 REGIME: BORES AND BILLOWS

Regime "Bores and billows" can also be treated as the "Supercritical flow" in the sense that the flow in the middle of the basin is supercritical. The last circumstance makes process of wave evolution in these two cases very similar. Comparison of the upper three panels in Figs. 3 and 4 clearly shows the similarity of runs 1 and 2: supercritical flow in the basins' centre doesn't allow evolving solitary waves, as it was in the "Solitons" regime (see also Fig. 2).

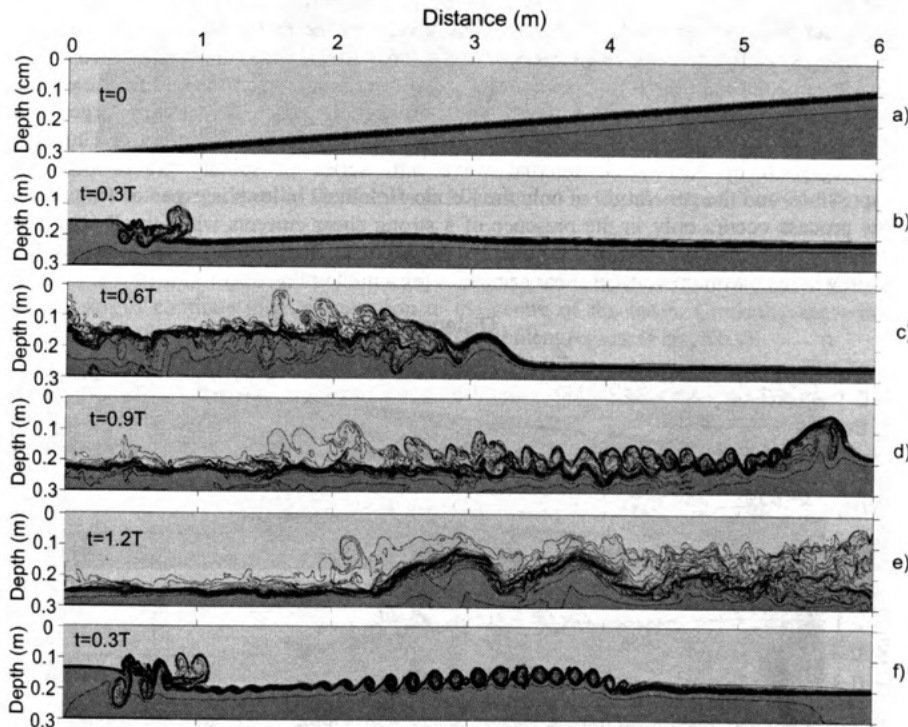


Figure 4 (a)-(f) Density field evolution at  $h/H=0.3$ ,  $\eta/h=1.25$  (Regime "Bores and billows", Run 2 in Fig. 1b). (f) Density field at  $t=0.3T$  for  $h/H=0.4$ ,  $\eta/h=1.25$  (Run 3 in Fig. 1b).

The only difference between considered cases is that the amplitude of the initial wave in run 2 is larger. It is quite enough to produce strong shear at the interface, which is sufficient for generation of billows. They are seen in the middle part of the basin in Fig. 4d behind the leading wave of elevation. These billows provide strong water mixing, which is seen on the right hand side of the tank in Fig. 4e. Note also that in addition to the enhanced mixing, fast attenuation and energy dissipation also takes place in the turbulent area. This circumstance eventually leads to the "Solitons" scenario of flux evolution. As a confirmation, two nonregular waves of elevation in Fig. 4e in the middle of the basin can be considered as initial stage of soliton formation.

Generation of billows by strong vertical shear in the central part of the tank is seen even more clearly for larger initial amplitudes. Panel 4f represents the same moment of time as Fig. 4b, but for  $h/H=0.4$  (Run 3, see Fig. 1b). Evidently, in the last case the flux becomes unstable even by the time span  $t=0.3T$ .

### 3.5 REGIME: KELVIN-HELMHOLZ BILLOWS

The example of rapid change of the background stratification presented in Figure 4 implies the existence of strong water mixing in the interface layer. The mixing process in the considered case was provided by the development of numerous billows, which accompany the gravity current.

The regime "K-H billow" is peculiar to basins with deep interface. Deep position of the density jump (near the middle between bottom and surface) provides the specific conditions when generation of nonlinear waves is hampered by weak nonlinearity. Really, the parameter of nonlinearity,  $3c(h_2-h_1)/(2h_2h_1)$ , ( $c$  is the linear phase speed and  $h_1$ ,  $h_2$  are the thickness of upper and lower layers, respectively) of the first-order Kortevég-de Vries equation is relatively small when  $h_1$  and  $h_2$  are comparable. It even equals zero when  $h_2=h_1$ . This means that the time of nonlinearity (or steepening time), which defines the time scale of generation of solitary wave from initial disturbance, becomes substantially larger than the temporal scale of the development of the Kelvin Helmholtz billows. Thus the disintegration of basin-scale internal wave into series of solitary waves becomes impossible, and the generation of only the Kelvin-Helmholtz billows is expected (of course, this process occurs only in the presence of a strong shear currents when the Richardson number is less than 0.25 and the flow loses its stability). They evolve in the centre of the basin where maximum vertical shear occurs, as presented in Fig. 5b.

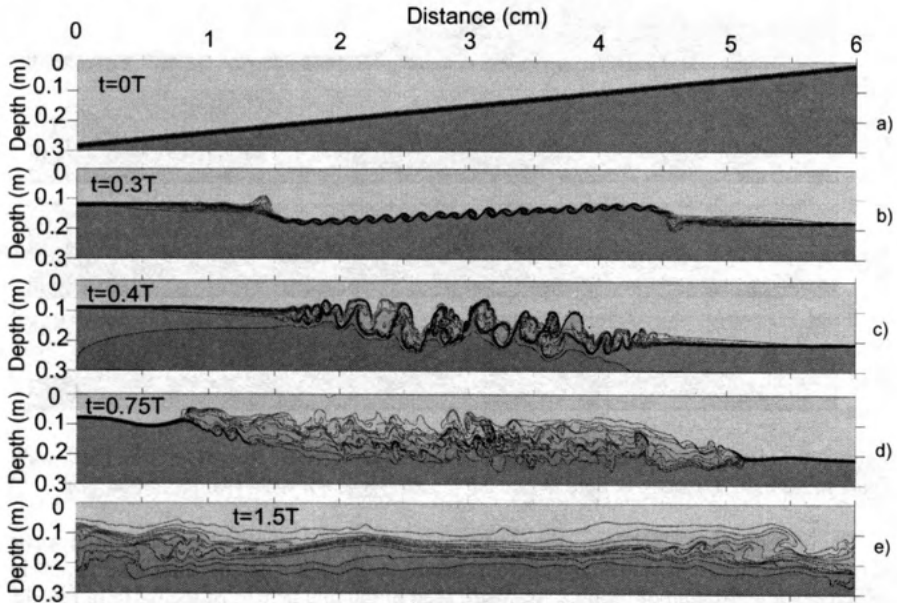


Figure 5 Evolution of the density field at  $h/H=0.5$ ,  $\eta/h=0.9$  (Regime "Kelvin-Helmholtz" billows; Run 7 in Fig. 1b).

Two surges are generated in the very beginning of the motion near the left and right walls. They move to the centre of the tank and intensify ("compress") the motion in the central part of the basin: the values of horizontal velocities of currents are increased between two surges as they approach the centre. This intensification leads to the increase of the horizontal velocity shear. By the time span  $t=0.3T$  the Richardson number falls below the critical value, and the process of generation of the billows due to the Kelvin-Helmholtz instability takes place.

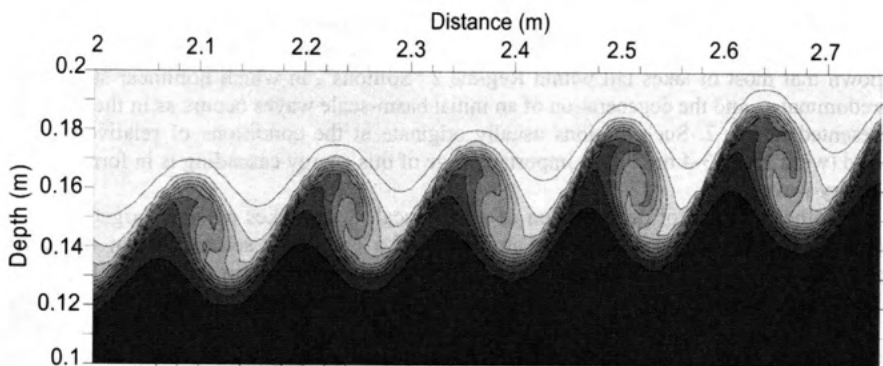


Figure 6. Enlarged part of the density field presented in Fig. 5 with eddies ( $t=0.3T$ )

The more detailed structure of the density fields with billows (zoom of the panel at  $t=0.3T$ ) is shown in Fig. 6. The billows grow in amplitude and loose their regular structure as the surges continue their propagation to the centre of the basin. Gradually the wave motions transform from the laminar form to the turbulent regime (Figs. 5 b,c).

The interface restores its initial position at  $t=1.5T$ ; but it is much wider now. The light and heavy water are mixed and pycnocline thickness becomes ten times larger than it was before the beginning of seiche oscillations. This process of the pycnocline erosion continues as long as essential turbulent pulsations exist within the interface area. The turbulence gradually attenuates with time and finally the density fields takes the form similar to those presented in the lower panel in Fig. 5. Instead of initial sharp interface, vertical density profile gets much more smoothed form.

The correct numerical modelling of the Kelvin-Helmholz instability and successive transformation of the initial generated billows into homogeneous turbulence and its final attenuation is possible only with the use of a very fine grid. Some remarks on this topic based on the ideas of the Kolmogorov's theory of turbulence (Kolmogorov, 1941) are pertinent here.

The turbulent density field can be thought of as being made of many eddies of different sizes. Energy must be fed at some rate  $\varepsilon$  per unit mass per unit time at the largest eddies of size  $L$  and velocity  $U$ , for which the Reynolds number is  $Re = LU/\nu \gg 1$ . The energy then cascades to smaller eddies until it reaches eddies for which  $Re \sim 1$ . Energy does not build up at any smaller scale; the intermediate eddies transmit energy  $\varepsilon$  to the smaller eddies. Kolmogorov postulated that it must be possible to express  $\varepsilon$  in terms of scales  $l$  and  $u$ , inherent to smallest eddies and on the dimensional ground the only way of writing  $\varepsilon$  in terms of  $l$  and  $u$  is  $\varepsilon \sim u^3/l$ . Now it is easy to find that  $L/l_s \sim Re^{3/4}$ , or in other words, the Reynolds number associated with the largest eddies determines how small the smallest eddies will be compared to them.

According to Figure 6 the first eddies with vertical scale  $L \sim 0.05$  m appear when  $t=0.3T$ . Taking into account that the value of the particles velocity in eddies is  $U \sim 8 \cdot 10^{-2}$  m s<sup>-1</sup> the corresponded Reynolds number  $Re$  attains  $4 \cdot 10^3$ . This gives that the smallest scale of expected eddies will be not greater than  $l_s \sim 10^{-4}$  m and thus spatial step of the numerical scheme should not be more than  $10^{-4}$  m. Namely this value of the spatial grid step was used in our numerical experiments.

#### 4 CONCLUSIONS

Analysis performed by Horn et al. (2001) on the basis of field data from long and narrow lakes (viz. Loch Ness (Thorpe et al., 1972), and Babine Lake (Farmer, 1978)) has shown that most of lakes fall within Regime 2 "Solitons", in which nonlinear steepening predominates, and the degeneration of an initial basin-scale waves occurs as in the example presented in Fig 2. Such motions usually originate at the conditions of relatively weak wind (wind speed  $3\text{--}4 \text{ m s}^{-1}$ ). An important stage of this energy cascading is in formation of solitary waves.

Another scenario of degeneration of a basin-scale wave takes place at larger external impacts. Strong wind increases the amplitude of a baroclinic seiche so that the latter generates seiche-induced hydrodynamics instabilities presented as an example in Figs. 3-9. Formation of billows, their successive disintegration into turbulent patches which finally attenuate and form new background stratification (see Fig. 5). This process was reported, for instance, in laboratory experiments by Thorpe (1971, 1973). For such regimes we can expect considerable mixing and remarkable change of the pycnocline structure for the entire basin. As to the regimes "Baroclinic bore" and "Supercritical flow", in the conditions of low dissipation they gradually transform into a solitary wave regime (see Figs. 3,4).

Obtained results can be helpfull in interpretation of observation data on the mixing processes in real lakes.

#### ACKNOWLEDGEMENTS:

This work was supported by INTAS, project 03-51-3728 "Strongly nonlinear internal waves in lakes: generation, transformation and meromixis".

#### 5 REFERENCES:

- Farmer, D.M., 1978: Observations of long nonlinear internal waves in a lake. *J. Phys. Oceanography*, **8**, 63-73.
- Horn, D. A., J. Imberger, and G.N. Ivey, 2001: The degeneration of large-scale interfacial gravity waves in lakes. *J. Fluid Mech.*, **434**, 181-207.
- Kolmogorov, A.N., 1941: The local structure of turbulence in incompressible viscous fluid for very large Reynolds numbers. *Dokl. Akad. Nauk SSSR*, **30**, 301-305.
- Vlasenko, V.I., N.M. Stashchuk, and k. Hutter, 2005: Baroclinic tides: theoretical modelling and observational evidence. *Cambridge University Press*, 350p.
- Mortimer, C.H., 1952: Water movements in lakes during summer stratification: Evidence from the temperature distribution in Windermere. *Phil. Trans. R. Soc., London*, **236**, 255-404.
- Thorpe, S.A., 1971: Experiments on the instability of stratified shear flows: miscible fluids. *J. Fluid Mech.*, **46**, 299-319.
- Thorpe, S.A., 1973: Experiments on instability and turbulence in a stratified shear flow. *J. Fluid Mech.*, **61**, 731-751.
- Thorpe, S. A., Hall, A., and Crofts, I. 1972: The internal surge in Loch Ness. *Nature*, **237**, 96-98.

## RIVERINE AND SHALLOW WATERS

the riverine and shallow waters of the basin. The basin is characterized by a large number of rivers and streams, which are the primary source of water for the region. The rivers and streams are fed by precipitation, groundwater, and surface runoff. The basin is also characterized by a large number of lakes and reservoirs, which are used for irrigation, hydroelectric power generation, and recreation. The basin is also characterized by a large number of wetlands, which are important for the conservation of biodiversity and the regulation of water flow.

The basin is characterized by a large number of rivers and streams, which are the primary source of water for the region. The rivers and streams are fed by precipitation, groundwater, and surface runoff. The basin is also characterized by a large number of lakes and reservoirs, which are used for irrigation, hydroelectric power generation, and recreation. The basin is also characterized by a large number of wetlands, which are important for the conservation of biodiversity and the regulation of water flow.

1970-1971, 1972-1973, 1974-1975

1970-1971

1971-1972

1972-1973

1973-1974, 1974-1975

1974-1975, 1975-1976

1975-1976, 1976-1977

1976-1977, 1977-1978

1977-1978, 1978-1979

1978-1979, 1979-1980

1979-1980, 1980-1981

1980-1981, 1981-1982

1981-1982, 1982-1983

1982-1983, 1983-1984

1983-1984, 1984-1985

1984-1985, 1985-1986

1985-1986, 1986-1987

1986-1987, 1987-1988

1987-1988, 1988-1989

1988-1989, 1989-1990

1989-1990, 1990-1991

1990-1991, 1991-1992

1991-1992, 1992-1993

1992-1993, 1993-1994

1993-1994, 1994-1995

1994-1995, 1995-1996

1995-1996, 1996-1997

1996-1997, 1997-1998

1997-1998, 1998-1999

1998-1999, 1999-2000

1999-2000, 2000-2001

2000-2001, 2001-2002

2001-2002, 2002-2003

2002-2003, 2003-2004

2003-2004, 2004-2005

2004-2005, 2005-2006

2005-2006, 2006-2007

2006-2007, 2007-2008

2007-2008, 2008-2009

2008-2009, 2009-2010

2009-2010, 2010-2011

2010-2011, 2011-2012

2011-2012, 2012-2013

2012-2013, 2013-2014

2013-2014, 2014-2015

2014-2015, 2015-2016

2015-2016, 2016-2017

2016-2017, 2017-2018

2017-2018, 2018-2019

2018-2019, 2019-2020

2019-2020, 2020-2021

2020-2021, 2021-2022

2021-2022, 2022-2023

2022-2023, 2023-2024

2023-2024, 2024-2025

2024-2025, 2025-2026

2025-2026, 2026-2027

2026-2027, 2027-2028

2027-2028, 2028-2029

2028-2029, 2029-2030

2029-2030, 2030-2031

2030-2031, 2031-2032

2031-2032, 2032-2033

2032-2033, 2033-2034

2033-2034, 2034-2035

2034-2035, 2035-2036

2035-2036, 2036-2037

2036-2037, 2037-2038

2037-2038, 2038-2039

2038-2039, 2039-2040

2039-2040, 2040-2041

2040-2041, 2041-2042

2041-2042, 2042-2043

2042-2043, 2043-2044

2043-2044, 2044-2045

2044-2045, 2045-2046

2045-2046, 2046-2047

2046-2047, 2047-2048

2047-2048, 2048-2049

2048-2049, 2049-2050

2049-2050, 2050-2051

2050-2051, 2051-2052

2051-2052, 2052-2053

2052-2053, 2053-2054

2053-2054, 2054-2055

2054-2055, 2055-2056

2055-2056, 2056-2057

2056-2057, 2057-2058

2057-2058, 2058-2059

2058-2059, 2059-2060

2059-2060, 2060-2061

2060-2061, 2061-2062

2061-2062, 2062-2063

2062-2063, 2063-2064

2063-2064, 2064-2065

2064-2065, 2065-2066

2065-2066, 2066-2067

2066-2067, 2067-2068

2067-2068, 2068-2069

2068-2069, 2069-2070

2069-2070, 2070-2071

2070-2071, 2071-2072

2071-2072, 2072-2073

2072-2073, 2073-2074

2073-2074, 2074-2075

2074-2075, 2075-2076

2075-2076, 2076-2077

2076-2077, 2077-2078

2077-2078, 2078-2079

2078-2079, 2079-2080

2079-2080, 2080-2081

2080-2081, 2081-2082

2081-2082, 2082-2083

2082-2083, 2083-2084

2083-2084, 2084-2085

2084-2085, 2085-2086

2085-2086, 2086-2087

2086-2087, 2087-2088

2087-2088, 2088-2089

2088-2089, 2089-2090

2089-2090, 2090-2091

2090-2091, 2091-2092

2091-2092, 2092-2093

2092-2093, 2093-2094

2093-2094, 2094-2095

2094-2095, 2095-2096

2095-2096, 2096-2097

2096-2097, 2097-2098

2097-2098, 2098-2099

2098-2099, 2099-20100

2099-20100, 20100-20101

20100-20101, 20101-20102

20101-20102, 20102-20103

20102-20103, 20103-20104

20103-20104, 20104-20105

20104-20105, 20105-20106

20105-20106, 20106-20107

20106-20107, 20107-20108

20107-20108, 20108-20109

20108-20109, 20109-20110

20109-20110, 20110-20111

20110-20111, 20111-20112

20111-20112, 20112-20113

20112-20113, 20113-20114

20113-20114, 20114-20115

20114-20115, 20115-20116

20115-20116, 20116-20117

20116-20117, 20117-20118

20117-20118, 20118-20119

20118-20119, 20119-20120

20119-20120, 20120-20121

20120-20121, 20121-20122

20121-20122, 20122-20123

20122-20123, 20123-20124

20123-20124, 20124-20125

20124-20125, 20125-20126

20125-20126, 20126-20127

20126-20127, 20127-20128

20127-20128, 20128-20129

20128-20129, 20129-20130

20129-20130, 20130-20131

20130-20131, 20131-20132

20131-20132, 20132-20133

20132-20133, 20133-20134

20133-20134, 20134-20135

20134-20135, 20135-20136

20135-20136, 20136-20137

20136-20137, 20137-20138

20137-20138, 20138-20139

20138-20139, 20139-20140

20139-20140, 20140-20141

20140-20141, 20141-20142

20141-20142, 20142-20143

20142-20143, 20143-20144

20143-20144, 20144-20145

20144-20145, 20145-20146

20145-20146, 20146-20147

20146-20147, 20147-20148

20147-20148, 20148-20149

20148-20149, 20149-20150

20149-20150, 20150-20151

20150-20151, 20151-20152

20151-20152, 20152-20153

20152-20153, 20153-20154

20153-20154, 20154-20155

20154-20155, 20155-20156

20155-20156, 20156-20157

20156-20157, 20157-20158

20157-20158, 20158-20159

20158-20159, 20159-20160

20159-20160, 20160-20161

20160-20161, 20161-20162

20161-20162, 20162-20163

20162-20163, 20163-20164

20163-20164, 20164-20165

20164-20165, 20165-20166

20165-20166, 20166-20167

20166-20167, 20167-20168

20167-20168, 20168-20169

20168-20169, 20169-20170

20169-20170, 20170-20171

20170-20171, 20171-20172

20171-20172, 20172-20173

20172-20173, 20173-20174

20173-20174, 20174-20175

20174-20175, 20175-20176

20175-20176, 20176-20177

20176-20177, 20177-20178

20177-20178, 20178-20179

20178-20179, 20179-20180

20179-20180, 20180-20181

20180-20181, 20181-20182

20181-20182, 20182-20183

20182-20183, 20183-20184

20183-20184, 20184-20185

20184-20185, 20185-20186

20185-20186, 2

# THE SCALE CONSTRAINT ON VEGETATED-SHEAR-LAYERS AND ITS IMPLICATIONS FOR CANOPY FLUSHING.

H. Nepf and M. Ghisalberti

Civil and Environmental Engineering, Massachusetts Institute of Technology  
48-216D, Cambridge, MA 02139, [hmnepf@mit.edu](mailto:hmnepf@mit.edu)

**ABSTRACT:** The drag discontinuity at the top of a submerged canopy creates a shear-layer that in turn generates coherent vortices by Kelvin-Helmholtz (K-H) instability. These vortices control the exchange between the canopy and the overflowing water. Unlike free-shear-layers, the K-H vortices in a canopy-shear-layer do not grow continuously downstream, but reach and maintain a finite scale a short distance from their initiation. The arrested growth occurs when the canopy dissipation balances the shear-production. This balance yields an equilibrium parameter that defines the length-scale of vortex penetration into the canopy,  $\delta e$ , and the region of rapid exchange between the canopy and overflow. Deeper within the canopy transport is much slower. A two-box canopy model is proposed based on the length-scale  $\delta e$ . Using transport rates defined in previous studies, one can then predict the canopy flushing rate over a range of canopy density.

## 1. INTRODUCTION

The dominant feature of flow near the edge of a canopy is a region of strong shear, created by the discontinuity in drag. The velocity profile resembles a free-shear-layer (FSL), and includes an inflection point just within the canopy. A free-shear-layer is characterized by large coherent vortices that form via Kelvin-Helmholtz (K-H) instability and which dominate the transport across the layer (Brown and Roshko 1974, Winant and Browand 1974). A similarity between canopy-shear-layers and FSL has been shown first for terrestrial (Raupach et al 1996) and later aquatic canopies (Ghisalberti and Nepf 2002). The K-H vortices control the exchange of scalars and momentum between the canopy and overlying flow. In an unobstructed shear-layer, the vortices, as well as the shear-layer width, grow continually downstream, predominantly through vortex pairing (Winant and Browand, 1974). In contrast, in canopy-shear-layers the vortices initially grow, but eventually reach a fixed scale. The constraint on vortex scale is reflected in the arrested growth of the shear-layer (Ghisalberti 2000). Similarly, Cheng and Castro (2002) have shown that after a short development region the roughness sub-layer, the top of which corresponds to the top of the shear-layer, is independent of distance along a model canopy, remaining constant even as the overlying boundary layer continues to develop. The final vortex size defines the region of rapid exchange, and the canopy is segregated into an outer region of rapid water renewal and an inner region of slow renewal (Nepf and Vivoni, 2000). The goal of this paper is to predict the final vortex scale, and to evaluate how this scale controls canopy flushing.

## 2. DERIVATION OF EQUILIBRIUM PARAMETER

Consider a model canopy consisting of an array of circular cylinders of diameter  $d$  and number density,  $n$  [cylinders per area]. The frontal area per volume is denoted  $a = nd$ , and the average cylinder spacing is  $\Delta S = (d/a)^{1/2}$ . The canopy height,  $h$ , is less than the flow depth,  $H$ , so that open flow exists above the canopy, as shown in Figure 1. The canopy interface is parallel to the flow direction.

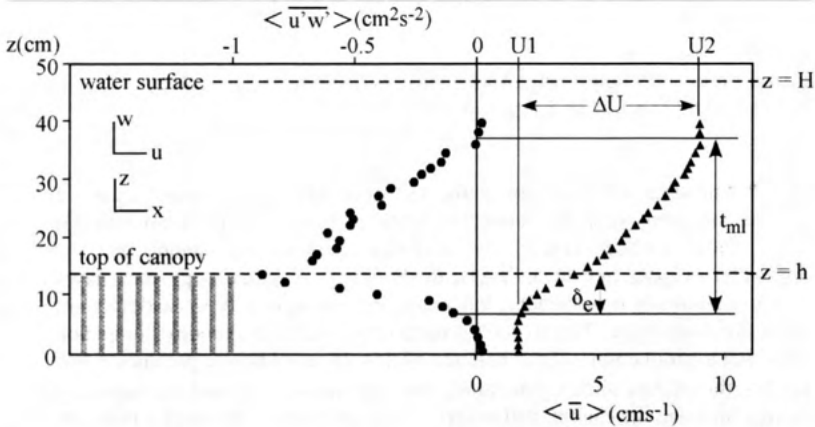


**Figure 1.** The discontinuity in drag at the top of the canopy ( $z = h$ ) creates a shear layer of width  $t_{ml}$ . The velocity difference across the layer is  $\Delta U = U_2 - U_1$ . The layer penetrates downward into the canopy a distance  $\delta_e$  from the canopy top.

The principal flow,  $u$ , is along the  $x$ -coordinate, with  $y$  ( $v$ ) and  $z$  ( $w$ ) denoting the lateral and vertical directions, respectively. Because the flow is forced to move around each cylinder, the velocity field within the canopy is spatially heterogeneous at the scale  $\Delta S$ . A one-dimensional description can be derived using a horizontal averaging scheme, in which the averaging volume excludes the space occupied by canopy elements. The method is nicely described in Raupach and Thom (1981) and Raupach and Shaw (1982). Following their notation, the velocity ( $u, v, w$ ) and pressure ( $p$ ) field is first decomposed into a time average (overbar) and deviations from the time-average (single prime) leading to the familiar Reynolds-averaged Navier-Stokes equations. The time-averaged quantities are then decomposed into the spatial mean in a horizontal plane (angle bracket) and deviations from this horizontal average (double prime). The horizontal average must be taken over a length-scale greater than the cylinder spacing,  $\Delta S$ .

This averaging scheme is used to develop an equation for turbulent kinetic energy. In a submerged canopy flow there are two dominant turbulence scales in the flow: the shear (K-H vortex) scale and the element-scale. The element-scale turbulence is generated in the wakes of individual elements within the array (scale  $d$ ). If the element-scale ( $d$ ) and shear-scale,  $O(h)$ , are distinct ( $d \ll h$ ), the turbulent kinetic energy budget can be separated into shear-scale and wake-scale budgets (Shaw and Segner 1985). As the shear-scale vortices dominate vertical transport and govern shear layer growth, only the budget for shear-scale turbulent kinetic energy ( $k_s$ ) is considered here.

$$\frac{D}{Dt} \langle \bar{k}_s \rangle = -\langle \bar{u}' \bar{w}' \rangle \frac{\partial}{\partial z} \langle \bar{u} \rangle - \frac{\partial}{\partial z} \langle \bar{w}' k_s \rangle - \frac{1}{\rho} \frac{\partial}{\partial z} \langle \bar{w}' p' \rangle - \frac{\partial}{\partial z} \langle \bar{w}'' \bar{k}_s'' \rangle - e_c - e_v \quad (1)$$

1.a                  1.b                  1.c                  1.d

Term 1.a is the shear production. Terms 1.b and 1.c represent vertical transport associated with turbulence and pressure fluctuations, respectively. Observations in free- and canopy-shear-layers suggest that these terms are comparable in magnitude, but opposite in sign, such that to first order the sum of the pressure and turbulent transport is negligible within

the shear-layer (e.g. Rogers and Moser 1994, Brunet et al. 1994, Raupach et al. 1986). Term 1.d is a new term arising from spatial correlations in the time-averaged field. Poggiani et al. (2004b) has shown that this term, called the dispersive transport, is negligible for  $ah > 0.1$ . In the following discussion we restricted our attention to canopies with  $ah > 0.1$ , and neglect this term. The canopy dissipation,  $e_c$ , represents the damping of shear-scale turbulence by canopy drag (e.g. Wilson 1988).

$$e_c = \frac{1}{2} C_D a \langle \bar{u} \rangle \left( 2 \langle u'^2 \rangle + \langle v'^2 \rangle + \langle w'^2 \rangle \right) \quad (2)$$

Here  $C_D$  is the drag coefficient for elements within the array, and it may differ in magnitude from the drag coefficients of isolated elements of the same form (see, e.g., Brunet et al. 1994, Nepf 1999, Poggiani et al. 2004c). The drag parameterization used in (2) represents both the viscous and form drag associated with the individual elements. Finally, the viscous dissipation,  $e_V$ , is generally negligible relative to the canopy dissipation (Wilson 1988).

Neglecting terms 1.b, 1.c, 1.d, and  $e_V$ , the remaining terms suggest that the vortex (and shear-layer) growth will be arrested ( $D \langle \bar{k}_s \rangle / Dt = 0$ ) when the shear-production balances the canopy dissipation. This balance implies

$$\frac{\langle \bar{u} \rangle C_D a}{\partial \langle \bar{u} \rangle / \partial z} = - \frac{2 \langle u' w' \rangle}{2 \langle u'^2 \rangle + \langle v'^2 \rangle + \langle w'^2 \rangle}. \quad (3)$$

The ratio of turbulence statistics on the right-hand-side of (3) are available for several real and model canopies (Dunn et al. 1996, Vivoni, 1998, Segner et al. 1976, Wilson 1988, Katul and Change 1999), with an average value  $0.20 \pm 0.03$ , which is close to the value observed in free-shear-layers (0.21, e.g. Wynganski and Fielder 1970).

From (3) we define a canopy-shear-layer parameter

$$S = \frac{\langle \bar{u} \rangle C_D a}{\partial \langle \bar{u} \rangle / \partial z}. \quad (4)$$

This parameter is similar to one derived by Chu et al. (1991) for shallow-shear-layers, with canopy drag  $C_D a$  replacing the bed-friction parameter  $c_f h$ . We anticipate that  $S$  will have a universal value ( $S_{eq}$ ) for obstructed-shear-layers that have reached the equilibrium described above. From the observed turbulence statistics we anticipate  $S_{eq} = 0.20 \pm 0.03$ .

The equilibrium parameter provides an estimate for the penetration length-scale,  $\delta_e$ , that defines the region within the canopy influenced by the K-H vortices, and thus which experiences rapid exchange with the adjacent open water (Figure 1). First, the characteristic length-scale of the shear-layer vortices is  $L_h = \langle \bar{u} \rangle / \partial \langle \bar{u} \rangle / \partial z$ , where the subscript  $h$  indicates evaluation at the top of the canopy (at  $z = h$ ). Substituting into (4) and allowing  $\delta_e \sim L_h$

$$\delta_e \sim \frac{S_{eq}}{C_D a}, \quad (5)$$

This implies that the penetration length-scale is proportional to the momentum absorption scale  $(C_D a)^{-1}$ , and not directly dependent on free-stream velocity.

### 3. EXPERIMENTAL EVIDENCE FOR SHEAR-LAYER EQUILIBRIUM

Experimental data are drawn from a number of studies in the literature that provide profiles of both  $\langle \bar{u} \rangle(z)$  and  $\langle u'w' \rangle(z)$ : Ghisalberti and Nepf (2004); Seginer et al. (1976) – unconfined case; Tsujimoto et al. (1992) runs R43, A11, A31, A71; Dunn et al. (1996) runs 4, 8, and 10; Nepf and Vivoni (2000) runs 6B and 7A; Raupach et al. (1986); Brunet et al. (1994); and Finnigan (2000, Table 1). In each case  $C_D$  was reported or estimated from a momentum balance within the canopy. We only consider cases for which  $H/h > 2$ , so that the flow depth does not restrict shear-layer growth (Nepf and Vivoni 2000). And, we only consider cases for which  $C_D h > 0.1$ . i.e. dense canopy limit. These conditions ensure that the evolution of K-H vortices is not influenced by the bottom boundary or water surface, but only by the internal dynamics of the shear-layer itself, as assumed by (4). Finally, profiles of spatially-averaged Reynolds' stress define the vortex penetration into the canopy, and thus the length-scale of the exchange zone,  $\delta_E$ . Profiles of  $\langle u'w' \rangle(z)$  peak near the top of the canopy (e.g. Figure 1), and decay downward into the canopy. The limit of vortex penetration is estimated as the point at which the Reynolds' stress decays to 10% of its peak value, and  $\delta_E$  is taken as the distance from the top of the canopy to this point.

The observed values of  $S$  are constant across a wide range of canopy Reynolds' number,  $Re_h = U_h h / \nu$  (Figure 2). And, the observed  $S = 0.24 \pm 0.06$  is consistent with that predicted from turbulence statistics. This supports the theory that shear-layer size is constrained once shear-production is balanced by dissipation due to canopy drag. Finally, for dense canopies ( $C_{Dah} > 0.1$ ) the penetration length-scale follows the linear trend predicted by (5), specifically  $\delta_E/h = 0.2 (C_{Dah})^{-1}$ .

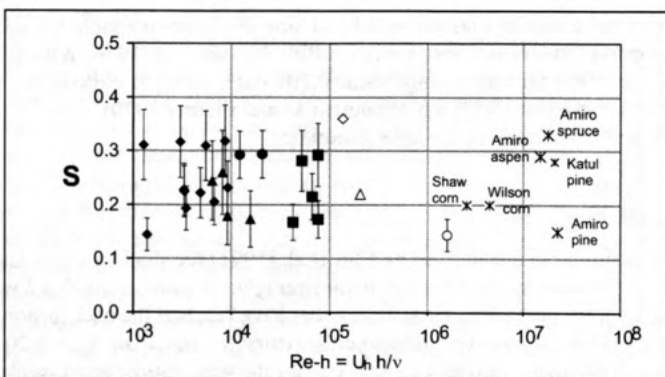


**Figure 2.** Equilibrium parameter,  $S$ , defined in (4). Data sources: Ghisalberti (2005) – solid diamond, Dunn et al (1996) – solid square, Vivoni (1998) solid circle, Tsujimoto et al. (1992) – solid triangle, Seginer et al. (1976) – open circle, Raupach et al. (1986) – open triangle, Brunet et al. (1994) – open diamond, Katul and Chang (1999), Shaw et al. (1974), Wilson (1988), Amiro (1990). For Katul Pine  $U_h$  is note provided. For plotting purposes we assume  $U_h = 1.5$  m/s, as in Amiro Pine.

#### 4. TIME- AND LENGTH-SCALES FOR CANOPY FLUSHING

The length-scale  $\delta_e$  divides a canopy into two regions. The upper region, between  $z = (h - \delta_e)$  and  $z = h$ , flushes rapidly through the direct action of the coherent vortices within the canopy-shear-layer. The exchange velocity between this upper canopy region and the overlying water is  $k_c = \Delta U / 40$  (Ghisalberti and Nepf 2005). A compilation of data from the several studies given above provides an empirical relation between  $\Delta U$  and  $u_{*h}$ , so that  $k_c$  can be predicted from  $u_{*h}$ , which in turn can be approximated from the momentum balance above the canopy as  $u_{*h} = (g S_p (H-h))^{1/2}$ , where  $S_p$  is the potential slope (bed or surface) driving the flow. Within the lower part of the canopy ( $z < h - \delta_e$ ), called the wake zone, flushing is limited by the vertical diffusion within this zone,  $D_w$ . Using relations developed for emergent canopies,  $D_w$  can be predicted from as shown in Figure 3 (Nepf 2004). The exchange between the upper and lower canopy is then characterized by exchange velocity  $k_w = D_w / (h - \delta_e)$ . A two-box model can now be used to evaluate the flushing time for the canopy. Assuming the entire canopy has an initial concentration  $C_0$ , a forward stepping numerical scheme predicts the evolution of concentration in the upper ( $C_c$ ) and lower ( $C_w$ ) zones of the canopy. The evolution of the mean canopy concentration,  $C_m$ , is fitted to an exponential decay to determine the net flushing rate.

As the canopy's momentum absorption capacity ( $C_D ah$ ) increases, the magnitude of shear ( $\Delta U$ ) increases and thus the rate of exchange across the top of the canopy,  $k_c$ , also increases (Figure 4). At the same time, however, the fraction of canopy flushed by the shear-layer vortices,  $\delta_e/h$ , declines. The net result is a non-linear variation in overall canopy flushing, with a minimum flushing time-scale at  $C_{Dah} = 0.25$ . This minimum occurs as the control on overall flushing switches from the exchange zone to the wake zone. Using the vertically-averaged velocity within the canopy, the flushing time-scale can be converted into a length-scale,  $L_{flush}$ . For the conditions considered in this run, canopies of length 100m or less will fully flush within four hours, or a typical tidal cycle. Longer canopies would not be expected to fully flush, allowing the generation of chemically distinct zones within the canopy.

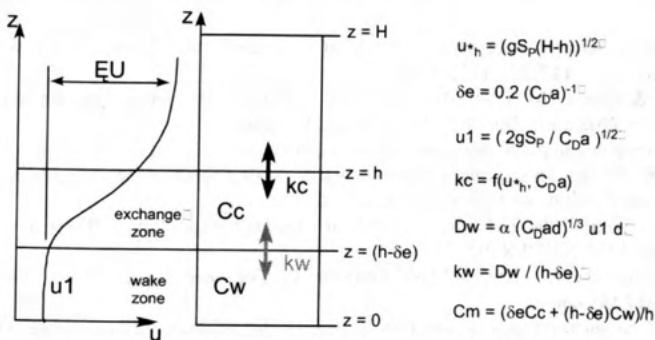


**Figure 3.** A schematic picture of the two-box model and model equations used to evaluate the evolution of concentration within the canopy.

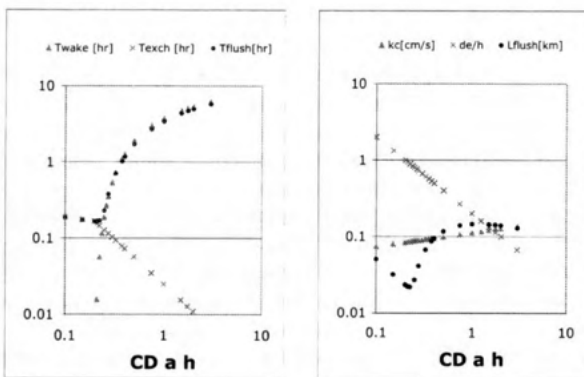


**Figure 4.** Canopy behavior with varying momentum absorption capacity,  $CDah$  for the following conditions:  $S = 10^{-5}$ ,  $H = 1$  m and  $h = 50$  cm.

#### ACKNOWLEDGEMENTS

This material is based upon work supported by the National Science Foundation under Grant No. EAR-0125056. Any opinions, conclusions or recommendations expressed in this material are those of the author(s) and do not necessarily reflect the views of the National Science Foundation

#### REFERENCES

- Amiro, B.D. 1990 Drag coefficients and turbulence spectra within three boreal forest canopies. *Boundary-Layer Met.* **52**, 227-246.
- Brown, G.L. & Roshko, A. 1974 On density effects and large structure in turbulent mixing layers. *J. Fluid Mech.* **64**, 775-816.
- Brunet, Y., J.J. Finnigan and M.R. Raupach. 1994 A wind tunnel study of air-flow in waving wheat: single-point velocity statistics. *Boundary-Layer Met.* **70**, 95-132.
- Cheng, H. and Castro, I., 2002 Near wall flow over urban-like roughness. *Boundary-Layer Met.* **104**, 229-259.
- Chu, V.H., Wu, J.-H. & Khayat, R.E. 1991 Stability of transverse shear flows in shallow open channels. *J. of Hydr. Eng.* **117**(10), 1370-1388.
- Dunn, C., Lopez, F. & Garcia, M. 1996 Mean flow and turbulence in a laboratory channel with simulated vegetation. *Hydraulic Eng. Ser.*, **51**, U. of Ill., Urbana, IL.
- Finnigan, J. 2000 Turbulence in plant canopies. *Ann. Rev. Fluid. Mech.* **32**, 519-571.
- Ghisalberti, M. 2000 *Mixing layers and coherent structures in vegetated aquatic flows*. M.S. Thesis, Massachusetts Institute of Technology, Cambridge.
- Ghisalberti, M. and H. Nepf. 2004 The limited growth of vegetated shear-layers. *Water Res. Res.*, **40**, W07502, doi:10.1029/2003WR002776.
- Ghisalberti, M. and H. Nepf. 2005 Mass Transfer in Vegetated Shear Flows. In press *Environmental Fluid Mechanics*.
- Ghisalberti, M. 2005 *Momentum and Scalar Transport in Vegetated Shear Flows*. PhD. Thesis, Massachusetts Institute of Technology, Cambridge.
- Katul, G. and W.-H. Chang. 1999 Principal length scales in second-order closure models for canopy turbulence. *J. Appl. Meteor.* **38**, 1631-1643.
- Nepf, H.M. 1999 Drag, turbulence, and diffusion in flow through emergent vegetation. *Water Resources Research* **35**(2), 479-489.
- Nepf, H. and Vivoni, E. 2000 Flow structure in depth-limited, vegetated flow. *J. Geophys. Res.* **105**(28), 547-557.

- Nepf, H. Vegetated flow dynamics. 2004. In *Ecogeomorphology of tidal marshes*. Eds. Sergio Fagherazzi, Marco Marani, and Linda Blum. Coastal and Estuarine Monograph Series. AGU. Doi:10.1029/59CE09
- Poggi, D., A. Porporato, L. Ridolfi, J. Albertson, G. Katul. 2004a The effect of vegetation density on canopy sub-layer turbulence. *Boundary-Layer Meteor.* **111**, 565-587
- Poggi, D., G. Katul, J. Albertson. 2004b A note on the contribution of dispersive fluxes to momentum transfer within canopies. *Boundary-Layer Meteor.* **111**, 615-621.
- Poggi, D., G. Katul, J. Albertson. 2004c Momentum transfer and turbulent kinetic energy budgets within a dense model canopy. *Boundary-Layer Meteor.* **111**, 589-614.
- Raupach, M., and R. Shaw. 1982 Averaging procedures for flow within vegetation canopies, *Boundary Layer Met.* **22**, 79-90.
- Raupach, M., P. Coppin, B. Legg. 1986 Experiments on scalar dispersion in a model plant canopy. Part 1: the turbulence structure. *Boundary-Layer Met.* **35**, 21-52.
- Raupach, M., J. Finnigan, and Y. Brunet. 1996 Coherent eddies and turbulence in vegetation canopies: The mixing-layer analogy. *Boundary Layer Met.* **60**, 375-395.
- Rogers, M. and R. Moser. 1994 Direct simulation of a self-similar turbulent mixing layer. *Phys. Fluids A* **6**, 903-922.
- Seginer, I., Mulhearn, P., Bradley, E. and Finnigan, J. 1976 Turbulent flow in a model plant canopy. *Boundary-Layer Met.* **10**, 423-453.
- Shaw, R. H., R. Silversides, and G. Thurtell. 1974 Some observations of turbulence and turbulent transport within and above plant canopies. *Bound. Layer. Meteor.*, **5**, 429-449.
- Shaw, R. H., and I. Seginer. 1985 The dissipation of turbulence in plant canopies, in Proceedings of the 7<sup>th</sup> Symposium of the American Meteorological Society on Turbulence and Diffusion, pp. 200-203, Am. Meteorol. Soc., Boston, Mass.
- Tsujiimoto, T., Shimizu, Y., Kitamura, T., and Okada, T. 1992 Turbulent open-channel flow over bed covered by rigid vegetation. *J. Hydroscience and Hydr. Eng.*, **10**(2), 13-25.
- Vivoni, E. 1998 *Flow through flexible vegetation*, M.S. Thesis, Massachusetts Institute of Technology, Cambridge, MA, USA.
- Wilson, N. R. 1988. A second-order closure model for flow through vegetation. *Boundary-Layer Met.* **42**, 371-392.
- Winant, C.D. & Browand, F.K. 1974 Vortex pairing, the mechanism of turbulent mixing-layer growth, at moderate Reynolds number. *J. Fluid Mech.* **63**, 237-255.
- Wygnanski, I. And H. Fiedler. 1970 The two-dimensional mixing region. *J. Fluid Mech.* **41**, 327-361.



## MODELLING HYDRODYNAMICS IN FLEXIBLE VEGETATION

J.T. Dijkstra<sup>1</sup> and R.E. Uittenbogaard<sup>2</sup>

<sup>1</sup>Delft University of Technology, Stevinweg 1, 2628 CN Delft, The Netherlands, [j.t.dijkstra@citg.tudelft.nl](mailto:j.t.dijkstra@citg.tudelft.nl)

<sup>2</sup>WL|Delft Hydraulics, Rotterdamseweg 185, 2629 HD Delft, The Netherlands, [rob.uittenbogaard@wl.delft.nl](mailto:rob.uittenbogaard@wl.delft.nl)

### Abstract

Estuaries are very rich areas, but they are also under high pressure due to human use, pollution and sea level rise. Aquatic vegetation can have an important role in an estuary by acting as a filter, food source or nursing area, but it is under pressure as well and some species have disappeared already in certain areas. Restoration efforts are made, but not always with a successful outcome. In order to make future restoration attempts more successful, more insight is needed in the interaction between vegetation, currents, waves and sediment transport, and how plants can protect each other.

This paper describes the integration of models for hydrodynamics and for the movement of vegetation, giving us the opportunity to study part of this interaction. The combined model has been tested for uniform flow and one set of vegetation properties only, but the code has been made with dynamic applications like wave action in mind. In the test case, the simulated velocity profile compares very well to the measured one. The simulated turbulence properties show somewhat larger values than the experimental data, but the shapes of the profiles are similar. Predictions made for higher flow velocities show increased bending of the vegetation and as a result differently shaped flow velocity profiles. Before the model can be used dynamically, data for the validation of plant bending are necessary.

### 1. Introduction

The Dutch Waddensea is one of the areas where seagrass (*Zostera marina*) almost disappeared in the 1930's. The cause of this disappearance is not really known, but it coincided with a combination of wasting disease, the closure of the Afsluitdijk and two subsequent years with a sunlight deficit (van Katwijk (2000)). Eutrophication in the following decades may have hampered the return of seagrass. Despite recent improvements in water quality and various restoration efforts, the seagrass population remains very small. In larger quantities, submerged aquatic vegetation may act as an eco-engineer, i.e. it can alter its environment, so creating more favourable living conditions for itself. In order to make future restoration attempts more successful, more insight is needed in this interaction between vegetation, currents, waves and sediment transport.

Such insight could be gained from field and laboratory experiments, but these are often expensive and difficult to conduct. Moreover, empirical results have a limited range of applicability. Therefore it seems logical to construct a computational model that is based on the processes that determine the interaction between vegetation and its environment. With such a generic model, a wide range of currents, waves, water depths and vegetation characteristics can be studied.

The first step is to model the water motion through vegetation, since the hydrodynamics determine the transport of sediment and nutrients, as well as the forces acting on plants. Vegetation elements are often modelled as rigid objects (see e.g. López and García (2001), Nepf (1999)), but flow patterns in highly flexible vegetation like seagrass are very different from flow patterns through rigid vegetation: The bending of plants allows for a greater flow over the canopy ('skimming flow') and a turbulence maximum closer to the bed, but the prone leaves can shield the bed from high shear stresses. Also, flexible plants will move –not only in waves, but also in stationary flow (e.g. Ghisalberti and Nepf (2002))– thus affecting the water motion. The presented 1DV model for flow through flexible vegetation is an extension of the Delft3D model of WL|Delft Hydraulics, which already has a module for rigid vegetation based on a  $k-\epsilon$  turbulence model (Uittenbogaard (2003)). This paper presents the model demands and model setup, followed by a comparison of model results with experimental results and a discussion of further improvements.

### 2. Model demands

The demands on the vegetation model follow from its possible applications, and with this the detail of the model. Since the model will be used to study the effect of a range of vegetation configurations on hydrodynamics, the ability to represent different natural vegetation types is important. This means vegetation properties have to be variable in time, in height and spatially.

Also, the non-stationary aspects of flow and plant motion in waves are of interest, so forces and plant motion need to be modelled dynamically. This has consequences for the numerical scheme because some forces depend linearly or quadratically on the velocity or acceleration of the leaf. However, since the dynamic movement of the plant complicates modelling, and since no suitable validation material is readily available, at the moment the modelling is limited to the semi-static behaviour (i.e. assuming an equilibrium position) of plants. This approach is suitable for stationary flow.

Real seagrasses show very large deflections in flow, up to a prone position. These deflections should not only be represented, but should also be taken into account in the way the flow acts on the leaf.

### 3. Model formulations

Though eventually a fully 3D simulation of a vegetation field will be necessary to incorporate all relevant processes in and around a vegetation field, the most essential phenomena can also be investigated using a 1DV model. This model is an extension of the 1DV turbulence model for rigid vegetation as presented by Uittenboogaard (2003). Here only the basic equations of the momentum balance and k- $\varepsilon$  turbulence model are presented. Where many models for flow through vegetation have used principles derived by studies on atmospheric boundary layer flow, this model also uses principles of flow through porous media.

#### 3.1 Momentum and continuity equations

This 1-DV model solves the momentum equation for the pore velocity  $u(z)$  (m/s):

$$\rho_0 \frac{\partial u(z)}{\partial t} + \frac{\partial p}{\partial x} = \frac{\rho_0}{1 - A_p(z)} \frac{\partial}{\partial z} \left[ (1 - A_p(z))(\nu + v_T(z)) \frac{\partial u(z)}{\partial z} \right] - \frac{F(z)}{1 - A_p(z)} \quad (3.1)$$

in which  $\rho_0$  is the fluid density ( $\text{kg/m}^3$ ),  $\partial p / \partial x$  the horizontal pressure gradient ( $\text{kg/m}^2 \text{s}^2$ ),  $\nu$  the kinematic viscosity ( $\text{m}^2/\text{s}$ ),  $v_T$  the eddy viscosity ( $\text{m}^2/\text{s}$ ), which is defined by the turbulence model (3.4), and  $A_p(\cdot)$  the solidity of the vegetation at a horizontal plane, i.e. the cross-sectional area  $b(z) \times d(z)$  ( $\text{m}^2$ ) of a leaf times the number of leaves ( $m$ ) per  $\text{m}^2$ .

$F(z)$  is the resistance imposed on the flow according to:

$$F(z) = \frac{1}{2} \rho_0 C_D a(z) |u(z)| \quad (3.2)$$

Where  $C_D$  is the drag coefficient (-) and  $a(z)=d(z)m(z)$  ( $\text{m}^{-1}$ ) is the solid area projected on the vertical plane perpendicular to the flow, per unit of depth and per unit of width.

Because the 1DV model assumes uniform flow in horizontal direction, the continuity equation reads:

$$\frac{\partial}{\partial z} \int_{-d}^z u(z) dz = 0 \quad (3.3)$$

with bed level  $z=-d$  and free surface level  $z=\zeta$ .

#### 3.2 k- $\varepsilon$ turbulence model equations

The purpose of the turbulence model is to estimate the eddy viscosity through:

$$v_T = c_\mu \frac{k^2}{\varepsilon} \quad (3.4)$$

with  $c_\mu$  a constant (0.09),  $k$  the turbulent kinetic energy or TKE ( $\text{m}^2/\text{s}^2$ ), and  $\varepsilon$  the dissipation rate ( $\text{m}^2/\text{s}^3$ ).

The equation for  $k$  reads:

$$\frac{\partial k}{\partial t} = \frac{1}{1 - A_p} \frac{\partial}{\partial z} \left[ (1 - A_p)(\nu + v_T / \sigma_k) \frac{\partial k}{\partial z} \right] + T_k + P_k - \varepsilon \quad (3.5)$$

The first term in the RHS represents the vertical diffusion of TKE by its own mixing action, corrected for the available horizontal surface;  $\sigma_k=1$  is a closure coefficient.  $T_k$  is the additional turbulence generated by the vegetation ( $\text{W/m}^3$ ). The amount of power spent by the mean flow  $u(z)$  spent against the drag  $F(z)$  depends on the Reynolds number  $Re_p$ :

$$T(z) = F(z)u(z)$$

$$T_k = f(Re_p)T ; Re_p = \frac{ud}{\nu} \quad (3.6)$$

The third term,  $P_k$ , represents the shear production:

$$P_k = v_T \left( \frac{\partial u}{\partial z} \right)^2 \quad (3.7)$$

Buoyancy is left out of this equation because, for the moment, the density is considered uniform.

The last term in (1.4) is the dissipation of TKE by its work against viscous stresses, according to the following  $\varepsilon$ -equation:

$$\frac{\partial \varepsilon}{\partial t} = \frac{1}{1 - A_p} \frac{\partial}{\partial z} \left[ (1 - A_p)(\nu + v_T) / \sigma_\varepsilon \frac{\partial \varepsilon}{\partial z} \right] + P_\varepsilon + c_{2\varepsilon} \frac{T_k}{\tau_{eff}} - c_{2\varepsilon} \frac{\varepsilon^2}{k} \quad (3.8)$$

Here, the first term on the RHS represents vertical diffusion of  $\varepsilon$  by the turbulent eddies. For the closure coefficient  $\sigma_\varepsilon=1.3$  is applied. The last term seems to represent the dissipation of dissipation, but it actually represents the rate at which the energy cascade converts TKE-dissipating eddies into smaller enstrophy-dissipating eddies.

The second term,  $P_e$ , is the production of eddies, scaled to the turbulence production  $P_k$  by:

$$P_e = c_{1e} \left( \frac{\varepsilon}{k} \right) P_k \quad (3.9)$$

where the closure coefficient  $c_{1e}=1.44$ .

The third term of (3.8) corresponds to the enstrophy production (dissipation due to vegetation), which depends on the effective time scale  $\tau_{eff}$  and a closure coefficient  $c_{2e}=1.92$ . This time scale is related to the different length scales controlling turbulence in and above vegetation. Internally generated turbulence (IGT) is created at sufficient distance from the bed as well as from the top of the vegetation. Here, the wake turbulence length scale is smaller than the available fluid space. Therefore the time scale of this small scale IGT equals the intrinsic turbulence time scale:

$$\tau_{int} = \frac{k}{\varepsilon} \quad (3.10)$$

This time scale is used as effective time scale by Shimizu and Tsujimoto (1994) and López and García (2001). However, above the vegetation a shear layer exists that creates eddies at larger length scales. These can be advected into the vegetation, thus being squeezed into smaller-scale eddies, with a size depending on the available space inside the vegetation ( $L_p$ ). Hence the relevant time scale for dissipation of this penetrated flow turbulence (PFT) is imposed by the geometry of the vegetation:

$$\tau_{geom} = \left( \frac{L_p^2}{c_\mu^2 T} \right)^{1/3} \quad (3.11)$$

With  $c_\mu=0.09$ . After calculation of both internal and geometrical time scales over the vertical, the effective time scale for enstrophy production is evaluated by:

$$\tau_{eff} = \min(\tau_{int}, \tau_{geom}) \quad (3.12)$$

#### 4. The vegetation model

A big difference with the earlier rigid vegetation model, is the fact that the movement (the position) of the vegetation also needs to be modelled. Verduin and Backhaus (2000) coupled a canopy model that simulates motions of plant ensembles to a hydrodynamic model, but their paper does not reveal how this is done. Ikeda et al. (2001) used a 'plant grid' within a large eddy simulation grid to model groups of leafs, assuming the movement of the plant can be described by the equation of motion for a flexible cantilever. Because seagrass shows very large deflections, our method is to follow a Lagrangian approach by setting up a force balance of a leaf segment, see Figure 1.

The distance measured along the leaf is  $s$ , at  $s=0$  it is connected to the bed,  $s=s_{max}$  is the tip of the leaf. On every leaf segment  $ds$  acts a distributed force  $q$  (N/m) as a result of its relative weight and fluid motions relative to the position and velocity of the segment. The force components  $F$  (N) act on the ends of the leaf segment. These are a combination of internal normal and shear stresses, integrated over the leaf cross section. The properties –number, specific density, thickness, width, drag coefficient, and elasticity modulus– of stems or leaves are variable along the length of the leaf.

The following limitations apply:

- A leaf moves in the vertical plane only.
- A leaf cannot fold around itself.
- A leaf can only bend, and not elongate. Because seagrass leaves are very thin, their moment of inertia is very small and thus bending dominates.
- The model is semi-static, i.e. it does not take the acceleration of the vegetation into account.

The force balance for an element reads:

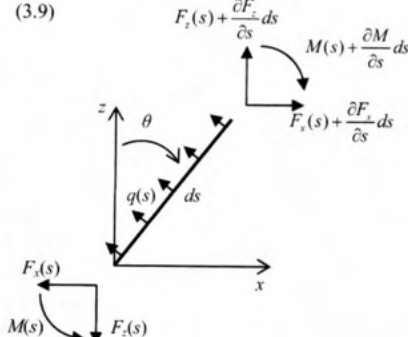


Figure 1. Forces acting on a leaf segment  $ds$ .

$$\begin{aligned} q_x + \frac{\partial F_x}{\partial s} &= 0 \\ q_z + \frac{\partial F_z}{\partial s} &= 0 \end{aligned} \quad (4.1)$$

The internal force components  $F_x(s)$  and  $F_z(s)$ , as well as the positions  $x(s)$  and  $z(s)$  are unknown. A first additional equation couples the internal moment on a cross section to the internal forces:

$$\frac{\partial M}{\partial s} = \frac{\partial x}{\partial s} F_z - \frac{\partial z}{\partial s} F_x \quad (4.2)$$

The internal moment itself is also unknown, but it is related to the leaf's curvature  $\partial\theta/\partial s$  through:

$$EI \frac{\partial\theta}{\partial s} = M \quad (4.3)$$

with  $E$  the elastic modulus ( $N/m^2$ ) and  $I$  the moment of inertia ( $m^4$ ) of the leaf.

Although angle  $\theta$  is the essential unknown here, it serves in the leaf's position assuming no elongation of the leaf:

$$\begin{aligned} \frac{\partial x}{\partial s} &= \sin \theta \\ \frac{\partial y}{\partial s} &= \cos \theta \end{aligned} \quad (4.4)$$

Consequently,  $x(s)$  and  $z(s)$  follow directly from a given  $\theta(s)$ . With equations (4.1) to (4.4), the problem is closed.

The following set of boundary conditions applies:

$$\begin{aligned} s = s_{mx} : M &= 0; F_x = 0; F_z = 0 \\ s = 0 : x &= 0; \frac{\partial x}{\partial t} = 0; \\ s = 0 : z &= 0; \frac{\partial z}{\partial t} = 0; \\ s = 0 : \theta &= \theta \{M(0)\} \end{aligned} \quad (4.5)$$

The first condition states that the leaf tip is not loaded; the others fixate the position at the bed, but allow for the angle to vary with the total exerted moment  $M(0)$ .

The most prominent forces acting on the leaf are those due to pressure differences caused by turbulent wakes, but when the relative flow direction is nearly parallel to the leaf, also shear stresses need to be considered:

$$\begin{aligned} q_s &= \frac{1}{2} \rho_w C_D b |\bar{u}_w - \bar{u}_v| u_s \\ q_n &= \frac{1}{2} \rho_w C_L b |\bar{u}_w - \bar{u}_v| u_n \end{aligned} \quad (4.6)$$

Where  $q_s$  and  $q_n$  are the force components parallel and perpendicular to the leaf, respectively. On the right hand side,  $\rho_w$  is the specific density of water,  $C_D$  and  $C_L$  the drag and lift coefficients and  $b$  is the leaf width. Further,  $\bar{u}_w$  and  $\bar{u}_v$  are the horizontal velocities of water and vegetation, and  $u_s$  and  $u_n$  the local velocity components with respect to the leaf.

## 5. Simulations

The data of Nepf and Vivoni (2000) have been used for a first validation of the model. After this validation, the same setup is used to study the effects of higher flow velocities on the position of the leafs. With the changing position, also the change in drag contribution and flow velocity profile is studied.

### 5.1 Model input

Nepf and Vivoni (2000) studied uniform flow through flexible artificial vegetation for water depth over vegetation height ratios ( $H/h$ ) ranging from 1.0 to 2.75. Mean and turbulent velocities were measured using an ADV and an LDV in a position with representative uniform flow conditions. The flume they used was 24 m long and 0.38 m wide, with a 7.4 m long canopy section. This canopy consisted of 330 randomly placed 0.16 m high plants per  $m^2$ , each made of six 3 mm wide, 0.25 mm thick vinyl blades attached to a 2 cm high wooden base (6.4 mm diameter). The values for  $C_D$  and  $a$  come from fig. 3 in their paper. Table 1 describes the vegetation properties in our model:

vegetation layer	level above bed (m)	$C_d$ (-)	diameter (mm)	number of leafs ( $m^{-2}$ )
1	0.165	1.0	3.0	0
2	0.160	1.0	2.8	1980
3	0.072	1.0	2.8	1980
4	0.048	1.0	3.0	1200
5	0.032	1.0	4.5	550
6	0.020	1.0	6.4	330
7	0.000	3.0	6.4	330

Table 1. Properties along the plant length used for validation.

The flexural rigidity of the leafs in the experiment was  $1.0 \cdot 10^{-5} \text{ Nm}^2$ , constant along the leaf length. Given the moment of inertia  $I = 3.91 \cdot 10^{-15} \text{ m}^4$ , the elasticity modulus  $E = 2.56 \text{ N/m}^2$ . The specific density of the plants is not given, therefore it is assumed equal to the density of the water, thereby discarding buoyancy effects. Since the case  $H/h=2.75$  ( $H=0.44 \text{ m}$ ) is the best described by profiles of mean flow velocity, Reynolds stress and eddy viscosity, this is the case used for validation. This flow depth corresponded to a depth averaged flow velocity of  $0.11 \text{ m/s}$ . To study the effect of larger flow velocities, we increased the flow from 0 to  $0.80 \text{ m/s}$  in 240 s at a depth of  $0.28 \text{ m}$  with the same vegetation properties. We used the low Reynolds number k- $\epsilon$  turbulence model of Goldberg and Apsley (1997), extended with the dissipation and production terms mentioned in section 3.2. We used 100 layers, which zoom in at the bed and the area around the top of the vegetation while following the canopy top. The distribution is as follows: 50 layers with a single-sided exponential distribution above the vegetation top, and 50 layers below following a double-sided exponential distribution. The cell height around the vegetation top is  $0.01 \text{ mm}$ , and at the bed it is  $0.1 \text{ mm}$ . The time step is taken very small ( $0.01 \text{ s}$ ) to ensure a stable plant motion at increasing velocity, as well as a proper allocation of plant properties to the layers and the position along the leaf.

## 5.2 Results

Figure 2 shows the model data in comparison to the experimental data from Nepf and Vivoni (2000). Overall, model and measurement data seem to agree well. The discrepancies near the surface may have to do with the rather narrow flume used in the experiment.

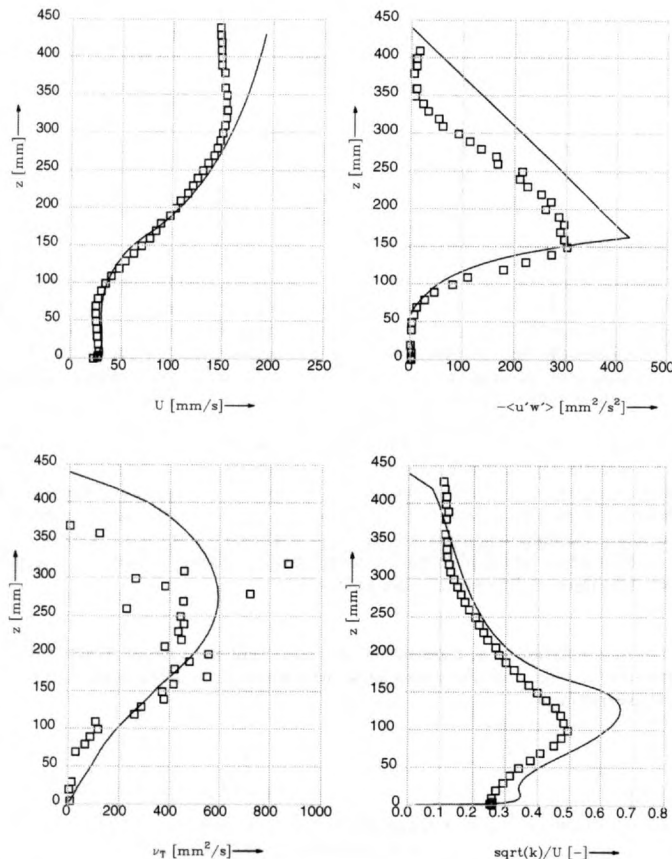


Figure 2. Measurements (squares) by Nepf and Vivoni (2000) and model results (line) for vertical profiles of mean velocity, Reynolds stress, eddy viscosity and normalized turbulent kinetic energy.

Figure 3 shows a prediction of what should happen as the bulk velocity is increased: the vegetation assumes an almost prone position at higher flow velocities, meaning  $H/h$  increases from 1.75 to 5.6. The effect of this bending is clearly visible in the flow velocity profiles: as bending increases, these profiles look more like the logarithmic velocity profiles for unvegetated channels. Still, there is a distinct inflection around the top of the vegetation.

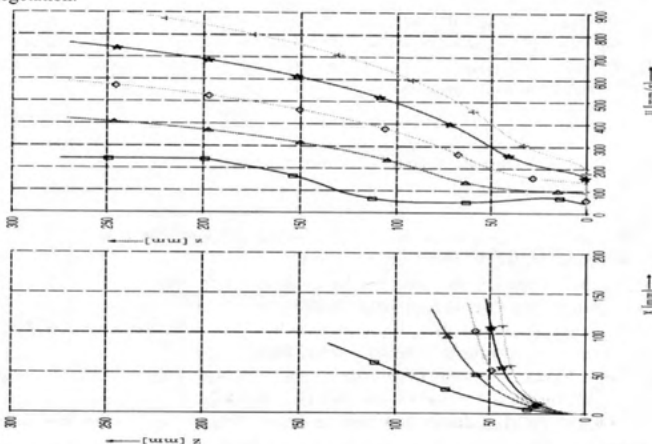


Figure 3. Leaf positions (left) and mean velocity profiles (right) for different bulk velocities. Squares=0.14 m/s, triangles=0.27 m/s, trapezoids=0.41 m/s, stars=0.54 m/s and crosses=0.67 m/s.

The predicted height of the top ( $h_{top}$ ) of the bended vegetation is depicted in Figure 4, in combination with the bulk velocity ( $\bar{U}$ ) and the equivalent plant drag ( $C_D$ ). This equivalent plant drag is calculated as:

$$C_{D, \text{equiv}} = \frac{F_{x, \text{plant}}}{\frac{1}{2} \rho_w h_{top} \bar{U}^2} \quad (5.1)$$

Where  $F_{x, \text{plant}}$  is the plants resistance force per unit width. The reduction of  $C_{D, \text{equiv}}$  with flow velocity comes from the change of form drag to boundary layer drag as the leaf becomes more aligned with the flow.

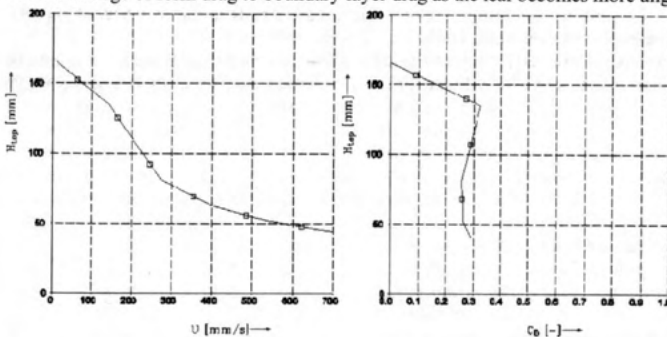


Figure 4. Predicted height of canopy top at increasing bulk velocity (left) and reduction of equivalent drag factor at lower top heights.  $C_D$  is calculated according to Equation (5.1).

## 6. Conclusions

Integrating models for flow and the movement of vegetation gives us the opportunity to study the interaction between flow and various types of vegetation. So far, the combined model has only been tested for uniform flow and one set of vegetation properties. In this case, the simulated velocity profile compares very well to the measured one. The simulated turbulence properties show somewhat larger values, but the shapes of the profiles are similar. Increased bending at higher flow velocities results in different flow velocity profiles, and leads to a reduction of the equivalent drag coefficient as boundary layer drag becomes more important than form drag. However, more experimental data –especially on the bending of plants and representative drag–are necessary to validate the model more thoroughly.

## 7. Discussion

As always when modelling the interaction between a fluid and a body, it is difficult to define a good drag coefficient. In the case of vegetation, which almost always appears in fields rather than as an individual, stems can be in the wakes of others, depending on the spatial distribution. This gives a sheltering effect that further complicates things. The same applies to the lift coefficient.

When modelling real vegetation, the variation in plant properties is also a complicating factor: some plants are longer, others more rigid or have a larger area. Consequently, their bending angle will vary and the plants may touch and exert forces on each other. This on its turn influences the flow and the length scale of penetrating flow turbulence.

Though the model has been used and validated in a semi-static way only, the code has been made with dynamic applications in mind. This requires validation data however, which are scarce: only a few experiments have been done, and often the measurements are limited or the description of the vegetation properties is not sufficient for modelling. Therefore, we would like to encourage experimental researchers to obtain more data on the behaviour of plants in dynamic situations.

### Acknowledgements

We would like to thank Prof. Nepf for providing the data in Figure 3 of this paper.

### References

- Ghisalberti, M. and H. M. Nepf (2002). "Mixing layers and coherent structures in vegetated aquatic flows." *Journal of Geophysical Research* 107: 3/1-3/11.
- Goldberg, U. and D. Apsley (1997). "A wall-distance-free low Re k - epsilon turbulence model." *Computer Methods in Applied Mechanics and Engineering* 145(3-4): 227-238.
- Ikeda, S., T. Yamada and Y. Toda (2001). "Numerical study on turbulent flow and honami in and above flexible plant canopy." *International Journal of Heat and Fluid Flow* 22: 252-258.
- López, F. and M. H. García (2001). "Mean Flow and Turbulence Structure of Open-Channel Flow Through Non-Emergent Vegetation." *Journal of Coastal Engineering* 127: 392-402.
- Nepf, H. M. (1999). "Drag, turbulence, and diffusion in flow through emergent vegetation." *Water Resources Research* 35(2): 479-489.
- Nepf, H. M. and E. R. Vivoni (2000). "Flow structure in depth-limited, vegetated flow." *Journal of Geophysical Research* 105(C12): 28,547-28,557.
- Shimizu, Y. and T. Tsujimoto (1994). "Numerical analysis of turbulent open-channel flow over a vegetation layer using a k-e turbulence model." *Journal of Hydroscience and Hydraulic Engineering* 11(2): 57-67.
- Uittenbogaard, R. E. (2003). "Modelling turbulence in vegetated aquatic flows". Riparian Forest Vegetated Channels Workshop, Trento (Italy).
- van Katwijk, M. M. (2000). Possibilities for restoration of Zostera marina beds in the Dutch Wadden Sea, University of Nijmegen, The Netherlands: 160.
- Verduin, J. J. and J. O. Backhaus (2000). "Dynamics of Plant-Flow Interactions for the Seagrass Amphibolis antarctica: Field Observations and Model Simulations." *Estuarine, Coastal and Shelf Science* 50(2): 185-204.

## HYDRODYNAMIC MEASUREMENTS IN A SHALLOW LAGOON

Carmelo Nasello, Giuseppe Ciraolo, Goffredo La Loggia

Dipartimento Ingegneria Idraulica ed Applicazioni Ambientali  
Università di Palermo – Viale delle Scienze, 90128 – Palermo (Italy)  
Tel: +39 0916657727; Fax: +39 0916657749; email: giuseppe@idra.unipa.it

### ABSTRACT

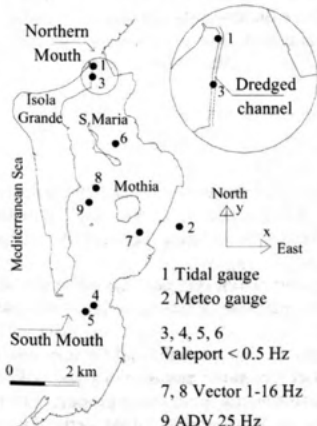
The numerical modelling of the hydrodynamics in lagoons and coastal areas requires a sound knowledge of the *in-situ* dynamical behaviour of the simulated variables (velocities, water elevations, etc). These measurements are essential in calibration and validation procedures and they are also important to understand the physical system. This paper illustrates results of field measurements carried out in a shallow coastal lagoon, called Stagnone di Marsala, in the western part of Sicily (Italy). The water exchange with the Mediterranean Sea occurs through two openings in the basin: the northern one is narrower and shallower than the southern one.

Three field campaigns have been carried out: July 2003, July 2004 and December 2004. The measured physical variables are: 1) tide at the lagoon mouths; 2) velocities and elevations in selected stations within the lagoon; 3) wind speed. Under windy conditions, velocities collected near the surface show the typical orbital behaviour and it is possible to recognize the tidal influence on the flow superimposed to this signal. The mean horizontal flow field seems influenced mainly by the tide, while the wind affects mostly the vertical momentum exchange. Under strong-wind conditions, the horizontal mean-flow field seems to be slowed if compared with the measurements on low winds.

The collected data will be used for the calibration of a quasi-3D hydrodynamic finite-element model. The parameter to tune are the bottom roughness coefficient and the parameters controlling the horizontal and vertical turbulent diffusions.

### The Study Area

The *Stagnone di Marsala* is a shallow lagoon located in the western part of Sicily, delimited by the dry land and the *Isola Grande* island. This lagoon is 12 km<sup>2</sup> in area (1.8 km wide by 6.8 km long) (Fig. 1). Within the lagoon there are two small islands (*Mothia* and *Santa Maria*). From ecological viewpoint, the *Stagnone di Marsala* is considered an environment peculiar within the Mediterranean Sea owing to the particularity of vegetal and animal species living in it. The most important submerged vegetation is the *Posidonia oceanica*, a typical sea-grass (rooted marine macrophytes) in the Mediterranean Sea whose formations, in form of plateaus and barrier reefs, largely contribute to the sustenance of lagoon ecosystems (Calvo *et al.*, 1996). For these reasons, the lagoon and the surrounding areas are a natural reserve.



The lagoon has a northern narrow and shallow mouth to the sea (400 m wide, 0.2-0.3 m deep) and a southern wider and deeper one (1200 m wide, 1.0-1.5 m deep). At the left end of the northern mouth a 20 m wide and 1 m deep channel was dredged, somehow enhancing the local flushing capability (see inset in Fig. 1).

In order to calibrate an *in-house* hydrodynamic numerical models (Balzano *et al.* 2002), a meteorological station and tidal gauges have been installed in the lagoon in 2002. A first measurement campaign was carried out in July 2003 to measure velocities in 4 sites (Nasello and Ciraolo, 2004). Two other measurements campaigns were performed in July and December 2004. In particular, processed data from these last two campaigns are reported here.

Fig. 1 – The Stagnone di Marsala lagoon and the experimental stations with indications of the equipment

### The equipments

The tidal data have been acquired using a float-operated Shaft Encoder (Ott Thalimedes), located in a box connected with the dredged channel of the northern mouth (station 1, Fig.1). The sea level is measured every minute and the mean value is recorded every 5 minutes.

The meteorological gauge is located over a building at about 10 m above the ground in the mid lagoon (station 2, Fig. 1). This weather station is able to record several climatic data: in particular wind speed and direction are measured every 5 seconds and the mean values for each sector are recorded every 15 minutes. Figure 2a shows the intensity and directions of the prevalent sector of the July 2004 campaign. The wind speeds (Fig. 2b) are typically low overnight and increase during the morning; in particular, on 23<sup>rd</sup> July a daytime northerly wind blew with intensity from 5 up to 10 m/s.

During the December 2004 survey, a south-easterly wind blew on the first day of measurements and a north-westerly wind blew in the subsequent two days. The wind intensity increased from 5 to 15 m/s during these three days (not shown).

Water velocities have been measured using two electromagnetic sensors and two ultrasonic sensors. Special platforms rising above the sea surface were designed for each instrument and built using aluminium metal tubes (3 m times 3 m). We chose aluminium not to influence the compasses built-in the gauges. The platforms enabled us to shift the instrument upwards and downwards to record velocities at selected water depths.

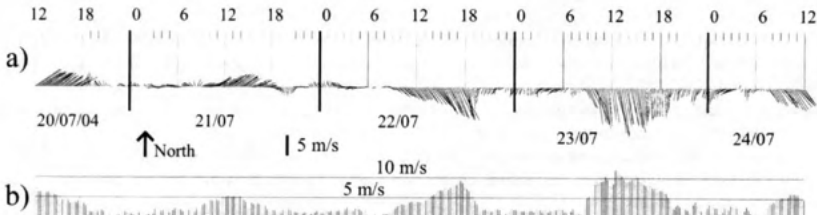


**Fig. 2 – Wind direction and intensity during the July 2004 survey**

The two electromagnetic velocimeters (Valeport 808 EM) are two-dimensional ( $V_{est}$  and  $V_{north}$ ). The maximum acquisition rate is 0.5 Hz, *i.e.* with velocities recorded every 2 s. The first velocimeter was located in the dredged channel at the northern mouth (station 3 of Fig. 1). The second electromagnetic velocimeter was installed next to the southern mouth (stations 4 and 5 of Fig. 1). These instruments are able to measure the water depth  $h$  above the gauge using a pressure sensor and thus detect level oscillations.

One of the three-dimensional ultrasonic velocimeters, a Vector by Nortek, is able to measure and record the three water velocity-components with a sampling rate of 1 up to 16 Hz. This instrument is also able to measure the instantaneous water level. The Vector was located south-east of Mothia in July 2004 and north-west of it in December 2004 (stations 7 and 8 of Fig. 1). The second three-dimensional acoustic velocimeter is an ADV by Nortek; the acquisition rate is between 1 and 25 Hz. This instrument was positioned west of Mothia (station 9 of Fig. 1).

### Velocity profiles

The ADV has been used to record velocities at different depths in order to describe the shape of the velocity profiles in a point within the lagoon. The acquisition rate was set up at 25 Hz and we recorded for 3 minutes velocities in each point of the profile. We take about 30 minutes. In the station 9, during the acquisition time, the mean sea level over the bottom was of 150 cm.

In Figure 3 we report velocities recorded in two points. The first point is located near the water surface ( $z=133$  cm from the bottom – Fig. 4a; relative depth  $z/H=0.89$ ); the second point is located in the central part of the water column ( $z = 70$  cm from the bottom;  $z/H = 0.47$  – Fig. 4b).

Near the surface is evident the influence of wind waves on the velocity field (Nasello and Ciraolo 2004). The three velocity components show the typical oscillating behaviour of the orbital motion of a velocity field influenced by wind waves (Kundu and Cohen, 2002). During the acquisition the wind waves propagate from west to east. The period of this oscillations is about one second (like the wind waves). In the vertical east-west plane, within a one-second lapse of time, the instantaneous velocity vector is directed upwards, then rotates eastwards, downwards and westwards, and eventually points its original direction (Fig. 4a)

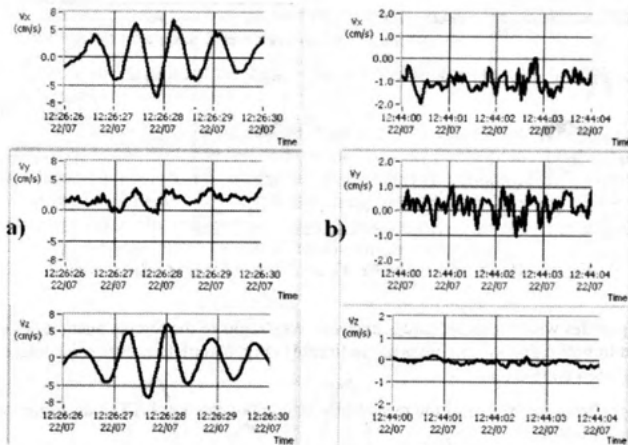


Fig. 3 – Velocity Components  $V_x$ ,  $V_y$ ,  $V_z$ ; a)  $z/H=0.89$ ; b)  $z/H=0.47$

Near the surface (Fig. 3a), the two components  $V_x$ ,  $V_z$  oscillate around zero, so that the mean flow in the east-west and vertical directions is almost insignificant, which supports that the wind waves do not induce any flow but only an orbital motion (Kundu and Cohen, 2002). The velocities in north-south direction,  $V_y$ , are affected by the wind waves and tide: the mean flow in this direction is significant and, upon scrutiny of a longer lapse of time, it is possible to recognise the sinusoidal behaviour of the tide. The time-evolution of the velocity vector in the horizontal plane shows a main flow northwards (fig. 4a).

The analysis of velocities measured as deep as the mid water column ( $z/H=0.47$ ) shows two main facts: 1) the influence of the wind waves is not evident there and the frequency of the oscillations around zero increases (fig. 3b); 2) the velocity intensities are low compared to the near-surface values (fig. 4b).

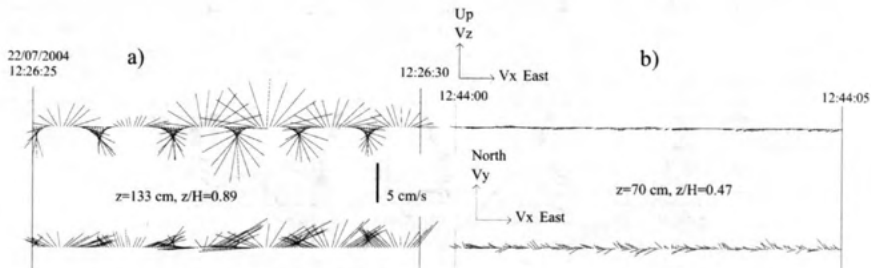


Fig. 4 – Velocity vectors evolution in xz and xy plane; a)  $z/H=0.89$ ; b)  $z/H=0.47$

A Fast Fourier Transform (FFT) algorithm applied to the three velocity components confirms the influence of wind waves on the flow field. The power spectra of these near-surface velocity components ( $z/H=0.89$ ) show a peak at 1.3 Hz, which is similar to frequency of the wind waves (Fig. 5).

This suggests that some fraction of water-current kinetic energy is related to the orbital eddies generated by the wind action. Part of this kinetic energy is then transferred to small vortices where is dissipated and for this reason is not available for the deeper layers. This peak disappears at the middle of water column ( $z/H=0.47$ ) and so do the large eddying caused by wind waves. Arguably, part of the kinetic energy of the eddies went into dissipation and part was transferred into turbulence structures of smaller scale (Pope, 2000).

Because of the wind waves, the flow field near the surface is anisotropic. The  $-5/3$  slope of the Kolmogorov law does not fit the experimental spectra power (Kundu and Cohen, 2002) (Fig. 5). At a lower relative-depth ( $z/H=0.10$ ), instead the Kolmogorov law and experimental data fit well. This suggests that the flow field near the bottom is more isotropic in nature than the near-surface one.

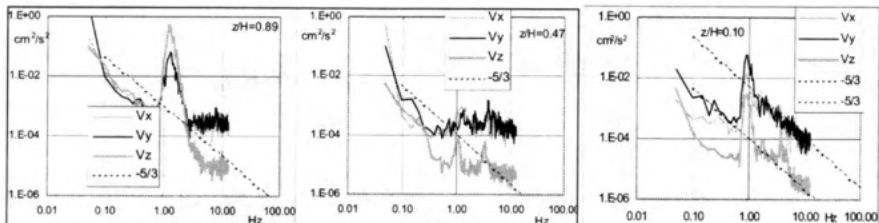


Fig. 5 – Power spectra of  $V_x$ ,  $V_y$  and  $V_z$  for different relative depths

The velocity profiles were measured under unsteady conditions of the forcing agencies (wind and tide): the wind changed in both direction and intensity noticeably (Fig. 6, top). However some interesting consideration has been carried out.

Fig. 6 (middle) shows the profile of the mean velocity components  $V_x$ ,  $V_y$ . The deviations around the mean value are also plotted.

The turbulence intensity (Fig. 6, bottom) is highest near the surface and decreases downwards. As also found by other authors (Yang 1998, Leonard and Reed 2002), the velocities and turbulence strongly decrease close to the vegetated layer ( $z = 65$  cm, vertical segment in fig. 6). It is possible to distinguish two different layers of the flow-field: the upper one characterized by larger velocities and the lower vegetated layer characterized by low and uniform velocities (Christiansen *et al.* 2000).

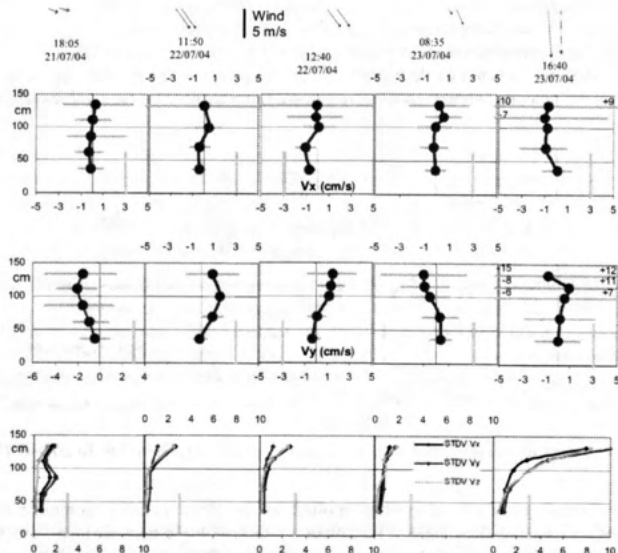


Fig. 6 – Velocity profiles components and turbulence intensity measured under different wind condition

Under windy conditions (as of 23 July) wind waves occurred: this caused the increasing of  $V_x$  and  $V_y$  variations and of the turbulence intensity (Fig. 6 below).

#### Water levels in the lagoon and at the two mouths

Tidal oscillations were recorded continuously at the Station 1 near the northern mouth. These oscillations have been filtered using a digital low-pass filter (Inverse Chebyshev) using a cut-off frequency of  $10^{-4}$  Hz (Fig. 7). We assume that the Station 1 has recorded the tide levels because of its proximity to the open sea: thence, we also suppose that this signal is the same as that at the southern mouth.

In line with the Newton theory, we observed the highest tide level occurring during the night when the meridian crossing the lagoon is internal to the moon-earth alignment.

Fig. 7 shows the water levels recorded at the southern mouth (station 4) and at station 7 (south-east of Mothia): all these signals have been filtered as above.

The comparison of water levels recorded near the mouths and those recorded in the inner stations shows that the water oscillations inside the lagoon are smaller than outside. Furthermore, there occurs a temporal shift between the water-level minima and maxima recorded in the two locations: the water-level peak near Mothia shows a time lag of about 30 minutes with respect the 'open sea' peaks, while the time lag of the minima increases up to 1 hour. This means that, when the water at the lagoon boundary is at its lowest level and the tide starts rising, the water level are still decreasing inside the lagoon.

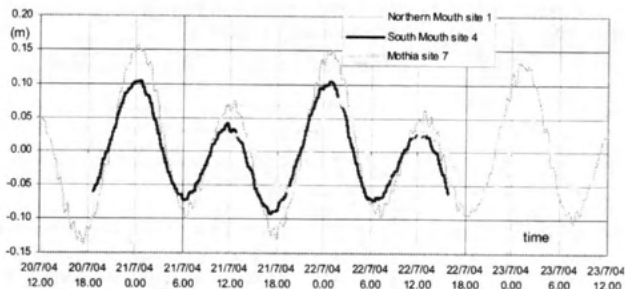


Fig. 7 – Levels oscillations in: Northern Mouth (stat. 1), Southern Mouth (stat. 4) and Mothia (stat. 7)

#### Records at the southern mouth

In July 2004, the velocities were measured near the southern mouth (station 4) using the two-dimensional electromagnetic velocimeter. The mean depth of Station 4 is 118 cm; the measurement point was located at 70 cm above the bottom ( $z/H=0.59$ ) and the recording rate was 20 s. Fig. 8 shows two days of recordings:  $h$  is the depth of the pressure sensor below the free surface;  $V_x$  and  $V_y$  are positive eastwards and northwards respectively. Each of the three parameters shows a sinusoidal behaviour clearly related to the tide oscillations. The effect of wind waves is superimposed to the tide signals.

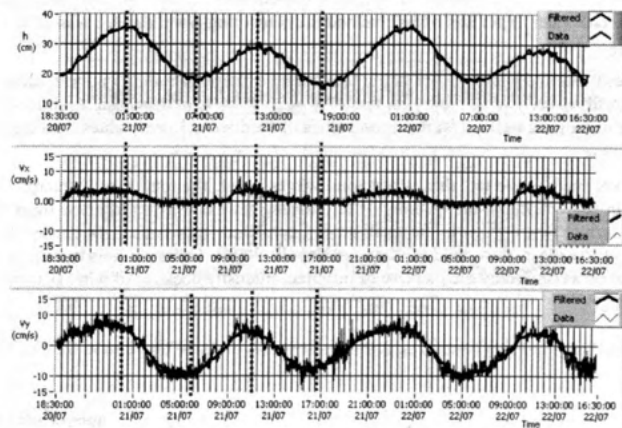


Fig. 8 – Levels and velocities in the southern Mouth ( $z/H=0.59$ )

A low-pass digital filter with cut-off frequency  $6 \cdot 10^{-5}$  Hz has been applied to extract the some information on the mean flow.

The northward component  $V_y$  is strongly influenced by the tide: when tide enters the lagoon,  $V_y$  is positive: the opposite happens when the tide flows out. As recognized by other authors, the maximum velocities measurements are expected approximately when the water level takes minimum or maximum values (Leonard *et al.* 1995; Christiansen *et al.*, 2000).

In our case, the levels and velocities are not in phase. When  $h$  reaches the maximum (e.g. 00:00 of 21 July, Fig. 8) and begins to decrease,  $V_y$  is still positive, which means water flowing northwards. This process carries on as long as the water level of the Southern mouth is larger than the one inside the lagoon.

Comparing the filtered water-oscillations  $h$  and the filtered  $V_y$ 's at the southern mouth and near Mothia (Fig. 9) (sites 4 and 7), it is possible to recognise that, if the water level at the inner station is higher than that at the southern mouth, then the  $V_y$  values are negative, *i.e.* water is flowing out. The opposite occurs when the water level of the inner station is lower than at the lagoon boundary.

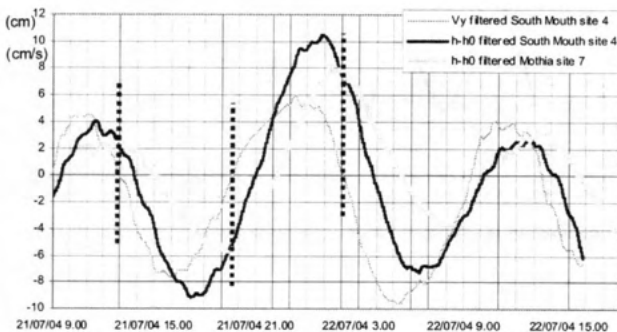


Fig. 9 – Water velocity component,  $V_y$ , related to the water levels

During the subsequent days (22 and 23 of July), the velocities were measured at a higher depth ( $z=85$  cm;  $z/H=0.72$ ). The influence of wind waves on velocities is more evident. Moreover, the higher wind speed (5–10 m/s) caused the increase of turbulence and the reduction of the mean velocities values compared to the previous days of calmer wind (not shown). This fact was also confirmed by the next field survey.

In December 2004, we positioned the electromagnetic current meter at the southern mouth (station 5) recording at 0.1 Hz. The water depth was of 147 cm and the measuring-point depth  $z$  was at 95 cm ( $z/H=0.65$ ).

Again, water elevations and velocities are not in phase with a shift of about 1.5 hour. During the night of the 18/12/2004, a north-westerly wind blew with intensity of 10–15 m/s; under these conditions the instantaneous value of  $V_x$  increased whilst the mean values of  $V_y$  display lower values than the previous days (Fig. 10).

This could be explained by the fact that, when wind waves occur, the total kinetic energy and turbulence intensity increase. In this condition, the quantity of turbulent kinetic energy transferred from the mean flow and the large-scale turbulent structures to the small-scale fluctuations increases. This causes the reduction of the kinetic energy of the mean flow field (Curto and Napoli, 2004). Other authors similarly explained the mean-flow deceleration as caused by the increase of turbulent intensity because of wind (Li and Zhang, 1996; Davies *et al.*, 1997).

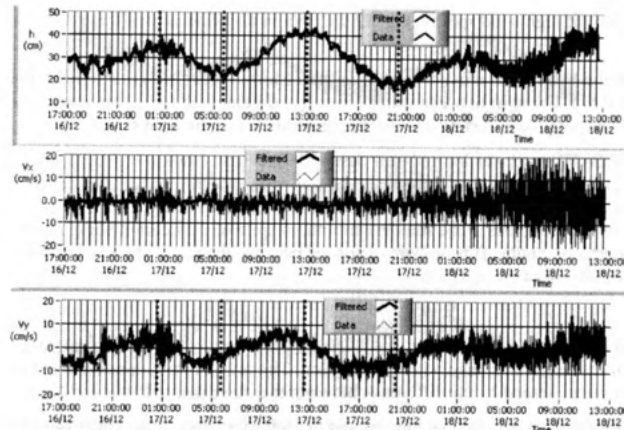


Fig. 10 - Velocities and levels in the southern mouth at station 5 ( $z/H = 0.65$ )

#### Records at the Northern Mouth

The velocities and water-depth oscillations on the dredged channel at the northern mouth (station 3) were measured with the two-dimensional electromagnetic velocimeter ( $H=108$  cm,  $z=55$  cm,  $z/H=0.51$ ).

The channel has a north-south main orientation: that explains why the  $V_x$  velocities are low compared to the  $V_y$ . Moreover, the bottom morphology of the northern mouth makes the channel a preferential route for the water to flow through: for this reason the velocities recorded in this channel (up to 40 cm/s) are higher than elsewhere.

The  $V_y$  component is strictly related to the sinusoidal behaviour of the tide. Like in the southern mouth, water levels and velocities are shifted apart. When the water level is minimum (18:30 of 21/07) and begins to rise, the  $V_y$  is still positive, meaning a flow out of the lagoon. Two hours later, when the water level is higher than inside the lagoon, the  $V_y$  becomes negative with sea water entering the lagoon. The opposite process occurs to the recorded highest levels in the channel.

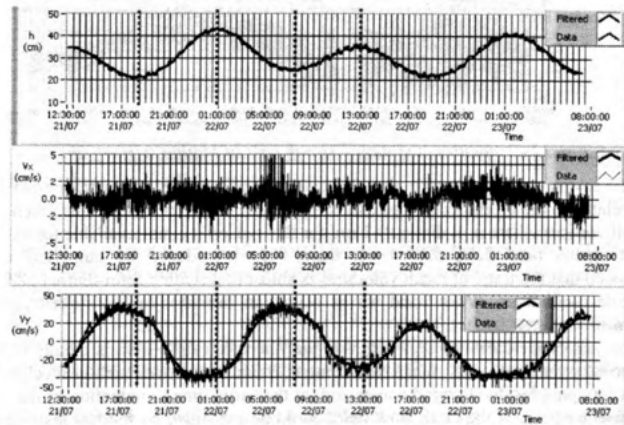


Fig. 11 - Velocities and levels in the northern dredged channel (station 3;  $z/H = 0.51$ )

#### Records within the lagoon

In July 2004, the Vector gauge was located inside the lagoon south-east of Mothia (station 7;  $H=112$  cm,  $z=63$  cm,  $z/H=0.56$ ). Like in the other cases, the near-surface velocities were strictly related to the presence of wind waves. The application of a low-pass filter (cutoff frequency of  $10^{-4}$  Hz) shows that the mean flow seems to slow down under high wind intensity (Fig. 12). The comparison of the daytime hours of 23 July (wind intensity: 5-10 m/s) and the night conditions of 24 (wind intensity  $\leq 3$  m/s) shows the reduction of the

mean flow in presence of high wind speeds (Fig. 12 up). When the wind is low,  $V_x$  and  $V_y$  oscillate according to the tide signal.

In December 2004, the Vector was moved to north-west of Mothia (station 8) (a recording rate of 1Hz;  $H=97$  cm,  $z=49$  cm,  $z/H=0.51$ ). The shift between water levels  $h$  and velocities  $V_x$ ,  $V_y$  amounts to nearly 30 minutes (Fig. 13). It is possible to distinguish the strong influence of the tidal signal.

In December 2004, the Valeport was located near Santa Maria island (station 6; record rate 0.1 Hz;  $H=88$  cm,  $z=46$  cm,  $z/H=0.52$ ). The temporal shift of water levels and velocities disappears there (Fig. 14). During the rising tide,  $V_y$  is positive while the opposite occurs when the tide is lowering. This suggests that this station is mainly influenced by the dynamics at the southern mouth, in spite of its location being closer to a zone influenced by the northern mouth. This probably happens because the really shallow conditions of the northern mouth area (30 cm of mean depth).

### Conclusions

During the two field campaigns performed in the *Stagnone di Marsala* lagoon, velocities and levels have been measured near the two mouths and within the lagoon. The levels oscillations recorded in these sites showed that the flow is governed by the difference between the inner points levels and the boundary levels.

When the tide level is minimum at the two mouths and the tide starts rising, the water fluxes are still flowing out. This because the waters levels inside the lagoon are higher than the mouths levels. After a lag time, tide fluxes start flowing inside the lagoon. Because this time shift, the levels oscillations inside the lagoon are shorter than the one of the mouths.

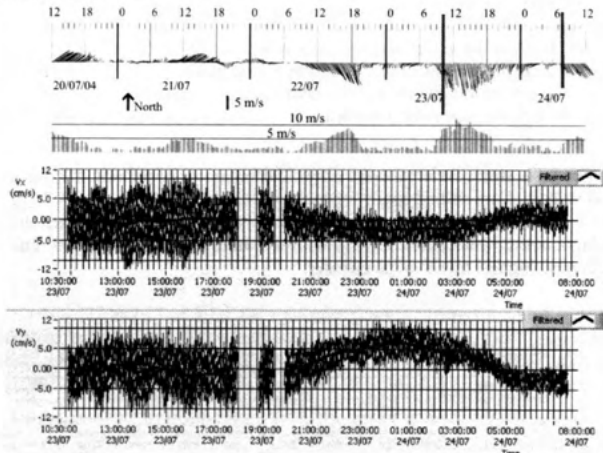


Fig. 12 - Velocities at station 7 (south east of Mothia;  $z/H = 0.56$ )

The measured velocity profiles showed that, near the water surface, some fractions of water-current kinetic energy is related to the orbital eddies generated by the wind action. Part of this kinetic energy is then transferred to small vortices where it is dissipated and for this reason it is not available for the deeper layers.

As regards the mean flow field, that is the main field reproduced by numerical models, all the measurements showed that the trend of mean velocities is sinusoidal (with a semi-diurnal period) and strictly related with the tide oscillations. When wind waves occur, an orbital signal is superimposed on the tide signal, especially near the water surface.

Preliminary analysis of the collected data suggests that the mean flow field is mainly related to the tide oscillation and secondary to the wind. When wind intensity increases over certain level, it is evident the increasing of signal amplitudes due to wind waves and, at the same time, a reduction of the mean flow. The reduction of the kinetic energy of the mean flow field, could be explained by the fact that, when wind waves occur, the total kinetic energy and turbulence intensity increase: in these conditions, the quantity of turbulent kinetic energy transferred from the mean flow and the large-scale turbulent structures to the small-scale fluctuations increases.

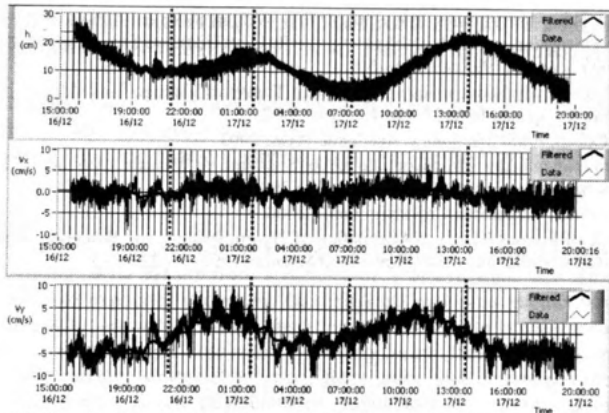


Fig. 13 – Levels and velocities at station 8 (north west of Mothia island;  $z/H = 0.51$ )

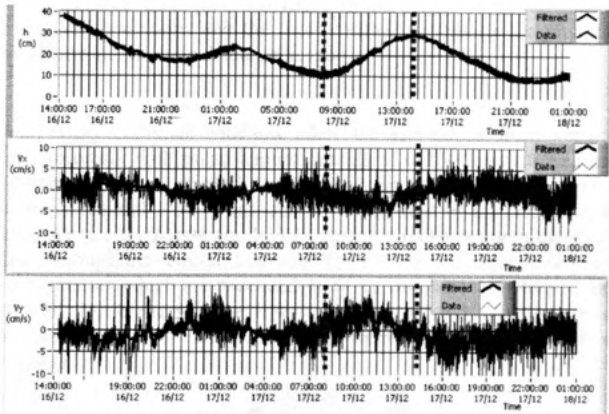


Fig. 14 – Levels and velocities at station 6 (east of Santa Maria island;  $z/H = 0.52$ )

#### Acknowledgments

Authors want to thank Domenico Tuttolomondo for his effort in set up the experimental equipments and Giordano Lipari for checking the English version of this paper.

#### References

- A. Balzano, G. Ciraolo, C. Nasello. Hydrodynamic Finite Element Numerical Simulations in a Shallow Coastal Lagoon of Sicily. *Atti della Fifth International Conference on Hydroinformatics*. Vol. 1, pp. 358-364. Cardiff (UK), July 1-5, 2002.
- S. Calvo, G. Ciraolo, G. La Loggia, T. J. Malthus, E. Savona and A. Tomasello. Monitoring posidonia oceanica meadows in the mediterranean sea by means of airborne remote sensing techniques. *Second International Airborne Remote Sensing Conference and Exhibition*. San Francisco, California, 24-27 June, 1996.
- T. Christiansen, P. L. Wiberg, T. G. Milligan: Flow and Sediment Transport on a Tidal Salt Marsh Surface. *Estuarine, Coastal and Shelf Science* (2000) 50, 315-331.
- G. Curto, E. Napoli: *Idraulica*. Vol. primo, Editoriale Bios, 2004.
- A. M. Davies, J. E. Jones, J. Xing: Review of recent developments in tidal hydrodynamic modeling. I: spectral models. *Journal of Hydraulic Engineering*, Vol. 123, No. 4, April 1997, pp. 278-292.
- LabView 7.0: *User Manual*, National Instruments, April 2003.
- Y.S. Li, M.Y. Zhang: A semi-implicit three-dimensional hydrodynamic model incorporate the influence of flow-dependent eddy viscosity, bottom topography and wave-current interaction. *Applied Ocean Research*. 18 (1996), 173-185.

- L.A. Leonard, A.C. Hine, M.E. Luther, R.P. Stumpf, E.E. Wright: Sediment Transport Processes in a West-central Florida Open Marine Marsh Tidal Creek; the Role of Tides and Extra-tropical Storms. *Estuarine, Coastal and Shelf Science* (1995) 41, 225–248.
- L.A. Leonard, D.J Reed.: Hydrodynamics and Sediment Transport Through Tidal Marsh Canopies. *Journal of Coastal Research*. Special Issue 36, pp. 459–469, 2002.
- P.K. Kundu, I.M. Cohen, *Fluid Mechanics*, Academic Press, 2002.
- C. Nasello, G. Ciraolo: Misure idrodinamiche nello Stagnone di Marsala. Atti del XXIX Convegno di Idraulica e Costruzioni Idrauliche. Trento, settembre 2004.
- S. Pope: *Turbulent flows*. Cambridge University Press, 2000.
- S.L. Yang: The Role of Scirpus Marsh in Attenuation of Hydrodynamics and Retention of Fine Sediment in the Yangtze Estuary. *Estuarine, Coastal and Shelf Science* (1998) 47, 227–233.

## PHYSICAL PROCESSES CONTROL THE VARIABILITY IN PHYTOPLANKTON POPULATIONS IN BOTH TEMPERATE AND TROPICAL AUSTRALIAN RIVERS

Bormans, M., CSIRO Land and Water, Canberra, Australia, now at Université de Rennes 1, Rennes, France, [myriam.bormans@univ-rennes1.fr](mailto:myriam.bormans@univ-rennes1.fr)  
 Ford, P.W., CSIRO Land and Water, Canberra, Australia, [Phillip.Ford@csiro.au](mailto:Phillip.Ford@csiro.au)

### ABSTRACT

Physical factors are known to dominate phytoplankton dynamics in river systems over biological factors. Here we summarise results from a number of intensive studies in Australian rivers to emphasise the need to explicitly understand how physical processes interact with chemical and biological processes to ultimately create conditions favourable to phytoplankton growth. In temperate Australia, we show that flow is the overriding control factor in the Murrumbidgee River which sets vertical mixing, stratification and light climate and determines the phytoplankton response. In the Murray River, phytoplankton populations are controlled by flow through horizontal advection and light climate and by silica availability. In tropical Australia, two sites on the Fitzroy River with initially identical nutrient, turbidity and temperature characteristics, and located only 30 km apart, develop quite different patterns of cyanobacterial succession. We show that large-scale climatic conditions and the local weather pattern set the physical and chemical conditions which determine the cyanobacterial response.

### Introduction

Australia is largely a dry continent with low relief. Climate ranges from wet monsoonal in the northern tropical rainforests with mean annual rainfall of ~ 1500 mm; to seasonally wet in the tropical savannas (mean annual rainfall ~ 600 mm); temperate or Mediterranean in southern Australia (mean annual rainfall ~500 mm); and arid over most of the central desert. The Murray and Murrumbidgee are two temperate and highly regulated rivers rising in the Australian Alps and draining westwards through the semi-arid interior. The Fitzroy is a major river of the dry tropics. It has 5 significant tributaries which are regulated by weirs which become totally transparent during the monsoonal floods. Differences in the flow regimes in these 3 systems represented in Fig. 1 allow us to start disentangling the various processes controlling the dynamics of phytoplankton in these Australian rivers.



**Fig. 1:** Map of the 3 study sites on the Fitzroy River, the Murrumbidgee River (Maude Weir pool), and the Murray River (between Yarrawonga and Merbein).

## 1. The Murray: flow controlled flushing times, horizontal advection and light climate

Most temperate inland rivers in Australia are highly regulated with dams and weir pools for hydroelectric power, water storage and irrigation schemes. This has affected the delivery and cycling of nutrients, water temperature, turbidity and residence time. There is a pronounced seasonal cycle in the discharge with high flow in late winter-early spring due to snow-melt and the beginning of the irrigation season and much reduced flow in summer. Rivers are typically well mixed in summer.

The average discharge along the section of the river (between Yarrawonga and Merbein) exhibits a strong seasonal cycle which is also reflected in the turbidity and the silica concentration (Fig. 2). Both silica and turbidity reach high values under high flows. The high turbidity originates from easily eroded soils and large amount of fine clay sediments carried by high flows. In the Murray River, high flows are released from the bottom of dams located in the upstream reaches.

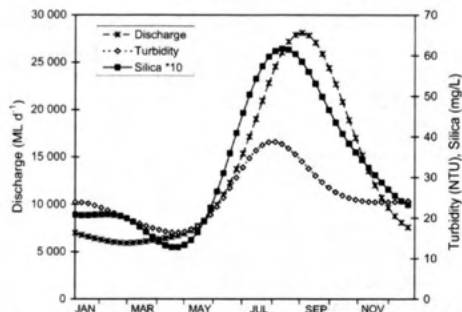


**Fig. 2:** Monthly average discharge, turbidity and silica concentrations for the section between Yarrawonga and Merbein.

Bormans and Webster (1999) developed a simple mechanistic model which simulates the temporal and spatial variability of concentrations of the diatom *Aulacoseira granulata* in the Murray River over large distances under different flow conditions. *Aulacoseira* was the most abundant species of phytoplankton in the river accounting for ~90% of all the diatoms present in the river. The model incorporates a simple growth function determined by the availability of silica and light and by temperature. It also includes losses due to sinking and downstream advection. The model is tested against weekly measurements for the period 1981-1990, at three sites separated by 1100 km (Yarrawonga, Torrumberry and Merbein). This river section is chosen as being typical of a river section without major tributaries inputs or reservoir of any significant size. The simulation is based on the full 10 years of weekly data. To facilitate the presentation, the weekly values have been averaged over the 10-year period for the data as well as for the simulations.

The seasonal cycle of *Aulacoseira* concentrations along the river is well represented by the model as seen on Fig. 3. During times of low flow, *Aulacoseira* concentrations increase through substantial growth in the upstream part of the river, between Yarrawonga and Torrumberry. Further downstream, between Torrumberry and Merbein, *Aulacoseira* concentrations diminish where losses exceed growth which is reduced due to silica limitation. During times of high flow, the concentrations of *Aulacoseira* remain low and fairly uniform along the river as the diatoms have insufficient time to grow before being advected downstream.

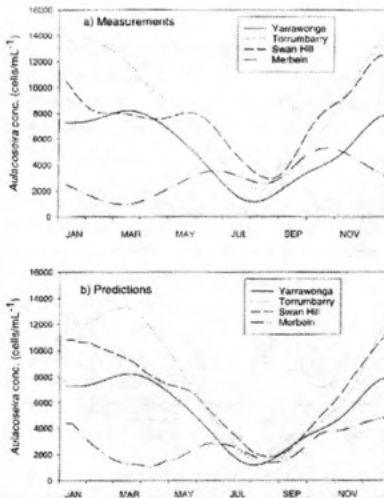


Fig. 3: Measured and simulated *Aulacoseira* concentrations at 4 sites separated by 1100km.

## 2. The Murrumbidgee: flow control of diatom vs. cyanobacterial growth through stratification

A second type of river environment, in the temperate regulated sections of Australian rivers, are the weir pools. Most inland rivers in Australia are slow flowing due to the very low slope of the landscape. Weirs placed along the rivers to provide water storage slow the flow even further. This creates a physical environment that is conducive to cyanobacterial growth. During low flows, stratification develops often during the summer months during the day due to high solar radiation. At night, cooling of the water surface mixes the layers to a certain extent. The high turbidity associated with high concentrations of clay particles in the water results in low light penetration through the water, limiting algal growth to the region near the surface. The euphotic depth is defined as the depth at which 1% of the incident light is penetrating. Below the euphotic depth algae receive insufficient light to grow. Most cyanobacteria can control their buoyancy. When rivers are stratified, a population of buoyant algae such as cyanobacteria will float into the well-lit water layer close to the surface. Cyanobacteria tend to bloom when flow is reduced to low levels and stratification sets in.

During high flows, the turbulence caused by the flow over the river's bed is strong enough to mix the entire water column from top to bottom. Diatoms are dominant in high flows, as they are heavier than water and require well-mixed conditions to stay in suspension. They are also adapted to low light conditions and therefore can grow better and out-compete cyanobacteria under the reduced light climate associated with mixed conditions. Once high flows recede, and the water column stratifies, diatoms immediately sink slowly to the bottom away from the light and cease to grow.

Fig. 4 reproduced from Sherman et al. (1999) illustrates well the transitions between cyanobacterial (*Anabaena*) dominance and diatom (*Aulacoseira*) dominance in a turbid weir pool on the Murrumbidgee river as a result of variable flow conditions associated with flow regulation for irrigation purposes in summer.

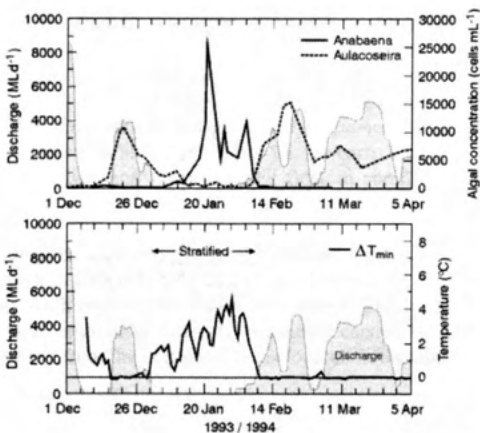


**Fig. 4:** Transitions between *Anabaena* and *Aulacoseira* dominance as a function of stratification.

The transition from *Aulacoseira* to *Anabaena* dominance began with the loss of *Aulacoseira* immediately upon the development of persistent stratification, when the heavy diatoms began to sink out of the water column. This occurred as the flow decreased significantly. The next phase of the transition was the increase in abundance of *Anabaena* as the low flow conditions and stratified water column persisted for a long enough period to allow in situ growth to significant concentration levels. As the flow increased again, stratification was destroyed, *Anabaena* numbers decreased and *Aulacoseira* numbers increased again.

Bormans and Condie (1998) successfully modelled the temporal changes in the distribution of *Anabaena* and *Aulacoseira* in Maude weir pool in response to buoyancy, light limitation and the stratification dynamics.

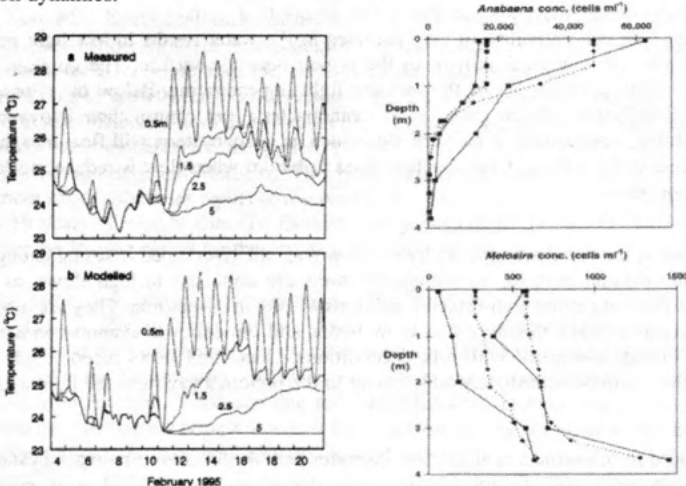


**Fig. 5:** Measured and simulated stratification evolution and vertical profiles of both positively buoyant and negatively buoyant algal species in Maude weir pool. Dashed lines represent simulations and solid lines are measurements.

The model incorporated the predictions under low flow of the diurnal changes in stratification in response to daytime heating, nighttime cooling and wind mixing and their influence on the vertical distribution of the populations. The predictions reproduced accurately the observed depth integrated increased in *Anabaena* and decrease in *Aulacoseira* over a 3 weeks period, as well as their vertical distributions as shown on Fig. 5.

### 3. The Fitzroy: flow and wind control the cyanobacterial populations

In 1970 a barrage was constructed across the then estuarine Fitzroy River near Rockhampton on the Tropic of Capricorn. The storage (capacity 60,000 ML) provides drinking water to Rockhampton and stretches more than 50 km upstream. For much of the year the flow is negligible but in the monsoon season (December to March) episodic flows occur which flush the whole storage several times a day carrying high concentrations (up to 2000 mg/L) of suspended sediment which consists almost exclusively of fine particles ( $80\% < 2\text{ }\mu\text{m}$ ). We compare the cyanobacterial populations at two sites separated by 30km. Details are provided in Bormans et al. (2005).

Immediately after the summer floods the water column at the two sites – Fitzroy Below Alligator Creek (FBA) and Water Treatment Plant (WTP) had identical chemical and physical characteristics and was exposed to identical levels of incoming solar radiation. Despite starting from the same conditions the development of the cyanobacterial populations at the 2 sites followed markedly different trajectories (Fig. 6). These differences include:

- Initiation of cyanobacterial growth at FBA 2 months before it starts at WTP;
- FBA populations are initially dominated by large blue greens (*Anabaena circinalis*) while the WTP populations are dominated by small cyanobacterial species
- The FBA population of *Anabaena circinalis* collapses within a month of forming, while the WTP population persists until flushed away by floods in February the following year.
- The overall biomass is significantly larger at WTP than at FBA.

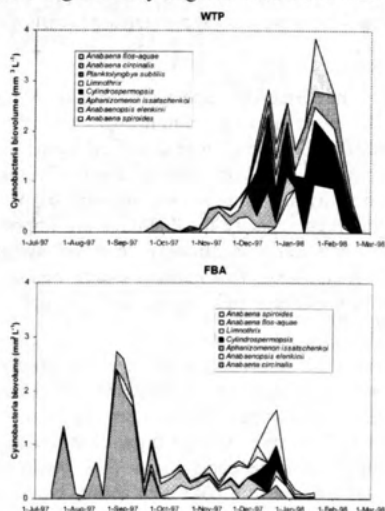


**Fig. 6: Dominant species contribution to the biovolume of cyanobacteria at both sites.**

All these phenomena are explicable by 2 factors: the differences in light availability at the 2 sites as reflected in the differences in both the surface mixed layer depths and the euphotic depths, and the differing bio-availability at the 2 sites of phosphorus – the limiting nutrient. While these are the proximate factors, ultimate control is exercised by the differing inter-site local meteorological conditions which prevail, despite the synoptic scale meteorology being identical at the 2 sites.

### ***Evolution of differing light climates***

In the Fitzroy River impoundment, post-flood turbidity reduces the available light in the well-mixed water column at both sites to levels insufficient for cyanobacterial growth. Only when the water column stratifies and the slowly sinking particles are removed from the surface layer does  $z_m / z_{eu} < 3$  and cyanobacterial growth commences and dominates when  $z_m / z_{eu} \sim 1$ . Because of different mixed layer dynamics between the two sites (due to different wind exposure) and different light climate dynamics (due to different depths and wind mixing) the ratio  $z_m / z_{eu}$  evolved at different rates at both sites. At FBA the ratio  $z_m / z_{eu} \sim 1$  from August, while at WTP the ratio  $z_m / z_{eu} > 3$  until November.

### ***Nutrient availability***

The growth of cyanobacteria at FBA from July onwards was occurring under very low nitrate concentrations in the surface layer influencing the types of species present. By the time the ratio  $z_m / z_{eu} \sim 1$  at the upstream site (FBA) large cyanobacteria (*Anabaena circinalis*) were observed and the nutrient concentrations (FRP) in the surface layer were still sufficient to support their growth. The collapse of the cyanobacteria in mid-September coincided with a total depletion of surface FRP suggesting that *Anabaena* was not regulating its buoyancy to access the nutrient rich hypolimnion waters only a meter or two below. The cyanobacterial species assemblage which followed were smaller in size in accordance with Reynolds' (1984) suggestion that smaller species have higher uptake rates and can survive in waters with higher intermittency of nutrient supply than larger species. Because the river at FBA is perpendicular to the prevailing wind direction the seiching mechanism, which "pumps" dissolved inorganic nutrients from the anoxic hypolimnion into the surface layer (see below), cannot operate. The cyanobacterial population at FBA is thus nutrient limited and the overall biomass of cyanobacteria stayed lower at that site from November onwards.

At the WTP site when the light climate became favourable by November (two months after the upstream site) most of the dissolved nutrients (both nitrogen and phosphorus) had been scavenged from the water column. Thus the concentration of dissolved inorganic nutrients was very low. The cyanobacterial species dominating that environment were therefore very small and had high specific uptake rates required by the intermittent nutrient supply. High uptake rates at low phosphorus concentration and high capacity for P storage are important characteristics that favor *Cylindrospermopsis* over other species in strongly stratified systems with highly intermittent nutrient supply (Istvanovics et al, 2000). This nutrient source was provided by wind induced deep mixing events which entrained nutrient rich anoxic hypolimnion waters into the surface layer (Bormans et.al. 2004) see Fig. 7.

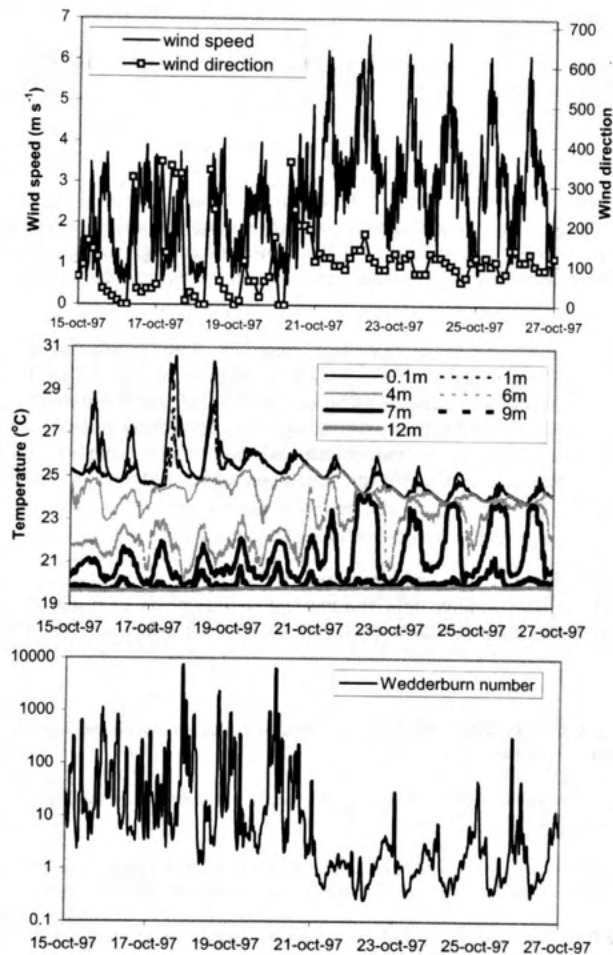


**Fig. 7:** Time series of wind speed & direction, temperature distribution and Wedderburn number at the WTP site.

Although the monthly average wind speeds in summer were relatively low ( $U < 2.5 \text{ ms}^{-1}$ ), much higher wind events of few day durations with daytime wind speeds above  $5 \text{ ms}^{-1}$  occurred regularly at frequencies varying between 5 and 10 days. During daytime, high winds coming from the coast originated from the S-SE, which is the direction of the river fetch between the barrage and the WTP. A daily periodic oscillation of the thermocline was observed repeatedly in the thermistor chain data at WTP in response to the daily wind forcing (Fig. 7). The seiching of the thermocline was strongly correlated and in phase with winds oriented along with the river fetch from the barrage towards the WTP when wind speeds exceeded  $5 \text{ m s}^{-1}$ . We calculated that in this system where the length of the fetch between the barrage and the WTP site was  $L = 5 \text{ km}$ , a wind speed  $U = 5 \text{ m s}^{-1}$  corresponded to a Wedderburn number  $W = 1$  (Fig. 7). This value has been observed in many lakes to correspond to the critical value below which increased hypolimnetic mixing caused by internal shear is observed (Spigel and Imberger 1980; MacIntyre et al. 1999). The shear across the base of the mixed layer generates turbulence through shear production enhancing the ability of the wind to deepen the mixed layer and entrain the top of the bottom layer. This nutrient flux from the hypolimnion was sufficient at WTP to support a bloom of mixed small cyanobacteria

species which persisted, for almost three months, until an inflow of about 35,000 ML flushed the impoundment in late February 1998.

### Conclusions

In temperate Australian rivers, flow is the dominant factor governing phytoplankton dynamics through residence time, horizontal advection, vertical mixing and light climate. Growth is dominant in summer due to higher temperature and low flows. Diatom growth dominates in well mixed systems while cyanobacterial growth is confined to stratified weir pools.

In tropical Australian rivers large scale climatic conditions, through monsoonal rainfall resulting in high flow discharge, reset the light climate and the input of nutrients from the catchment on an annual basis. Local weather conditions (solar radiation, wind speed and direction) combined with local river geometry and size determine the timing of water clearing and nutrient removal from the water column. We show that large scale climate and local wind forcing were the dominant drivers in setting up the physical and chemical conditions which led to the observed succession of cyanobacteria.

We have shown that the physical processes of horizontal advection, heat flux, mixing and stratification set the temperature, light and nutrient environments such that models that explicitly resolve these processes are essential to explain phytoplankton dynamics in these rivers.

### References

- Bormans M. & S.A. Condie (1998): Modelling the distribution of *Anabaena* and *Melosira* in a stratified river weir pool. *Hydrobiologia* **364**, 3-13.
- Bormans, M & I.T Webster (1999): Modelling the spatial and temporal variability of diatoms in the River Murray. *J. Plankton Res.* **21** (3), 581-598.
- Bormans, M., P.W. Ford, L. Fabbro and G. Hancock (2004). Onset and persistence of cyanobacterial blooms in a large impounded tropical river, Australia. *Marine and Freshwater Res.*, **55**, 1615.
- Bormans, M. & P.W. Ford (2005). Spatial and temporal variability in cyanobacterial populations controlled by physical processes. *J. Plankton Res.*, **27** (1), 61-70.
- Istvanovics, V., Shafik, H. M., Presing, M., and Juhos, S. (2000). Growth and phosphate uptake kinetics of the cyanobacterium, *Cylindrospermopsis raciborskii* (Cyanophyceae) in throughflow cultures. *Freshwater Biology* **43(2)**: 257-275.
- MacIntyre S., Flynn, K. M., Jellison, R., and Romero, J. R. (1999). Boundary mixing and nutrient flux in Mono Lake, California. *Limnol. Oceanog.* **44**: 512-529.
- Reynolds, C. S. (1984). *The ecology of freshwater phytoplankton*. Cambridge University Press, Cambridge.
- Sherman, B.S., I.T. Webster, G.J. Jones & R.L Oliver (1998): Transitions between *Aulacoseira* and *Anabaena* dominance in a turbid river weir pool. *Limnol.Oceanog.* **43** (8), 1902-1915.
- Spigel R. H., and Imberger, J. (1980). The classification of mixed layer dynamics in lakes of small to medium size. *J. Phys. Ocean.* **10**: 144-154.

## EVOLUTION OF ESTUARIES - PAST AND FUTURE

David Prandle , Proudman Oceanographic Laboratory,  
Joseph Proudman Building, 6 Bronlow St, Liverpool L3 5DA  
[dp@pol.ac.uk](mailto:dp@pol.ac.uk)

New generic theories have been developed to explain and inter-connect tidal response, salinity intrusion, sediment regimes and bathymetric evolution in estuaries. These theories offer the potential of understanding how aspects of estuarine behaviour evolved over the Holocene. By comparing such theory with specific archaeological evidence, the role of various controlling factors (including changes in: sea level , river flow, air and sea temperatures, rainfall and winds, sediment supply, 'hard' geology, mediation of surficial sediments by flora and fauna etc) may be distinguishable. Construction of such time-sequences can also be used to indicate consequent changes in: stratification, residence times and net export / import of nutrients and other dissolved/adsorbed tracers. These studies provide perspective for estimates of possible future impacts of both Global Climate Change scenarios and more localised 'interventions'. While such generic approaches cannot replace in-depth studies of specific estuaries, they do provide a framework for inter-comparison of predicted changes in differing estuaries. Moreover they can predict which estuaries (and what and where within these) are likely to be most sensitive to change. Thus , these results can be used to develop monitoring policies that should be effective in determining early signs of change in estuaries.



## ATMOSPHERIC INFLUENCES



## The influence of lake-size on the value of transfer coefficients

*Ian Jones*

*CEH Lancaster, LEC, Library Avenue, Bailrigg, Lancaster, LA1 4AP*

### Abstract

*Heat and momentum fluxes at a lake surface are fundamental drivers of the physical processes that take place in a lake. The momentum flux and the sensible and latent heat fluxes are frequently calculated by using bulk formulae, as accurate measurements of these fluxes are both expensive and rather difficult. These formulae have the advantage of using routinely measured variables, such as wind speeds and air temperatures, but tend to disguise the more complicated physics in the transfer coefficients they use. Transfer coefficients depend upon many parameters, the most important ones being wind speed, atmospheric stability and fetch. The majority of the work that has been carried out on these transfer coefficients has taken place in the field of oceanography rather than limnology. Whilst this allows useful estimates of the effects of wind speed and stability to be taken into account, the lack of fetch limitation raises questions about the applicability of these oceanographic transfer coefficients to studies over lakes.*

*Here, one of the few existing studies of drag coefficients over limited fetch has been taken as a basis for estimating drag coefficients over lakes of varying size. A key parameter is the Charnock constant, which is used in the theoretical calculation of surface roughness caused by gravity waves. This empirical 'constant' is thought to vary with wave-age and can therefore be linked to fetch. By doing this, different values of the Charnock constant can be used for calculating roughness lengths, and hence drag coefficients, for differently sized lakes. Drag coefficients calculated in this manner are substantially larger over lakes than oceans when the wind speed is high.*

### Introduction

The atmosphere is a key driver of the physical processes within a lake, with these physical processes, in turn, having a major impact upon the ecology within a lake (George & Taylor, 1995; DeStasio *et al.*, 1996; George, 2000; Winder & Schindler, 2004). In order to understand the workings of the lake ecosystem it is therefore necessary to have a full understanding of the atmospheric forcing at the lake surface. This is particularly true in the context of a changing climate: it is necessary to be able both to quantify the heat and momentum fluxes across the air-lake surface under present climatic conditions, in order to be able to detect any future changes in them, and to understand the processes underpinning the fluxes in order to predict the way they might change in the future.

Heat and momentum fluxes are frequently represented as bulk formulae. Such formulae offer the advantage of calculating the fluxes from relatively well known and frequently measured variables such as the near surface wind speed and temperature, but also require the use of transfer coefficients. Whilst often being parametrised as constants or relatively simple functions of known variables, in reality these transfer coefficients represent much of the physics within the formulae. Owing to their importance for climatology, transfer coefficients have been studied for many years (see, for example, various reviews by Garratt, 1977; Blanc, 1985; Garratt, 1992).

These studies have suggested a number of factors that influence the magnitude of these coefficients, in particular, wind speed and atmospheric stability. Higher wind speeds increase wave height and therefore roughness length, which in turn acts to increase the transfer coefficients. At low wind speeds, waves cease to be the most important interface between the water and air, and other transfer mechanisms control the value of the transfer coefficients. Atmospheric stability can cause much variation in the transfer coefficients as the more stable the atmosphere the more restricted is the mixing from higher levels towards the surface. Thus, the transfer coefficient is lower in a stable atmosphere than an unstable atmosphere.

Actual estimates of the transfer coefficients vary enormously in the literature. Work by Smith (1988) examining the effects of wind speed and atmospheric stability on the value of the drag coefficient suggests almost an order of magnitude increase between values in stable low wind speed conditions and those in unstable high wind speed conditions. The review by Blanc (1985) reports a range of values for the *neutral* drag coefficient from less than  $1 \times 10^{-3}$  to nearly  $3 \times 10^{-3}$ . Even at a given wind speed, the estimated values vary by around 50% (Blanc, 1985). A similar review by Hsu (1986) shows even larger variations.

For lakes, there is an additional difficulty. Most research on transfer coefficients has taken place in the open ocean, in situations of effectively unlimited fetch, or in coastal waters with rather larger fetches than most lakes. Lakes, though, are water bodies of limited fetch. A number of authors have found a relationship between the efficiency of the transfer of properties and wave-age: the younger the waves, the more effective their ability to transfer momentum between the air and the water, with wave-age itself being implicitly related to fetch (Wu, 1985; Geernaert *et al.* 1986; Hsu, 1986; Donelan *et al.* 1993). Only when the wave-state reaches an equilibrium with the atmosphere is the efficiency of transfer reduced to open ocean values. It therefore follows that the smaller the water body the larger the transfer coefficient. By using the transfer coefficients calculated from the open ocean, even when taking atmospheric stability and wind speed into account, limnologists are in danger of severely underestimating the turbulent fluxes across the air-lake interface. This paper seeks to highlight this issue and to provide a possible mechanism for taking fetch into account when calculating transfer coefficients for lakes. The work is restricted to the momentum flux and the associated drag coefficient rather than also looking at the latent and sensible heat fluxes, although the arguments are in general applicable to these fluxes too.

## Results

Monin-Obukhov similarity theory provides a description of flow near to a surface,

$$\frac{\partial U}{\partial z} = (u^*/\kappa z) \cdot \Phi_m(z/L), \quad (1)$$

where  $U$  is the wind speed,  $z$  the height above the surface,  $u^*$  the friction velocity,  $\kappa$  the non-dimensional von Kármán constant,  $L$  the Monin-Obukhov length and  $\Phi_m(z/L)$  a function describing the dependence on atmospheric stability. A variety of such (empirical) stability functions exist; see, for example, Businger *et al.* (1971) or Höglström (1988).

The drag coefficient,  $C_d$ , is defined in the bulk formula for wind stress,

$$\tau = \rho_a C_d U^2, \quad (2)$$

where  $\tau$  is the wind stress and  $\rho_a$  the density of the atmosphere. The friction velocity is defined by,

$$u^* = \tau / \rho_a, \quad (3)$$

(Garratt, 1992). Integration of (1) between the roughness length,  $z_0$ , at which the flow is defined to be zero, and the reference height  $z_r$  with wind speed  $U_r$ , and combining (2) and (3) gives the following,

$$u^* = \kappa U_r / (\ln(z_r/z_0) - \Psi_m(z_r/L)), \quad (4)$$

$$C_d = (u^* / U_r)^2, \quad (5)$$

where  $\Psi_m(z/L)$  is obtained from integration of the function  $\Phi_m(z/L)$ . To avoid stability complications, this paper will focus only on the neutral drag coefficient, where  $\Phi_m(z/L)$  has the value 1 and  $\Psi_m(z/L)$  the corresponding value 0. Thus,

$$u^* = \kappa U_r / \ln(z_r/z_0). \quad (6)$$

Incorporating stability corrections by using functions for  $\Phi_m(z/L)$  and therefore  $\Psi_m(z/L)$  is relatively straightforward, if a little tedious, but does not alter the thrust of the arguments presented here.

The roughness length of a water surface is unusual in that it is dependent on the wind speed, as winds influence the height of the waves. A much used formulation (see Renfrew *et al.*, 2002;

Garratt, 1992) for the roughness length, incorporating both a theoretical basis and empirical values, is,

$$z_0 = \beta \nu / u_* + \alpha_c u_*^2 / g, \quad (7)$$

where  $\nu$  is the viscosity of air,  $g$  is gravity, and  $\beta$  is a constant.  $\alpha_c$  is the Charnock constant (Charnock, 1955). The first term on the left hand side represents the smooth flow estimate for roughness length, when waves are not present on the water surface; the second term is the theoretical estimate of the effect of gravity waves. Usually in the literature  $\beta$  is zero if the smooth flow approximation is ignored or it is given the value 0.11, although there are some suggestions for it to be higher owing to the gustiness of the wind (Smith *et al.*, 1996). Despite its name, the value of the Charnock constant varies widely. Charnock himself suggested the value 0.012. Probably the most commonly accepted value for the open ocean is 0.011 from Smith (1988). Garratt (1992) lists various studies estimating the value of the constant to range from 0.011 to 0.035, the largest values reported being those associated with limited fetch. The value of 0.016 has been put forward from work carried out on Lake Michigan (Hicks, 1971). Heikinheimo *et al.* (1999) estimated a value of 0.02 for a shallow lake with a surface area of 37 km<sup>2</sup>. Vickers & Mahrt (1997) in an experiment in the Baltic Sea reported values for on-shore flow, with fetch of approximately 15–25 km, of 0.015 and for off-shore flow, with a fetch of 2–5 km, of 0.073. There are even cases of the Charnock constant being estimated to be over 0.1 (Johnson *et al.*, 1998). Normally, values less than about 0.015 are associated with the open ocean, whereas values higher than this are associated with restricted fetch; generally the smaller the fetch, the larger the value of  $\alpha_c$ . This is unsurprising given the link various authors have made between the value of  $\alpha_c$  and sea state characteristics such as wave-age (Geernaert *et al.*, 1986; Nordeng, 1991; Donelan *et al.*, 1993; Smith *et al.*, 1996).

Taking  $\rho_a$  to be 1.2 kg m<sup>-3</sup>,  $\nu$  to be  $1.5 \times 10^{-5}$  m<sup>2</sup> s<sup>-1</sup>,  $g$  to be 9.8 m s<sup>-2</sup>, giving  $\kappa$  its most usual value of 0.4, and then combining Eqns 5, 6 and 7, the neutral drag coefficient, at the standard reference height of 10 m, can be calculated. Using this calculation Figure 1a shows the value of the transfer coefficient owing to a) only smooth flow, b) just gravity waves ( $\beta = 0$ ) using the Smith (1988) value of 0.011 for  $\alpha_c$  and c) the value using the full formula for both smooth flow and gravity waves. It can be seen that it is the smooth flow that dominates at low wind speed, but above roughly 6 m s<sup>-1</sup> the transfer of momentum is governed almost solely by the gravity waves.

A range of values for  $\alpha_c$  between 0.011 and 0.1, are used to calculate the neutral drag coefficient, the results being shown in Figure 1b. It can be seen from Figure 1b that at wind speeds of 20 m s<sup>-1</sup> the value of  $\alpha_c$  changes the value of the drag coefficient by more than 100 per cent. Even at a 10 m wind speed of 5 m s<sup>-1</sup> the value of the drag coefficient is altered by around 50 per cent. The implication of this result is that for most wind speeds, but particularly high wind speeds, the drag coefficient over water bodies of limited fetch should be considerably higher than those for the open ocean.

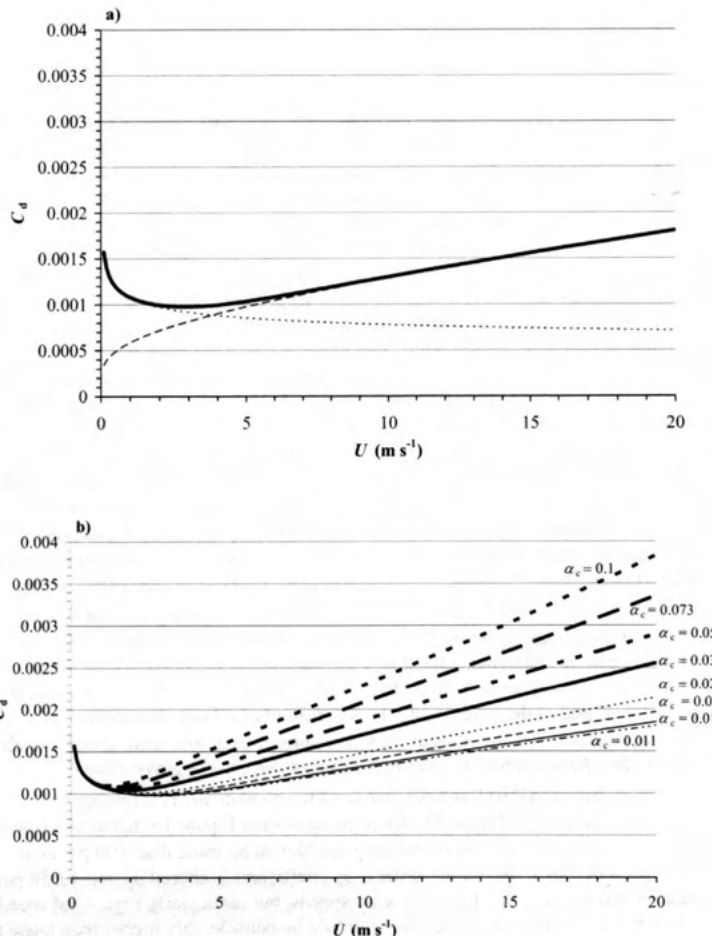


**Figure 1.** a) Variation of the neutral drag coefficient,  $C_d$ , with wind speed,  $U$ , for smooth flow (dotted line), just gravity waves (dashed line) and for smooth flow and gravity waves combined (solid line). b) Variation of the neutral drag coefficient with wind speed using a variety of values for the Charnock constant,  $\alpha_c$ , in Eqn 7.

The work by Vickers & Mahrt (1997) used results from a platform in the Baltic Sea approximately 2 km from the shore. The positioning of the platform enabled them to calculate drag coefficients from a variety of fetches. This allowed them to develop an empirical formula representing the effects of fetch on drag coefficients,

$$C_d = C_0(1 + a_0 \text{EXP}(-F_* / F_c)), \quad (8)$$

where,

$$F_* = (gX/u^*)^{1/3}$$

is non-dimensional fetch,  $X$  is dimensional fetch and  $a_0$  and  $F_c$  are empirical constants given the values 0.7 and 100, respectively.  $C_0$  is the drag coefficient for fully developed seas, using the  $\alpha_c$  value of 0.011, but assuming rough flow only. Eqns 8, 5 and 6 can be used to solve iteratively for

$z_0$ . Vickers & Mahrt (1997) assumed no smooth flow in their drag coefficients owing to the prevailing windy conditions during their experiment and calculated the variations in the drag coefficient caused by fetch accordingly. They did not explicitly calculate the implied variation in  $\alpha_c$  with fetch, but this can be done, the results being shown in Figure 2. Note that the value of  $\alpha_c$  varies with wind speed as well as with dimensional fetch as wind speed influences the value of non-dimensional fetch ( $F_*$ ). This variation is somewhat larger at low wind speeds than at high wind speeds.

As can be seen in Figure 1a, for moderate or low wind speeds the smooth flow is an important part of Eqn 7, but does not noticeably affect the values at high wind speeds. Such low wind conditions are more frequently observed over lakes than oceans as wind speeds themselves have frequently not increased to equilibrium values but are still influenced by the additional frictional drag of the surrounding countryside. Neutral drag coefficients can therefore be calculated by using  $\alpha_c$  as shown in Figure 2 but using Eqn 7 including the smooth flow approximation ( $\beta = 0.11$ ). Calculated in this manner, the neutral drag coefficients are appropriate for all, not just high, wind speeds. Results are shown in Figure 3a. Values can be seen to occupy the same range as shown in Figure 1b, with the drag coefficient at short fetches obtaining much higher values than those at large fetches. Thus, this formulation shows an appropriate variation in the drag coefficient with both fetch and with wind speed, for high and low wind speeds.

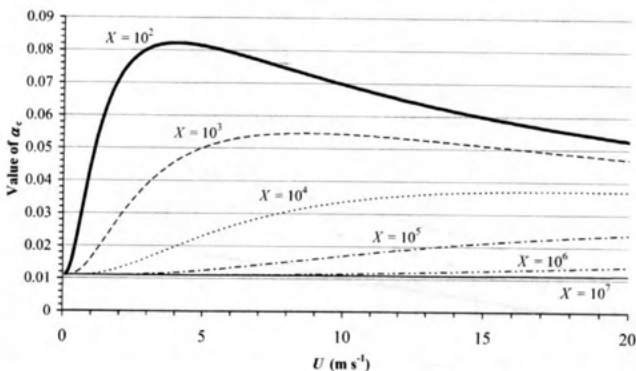


Figure 2. Variation of  $\alpha_c$  with wind speed for different fetches,  $X$ .

The current formulation requires a relatively complicated procedure for calculating  $\alpha_c$ . This can be simplified by noting firstly, that at low wind speeds smooth flow dominates the gravity waves in Eqn 7 and so the exact value of  $\alpha_c$  becomes unimportant and secondly, that in Figure 2 it can be seen that there is an increase in the value of  $\alpha_c$  with decreasing dimensional fetch. Away from low wind speeds this increase becomes quasi-systematic. An empirical equation can therefore be postulated that approximates  $\alpha_c$  as a function of dimensional fetch for all wind speeds. Such an empirical equation is,

$$\alpha_c = 0.01 + (1/1000)*(2^P), \quad (9)$$

where,

$$P = \text{LOG}_{10}(10^8/X).$$

Figure 3b compares values of  $C_d$  calculated using  $\alpha_c$  from Figure 2 with values of  $C_d$  calculated using  $\alpha_c$  obtained from Eqn 9. Clearly there is some deviation at very high wind speeds, but the discrepancy is nearly always less than ten per cent.

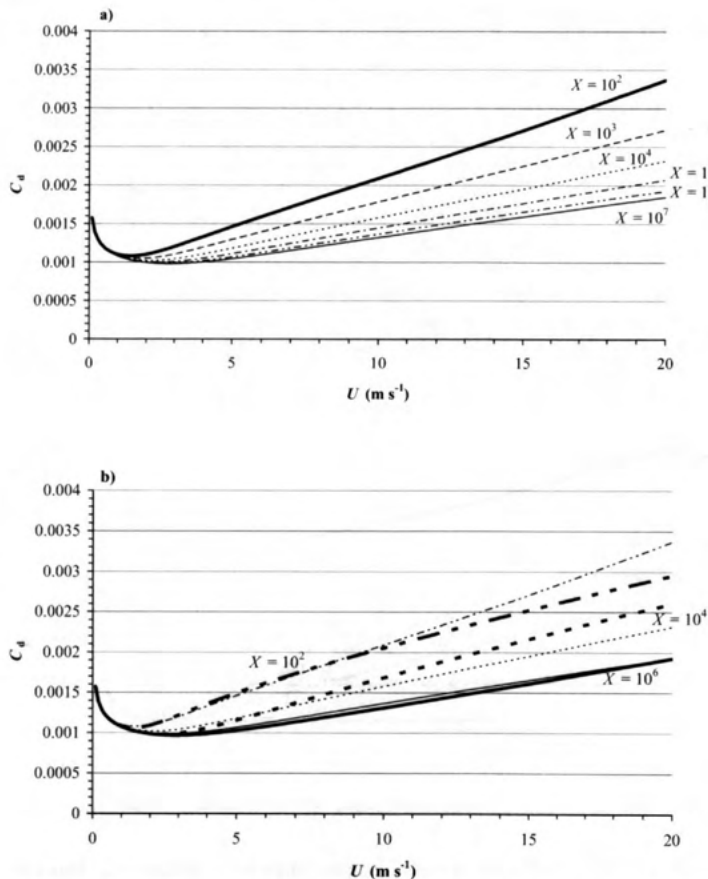


**Figure 3.** a) Variation of  $C_d$  with wind speed, including the smooth flow approximation, for different dimensional fetches. b) Comparison of  $C_d$  for different wind speeds and a selection of fetches from those shown in a) (thick lines) and those calculated using Eqn 9 (thin lines).

Thus, for given fetch,  $\alpha_c$  can be calculated from Eqn 9, the resultant  $\alpha_c$  can then be used in Eqn 7 from which an iterative calculation with Eqns 6 and 5 will give the neutral drag coefficient. This formula gives a transfer coefficient that decreases with increasing fetch, agrees with the open ocean value for high fetch, by virtue of  $C_o$  used in Eqn 8 and is consistent with the results for various reduced fetches from Vickers & Mahrt (1997). Furthermore, computationally it follows the same form, that is Eqn 7, that is commonly used for atmospheric calculations, excepting the simple extra step of initially calculating  $\alpha_c$  from Eqn 9. By incorporating an appropriate function for  $\Phi_m(z/L)$  in Eqn 1, and thus  $\Psi_m(z/L)$ , then using Eqn 4 rather than Eqn 6 allows stability corrections to be included in the calculation. This final formulation therefore allows a drag coefficient to be calculated that includes effects of stability, wind speed and fetch.

## Discussion

The formulation offered above gives a relatively straightforward way of calculating drag coefficients that are relevant for lakes rather than oceans. Given the range of values illustrated in Figure 1b, such a formulation could improve the accuracy of bulk formulae calculation for lakes considerably and by the order of 100 % when wind speeds are high.

There are a number of caveats. First and foremost, excepting the Vickers & Mahrt (1997) data from the Baltic, this formulation is based on theoretical manipulation rather than observation. It is imperative that results such as these be verified with actual observations taken over lakes of different sizes.

There are a number of other considerations, many of which are relatively more important for lakes than for oceans. Eqn 7 assumes roughness to be dependent on only smooth flow and gravity waves, whereas it is likely that capillary waves will also affect the roughness, as detailed by Alam & Curry (1997). Whilst many authors have discussed the link between wave-age, fetch and drag coefficients (e.g. Geernaert *et al.*, 1986; Donelan *et al.*, 1993; Smith *et al.*, 1996) not all authors are convinced by this. Indeed, Taylor & Yelland (2001) argue that, other than for very young waves, wave-age and fetch are irrelevant to the value of the drag coefficient, but the presence, or otherwise, of swell is important. The lack of swell in lakes, though, still implies the need for larger drag coefficients for lakes than for open oceans. For lakes, as opposed to oceans, shallowness becomes a relevant factor, as for sufficiently shallow water bodies waves heights are influenced by bottom topography. Parametrisation for shallow-water effects would therefore be a further requirement for many lakes. A general problem with all studies on transfer coefficients is that little beyond the smooth flow approximation has been established about their value in conditions of very low wind speed; studies that do exist suggest that they increase markedly in these conditions (Greenhut & Khalsa, 1995). Such wind speeds are more prevalent over lakes than oceans, owing to the surrounding topography. Variation over a lake surface is a further complication. The very idea of limited fetch implies that the fetch will be continuously changing across a lake. Therefore, transfer coefficients should be changing accordingly, implying use of a single value to cover a whole lake would be problematic.

## Conclusions

In the open ocean the drag coefficient is influenced by both wind speed and atmospheric stability. Even accounting for these effects, its exact value is not well known, particularly at low wind speeds. Over lakes, the effect of fetch-limitation also needs to be taken into account; not doing so is likely to result in severely underestimating the drag coefficient and thus the momentum flux. A formulation has been presented here that takes this fetch-limitation into account and reduces to open ocean values at high fetch. Whilst the paper has concerned itself with the momentum flux, the same arguments hold for the sensible and latent heat fluxes for which fetch limited transfer coefficients are also required. Testing of all such transfer coefficients against real lake data is a necessity.

## References

- Alam, A. and J. A. Curry. 1997. Determination of surface turbulent fluxes over leads in Arctic sea ice. *Journal of Geophysical Research*, **102**, 3331–3343.
- Blanc, T. V. 1985. Variation of bulk-derived surface flux, stability, and roughness results due to the use of different transfer coefficient schemes. *Journal of Physical Oceanography*, **15**, 650–669.
- Businger, J. A., J. C. Wyngaard, Y. Izumi and E. F. Bradley. 1971. Flux-profile relationships in the atmospheric surface layer. *Journal of the Atmospheric Sciences*, **28**, 181–189.
- Charnock, H. 1955. Wind stress on a water surface. *Quarterly Journal of the Royal Meteorological Society*, **81**, 639–640.
- DeStasio Jr, B. T., D. K. Hill, J. M. Kleinhans, N. P. Nibbelink and J. J. Magnuson. 1996. Potential effects of global climate change on small north-temperate lakes: Physics, fish and plankton. *Limnology and Oceanography*, **41**, 1,136–1,149.
- Donelan, M. A., F. W. Dobson, S. D. Smith and R. J. Anderson. 1993. On the dependence of sea surface roughness on wave development. *Journal of Physical Oceanography*, **23**, 2143–2149.

- Garratt, J. R. 1977. Review of Drag Coefficients over Oceans and Continents. *Monthly Weather Review*, **105**, 915–929.
- Garratt, J. R. 1992. *The atmospheric boundary layer*. Cambridge University Press. Cambridge, United Kingdom, 316 pp.
- Geernaert, G. L., K. B. Katsaros and K. Richter. 1986. Variation of the drag coefficient and its dependence on sea state. *Journal of Geophysical Research*, **91**, 7,667–7,679.
- George, D. G. 2000. The impact of regional-scale changes in the weather on the long-term dynamics of Eudaptomus and Daphnia in Esthwaite Water, Cumbria. *Freshwater Biology*, **45**, 111–121.
- George, D. G. and A. H. Taylor. 1995. UK lake plankton and the Gulf Stream. *Nature*, **378**, 139.
- Greenhut, G. K. and S. J. S. Khalasa. 1995. Bulk transfer coefficients and dissipation-derived fluxes in low wind speed conditions over the western equatorial Pacific Ocean. *Journal of Geophysical Research*, **100**, 857–863.
- Heikinheimo, M., M. Kangas, T. Tourula, A. Venäläinen and S. Tattari. 1999. Momentum and heat fluxes over lakes Tämnen and Räksjö determined by the bulk-aerodynamic and eddy-correlation methods. *Agricultural and Forest Meteorology*, **98**–**99**, 521–534.
- Hicks, B. B. 1971. Some evaluations of drag and bulk transfer coefficients over water bodies of different sizes. *Boundary-Layer Meteorology*, **3**, 201–213.
- Högström, U. 1988. Non-dimensional wind and temperature profiles in the atmospheric surface layer: a re-evaluation. *Boundary-Layer Meteorology*, **42**, 55–78.
- Hsu, S. A. 1986. A mechanism for the increase of wind stress (drag) coefficient with wind speed over water surfaces: a parametric model. *Journal of Physical Oceanography*, **16**, 144–150.
- Johnson, H. K., J. Hoejstrup, J. J. Vested and S. E. Larsen. 1998. Dependence of sea surface roughness on wind waves. *Journal of Physical Oceanography*, **28**, 1,702–1,716.
- Nordeng, T. E. 1991. On the wave age dependent drag coefficient and roughness length at sea. *Journal of Geophysical Research*, **96**, 7,167–7,174.
- Renfrew, I. A., G. W. K. Moore, P. S. Guest and K. Bumke. 2002. A comparison of surface layer and surface turbulent flux observations over the Labrador Sea with ECMWF analyses and NCEP reanalyses. *Journal of Physical Oceanography*, **32**, 383–400.
- Smith, S. D. 1988. Coefficients for sea surface wind stress, heat flux and wind profiles as a function of wind speed and temperature. *Journal of Geophysical Research*, **93**, 15,467–15,472.
- Smith, S. D., C. W. Fairall, G. L. Geernaert and L. Hasse. 1996. Air-sea fluxes: 25 years of progress. *Boundary-Layer Meteorology*, **78**, 247–290.
- Taylor, P. K. and M. J. Yelland. 2001. The dependence of sea surface roughness on the height and steepness of the waves. *Journal of Physical Oceanography*, **31**, 572–590.
- Vickers, D. and L. Mahrt. 1997. Fetch limited drag coefficients. *Boundary-Layer Meteorology*, **85**, 53–79.
- Winder, M. and D. E. Schindler. 2004. Climatic effects on the phenology of lake processes. *Global Change Biology*, **10**, 1,844–1,856.
- Wu, J. 1985. Parameterization of wind-stress coefficients over water surfaces. *Journal of Geophysical Research*, **90**, 9,069–9,072.

# INFLUENCE OF WEATHER ON LAKE TEMPERATURE AND THERMAL STRATIFICATION: A CASE STUDY BY MODEL SIMULATION FROM 1953–2004 ON THE DANISH LAKE ESRUM SØ

Rikke Margrethe Closter<sup>1,2</sup> and Annette Guldberg<sup>2</sup>

<sup>1</sup>Freshwater Biological Laboratory; University of Copenhagen, Helsingørsgade 51, DK-3400 Hillerød, Denmark. Corresponding author: [mcloster@bi.ku.dk](mailto:mcloster@bi.ku.dk)

<sup>2</sup>Danish Meteorological Institute, Lyngbyvej 100, DK-2100 Copenhagen, Denmark.

*Danish freshwater lakes are fully mixed in spring until an eventually temperature stratification occurs. The date of stratification, stratification strength and duration is a complex function of the external influence of weather especially wind and air temperature and internal factors such as depth, area, morphology and transparency. The thermal stratification separates heated less heavy surface water from colder and heavier bottom water, and almost no exchange of substances takes place between the two layers. Underneath the thermal stratification light conditions are usually insufficient for phytoplankton production, and so only oxygen consumption takes place. This can lead to severe anoxic conditions during stratification, as is the case for the Danish lake Esrum Sø.*

*In order to investigate the influence of weather on anoxic conditions in lakes it is important to be able to describe temperature and stratification trends. This can be done with a physical lake model, which combines the effects of external and internal factors. The 1-dimensional lake model PROBE has been setup for the Danish lake Esrum Sø. The model was forced with observed meteorological data from year 2001 and calibrated to observed logged temperature data from 6 depths. Subsequently the model was forced with observed meteorological data from 1953–2004. The 52 years of model output will be analysed with respect to monthly, seasonal and yearly trends in weather parameters, lake temperatures, and onset, duration and strength of thermal stratification. So far the analyses show that annual surface temperature has increased and bottom temperature decreased, which might indicate that strength in and duration of thermal stratification has increased.*

## *Introduction*

Danish freshwater lakes are fully mixed in spring until an eventually temperature stratification occurs. The thermal stratification separates heated less heavy surface water (epilimnion) from colder and heavier bottom water (hypolimnion), and almost no exchange of substances takes place between the two layers. The date of stratification, stratification strength and duration is a complex function of internal factors and the external influence of weather (Imberger 1985; Demers and Kalff 1993; Kalff 2002). When climate is changing it changes the energy transfer between the atmosphere and lake surface interface, and this might lead to altered mixing regimes in the lakes.

During stratification light conditions in the hypolimnion are usually insufficient for phytoplankton production. This means that there is no oxygen production in the hypolimnion and since the exchange of substances over the thermal stratification is non-existent only oxygen consumption takes place here. In many Danish lakes a large oxygen consuming sediment pool has been build up after years of pollution with nutrients from agriculture and urban industries. These large oxygen consuming sediment pools lead to anoxic conditions in the hypolimnion during stratification. If future climate changes alter the mixing regime of a lake it is possible that it will have serious consequences on the lake ecology. For

example has a Swedish lake model simulation forced with predicted future climate revealed, that elevated lake temperatures and changes in the mixing regime could result in increased nutrient cycling and lake productivity (Blenckner *et al.* 2002). It is therefore important to achieve detailed knowledge of the influence of weather on lake temperature and thermal stratification. This can be done with a physical lake model as for example the 1-dimensional lake model PROBE, which is forced with the standard meteorological parameters and describes physical conditions in the water like the vertically resolved lake temperature and the heat fluxes between the atmosphere and lake surface (e.g. Blenckner *et al.* 2002).

The aim of this study is to set up the lake model PROBE for analysis on the Danish lake Esrum Sø in the period 1953–2004. In order to describe changed tendencies during the 52 years of investigation the meteorological forcing parameters and the modelled lake surface and bottom temperatures will be analysed with measurements of monthly and annual means.

#### *Materials and Methods*

Lake Esrum Sø is located in Denmark which has a temperate climate. The lake has been subject for numerous investigations during the last 100 years (e.g. Berg 1938; Jónasson 1977) and regularly measurements of temperature profiles have been performed since 1953. Lake Esrum Sø covers an area on 17,29 km<sup>2</sup> and contains 233·10<sup>6</sup> m<sup>3</sup> water, which makes it to the lake that contains the largest amount of water and has the second largest area of lakes in Denmark (Høy og Dahl 1996). The maximum depth of Esrum Sø is 22,3 m, the mean depth 13,5 m and the lake has rather steep slopes with a large area of the lake bottom between 18–22 m (figure 1). The lake thermally stratifies in summer, and because of oxygen consumption in the hypolimnion and the sediment the hypolimnion gets anoxic

during the stratification period. In some winters the lake is covered by ice, but seldom the whole lake. Esrum Sø has a rather small upland area on 62 km<sup>2</sup> differentiated between 44% forest, 29% agriculture, 12% nature and 11% urban areas.

The physical lake-model PROBE has been applied to several case studies and is well documented (e.g. Omstedt and Rutgersson 2000; Rummukainen *et al.* 2000; Blenckner *et al.* 2002; Omstedt 2002; Svensson *et al.* 2002; Omstedt and Nohr 2004; and Sahlberg 2004). The equations are solved for lake Esrum Sø with a maximum depth of 22,5 m and an area-distribution described by the polynomial that made the best fit to the actual hypsographical curve ( $r^2 = 0,98$ ). The average light extinction coefficient during the period 1953–

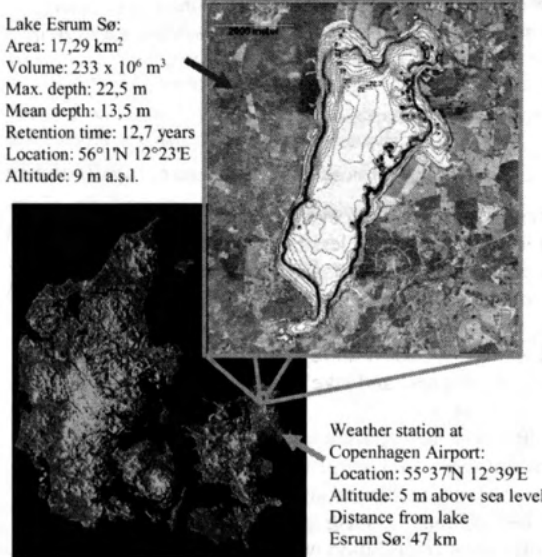


Figure 1: Location of lake Esrum Sø and the weather station.  
(© Kort & Matrikelstyrelsen, G. 15-03)

2004 is presumed to be on the same level as in year 2004, where it was  $0.5 (\pm 0.1) \text{ m}^{-1}$ . The turbulent mixing is described by a  $k-\varepsilon$  model, and mixing in hypolimnion during stratification is described by deep water mixing according to Stigebrandt (1987) and Omstedt (1990). Describing deep water mixing during stratification considerably improved the prediction of the bottom water temperature.

The meteorological forcing data has a time resolution of 3 hours and is from a weather station located 47 km from lake Esrum Sø (figure 1). The meteorological parameters used for the lake model simulations are air temperature at 2 m, relative humidity at 2 m, total cloudiness and the wind at 10 m in U- and V-components. The U- and V-components are calculated from wind speed and direction.

The lake model was calibrated with temperature measurements logged each hour in six depths during year 2001 by Klaus P. Brodersen (figure 2). The model output is correlated with the observed data in all 6 depths, but it should be noticed that the modelled temperatures are overestimated in the deeper layers on 15 and 20 m (figure 2). Observed data from 0.5–5 m are missing in some periods during summer, because temperatures above  $20.6^\circ\text{C}$  exceeded the data loggers capacity. The model output fills in for these missing data in a realistic manner. The data is furthermore verified with periodical temperature measurements performed by Petur M. Jónasson from 1953–1963 and by county Frederiksborg Amt from 1974–75, 1985–90, 1997–98 and 2001 (figure 3). Again the predicted surface temperatures are very close to the observed data. The modelled bottom temperatures also resemble the observed data, but are in some years especially during the 50ties overestimated.

In order to describe changed tendencies during the 52 years of investigation the meteorological forcing parameters and the modelled lake surface and bottom temperatures, stratification onset, length and strength will be analysed with measurements of monthly and annual means. So far has measurements of monthly and annual means been performed on the meteorological parameters and lake surface and bottom temperatures. The annual

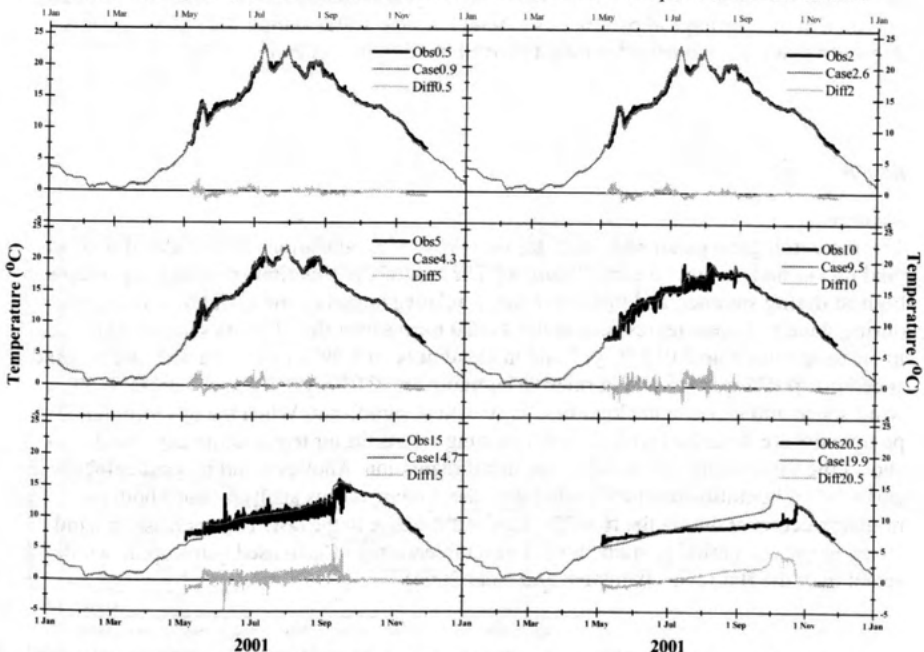


Figure 2: Lake temperatures 2001. The six figures represent each depth of logged data (black line), the closest corresponding depth from the model output (gray line), and the difference between model output and observed temperature (light grey line). The dataloggers had a maximum limit on  $20.6^\circ\text{C}$ .

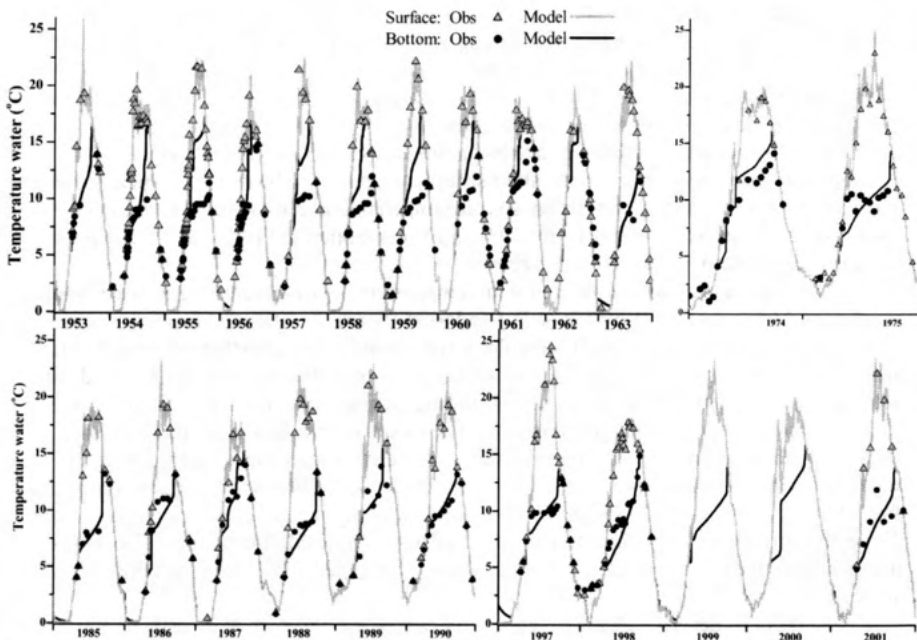


Figure 3: Lake temperatures 1953-63, 1974-75, 1985-90, 1997-98 and 2001. The figures shows surface and bottom temperatures from periodically observed data and model output.

means are analysed with linear regression and 15 years running means. Since 90% of the variance in meteorological parameters is found in time scales shorter than 15 years, it is expected that this time period shows a general trend (Omstedt *et al.* 2004).

## Results

### Weather

The meteorological parameters used for the lake model simulations are presented with annual means and monthly means (figure 4). The monthly means show that air temperature is highest during summer, and that wind speed, relative humidity and cloudiness is highest during winter. Linear regression on the annual means over the 51 years shows an increase in air temperature on  $0.013 \text{ }^{\circ}\text{C yr}^{-1}$  and in cloudiness on  $0.09\% \text{ yr}^{-1}$ , and a decrease in wind speed on  $-0.027 \text{ m/s yr}^{-1}$  and in relative humidity on  $-0.02\% \text{ yr}^{-1}$ . Only the decrease in wind speed and increase in cloudiness is statistically significant. When the meteorological parameters are described with 15 years running means the air temperature and cloudiness shows the same increasing trend as the linear regression. Another trend in wind velocity and relative humidity becomes visible with the running means analysis, since both parameters decrease during the first 25 years and increase in the last. This increase in wind speed in the last period is in line with a general tendency of increased geostrophic wind speed over the Baltic Sea (Omstedt and Nohr 2004).

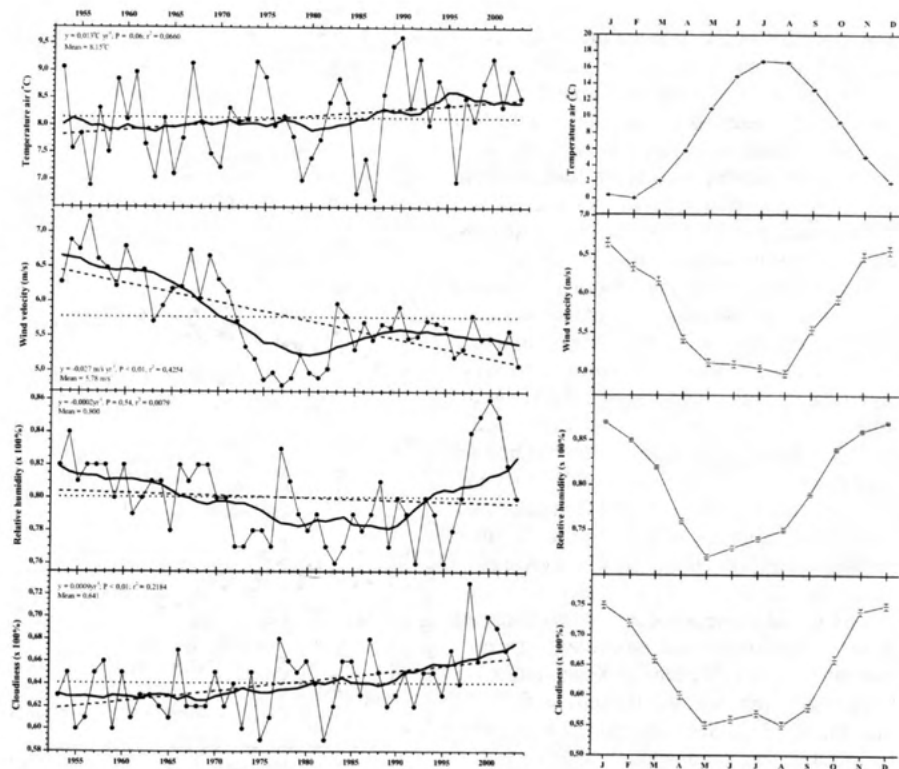


Figure 3: Meteorological parameters from the weather station 1953-2003. Yearly means (left) with 15 years running means (solid line), linear regression (dashed line) and average value (dotted line). Monthly means (right) shows the average value of each meteorological parameter each month during the 51 years and 95% confidence interval.

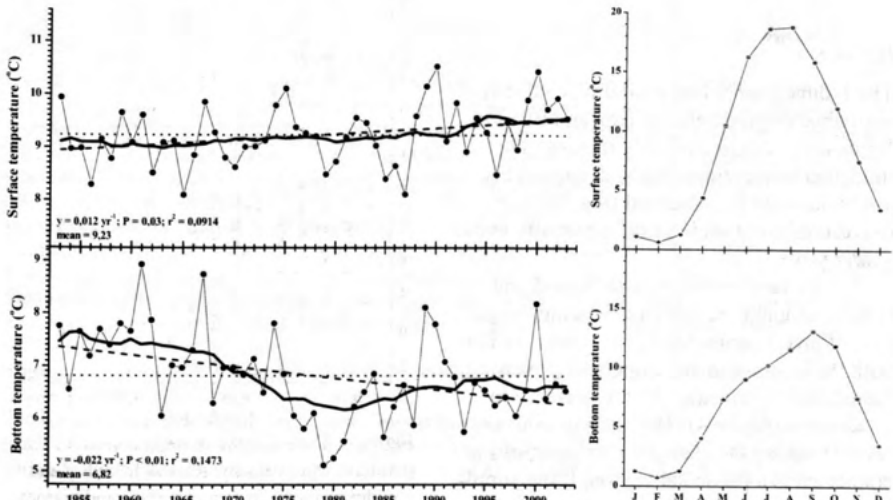


Figure 5: Lake parameters from the model simulation. Yearly means (left) with 15 years running means (solid line), linear regression (dashed line) and average value (dotted line). Monthly means (right) shows the average value of each parameter each month during the 51 years and 95% confidence interval.

### Lake temperature

The modelled surface and bottom temperatures are presented with annual and monthly means (figure 5). The average monthly surface temperature peaks in August with 18,9 °C, and has the lowest value in February on 0,6 °C. The monthly bottom temperature also has the lowest value in February on 0,7 °C, but the highest temperature on 13,2 °C occurs a month later in September compared to highest surface temperature. During the period of investigation annual means of the surface temperature increases significantly with 0,012 °C yr<sup>-1</sup> and the bottom temperature decreases significantly with -0,022 °C yr<sup>-1</sup>. The 15 years adjacent averaging illustrates the same trend for the surface temperature, but for the bottom temperature another trend is revealed, since it decreases the first 25 years and then increases.

The influence of annual mean weather parameters on lake surface and bottom temperatures are analysed with linear regression (figure 6). Likewise is the influence of surface water temperature on bottom water temperature investigated. The annual mean bottom temperature increases significantly with annual means of surface water temperature, air temperature and wind velocity (figure 6). Only the air temperature has a significant influence on the surface water temperature.

### Discussion

The 1-dimensional lake model was validated with observed temperature data and filled in for missing data in a reliably manner. The modelled temperatures in the deeper layers also resembled the observed data, but were overestimated in some years, especially in the yearly years.

Surface temperature increased and bottom temperature decreased during the period of investigation (figure 5). This is in line with the increase in air temperature, even though not significant, and the decrease in wind speed (figure 4). The analysis does not reveal whether the change in temperatures is connected to a particular season. If the simultaneous increase in surface temperature and decrease in bottom temperature is connected to the summer period, then thermal strata-

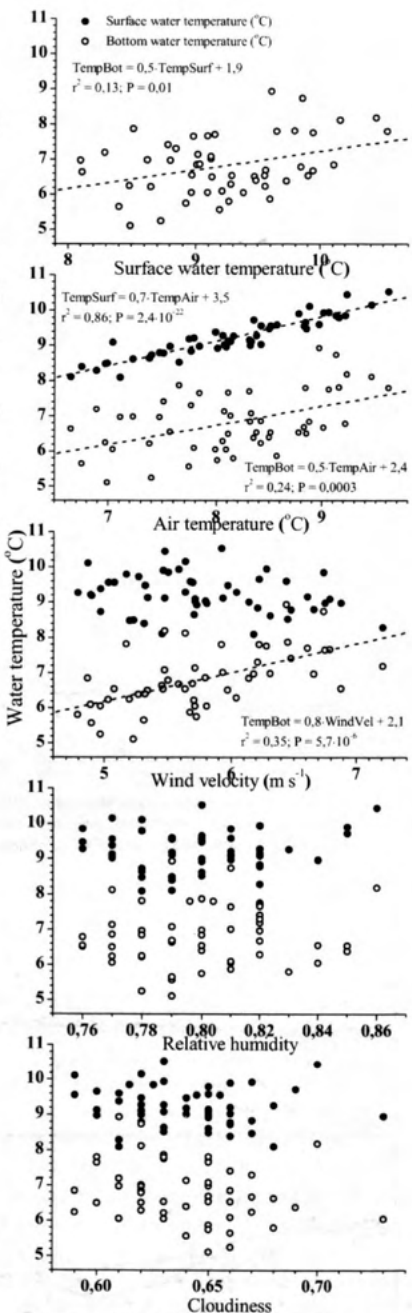


Figure 6: The influence of mean annual air temperature, wind velocity, relative humidity and cloudiness on mean annual surface and bottom water temperatures.

tion has become stronger and the duration of stratification has increased. Since the hypolimnion gets very low in oxygen during stratification, this may lead to serious ecological consequences.

The annual mean wind velocity had a positive influence on annual mean bottom water temperature, and had no significant influence on the surface water temperature. Both surface and bottom water temperature increases with air temperature. This shows that the surface water temperature is directly connected to the atmosphere through heat fluxes, were air temperature has the greatest influence of the weather parameters. The annual mean bottom water temperature is more complex, because it is dependent on the temperature in the water column at onset of stratification, stratification strength and duration. Further investigation is expected to reveal if there has been any changes in these parameters during the period of investigation and if changes have been connected to a particular season.

#### *Acknowledgement*

I am greatly thankful to Petur M. Jónasson; Klaus P. Brodersen and county Frederiksborg Amt for providing me with temperature data.

#### *References*

- Berg, K. (1938). Studies on the bottom animals of Esrom Lake. *Det Kongelige Danske Videnskabers Selskabs Skrifter*. 9 R. 8: 1–255.
- Blenckner, T.; Omstedt, A. and Rummukainen, M. (2002). A Swedish case study of contemporary and possible future consequences of climate change on lake function. *Aquat. Sci.* 64: 171–184.
- Demers, E. og Kalff, J. (1993). A simple model for predicting the date of spring stratification in temperate and subtropical lakes. *Limnol. Oceanogr.* 38: 1077–1081.
- Høy, T. og Dahl, J. (1996). Danmarks Søer – Søerne i Frederiksborg Amt. Strandbergs Forlag. Denmark.
- Imberger, J. (1985). The diurnal mixed layer. *Limnol. Oceanogr.* 30: 737–770.
- Jónasson, P. M. (1977). Lake Esrom Research 1867–1977. *Folia Limnologica Scandinavica*. 17: 111–123.
- Kalff, J. (2002). Limnology. Prentice Hall. New Jersey, United States of America.
- Omstedt, A. (1990). Modelling the Baltic Sea as thirteen sub-basins with vertical resolution. *Tellus*. 42A: 286–301.
- Omstedt, A. (2002). Introduction to lake and ocean modelling. *A compendium from Department of Earth Sciences-Oceanography, Göteborg University, Sweden*.
- Omstedt, A. and Nohr, C. (2004). Calculating the water and heat balances of the Baltic Sea using ocean modelling and available meteorological, hydrological and ocean data. *Tellus*. 56A: 400–414.
- Omstedt, A.; Pettersen, C.; Rodht, J. and Winsor, P. (2004). Baltic Sea climate: 200 yr of data on air temperature, sea level variation, ice cover, and atmospheric circulation. *Climate Research*. 25: 205–216.
- Omstedt, A. and Rutgersson, A. (2000). Closing the water heat cycles of the Baltic Sea. *Meteorologische Zeitschrift* 9: 59–66.
- Rummukainen, M.; Räisänen, J.; Bringfelt, B.; Ullerstig, A.; Omstedt, A.; Willén, U.; Hansson, U. and Jones, C. (2000). A regional climate model for northern Europe: Model description and results from the downscaling of two GCM control simulations. *Climate Dynamics*. 17: 339–359.
- Sahlberg, J. (2004). Physical control of primary production in a sub-arctic reservoir. *Department of Water and Environmental Studies, Linköping University. S-581 83 Linköping, Sweden. ISBN: 91-7373-949-9*
- Stigebrandt, A. (1987). A model for the vertical circulation of the Baltic deep water. *J. Phys. Oceanogr.* 13: 411–427.
- Svensson, U.; Axell, L.; Sahlberg, J. and Omstedt, A. (2002). PROBE. Program for boundary layers in the environment. System description and manual. Version 2002. Available from Sahlberg, J. and Omstedt, A. (*The older version from 1998: SMHI report RO 24, SMHI, Norrköping, Sweden*).



## Studies of Physical Processes in Lake Erie

**Yerubandi R. Rao**

Environment Canada

National Water Research Institute

867 Lakeshore Road, Burlington, Ontario, L7R 4A6

Canada

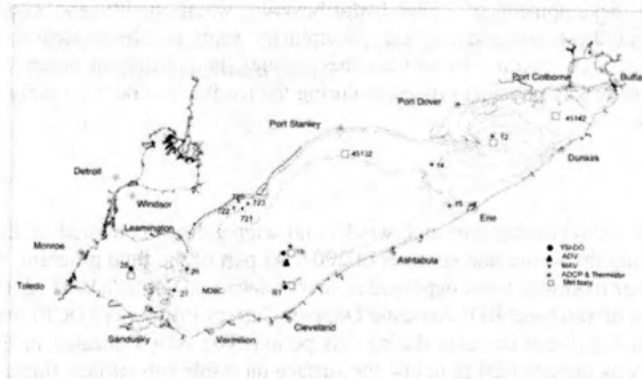
Email: Ram.Yerubandi@ec.gc.ca

### Abstract

Physical processes relevant to water quality in Lake Erie during summer stratified season are discussed in this paper. Currents, water temperature, winds, radiation and waves were recorded at fixed moorings in Lake Erie from April 2004 through October 2004. Surface winds and heat flux components were computed from the meteorological buoy observations in each of the three basins. Circulation within and between the basins were studied. The thermal structure and exchange processes during summer stratification in Lake Erie have also been examined using a time series data of horizontal velocity profiles from broadband ADCPs and temperature profiles from thermistor moorings.

### Introduction

Lake Erie is located between the US and Canada. By volume it is the smallest, and by surface area it is the second smallest lake in the Great Lake system (Fig. 1). The physical characteristics of Lake Erie directly influence the functioning of the lake ecosystem to various stressors. As the shallowest of the Great Lakes, it warms quickly in the spring and summer and cools quickly in the fall. The shallowness of the basin and the warmer temperatures make it the most biologically productive of the Great Lakes.



stratification in the shallow western basin is rare and very brief. Stratification impacts the internal dynamics of the lake, physically, biologically and chemically. These physical characteristics cause the lake to function as virtually three separate lakes. Eighty percent of Lake Erie's total inflow of water comes through the Detroit River. The remaining comes from precipitation and other tributaries flowing directly into the lake. The Niagara River is the main outflow from the lake.

Lake Erie is exposed to the greatest stress from urbanization, industrialization and agriculture from both the US and Canada. About one-third of the total population of the Great Lakes basin resides within the Lake Erie watershed. Eutrophication during 1950s to the 1970s caused anoxic conditions in the central basin. Phosphorus was deemed to be the main culprit. A comprehensive binational phosphorus reduction strategy was implemented to reduce phosphorus discharge from wastewater treatment plants and limit the use of phosphorus containing detergents in the watershed. The hoped-for elimination of low oxygen in the central basin hypolimnion has not occurred. Relatively large increases in nitrogen continue. Recently, a decrease in phosphorus concentrations around 1995 has been reversed as concentrations have rebounded through 2000-2001 (Charlton and Milne, 2004). The introduction of zebra mussels in the late 1980s triggered a tremendous ecological change in the lake. Zebra mussels have changed the habitat in the lake, altering the food web dynamics, energy transfer and how nutrients and contaminants are cycled within the lake ecosystem.

The last major physical experiments conducted in Lake Erie were Project Hypo in 1970 (Burns and Rosa, 1972) and the Lake Erie Bi-National Investigation in 1979/80 (Boyce et al. 1987). These were intensive investigations that resulted in better understanding of the dynamics of the lake thermal regime, circulation and inter-basin transports applied to water quality problems in the lake. Application of water quality models suggest that simulations of nutrients and dissolved oxygen are diverging from the observations (Lam et al. 2002). This suggests that there may be very real effects that can be attributable to the influence of invasive species like zebra mussels and climate change. To resolve these pressing issues there is a critical need for better estimates of lake circulation, thermal structure and mixing to support further development of lake hydrodynamic, water quality and ecosystem models. Because of these concerns a multi-disciplinary team has been formed in the National Water Research Institute to address these issues. In the present paper we will discuss observations of key physical processes during the ice-free period from early spring to late fall of 2004.

### **The Experiment**

The measurements for obtaining currents, winds, and temperatures consisted of Eulerian measurements during the spring and summer of 2004. As part of the field program, current meter and thermistor moorings were deployed at several locations in the lake (Fig. 1). Five broadband and one narrowband RDI Acoustic Doppler Current Profilers (ADCP) provided vertical profiles of horizontal currents during this period. The ADCP located in the east basin (station 12) was mounted 20 m below the surface on stable sub-surface floats facing up and the rest are installed at the bottom facing up. The ADCP deployed at station 14 also measured the wave conditions. In addition to ADCPs, single point current meters (Nobska-MAVS) at sub-surface (10 m) were deployed at four locations. The accuracy of all these measurements is of considerable significance in the analysis. The current speed measurements are accurate to the order of  $0.3 \text{ cm s}^{-1}$  for MAVS,  $0.25 \text{ cm s}^{-1}$  for ADCPs, whereas directions are accurate to  $\pm 2^\circ$  for both types of instruments. The data return of currents from ADCPs was excellent; however, the data from one point current meters is

not complete because of the directional problems encountered in the deployment. In the central basin at 23-m depth a current measuring system, Sontek-Acoustic Doppler Velocimeter (ADV) was deployed. This instrument provided high frequency current information every three hours during the deployment. It has been used to estimate the wave conditions in the central basin.

Water temperature data were obtained from six moorings with thermistors deployed at 1-3 m intervals in the epilimnion, and at a lesser frequency (5 m) in the bottom waters. Apart from this water temperature was also obtained from the current meters and the ADCP instrument location at the bottom. The different temperature sensors used in the experiment yielded an accuracy of temperature from  $\pm 0.002^{\circ}\text{C}$  to  $\pm 0.2^{\circ}\text{C}$ . Three meteorological buoys, one in each basin of the lake provided the wind and radiation data. The incoming and net radiations were measured with Eppley pyranometers and radiometers. Apart from these meteorological data were also obtained from NDBC and Environment Canada (EC) real-time buoy network. The experiment also consisted of several joint EC and USEPA surveillance cruises measuring the water quality parameters from research vessels during the whole season.

### Meteorological observations

The variability of currents is determined by prevailing winds over the lake. As an example the wind measurements at station 19 have been presented as approximate meteorological forcing during this period. The wind stress was obtained from the quadratic law given as  $\tau = \rho_a C_d |W|W$ , where  $\rho_a = 1.2 \text{ kg m}^{-3}$  is the air density,  $W$  is wind velocity. In general, drag coefficient  $C_d$  increases with the wind speed and estimated as  $C_d = (0.8 + 0.065 W) \times 10^{-3}$  for  $W > 1 \text{ m s}^{-1}$ . A low-pass filter, using a 24-h period for the cut-off, was used to remove the high frequency information in the wind stress (Fig. 2a). The filtered time series has peaks of over  $0.2 \text{ N m}^{-2}$  during some episodes, usually associated with easterly storms towards the end of the summer. The winds were moderate during the rest of the experimental period, except on day 252. On this day, strong easterlies blew over the entire lake. The surface heat flux is calculated as a balance between the heat sources and sinks. Figure 2b shows the hourly (thin curve) and daily averaged (thick curve) surface heat flux during the experimental period. The daily averaged heat flux ranged from  $-258 \text{ W m}^{-2}$  to  $191 \text{ W m}^{-2}$  during this deployment period.

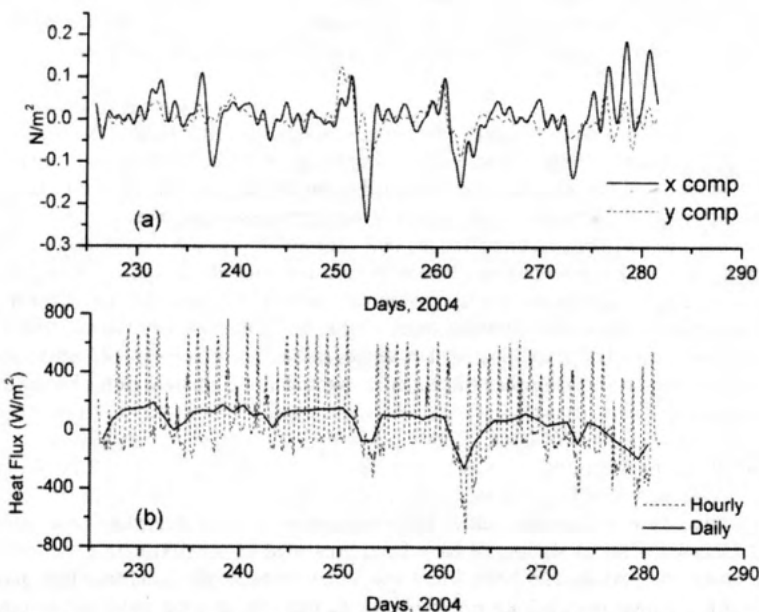


Fig 2: The time series of wind stress and surface heat flux at station 12 during summer.

### Currents and Thermal Structure

Mean circulation in Lake Erie during summer were discussed in earlier contributions (Saylor and Miller, 1987). These investigations revealed large scale lake response to prevailing meteorological forcings. However, these studies were based on data with coarse vertical resolution. In this section, by using a time series of horizontal velocity and temperature profiles, we provide some examples of the variability of circulation and thermal structure during the summer at selected stations in the east basin and in the Pennsylvania channel in Lake Erie. Figures 3a &3b show temperature ( $^{\circ}C$ ) obtained in the east basin at station 12. The mean temperature decreases as we go to deeper layers. In 2004 stratification was established by the middle of June (Day 165) and persisted till the middle of September (Day 262). During the early stratification the thermocline was located at 10-12 m below the surface. Once the full stratification was established in the summer, the thermocline migrated to 20 m or so. Comparison of temperature (Fig 3b) and wind stress (Fig 2a) time series reveals that upwelling and downwelling of the thermocline correspond to north-eastward and westward winds (Days 230 to 238).

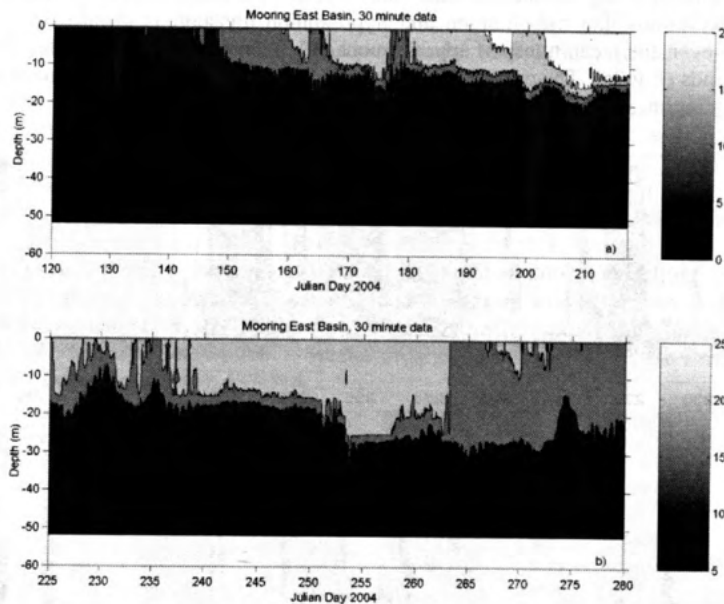


Fig 3: Time series of vertical thermal structure in the east basin during spring and summer seasons.

Typical plots of clock-wise and anti-clockwise rotary spectra of currents at all ADCP bins are plotted in Figures 2a and 2b, respectively. In general the spectra are characterized by a flat peak around 4-6 days (0.01 cph) and a spectral minimum around 24-30 hours. The dominant peak near 17-18 hr corresponds to the near-inertial period of Lake Erie. The near-inertial oscillations are characteristic feature of summer stratification and are observed to be intermittent. The spectral minimum at 24 to 30 hours is a characteristic feature of energy transfer from large scale lake wide circulation to small scale oscillations.

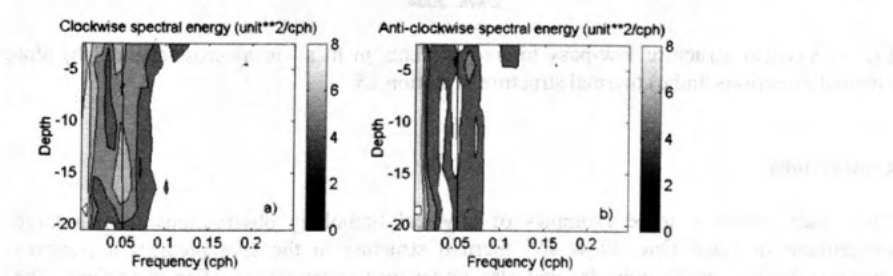


Fig 4: Rotary spectra of currents at station 15.

The transport of cold, oxygenated hypolimnion water from the eastern to the central basin has been considered as a possible oxygen renewal mechanism for the central basin bottom waters (Burns and Rosa, 1972; Boyce et al., 1987). Figures 5a to 5c show the variations of low-pass filtered currents and temperature at a station in the Pennsylvania channel. The two-

layer structure of along-channel currents can be seen on a few occasions supporting the earlier observations that mesolimnion and hypolimnion transport is towards the central basin. However, the mean transport appears more or less unidirectional and follows along-the-lake winds (Fig 2a). The current reversals associated with winds were common during the summer regime, with each episode on average lasting for 4-6 days.

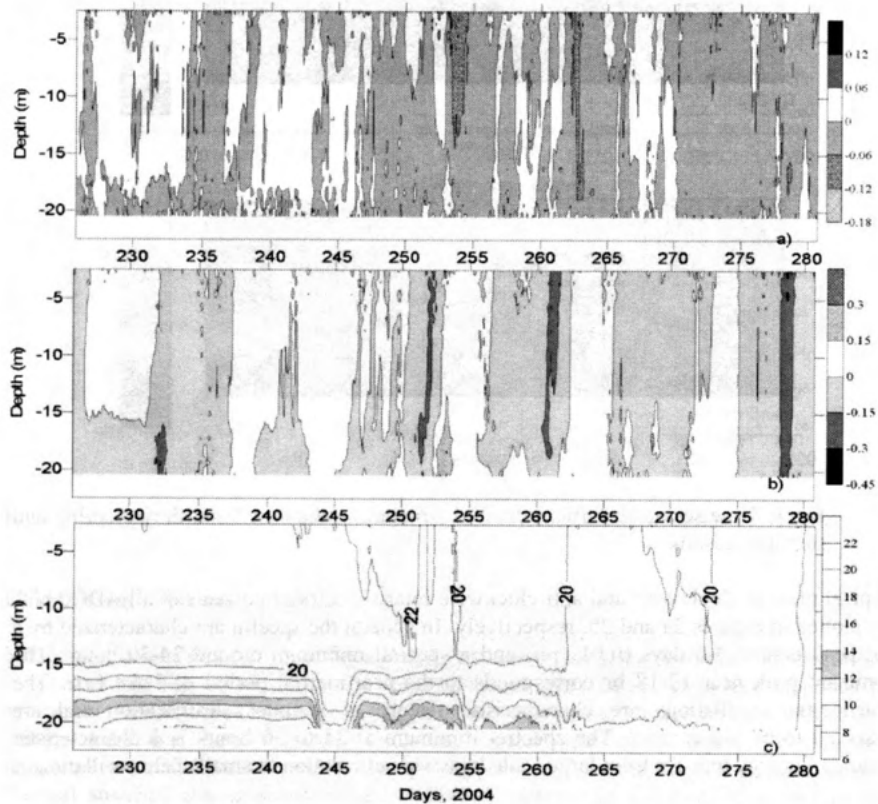


Fig 5: Vertical structure low-pass filtered currents in  $\text{m s}^{-1}$  in a) cross-channel b) along channel directions and c) thermal structure at station 15.

## Conclusions

This study presents some examples of physical limnology observations from a large experiment in Lake Erie. Flow and thermal structure in the lake presents a complex scenario during certain episodes and also under mean summer stratified conditions. The time series of vertical structure of along-channel currents and temperature in the Pennsylvania channel showed strong influence of along-the-lake winds, and two-layer structure probably associated with return currents due to surface and internal pressure gradients. Further studies using the complete data base and non-linear numerical models to investigate the circulation and mixing are in progress.

## References

- Boyce, F.M. et al. 1987, Lake Erie Binational Study :1979-1980 (Special issue), *J. Great Lakes Res.*, 13 (4).
- Burns, N. M. and C. Rosa, 1972, Project Hypo: An intensive study of Lake Erie central basin hypolimnion and related surface water phenomena. Paper No. 6, National Water Research Institute, Canada Centre for Inland Waters, Burlington, Ont.
- Charlton, M.N. and J. Milne, 2004, Review of thirty years of change in Lake Erie water quality, NWRI contribution No. 04-167, National Water Research Institute, Burlington, Ont.
- Lam, D.C.L., W.M. Scherzter and R.C. McCrimmon, 2002, Modelling changes in phosphorous and dissolved oxygen pre- and post-zebra mussel arrival in Lake Erie, NWRI contribution No. 02-198. National Water Research Institute, Burlington, Ont.
- Saylor, J.H. and G.S. Miller, 1987, Studies of large-scale currents in Lake Erie, 1979-80, *J. Great Lakes Res.*, 13(4), 487-514.



# Wind profile restructuring due to the roughness reduction in land-water transition

M. De Marchis<sup>1</sup>, J. Józsa<sup>2</sup>, B. Milici<sup>1</sup> and E. Napoli<sup>1</sup>

<sup>1</sup>Department of Hydraulic Engineering and Environmental Applications, University of Palermo, Italy

<sup>2</sup>Department of Hydraulic and Water Resources Engineering, Budapest University of Technology and Economics, Hungary

## Abstract.

A finite-volume numerical model is employed to investigate the adaptation of the atmospheric boundary layer to a change in the underlying surface roughness, like that existing in the transition from the land to the free surface of a water body. Numerical results are validated by comparison with neutral-stratification atmospheric data and compared with the IBL heights computed using a number of existing empirical formulae. The numerical analysis allows to extend the fetch range in which the existing formulae, calibrated only by comparison with short fetch data, may be applied. An argument is offered that the spatial variability of the water surface roughness should be also taken into account if the IBL development over the surface of a water body is analysed.

## 1. Introduction

The earth's surface presents irregular, often patchy surface properties for atmospheric flows. When boundary layers are advected over a boundary with different surface conditions, equilibrium with the underlying surface is disturbed and the near-surface part of the mean airflow profile accelerates or decelerates according to the change in its properties including, in general, surface roughness, temperature, humidity as well as surface flux of heat or moisture. The region of the atmospheric boundary layer adjacent to the surface affected by these changes, termed the Internal Boundary Layer (IBL), develops over the new condition, growing in height with downstream distance. The development and the main characteristics of IBLs were extensively described in the literature. For extensive reviews one is referred to Garratt (1990, 1992).

A particular situation occurs when air masses flow from land to the free surface of a water body experiencing significant moisture and occasional temperature differences and an abrupt reduction in the surface roughness due both to waves of limited height compared to that of the elements making up the land roughness and to the wave mobility, generally in the same direction of the air motion, thus reducing difference between the wind speed and the roughness elements at the shearing interface. In this paper IBL development due to mechanical turbulence will be analysed without any attempt to include moisture and thermal properties, the latter giving rise to the so called Thermal Boundary Layer.

The abrupt change in the surface roughness at the shoreline results in fetch dependent wind speeds and correspondingly in a fetch dependent shear stresses distribution over the free surface, which significantly influences the flow field in the water basin. To take into account the effects of the wind field fetch dependence some semi-empirical models have been proposed in the past, which allow to obtain the near-surface wind speed profile restructuring from the knowledge of the IBL height and from the estimate of the water surface roughness (Taylor and Lee, 1984; Józsa, 2004).

A lot of formulae were proposed which allow to predict IBL height in neutrally stratified flow (for a review see Garratt, 1990 and Savelyev and Taylor, 2005). Most of these formulae were calibrated by comparison with wind tunnel and atmospheric data sets dominated by short-fetch range data (Walmsley, 1989) thus restricting the fetch range in which they may be applied. It should be useful, therefore, trying to understand how the formulae perform for medium and large fetches with particular attention to the land-water transition case characterised by a non-constant downwind surface roughness, the description of which depends on air-water interaction conditions.

Supporting analytical and experimental analysis with numerical modelling can, moreover, provide a better understanding of IBL features. In order to do it, in this paper IBL response to a step reduction in surface roughness is treated through numerical simulations, and steady-state solutions are obtained using an in-house finite-volume code which adopts a fractional-step method for the time advancement towards the steady-state. For a detailed description of the numerical code, which is not provided in this paper, see Cioffi et al. (2005).

In the following section the results of the numerical simulation of the IBL development downwind of an abrupt, step-like reduction in surface roughness are reported together with their comparison with the results predicted by some of the most popular formulae suggested in literature. Section 3, introduces a semi-empirical treatment of the Internal Boundary Layer developing over the free surface of a water body, shows the results of the numerical simulations and draws conclusions about which of the previously reviewed formulae adapt better to the case of non-constant downwind roughness.

## 2. Numerical simulations and comparison with experimental data and IBL height empirical formulae

A number of formulae were proposed to compute the IBL height downwind of a step-change in surface roughness in neutrally stratified flow, a compendium of which is presented by Savelyev and Taylor (Savelyev and Taylor, 2005). All the formulae allow to obtain the IBL height as a function of the distance downwind of the roughness change and, in most cases, that of both the upwind and downwind roughness, although in some of them only the upwind or the downwind roughness is used. Walmsley (1989) evaluated the accuracy of the most recognised formulae by comparison with wind-tunnel and short fetch atmospheric data sets, showing that the Panofsky-Dutton formula gives better agreement than the others to evaluate the IBL height. More recently, nevertheless, other notable formulae have been proposed (see Savelyev and Taylor 2001, 2005) which have shown a good agreement with experimental data sets.

Since we are mainly interested in land-water transition, in order to validate the numerical code and to evaluate which formulae apply better to the observed data for surface roughness reduction, in this paper we consider a selected set from Walmsley's data consisting only of rough-to-smooth atmospheric experiments, leaving out both smooth-to-rough and wind-tunnel measurements. Table I summarizes for each of the selected cases the  $z_{01}$  and  $z_{02}$  aerodynamic roughness upwind and downwind, respectively.

To model the air flow the Reynolds averaged continuity and momentum equations were solved, which in the conventional summation approach can be written as:

$$\frac{\partial \bar{u}_i}{\partial t} + \frac{\partial \bar{u}_i \bar{u}_j}{\partial x_j} - \nu \frac{\partial^2 \bar{u}_i}{\partial x_j \partial x_j} + \frac{1}{\rho} \frac{\partial \bar{p}}{\partial x_i} + \frac{\partial \bar{u}_i \bar{u}'_j}{\partial x_j} + g \delta_{ij} = 0; \quad \frac{\partial \bar{u}_i}{\partial x_i} = 0 \quad (1)$$

where  $t$  is time,  $\bar{u}_i$  is the  $i$ -th component of the time-averaged velocity (the bar denoting averaged quantities and the prime turbulent fluctuations),  $x_i$  the  $i$ -th axis (with the axis  $x_3$  vertical and oriented upward),  $\nu$  is the kinematic viscosity,  $\rho$  is the air density,  $p$  is the pressure,  $g$  is acceleration due to the gravity,  $\delta_{ij}$  is the Kronecker function and  $\bar{u}'_i \bar{u}'_j$  are the auto- and cross-covariances between fluctuating velocities components.

In this work the Smagorinsky model was used to represent the horizontal Reynolds stresses, while a two-equation  $k-\epsilon$  turbulence model was used to obtain the vertical Reynolds stresses.

2D numerical simulations in the streamwise vertical plane were performed using an in-house code second-order accurate both in time and space. A fractional-step method is used for the time advancement, to overcome the incompressible pressure-velocity decoupling. For a detailed description and validation of the numerical code, which is not provided in this paper, the reader is referred to Cioffi et al. (2005). Numerical results were obtained considering the atmosphere

Table I. Summary of experimental data used for comparison together with the dimensions of the computational domain in the streamwise ( $L_1$  and  $L_2$  upwind and downwind of the roughness change, respectively) and vertical directions (H).

Source	$z_{01}$ (mm)	$z_{02}$ (mm)	$L_1$ (m)	$L_2$ (m)	H(m)
Angle (1973)	120.0	10.00	50	200	20
Bradley (1968, spikes to tarmac)	2.5	0.02	20	80	10
Bradley (1968, grass to tarmac)	5.0	0.02	20	80	10
Cherrywood (trees to grass)	219.0	4.40	100	500	20
Cherrywood (trees to snow)	293.0	0.68	100	500	20

under neutral stability and the motion of the air flow as that of an incompressible fluid. In the simulation it was assumed that semi-infinite horizontally homogeneous surfaces border each other along a straight line, so that the problem can be considered as two-dimensional (plane flow).

For each of the selected cases of comparison we adopted a rectangular domain which was discretised using  $64 \times 64$  cells in the streamwise direction of the acting wind,  $x_1$ , and in the vertical direction,  $x_3$ , respectively, with a refinement of the grid both streamwise near the roughness change section and vertically near the bottom. Table I shows the dimensions of each domain for the performed simulations. As inflow condition we assumed velocity, eddy viscosity, dissipation and kinetic energy distributions obtained from numerical simulations performed in a domain with a single bottom roughness like the one of the upwind surface ( $z_{01}$ ) and periodic boundary conditions in the streamwise direction. The free slip condition was used for the lateral boundaries (actually, the employed code resolves the equations in a 3D domain with one cell only in the spanwise direction) while the logarithmic wall-law was implemented at the bottom and null normal derivatives at the upper and downwind boundaries.

Numerical simulations give results in terms of wind speed field allowing us to calculate the IBL height by comparing wind speed profiles that belong to upwind and downwind regions: in this paper we consider as IBL height the one where the profiles differ not more than 1%.

Figure 1 compares calculated, both numerically and by the application of the most widely accepted formulae, and observed values of IBL heights on a plot directly.

Of the existing formulae we considered only six of them: Elliott's formula, 1958 (one of the earliest formula used to calculate IBL height); Panofsky's, 1973; Jackson's, 1976; Panofsky's and Dutton's, 1984; the one proposed by Savelyev and Taylor in 2001 (Savelyev and Taylor, 2001) and its modification derived in 2005 (Savelyev and Taylor, 2005). The above mentioned formulae are summarized in table II, where the IBL height is  $\delta$  and the distance downwind of the roughness change is  $F$ .

Figure 1 clearly indicates that the numerical results fits well to the atmospheric data set. Table III confirms the qualitative assessment of Figure 1 introducing quantitative comparisons with observed heights through the computation of RMS absolute and percentage errors.

It can be seen that the numerical code gives the lowest root-mean-square percentage error, together with the Jackson's formula, and an RMS absolute error equal to that of Savelyev-Taylor's form recently proposed and second in magnitude only to that of Jackson's without a great difference among these three values. So these results confirm the ability of the numerical code to predict IBL development.

Table II. Short fetch IBL height formulae. IBL height  $\delta$  and distance  $F$  from the leading edge are in meters.

Formula	Author(s)	Notes
$\frac{\delta}{z_{02}} = (0.75 - 0.03M) \left( \frac{F}{z_{02}} \right)^{0.8}$	Elliott (1958)	$M = \ln \left( \frac{z_{02}}{z_{01}} \right)$
$1.5 \kappa \frac{F}{z_{0r}} = \frac{\delta}{z_{0r}} \left[ \ln \left( \frac{\delta}{z_{0r}} \right) 1 \right]$	Panofsky (1973)	$z_{0r} = \max(z_{01}, z_{02})$
$F'' = \left[ \delta'' (\ln \delta'' - 1) + 1 \right] \frac{1}{1.3\kappa}$	Jackson (1976)	$F'' = \frac{F}{z_0}; \delta'' = \frac{\delta}{z_0}$ $z_0' = [(z_{01}^2 + z_{02}^2)/2]^{1/2}$
$1.5 \kappa \frac{F}{z_{02}} = \frac{\delta}{z_{02}} \left[ \ln \left( \frac{\delta}{z_{02}} \right) 1 \right] + 1$	Panofsky-Dutton (1984)	
$\delta \left( \ln \frac{\delta}{z_{01}} - 1 \right) = 1.25 \kappa (1 + 0.1M) F$	Savelyev-Taylor (2001)	$M = \ln \left( \frac{z_{02}}{z_{01}} \right)$
$2\delta \left( \ln \frac{\delta}{\sqrt{z_{02} z_{01}}} - 1 \right) = F$	Savelyev-Taylor (2005)	

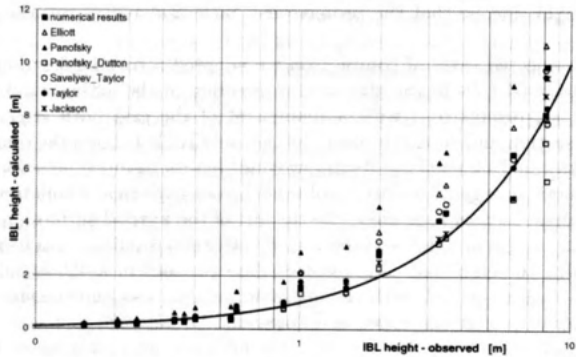


Figure 1. IBL height [m]: calculated vs. observed atmospheric data. Solid line represents perfect agreement.

### 3. Land-water transition: validation of the numerical results and evaluation of the existing formulae performance

As was mentioned above the step-like change in surface roughness caused by the land-water transition results in fetch dependent wind speeds and correspondingly in a fetch dependent wind shear stresses distribution on the free surface, which significantly influences the flow field in the water basin. Following the general description given by Taylor and Lee (1984), valid for a two-dimensional wind flow, the estimation of the wind speed acceleration can be performed by evaluating the IBL height.

Unlike the land surface roughness, which can be considered independent from wind fetch and speed, the water surface roughness depends on the wave field, changing in value with offshore distance. The most commonly used model to estimate the water surface roughness, taking into account the wave field by its dependence on wind speed, is the Charnock relation (Charnock, 1955) in which the water surface roughness is related to the wind shear velocity

Table III. Accuracy of IBL formulae: RMS of the absolute and percentage errors.

Formula	RMS error	RMS percentage error
Elliott	1.096	42.1
Panofsky	3.401	98.9
Jackson	0.506	21.0
Panofsky-Dutton	0.756	25.4
Savelyev-Taylor (2001)	0.727	36.4
Savelyev-Taylor (2005)	0.555	29.1
Numerical results	0.569	20.9

and the acceleration due to gravity through a constant parameter  $\alpha$ :

$$z_{0,w} = \alpha \frac{u^*}{g} \quad (2)$$

Although being considered a parameter to be calibrated, the constant value 0.0185 can be given to  $\alpha$ , as proposed by Wu (1982).

Assuming that both below and above the IBL height a logarithmic profile holds for the wind velocity, the wind velocity can be given as:

$$W_{x_3}(F) = \frac{u^*(F)}{\kappa} \ln \left( \frac{x_3}{z_{0,w}} \right) \text{ for } x_3 \leq \delta_b(F) \quad (3)$$

$$W_{x_3}(0) = \frac{u^*_{land}}{\kappa} \ln \left( \frac{x_3}{z_{0,land}} \right) \text{ for } x_3 \geq \delta_b(F) \quad (4)$$

where  $W_{x_3}(0)$  and  $W_{x_3}(F)$  are the wind speed on the land and on the water for a given fetch respectively,  $x_3$  is the height over the water surface,  $u^*(F)$  the shear velocity on the water,  $\kappa$  the Kármán constant and finally  $z_{0,land}$  and  $u^*_{land}$  are the roughness and the wind shear stress on the land.

Since at the height  $x_3 = \delta_b(F)$ , the condition  $W_{\delta_b}(0) = W_{\delta_b}(F)$  holds, the relationship is easily obtained

$$u^* = u^*_{land} \frac{\ln \left[ \frac{\delta_b(F)}{z_{0,land}} \right]}{\ln \left[ \frac{\delta_b(F)}{z_{0,w}} \right]} \quad (5)$$

Using equations (2) and (5) tailored to any of the previously mentioned IBL formulae, the shear velocity on the water surface can be obtained iteratively as a function of the fetch, the roughness and the wind shear stress over land, which are all 'measurable' quantities.

At last the wind shear stresses can be easily obtained as:  $\tau_s = \rho_{air} u^{*2}$

What said above emphasizes the importance of the evaluation of the IBL height in order to estimate wind shear stresses distribution over the water surface.

The previous section showed that the IBL height formulae of Panofsky and Dutton, Elliott and both formulae proposed by Savelyev and Taylor give reasonably good results for fetches of at most some hundred meters for IBL development over surfaces of constant roughness. In order to evaluate if these results also apply to the case of longer fetch and non-constant downwind roughness, additional numerical simulations were performed.

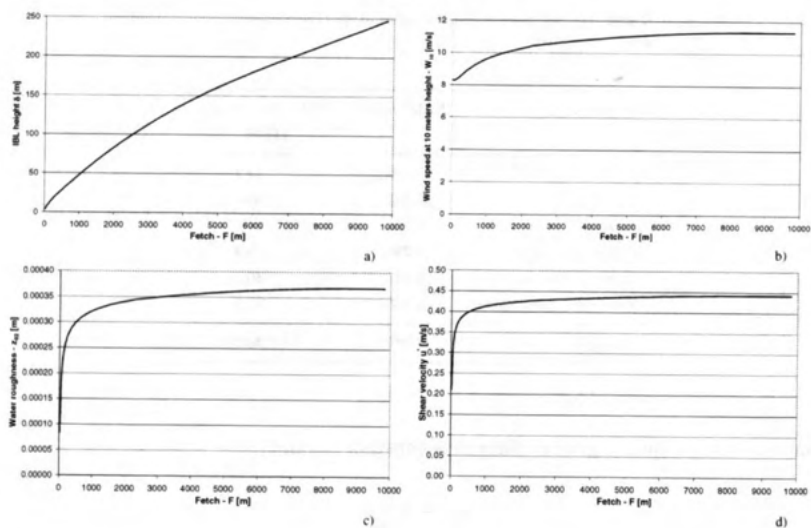


Figure 2. a) IBL development over the water surface along the fetch; b) roughness height of the water surface along the fetch; c) wind speed at 10 meter height above the water surface; d) wind shear velocity at the water surface along the fetch. Offshore wind speed at the shoreline  $W_{10} = 7.9$  m/s, land roughness  $z_{0,land} = 0.15$  m.

Numerical simulations were carried out in a two-dimensional domain 12000 m long and 500 m high, with an upstream (land) bottom roughness of 0.15 meters. The downwind water surface roughness was evaluated by the Charnock formula using the shear velocity values obtained numerically. The computational domain was discretised using 64 x 64 cells, with a refinement of the grid near the bottom and near the separation line of roughness change.

Numerical simulations were performed under the action of four different steady state wind flows over the land. It should be noted in fact that, unlike the cases considered in the previous section, the water surface roughness depends on the shear velocity on the water and consequently on the offshore wind speed. Figure 2 shows the IBL development, the water surface roughness, the wind speed at the height of 10 m and the shear velocity distributions over the water surface for a wind speed at the shoreline (at 10 m height) equal to 7.9 m/s. Referring to the steady-state this figure emphasizes the dependence of all the previously mentioned aerodynamic quantities over the fetch; in particular figure 2b puts in evidence an increase in the wind speed at the height of 10 m of about 40% at the distance of 5000 m downwind of the roughness change. Since the wind shear stresses on the water surface applied in circulation models are usually estimated based on the wind speed at the height of 10 m using the wind drag coefficient:

$$C_{10} = \frac{u_*^2}{W_{10}^2} \quad (6)$$

(for which Wu's formula (Wu, 1982) is extensively employed), the need to properly account for the wind profile restructuring resulting in such an acceleration is clearly seen.

As one of the possibly very few experimental datasets concerning IBL height development over the water surface, numerical results were validated by comparison with the results of a field measurement campaign carried out in Lake Fertö (Hungary) in nearly neutral stratification conditions by Józsa (2004). The wind speed along the prevailing wind direction axis at two sites No. 1 and 2, some 1.5 km far from each other and a bit more than 100 m far from the shoreline

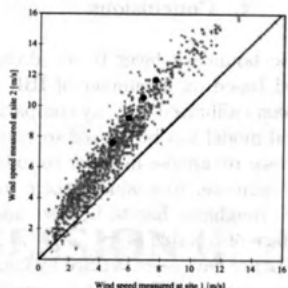


Figure 3. Simultaneous measured wind speeds at two sites in the Fertő (Hungary), corresponding to the prevailing wind sector; perfect agreement indicated by continuous line. The four large solid circles represent numerical results calculated for four different upwind onshore wind speeds (6.5, 7.9, 9.1 and 10.2 m/s).

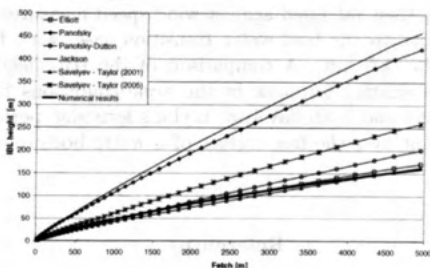


Figure 4. Development of the Internal Boundary Layer over the water surface along the fetch: numerical and analytical results. Upstream surface roughness  $z_{0,land} = 150$  mm.

(in fact the border of the wide littoral reed belt) each, was simultaneously measured at 3.3 m height. Figure 3 shows the simultaneous measured 10 min averaged wind speeds at the two sites, corresponding to the prevailing wind sector and not deviating too much from each other (less than 30 degree difference). In the same figure four large solid circles represent the numerical results for four different equilibrium onshore wind speed cases showing an overall reasonable agreement with the experimental data set, with a slight deviation for the biggest velocities probably due possibly to the land roughness estimate based on the inverse application of the previously described model (see equations 2, 5 and any of the IBL height formulae). A second reason of error can be also found in a partial lack of physical conditions justifying to adopt plane motion hypothesis for the application of the IBL model from which land roughness is derived.

Once the numerical results have been validated we tested IBL height formulae for the case of land-water transition. Figure 4 plots, for the previously mentioned case, IBL developments for 7.9 m/s onshore wind speed as predicted by the various formulae together with the numerical model outcome. It can be seen that Elliott's, Panofsky's and Dutton's formulae together with the one proposed by Savelyev and Taylor formula proposed in 2001 give IBL heights which are in a good agreement with the numerical results, although the second formula by Savelyev and Taylor shows also satisfactory performance.

Similar results have been obtained for the other three wind speed cases plotted in Figure 3 (equilibrium wind speed at 10 m height at the upwind shoreline equal to 6.5 m/s, 9.1 m/s and 10.2 m/s).

#### 4. Conclusions

The adaptation of the atmospheric boundary layer to an abrupt change in the underlying surface roughness can be predicted based on a number of IBL height formulae proposed so far. Most of these formulae have been calibrated only by comparison with short fetch data. In this paper a finite volume numerical model has been used to investigate the IBL development due to a step reduction in the surface roughness in order to extend the fetch range in which the formulae may be applied, furthermore, to evaluate their performance when the spatial variability of the downwind surface roughness has to be also taken into account, as studying IBL development over the free surface of a water body.

Numerical results showed in the paper have been verified by comparison with an atmospheric data set consisting of several measurements of IBL height for rough-to-smooth cases. Evaluation of the accuracy of the numerical results has been accomplished by plotting calculated vs. observed values and by tabulating RMS absolute and percentage errors. The comparison of the numerical results and the atmospheric data with the IBL height formulae shows that the numerical model performs very well with the fairly large subset of short-fetch data. The numerical model has been then validated against wind speed measurements collected in Lake Fertő (Józsa, 2004), relative to the land-water transition case, with fetches larger than the previously mentioned data (1.5 km). A comparison of the IBL heights obtained with the numerical model and the existing formulae in the same conditions finally showed that the Elliott's, Panofsky-Dutton's and both Savel'yev-Taylor's formulae perform reasonably well in predicting IBL development over the free surface of a water body, even for distances of few kilometres.

#### References

- Charnock, H. Wind stress on a water surface. *Q. J. Roy. Meteor. Soc.*, **81**: 639–640, 1955.
- Cioffi, F., F. Gallerano and E. Napoli. Three-dimensional numerical simulation of wind driven flows in closed channels and basins. *J. Hydraul. Res.*, **43**(3): 290–301, 2005.
- Curto, G., J. Józsa, E. Napoli, T. Kramar and G. Lipari. Large scale circulations in shallow lakes. In M. Brocchini F. Trivellato. *Advances in Fluid Mechanics: Vorticity and turbulence effects in fluid structure interactions*. Southampton: Wessex Institute of Technology Press (United Kingdom), 2005. (In press)
- Elliott, W. P. The growth of the Atmospheric Internal Boundary Layer. *Trans. Amer. Geophys. Union*, **39**: 1048–1054, 1958.
- Garratt, J. R. The Internal Boundary Layer - A Review. *Boundary-Layer Meteorol.*, **50**: 171–203, 1990.
- Garratt, J. R. The Atmospheric Boundary Layer. Cambridge University Press, U.K., 316 pp., 1992.
- Jackson, N. A. The Propagation of Modified Flow Downstream of a Change in Roughness. *Quart. J. Roy. Meteorol. Soc.*, **102**: 924–933, 1976.
- Józsa, J., J. Sarkkula and R. Tamsalu. Calibration of modelled shallow lake flow using wind field modification. In Springer, editor, *Proc. VIII Int. Conf. On Comput. Methods in Water Res.*, 1990.
- Józsa, J. Shallow Lake Hydrodynamics. Theory, measurement and numerical model applications. *Lecture Notes of the IAHR Short Course on Environmental Fluid Mechanics*, Budapest, 7–16 June, 2004.
- Panofsky, H. A. Tower Micrometeorology, in D. A. Haugen (ed.). *Workshop on Micrometeorology*. American Meteorological Society, Boston, 151–176, 1973.
- Panofsky, H. A. and J. A. Dutton. *Atmospheric Turbulence* Wiley (Interscience), New York, 397 pp., 1984.
- Savel'yev, S. A. and P. A. Taylor. Notes on Internal Boundary-Layer Height Formula. *Boundary-Layer Meteorol.*, **101**: 293–301, 2001.
- Savel'yev, S. A. and P. A. Taylor. Internal Boundary Layers; I. Height Formulae for neutral and diabatic flows. *Boundary-Layer Meteorol.*, **115**: 1–25, 2005.
- Taylor, P. A. and R. J. Lee. Simple guidelines for estimating wind speed variations due to small scale topographic features. *Climat. Bull. Canadian Meteorol. and Ocean. Soc.*, **3**(2): 3–32, 1984.
- Walmsley, J. L. Internal BoundaryLayer Height Formulae - A Comparison with Atmospheric Data. Cambridge University Press, U.K., 316 pp., 1992.
- Wu, J. Wind-Stress Coefficients Over Sea Surface From Breeze to Hurricane. *J. Geophys. Res.*, **87**: 9704–9706, 1982.

For many years, I have been writing and reading, and stand awaiting your comments  
on my list.

### "Second Thoughts"

1. *What is the best book you have ever read? Why?*  
2. *What is the best book you have ever written? Why?*  
3. *What is the best book you have ever edited? Why?*

### "Thoughts"

1. *What is the best book you have ever written? Why?*  
**POSTER SESSION II**

1. *What is the best book you have ever written? Why?*  
2. *What is the best book you have ever edited? Why?*  
3. *What is the best book you have ever written? Why?*

1. *What is the best book you have ever written? Why?*  
2. *What is the best book you have ever written? Why?*  
3. *What is the best book you have ever written? Why?*

1. *What is the best book you have ever written? Why?*  
2. *What is the best book you have ever written? Why?*  
3. *What is the best book you have ever written? Why?*

1. *What is the best book you have ever written? Why?*  
2. *What is the best book you have ever written? Why?*  
3. *What is the best book you have ever written? Why?*

1. *What is the best book you have ever written? Why?*  
2. *What is the best book you have ever written? Why?*  
3. *What is the best book you have ever written? Why?*



## Temperature variations within and outside reed stand causing horizontal mixing

Charlotta Lövstedt

*Department of Water Resources Engineering, Lund University, Box 118, 221 00 Lund,  
Sweden*

E-mail: charlotta.lovstedt@tvrl.lth.se

### *Abstract*

As the sun heats the surface water of a lake, the surface water in the reed belts will gain less heat due to shadowing. The temperature gradient between the reeds and the open water will cause a weak surface current towards the reeds and a current in the opposite direction at the bottom. During night the water cools slower within the reed belt and a temperature gradient in the other direction will form. This horizontal mixing due to these temperature gradients can be important in the exchange of nutrients, oxygen, CO<sub>2</sub> etc. for the ecosystem of the reed belts, and can also affect the location of plankton and fish during the day.

The object of the measurements presented here was to determine the daily pattern in temperature profiles inside and outside the reed belts and to investigate the speed of the surface current and the vertical profile of the current. Temperature measurements were made every 30 min during July-Nov 2004 and May-July 2005. Surface current and velocity profile measurements were made in May 2005.

During sunny days with low wind speeds, the temperature difference between open water and the reed belt was, in the surface water, on average 0.7°C and during the nights an opposite but smaller temperature difference was measured.

THE 1970 PREDICTION OF THE 1970 ELECTION IN THE UNITED STATES

### APPENDIX A

The following table contains the results of the 1970 prediction of the 1970 election in the United States. The table shows the predicted outcome of the election in each state, the total number of votes cast, and the percentage of the vote cast for each candidate.

The table also includes the results of the 1970 prediction of the 1970 election in the United States. The table shows the predicted outcome of the election in each state, the total number of votes cast, and the percentage of the vote cast for each candidate. The table also includes the results of the 1970 prediction of the 1970 election in the United States. The table shows the predicted outcome of the election in each state, the total number of votes cast, and the percentage of the vote cast for each candidate.

The table also includes the results of the 1970 prediction of the 1970 election in the United States. The table shows the predicted outcome of the election in each state, the total number of votes cast, and the percentage of the vote cast for each candidate. The table also includes the results of the 1970 prediction of the 1970 election in the United States. The table shows the predicted outcome of the election in each state, the total number of votes cast, and the percentage of the vote cast for each candidate.

The table also includes the results of the 1970 prediction of the 1970 election in the United States. The table shows the predicted outcome of the election in each state, the total number of votes cast, and the percentage of the vote cast for each candidate. The table also includes the results of the 1970 prediction of the 1970 election in the United States. The table shows the predicted outcome of the election in each state, the total number of votes cast, and the percentage of the vote cast for each candidate.

The table also includes the results of the 1970 prediction of the 1970 election in the United States. The table shows the predicted outcome of the election in each state, the total number of votes cast, and the percentage of the vote cast for each candidate. The table also includes the results of the 1970 prediction of the 1970 election in the United States. The table shows the predicted outcome of the election in each state, the total number of votes cast, and the percentage of the vote cast for each candidate.

The table also includes the results of the 1970 prediction of the 1970 election in the United States. The table shows the predicted outcome of the election in each state, the total number of votes cast, and the percentage of the vote cast for each candidate. The table also includes the results of the 1970 prediction of the 1970 election in the United States. The table shows the predicted outcome of the election in each state, the total number of votes cast, and the percentage of the vote cast for each candidate.

## The vertical distribution of soluble reactive phosphorus in the water column of Esthwaite Water and the effect of physical variables

Helen Miller\*, Ian Jones\*, Andrew Folkard\*\* and Stephen Maberly\*

Centre for Ecology and Hydrology, Lancaster Environment Centre\*,

Department of Geography, Lancaster University\*\*

Lancaster, LA1 4AP UK

### Abstract

The aim of this study was to understand the processes that influence the flux of soluble reactive phosphorus from the hypolimnion to the epilimnion in a small eutrophic lake.

A three-month study was made of the vertical distribution of nutrients and physical variables in the water column of Esthwaite Water in the English Lake District during the period of summer stratification in 2004. Data on meteorology and the temperature structure of the lake was obtained from an automatic water quality monitoring buoy on the lake.

During stratification the concentration of soluble reactive phosphorus increased in the hypolimnion and decreased in the epilimnion. There was evidence of an increased flux of soluble reactive phosphorus across the thermocline from the hypolimnion to the epilimnion in late June and in the middle of August. These periods were characterised by wet and windy weather. The importance of different variables in controlling the flux of soluble reactive phosphorus was analysed using the meteorological data and calculated Schmidt stability.

### Introduction

In many freshwater environments phosphorus is the limiting nutrient for growth because of its scarcity in the natural environment. Thus, increases in the amount of phosphorus can lead to increased productivity and eutrophication (Wetzel, 1983).

In stratified lakes, most of the mixing occurs in the surface waters, which are frequently turbulent. In the hypolimnion, there is much less turbulence (Kalff, 2002) and respiratory processes dominate (Stumm & Morgan, 1996). The decrease in the turbulent mixing imposed by the stratification means that the respired oxygen is not rapidly replenished from the surface, sometimes leading to the hypolimnion becoming anoxic (Wetzel, 1983).

A sufficient decrease in hypolimnion oxygen concentration causes the sediment surface to become anoxic. Oxidised substances are then reduced in the sediment and phosphorus and other substances, such as soluble ferrous iron, are liberated. The most important conditions that regulate phosphorus sediment release are the pH and redox potential (Bostrom *et al.*, 1988). As long as the redox potential at the sediment surface is maintained at a low level until the autumn turnover, the diffusion of phosphorus and ferrous iron from the sediment continues (Mortimer, 1941). This leads to a build up in the phosphorus and iron concentrations at the bottom of the lake. The build up of phosphorus at the bottom of the lake may effect the concentration of phosphorus in the epilimnion through mixing and entrainment of the hypolimnetic waters into the epilimnion (Blanton, 1973).

The cycling of phosphorus with iron and other elements can effect the distribution of phosphorus in the water column of lakes. Under oxic conditions ferric iron hydroxides bind to the phosphorus in solution. Phosphorus is only released from the iron hydroxides when most of the iron has been reduced (Golterman, 1995).

The hypolimnion and the deep lake sediments are only one possible source of phosphorus to the epilimnion. Other possible sources include plankton in the epilimnion, plants and sediments in the littoral zone (George, 2000) and external loading from point and diffuse sources in the lake catchment (Wetzel, 1983).

This paper is concerned with the potential mixing of soluble reactive phosphorus (SRP) from the hypolimnion to the epilimnion. The aim is to investigate whether the high concentrations of SRP at the bottom of Esthwaite Water are physically mixed up to the surface waters or whether the chemical interactions inhibit this process.

### Methods

Esthwaite Water is a glacial lake in the English Lake District approximately 1 km<sup>2</sup> in area and with a maximum depth and mean depth of 15.5 m and 6.4 m, respectively (Ramsbottom, 1976). Water samples were taken at 0.5 m depth and then every 2 m down to a depth of 14.5 m on a weekly basis from the 16<sup>th</sup> June to 13<sup>th</sup> October 2004 using a 1L friedinger. Occasional samples at intermediate depths were taken. Water samples were analysed for SRP following the method of Stephens (1963), and total iron, iron II and iron III following the method of Gibbs (1979). The water samples that were analysed for SRP were filtered in the field immediately after collection using a hand pump and 47 µm GF/C Whatman filters. The water samples that were analysed for iron were preserved immediately after collection with 5 M hydrochloric acid. Temperature, conductivity, dissolved oxygen and pH measurements were made at the same depths as the water samples were taken from using a Hydrolab Quanta® Water Quality Measurement System.

Temperature data was also collected every metre between 1 and 12 m depth from a thermistor chain on a buoy on Esthwaite Water. The data were collected on a minute-by-minute basis and averaged to give daily means.

The stratification of the lake was quantified using the Schmidt stability of the lake, *S*, which was calculated per unit area from the thermistor data collected at the buoy, using equation [1] below.

$$S = -\frac{g}{A_0} \int_0^{z_m} (z - z_g) A_z (\rho_{\max} - \rho_z) dz \quad [1]$$

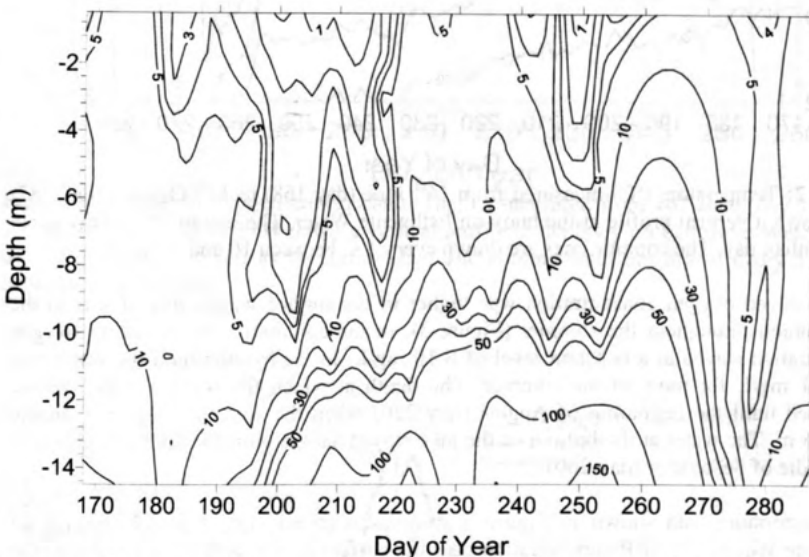
where  $A_0$  is the surface area of the lake,  $A_z$  is the area of the lake enclosed by a contour of depth  $z$ ,  $g$  is acceleration due to gravity ( $g=9.81 \text{ ms}^{-2}$ ),  $\rho_{\max}$  is the maximum density of the water ( $=999.9749608 \text{ kg m}^{-3}$ ),  $\rho_z$  is the density of water at depth  $z$  and  $z_m$  is the maximum depth (Hutchinson, 1957).  $A_0$  and  $A_z$  were obtained from Ramsbottom (1976). The depth to the centre of gravity of the lake,  $z_g$ , is given by:

$$z_g = \frac{1}{V} \int_0^{z_m} z A_z dz \quad [2]$$

where  $V$  is the volume of the lake (Ramsbottom, 1976). The temperature data were used to calculate the density of the water using the method of UNESCO (1981).

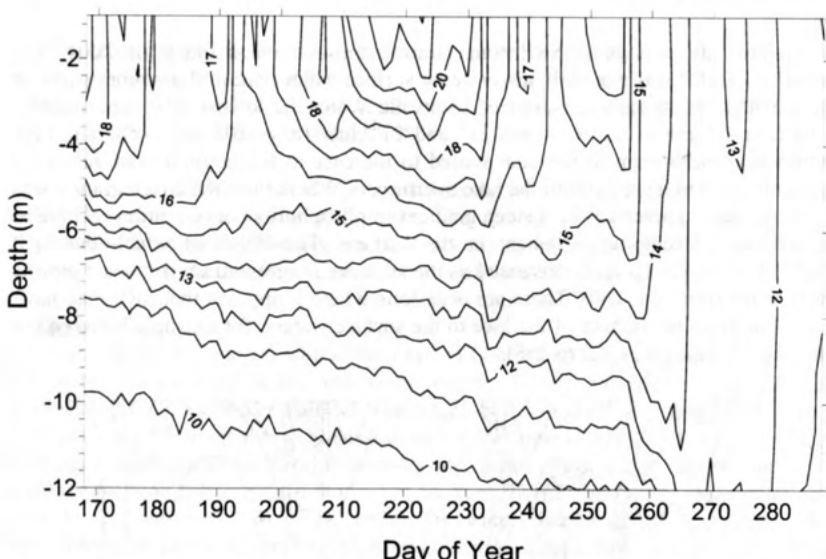
## Results

Figure 1 shows the change in SRP concentration through the summer of 2004. The concentration of SRP was generally lower in the surface water than in the bottom water of Esthwaite Water. In the surface waters of Esthwaite Water the lowest SRP concentration was 1 µg/L at a depth of 0.5 m on the 21<sup>st</sup> and 27<sup>th</sup> July (days 203 and 209). The SRP concentration at the bottom of the lake started to increase at the beginning of July (day 185) and continued to increase until the lake overturned. Where the SRP concentration was over 10 µg/L there appeared to be a steep gradient in phosphorus concentration relative to the phosphorus concentration gradient at the surface. The depth at which the SRP concentration was over 10 µg/L decreased as the summer progressed until it was below 4 m by mid-September (day 260). There are occasions where it appears that SRP may have been mixed up from the bottom of the lake to the surface waters, for example between the 9<sup>th</sup> and 25<sup>th</sup> of August (days 222 to 238).



**Figure 1:** SRP concentration ( $\mu\text{g/L}$ ) measured from 16<sup>th</sup> June (day 168) to 13<sup>th</sup> October (day 287) 2004 down a vertical profile at the deepest point in Esthwaite Water. The day of the year is given as the Julian day. The contour lines are drawn every 1  $\mu\text{g/L}$  between 1 and 5  $\mu\text{g/L}$ , every 10  $\mu\text{g/L}$  between 10 and 50  $\mu\text{g/L}$  and every 50  $\mu\text{g/L}$  between 50 and 150  $\mu\text{g/L}$ .

Figure 2 shows the change in the temperature of the water column of Esthwaite Water through the summer of 2004. Esthwaite Water became stratified at the beginning of May. Between the 9<sup>th</sup> and 11<sup>th</sup> July (days 191 and 193) the surface mixed layer of the lake increased to a depth of approximately 6 m. This part of the summer was cooler with some wet and windy weather. The stratification in the lake was re-established as the weather became warmer again. Between the 9<sup>th</sup> August and 26<sup>th</sup> September (days 222 and 260) the stratification was much weaker. At the start of this period (days 222 to 238) SRP appeared to be mixed up from the bottom of the lake to the surface waters. The lake overturned between the 16<sup>th</sup> and 26<sup>th</sup> September (days 260 and 270) and became fully mixed.



**Figure 2:** Temperature ( $^{\circ}\text{C}$ ) measured from 16<sup>th</sup> June (day 168) to 13<sup>th</sup> October (day 287) 2004 down a vertical profile at the buoy on Esthwaite Water. The day of the year is given as the Julian day. The contour lines are drawn every  $1^{\circ}\text{C}$  between 10 and  $21^{\circ}\text{C}$ .

The dissolved oxygen concentration was higher in the surface waters than it was in the hypolimnion throughout the summer (Figure 3). In the epilimnion the dissolved oxygen concentration stayed at a constant level of 8–10 mg/L. In the hypolimnion the water was below 1 mg/L for most of the summer. The depth at which the water became anoxic decreased until the beginning of August (day 220) when the water column was anoxic below 5 m. The water at the bottom of the lake stayed anoxic until the lake overturned in the middle of September (day 260).

The temperature data shown in Figure 2 were used to calculate Schmidt stability of Esthwaite Water. The SRP concentration near the surface (0.5 m and 2.5 m) and near the bed (13.5 m and 14.5 m) are shown with the Schmidt stability for June to October in Figures 4 and 5. In Figure 4 the SRP concentration appeared to vary inversely with the Schmidt stability. In Figure 5 the SRP and Schmidt stability appeared to vary in tandem.

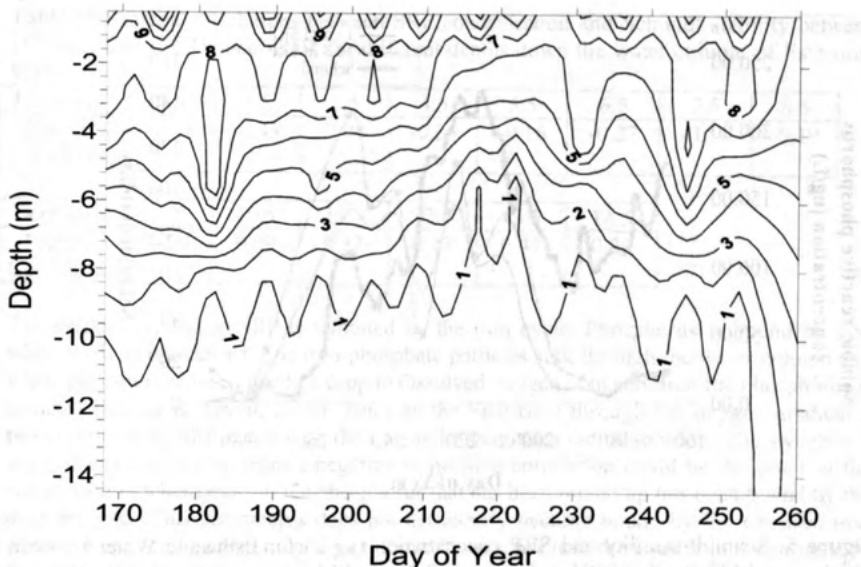


**Figure 3:** Dissolved oxygen concentration (mg/L) measured from 16<sup>th</sup> June (day 168) to 13<sup>th</sup> October (day 287) 2004 down a vertical profile at the buoy on Esthwaite Water. The day of the year is given as the Julian day. The contour lines are drawn every 1 mg/L between 1 and 10 mg/L.

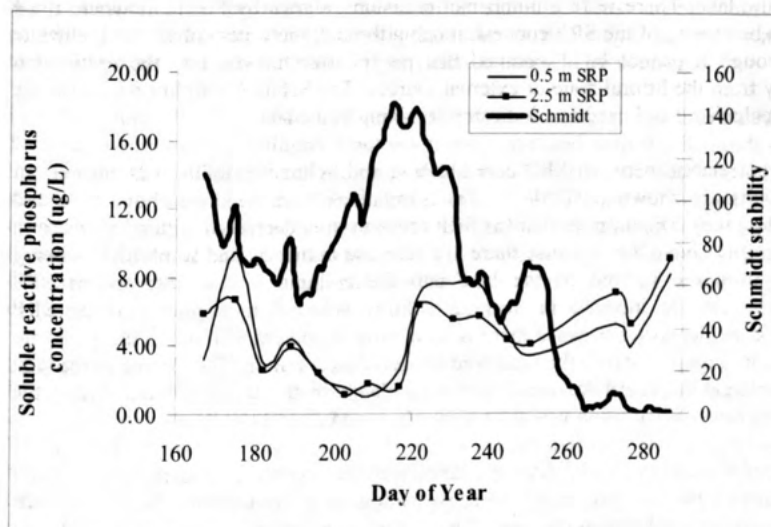


**Figure 4:** Schmidt stability and SRP concentration ( $\mu\text{g/L}$ ) for Esthwaite Water between 16<sup>th</sup> June and 13<sup>th</sup> October 2004 at depths of 0.5 m and 2.5 m.

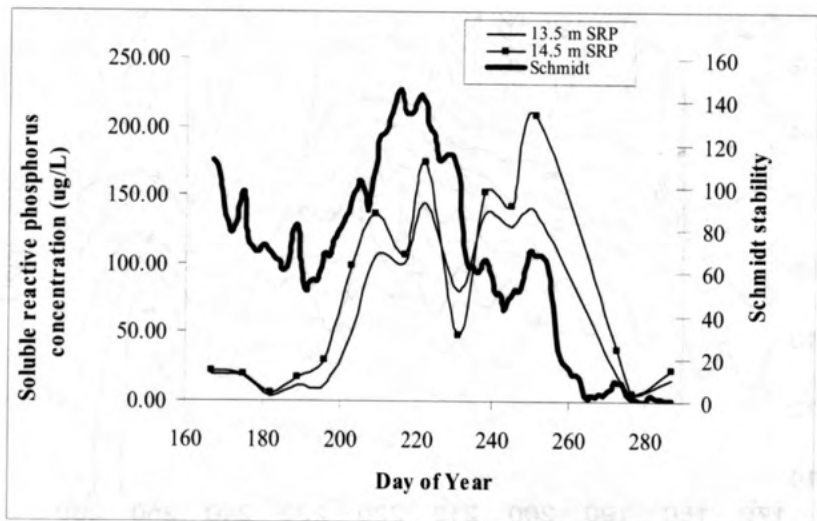


**Figure 5:** Schmidt stability and SRP concentration ( $\mu\text{g/L}$ ) for Esthwaite Water between 16<sup>th</sup> June and 13<sup>th</sup> October 2004 at depths of 13.5 m and 14.5 m.

#### Discussion and Conclusions

The SRP concentration was low in the surface waters of Esthwaite Water for much of the summer of 2004. At the bottom of the lake the SRP concentration began to build up from the beginning of July and reached 2 orders of magnitude higher than the concentration at the top of the lake. There were a number of occasions, shown by Figure 1, where there appeared to be mixing of the SRP concentration up through the water column of Esthwaite Water, although it cannot be discounted that phosphorus moved into the epilimnion horizontally from the littoral zone or external sources. The Schmidt stability for Esthwaite Water was calculated and used as a indicator of mixing in the lake.

A Pearson correlation between SRP concentration and Schmidt stability was carried out and the results are shown in Table 1. The correlations were negative above 9 m and positive below 9 m. This implies that the SRP concentration decreased with an increase in Schmidt stability above 9 m because there is a decrease in mixing and so no SRP is being moved up from the bottom of the lake into the epilimnion. The increase in SRP concentration with an increase in Schmidt stability below 9 m implies that the SRP concentration is increasing because there is no mixing taking place to move the SRP into the epilimnion. Figure 3 shows the dissolved oxygen concentration. The change in the sign of the correlation appeared to occur at 9 m, a depth in the water column where the dissolved oxygen concentration was approximately 1 mg/L.

As the Schmidt stability of the lake decreases and the amount of mixing in the water column increases the SRP concentration at the bottom of the lake decreases and the SRP concentration in the epilimnion increases. This is consistent with the physical mixing in the lake causing some SRP from the bottom of the lake to become available in the epilimnion. Despite Table 1 showing the expected pattern of mixing, the results themselves were not statistically significant but such a conclusion is too simplistic: the transfer of SRP from the hypolimnion to the epilmnnion via the concentration gradient is complicated by the iron cycle and dissolved oxygen concentration.

**Table 1:** Pearson correlations between SRP concentration and Schmidt stability between 16<sup>th</sup> June and 13<sup>th</sup> October 2004 for different depths down the water column of Esthwaite Water.

Depth (m)	0.5	2.5	3.5	4.5	5.5	6.5	7.5	8.5
Pearson Correlation	-0.15	-0.43	0.04	-0.26	-0.16	-0.27	-0.11	-0.19

Depth (m)	9.5	10.5	11.5	12.5	13.5	14.5
Pearson Correlation	0.09	0.09	0.22	0.25	0.41	0.34

The vertical mixing of SRP is inhibited by the iron cycle. Phosphorus is bound by iron when the iron is oxidised. The iron-phosphate particles sink through the water column and when the iron is reduced due to a drop in dissolved oxygen concentration the phosphorus is released (Mayer & Jarrell, 2000). Thus, as the SRP rises through the oxygen gradient a proportion of the SRP reacts with the iron and precipitates out of solution. The switch at 1 mg/L dissolved oxygen from a negative to positive correlation could be the point in the water column where most of the phosphorus that has been mixed up has been bound by the oxidised iron. This phosphorus does not necessarily become bound by the oxidised iron when the oxygen concentration is just above 0 mg/L because the equilibrium constants of the redox processes mean that nitrogen and manganese are oxidised before the iron (Stumm & Morgan, 1996).

The depth of the 1 mg/L dissolved oxygen contour will have been affected by the stability of the lake and the mixing taking place in the water column. For example, on the 9<sup>th</sup> August (day 220) the 1 mg/L contour line reached the highest point in the water column that corresponds to the peak of the Schmidt stability. This suggests an alternative possibility for the transfer of SRP, namely that it rises sufficiently high in the water column to become within the range of motile algae before it is bound by the iron.

In conclusion, the SRP concentration appeared to be negatively correlated with the Schmidt stability in the epilimnion but positively correlated with the Schmidt stability in the hypolimnion. This pattern indicates the vertical mixing of SRP but the lack of statistical significance in the results indicates the complications caused by the iron chemistry. Future work will investigate the direct relationship between SRP and diffusivity. Treating SRP as a passive tracer will allow an upper bound to be placed on the diffusive flux from the epilimnion and this can be compared with the actual measurements obtained.

### References

- Blanton, J.O (1973) Vertical entrainment into the epilimnia of stratified lakes. *Limnology and Oceanography*, **18** (5), 697-704.
- Bostrom, B., Persson, G., & Broberg, B. (1988) Bioavailability of different phosphorus forms in fresh-water systems. *Hydrobiologia*, **170**, 133-155.
- George, D.G. (2000) Remote sensing evidence for the episodic transport of phosphorus from the littoral zone of a thermally stratified lake. *Freshwater Biology*, **43**, 571-578.
- Gibbs, M.M. (1979) A simple method for the rapid determination of iron in natural waters. *Water Research*, **13**, 295-297.
- Gill, A.E (1982) *International Geophysics Series, Volume 30: Atmosphere-Ocean Dynamics*. Academic Press, Inc. (London) Ltd.
- Golterman, H.L. (1995) The role of the ironhydroxide-phosphate-sulfide system in the phosphate exchange between sediments and overlying water. *Hydrobiologia*, **297**, 43-54.

- Heinz, G., Ilmberger, J. and Schimmele, M. (1990) Vertical mixing in the Überlinger See, western part of Lake Constance. *Aquatic Sciences* **52** (3), 256-268.
- Hutchinson, G.E. (1957) *A treatise on limnology, Volume 1: Geography, physics and chemistry*. John Wiley and Sons, New York.
- Idso, S. B. 1973. On the concept of lake stability. *Limnology and Oceanography* **18**, 681-683
- Mayer, T.D. & Jarrell, W.M. (2000) Phosphorus sorption during iron(II) oxidation in the presence of dissolved silica. *Water Research*, **34**, 3949-3956.
- Mortimer, C.H. (1941) The exchange of dissolved substances between mud and water in lakes. *Journal of Ecology*, **29** (2), 280-329.
- Ramsbottom, A.E. (1976) Depth charts of the Cumbrian lakes. *Freshwater Biology Association Scientific Publication No. 33*
- Stephens, K. (1963) Determination of low phosphate concentrations in lake and marine waters. *Limnology and Oceanography*, **8**, 361-362.
- Stumm, W. & Morgan, J.J. (1996) *Aquatic chemistry: Chemical equilibria and rates in natural waters*. John Wiley and Sons, New York.
- UNESCO (1981) Tenth Report for the joint panel on oceanographic tables and standards, Unesco Technical Papers in Marine Science, 36.
- Wetzel, R.G. (1983) *Limnology*, second edn. Saunders College Publishing, U.S.A.

## SHORT-TERM VARIABILITY IN PHYSICAL FORCING IN TEMPERATE RESERVOIRS : EFFECTS ON PHYTOPLANKTON DYNAMICS IN TERMS OF SIZE STRUCTURE AND SPECIES COMPOSITION

Pannard A., Bormans M. and Lagadeuc Y.

UMR 6553 Ecobio, FR/IFR CAREN, University of Rennes, campus de Beaulieu, bâtiment 14b, Av. General Leclerc, 35 042, Rennes, France

E-mail : alexandrine.pannard@univ-rennes1.fr

myriam.bormans@univ-rennes1.fr

yvan.lagadeuc@univ-rennes1.fr

It is well known that seasonal forcing of solar radiation, air temperature, nutrient loads and turbulence, controls the succession of the phytoplankton communities in lakes (Anneville *et al.*, 2002; Noges *et al.*, 1998; Sommer *et al.*, 1986). On a daily time scale, it is also accepted that wind and rain events can modify the physical and chemical parameters, such as turbulence, water temperature, mixed layer depth and resources availability in the water column. Being on similar time scale than growth rate of phytoplankton, modifications of these factors may influence directly the dynamic of the phytoplankton (Reynolds, 1984). However few studies were performed on the short-term dynamic of the phytoplankton communities, in response to rapid events.

There are many ways by which wind and rain can modify the vertical distribution and the dynamics of phytoplankton. For example, the intensity of mixing can be increased by the occurrence of a rapid event, leading to a decrease of the vertical flux of phytoplankton by redistributing the populations over the mixed layer (Huisman & Sommeijer, 2002). The depth of the mixed layer can also be increased, thus decreasing the sedimentation loss (Ptacnick, Diehl & Berger, 2003). Loss rate by sedimentation increases with cell size and cell density. If loss rate exceeds growth rate, there will lead to the extinction of the population (Huisman, Van Oostveen & Weissing, 1999). The decrease of sedimentary loss due to both increase of mixing and mixed layer depth may thus favour the sustainability of large and sinking populations, such as diatoms. On the other hand, small cells and cells which can regulate their buoyancy to remain at their optimal depth in terms of light availability, such as cyanobacteria, are also redistributed over the mixed layer. They thus lose their vertical advantageous position and may be disadvantaged by rapid events. At the community level, increase of mixing may thus favour large cells and diatoms and disadvantage small cells and cyanobacteria.

A rapid event can also increase nutrient supply, in particular to the euphotic layer, by breaking down a nutricline, or in the case of a rain event, by bringing external nutrients from river inputs. At the cellular scale, nutrients fluxes induced by an increase of mixing can also favor cells larger than 20 µm, due to a decrease in the thickness of the cell boundary layer (Karp-Boss, Boss & Jumars, 1996; Metcalfe, Pedley & Thingstad, 2004). These modifications of nutrient availability, at the water column scale and at the cellular scale, may affect the issue of competition (Sommer, 1985). Finally, by keeping cells within the euphotic layer, reducing their sedimentary loss and increasing the nutrients fluxes, we can expect rapid events to increase large cells and diatoms, in particular in terms of production and biomass. The standing stock of biomass of large cells and diatoms being higher, the sedimentary fluxes should also increase at the end of the rapid events. The occurrence of rapid events, such as wind and rain, should induce a short-term variability of the size-structure and of the species composition.

We chose a field approach, by following the short-term dynamic of the phytoplankton community in two temperate lakes (Brittany, France) during three weeks

periods. To evaluate the seasonal context, one of the lake was studied three times over the year. Each time, meteorological data, change of physical and chemical structure of the water column and biological responses of phytoplankton communities were measured. We followed the modifications of the temperature and currents profiles and of the nutrients and light availability. The dynamic of the phytoplankton was characterized in terms of size fractionated biomass and productivity, species composition and sinking loss, measured with sediment traps.

The responses of phytoplankton, in terms of size structure and sedimentary fluxes, could be measured during the first three days following the perturbations (Pannard, Bormans & Lagadeuc, 2005). Increase of nutrient availability and of mixing favoured large cells in terms of biomass and productivity and was associated with an increase in sedimentary fluxes. On the other hand mixing decreased small cells in terms of both biomass and productivity. Lastly the increase of the dilution rate induced by rainfall was found unfavourable to both large and small cells. The community structure was also modified by rapid events. Indicative species responded to rapid events, while dominant species were controlled by seasonal forcing. Multivariate analysis demonstrated a modification of the phytoplankton community, during and after perturbations, occurring during all studies except the summer one. Indeed in summer, the water column was highly stratified and we just observed a vertical structure of the communities. An example of a modification of community is given by Fig.1, which is a procrustean analysis of two separate PCA, one on physical and chemical data and one on species data. The study was performed in spring, when light was the only limiting resource. A wind event increased the mean temperature over the mixed layer and induced a sharper thermocline, leading to a higher potential energy of the water column. Silica also decreased, but remained non limiting for diatoms growth. Large diatoms such as *Aulacoseira sp* and *Synedra sp* disappeared and were replaced by a smaller diatom, *Cyclotella sp*, which undergoes lower sinking loss. But such modifications of the communities' structure was less frequent than change of size structure. Size structure varies indeed with the species composition, and also with the size of colony and the aggregation process. We thus demonstrate that, on a daily time scale, rapid events modify the phytoplankton dynamic, both in terms of size structure and exported biomass and in terms of community's structure.

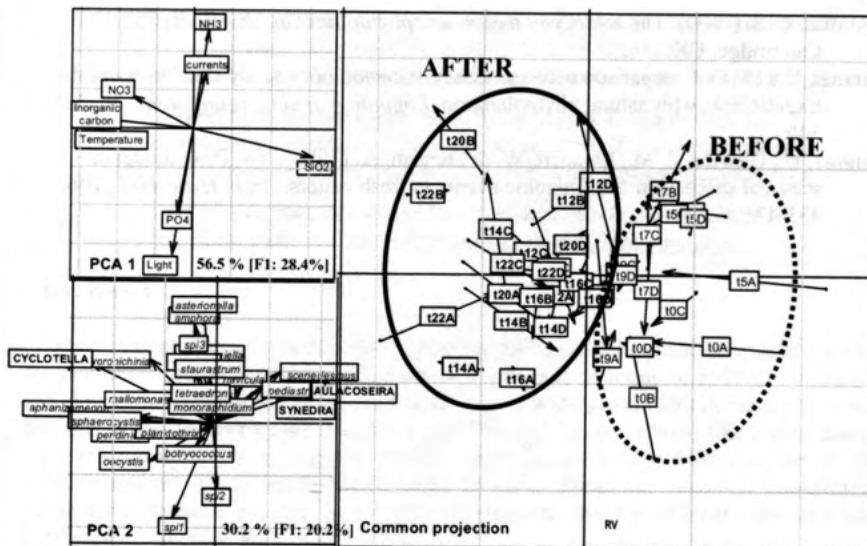


Fig.1 : procrustean analysis of the PCA of chemical and physical data (PCA 1) and of the PCA of species composition of communities (PCA 2) of spring :

## References :

- Anneville, O., Ginot, V., Druart, J.-C. & Angeli, N. (2002). Long-term study (1974–1998) of seasonal changes in the phytoplankton in Lake Geneva: a multi-table approach. *Journal of Plankton Research*, **24**, 993-1008.
- Huisman, J. & Sommeijer, B. (2002). Population dynamics of sinking phytoplankton in light-limited environments: simulation techniques and critical parameters. *Journal of Sea Research*, **48**, 83-96.
- Huisman, J., Van Oostveen, P. & Weissing, F. J. (1999). Species dynamics in phytoplankton blooms: Incomplete mixing and competition for light. *American Naturalist*, **154**, 46-68.
- Karp-Boss, L., Boss, E. & Jumars, P. (1996). Nutrient fluxes to planktonic osmotrophs in the presence of fluid motion. *Oceanography and Marine Biology, an Annual Review*, **34**, 71-107.
- Metcalfe, A. M., Pedley, T. J. & Thingstad, T. F. (2004). Incorporating turbulence into a plankton foodweb model. *Journal of Marine Systems*, **49**, 105-122.
- Noges, T., Kisand, V., Noges, P., Pollumae, A., Tuvikene, L. & Zingel, P. (1998). Plankton seasonal dynamics and its controlling factors in shallow polymeric eutrophic Lake Vortsjärv, Estonia. *International Review of Hydrobiology*, **83**, 279-296.
- Pannard, A., Bormans, M. & Lagadeuc, Y. (2005). Short-term variability in physical forcing in temperate reservoirs: effects on phytoplankton dynamics and sedimentary fluxes. *submitted to Freshwater Biology*.
- Ptačnick, R., Diehl, S. & Berger, S. (2003). Performance of sinking and non sinking phytoplankton taxa in a gradient of mixing depths. *Limnology and Oceanography*, **48**, 1903-1912.

- Reynolds, C. S. (1984). *The ecology of freshwater phytoplankton*. University Press, Cambridge, UK.
- Sommer, U. (1985). Comparison between steady state and non-steady state competition: Experiments with natural phytoplankton. *Limnology and Oceanography*, **30**, 335-346.
- Sommer, U., Gliwicz, Z. M., Lampert, W. & Duncan, A. (1986). The PEG-model of seasonal succession of planktonic events in fresh waters. *Arch. Hydrobiol.*, **106**, 433-471.

ON THE INFLUENCE OF FLEXIBLE VEGETATION ON FLOW FIELDS IN  
SHALLOW WATER: A FLUME EXPERIMENT

*Maltese A\*, Folkard A\*\*, Ciraolo G.\*, Cox E.\*, Ferreri G.B.\* and La Loggia G.\**

\*Dipartimento Ingegneria Idraulica ed Applicazioni Ambientali

Università di Palermo – Viale delle Scienze, 90128 – Palermo (Italy)

Tel: +39 0916657727; Fax: +39 0916657749; email: [giuseppe@idra.unipa.it](mailto:giuseppe@idra.unipa.it)

\*\*Department of Geography - Lancaster Environment Centre

University of Lancaster; email: [a.folkard@lancaster.ac.uk](mailto:a.folkard@lancaster.ac.uk)

## ABSTRACT

Management of coastal waters and lagoons by mathematical circulation models requires the determination of the submerged vegetation influence in terms of hydraulic resistance and flow turbulent structure. *Posidonia oceanica* is a widespread plant in the sandy coastal bottoms of the Mediterranean Sea. It has very thin and flexible ribbon-like leaves about 1 cm wide and up to 1.5 m long, and usually covers the sea bottom with a density of 500-1,000 plants/m<sup>2</sup>. From the hydraulic point of view, *Posidonia oceanica* constitutes a particular roughness, because, as the velocity increases, the leaves bend more and more until they lie down on the bottom.

In the paper, the characteristics of flow over a sea bottom covered by *Posidonia oceanica* are studied in a laboratory flume, using a coverage of artificial plants made by polyethylene sheeting. The planimetric distribution of the plants produced an areal density of 1037 plants/m<sup>2</sup>.

The turbulent phenomena in the presence of the simulated plants in two situations, continuously and discontinuously vegetated bottom, were also investigated. In faster flows, in which the bent plants are totally submerged, the velocity profile follows a logarithmic type law above the prone canopy; it presents an inflection point near the vegetation top, and uniformly low speeds within the vegetation. The Reynolds stress profile shows a maximum at the canopy roof, where a mixing layer occurs. In slower flows, in which the erect plants are quasi-emergent, flow velocities and Reynolds stresses are almost uniform.

Concerning to the hydraulic resistance, the experimental results allow one to recognize the influence of the Reynolds number of flow and the ratio between the leaf length and the flow depth on Darcy-Weisbach's friction factor, which is expressed as a function of a particular Reynolds number.

## INTRODUCTION

*Posidonia oceanica* (Fig. 1) is a species of seagrass that is widespread in coastal sandy areas of the Mediterranean Sea, up to depths of approximately 40 m. Each plant consists of a tuft of six leaves of different length. The leaves are ribbon-like and approximately 1 cm wide. They are very flexible and supported by a rhizome at the base. The older and longer leaves (up to 1.5 m) are located at the outside of each tuft, while the younger and shorter leaves grow between them (Cinelli et al., 1995). The seagrass forms meadows extending up to some square kilometres, with areal densities usually varying between 500 and 1000 plants per square metre. With low flow velocities the seagrass leaves remain almost vertical ("erect") within the water, but as the velocity increases they bend more and more, due to their flexibility, until they lie down on the sea bottom ("prone"). Therefore, *Posidonia oceanica* constitutes a specific roughness, whose effects are considerably marked in lagoon environments, characterized by large areas and low depths of about one metre. Usually, gaps form within the meadows, which are likely to play an important role

in the ecosystem, namely in influencing nutrient and sediment transport and distribution (Folkard et al., 2003).



Fig. 1 - *Posidonia oceanica* meadow

During the late 1990's the level of interest rose concerning the vegetative resistance, both of terrestrial and of aquatic vegetation, considerably increased, and many studies were published that were added to the numerous previous ones. Freeman et al. (1998) proposed a new approach for determining hydraulic resistance of floodplain vegetation, and Rahmeyer et al. (1999) continued with this work, verifying these theoretical results by laboratory and field experiments. Järvelä (2002) focused his research on a flume study of the flow resistance of flexible and stiff floodplain vegetation types, and how the resistance levels were affected by vegetation density and spacing. Research in the field of vegetative resistance has been enhanced by attempts to model the effects of vegetation on flow, rather than qualitatively describing and explaining it (Nepf et al., 1997). The applicability of these models was further increased by the addition of the ability of the models to explain the effect of flexible rather than rigid vegetation forms (Nepf, 1999; Nepf and Vivoni, 2000). Flow resistance of coverage of artificial plants, analogous to *Posidonia oceanica*, in shallow water was studied by Ciraolo et al. (2001), and Ciraolo and Ferreri (2002).

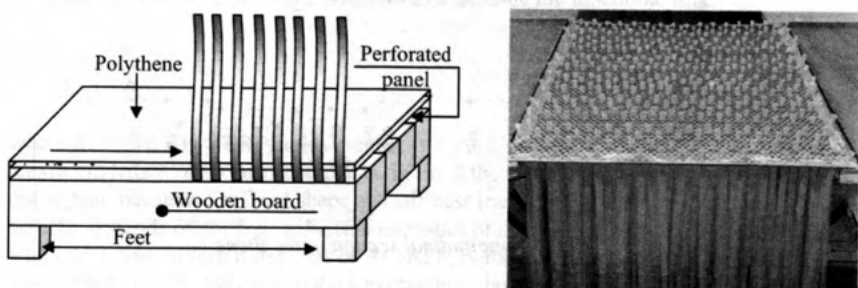
Recent studies involving both terrestrial (Raupach et al. 1996) and aquatic (Ikeda and Kanazawa 1996; Ghisalberti and Nepf 2002) vegetation have shown that the vegetation-flow interaction produces a mixing layer, with the formation of vortices responsible for the vertical transfer of momentum and, consequently, of nutrients.

The present paper reports some results relative to experimental research in a laboratory flume, whose bottom was covered by artificial vegetation analogous to *Posidonia oceanica*. These results concern flow resistance and velocity profiles. The latter are relative to a situation with continuous vegetated bottom and with discontinuous vegetated bottom. The aim is to provide a contribution to basic understanding of the complex phenomena, so that further work can better investigate the inter-relationships between flow, ecology and sediment within seagrass meadows.

## EXPERIMENTAL SETUP

The experiments were carried out in a horizontal laboratory flume 26.3 m long and 0.77 m wide, in which a maximum water depth of 0.53 m could occur. The upstream water supply tank was 4.95 m by 2.3 m and was deep enough to dissipate the turbulence caused by the water leaving the feed pipe. This allowed undisturbed conditions to be assumed in the flume, particularly at the measurement section, located 17.3 m downstream from the

tank. At the downstream end of the flume, a tilting metal grid allowed the water depth of a sub-critical flow to be regulated.



Figs. 2 a) plants insertion, b) plant distribution

On the flume bottom, several wooden panels (Fig. 2a) carrying the experimental plants were laid for a length of 9.6 m. Each panel, about 1 m long and 77 cm wide (as the flume), was fitted with adjustable screws under the four feet, to allow the vegetated bed resulted level. Actual plants of *Posidonia oceanica* were simulated by artificial ones, as in other analogous studies (e.g. Ghisalberti and Nepf 2002). Artificial shoots were made using strips of 0.2 mm thick polythene. Each shoot had three pairs of 1 cm wide leaves: the external pair was 50 cm long, the intermediate 25 cm and the inner 12.5 cm. The shoots were inserted in the holes of a pre-pierced 1 mm thick steel sheet (Fig. 2b), wrapped by a polythene sheet to reduce the friction caused by the empty holes. The plants were located with a regular distribution chosen to avoid the formation of preferential longitudinal paths. The resulting density was of  $1037 \text{ plants m}^{-2}$ , which is within the range of densities found in nature.

Velocity measurements were taken by a bi-dimensional ultrasonic instrument of ADV type made by Nortek. A sampling frequency of 25 measurements per second was chosen (the maximum allowed by the instrument), and the sampling time was of at least 2 minutes for each measurement point. Flow depths were measured by piezometers with diameter of 50 mm, equipped with a water gauge with a 1/10 mm nonius.

Two situations were considered: *continuous* and *discontinuous* vegetated bed, the latter obtained by the removal of a panel approximately 5.5 m downstream from the start of the vegetated bed (gap of 1 m). Fig. 3 shows the discontinuous vegetated stretch, and the measurement sections. The latter are marked by a number that indicates the distance (in centimetres) downstream from the start of the vegetated stretch.

The continuous situation was used for the study of both of flow resistance and velocity distribution. Thus, wide ranges of velocity (from 4 to 67 cm/s) and depth (from 11 cm to 45 cm) were examined. Flow depth was measured in sections 550 and 650, while velocity was measured in section 550.

The discontinuous situation was used to investigate the effects of the gap on the velocity distribution. Two flow velocities ("fast" and "slow") were considered. Fast velocity was of 5.49 cm/s, analogous to that observed for the tidal peak, while a value of 1.69 cm/s was chosen for slow velocity, close to an observed situation of tidal inversion, both at the same lagoon mouth (Nasello and Ciraolo, 2004). The water depth just downstream of the gap was 45.8 and 46.7 cm for fast and slow flow respectively. Velocity measurements were taken along the middle verticals of the eleven sections in Fig. 3. Along each vertical, the measurements were taken in points distant 2 cm or less each other.

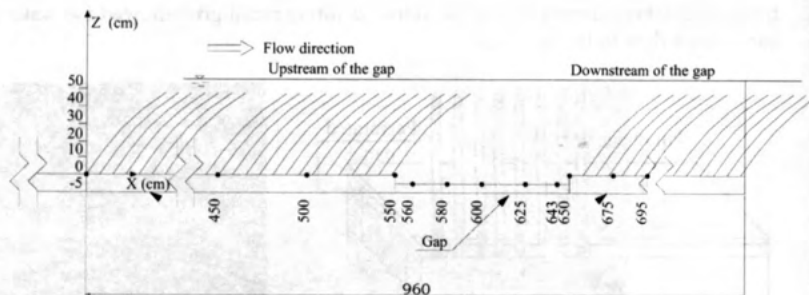


Fig. 3 Longitudinal section of the flume

## RESISTANCE LAW

A classic method to determine the flow resistance is the application of the momentum equation to a control volume, which allows one to calculate the hydraulic resistance  $T$ . The flow momentum equation applied to the control volume between sections 1 and 2 (Fig. 4), projected along the stream direction, gives:

$$T = G \sin \varphi + \Pi_1 + M_1 - \Pi_2 - M_2 = \gamma WS + \gamma h_{G,1} A_1 + \beta_1 \rho Q U_1 - \gamma h_{G,2} A_2 - \beta_2 \rho Q U_2 \quad (1)$$

in which  $G$  = the control volume weight,  $\varphi$  = the angle that the bottom forms with the horizontal,  $\Pi_1$  and  $\Pi_2$  = the pressure forces in sections, respectively, 1 and 2,  $M_1$  and  $M_2$  = the momenta in sections 1 and 2 respectively,  $\gamma$  = the specific weight of water,  $W$  = the control volume,  $S \approx \sin \varphi$  the bottom slope, in our case equal to zero,  $h_{G1}$  and  $h_{G2}$  = the depths of the centroids under the free surface of sections 1 and 2 respectively,  $A_1$  and  $A_2$  = the areas of sections 1 and 2 respectively,  $\beta_1$  and  $\beta_2$  = the momentum correction coefficients in sections 1 and 2 respectively, and  $U_1$  and  $U_2$  = the mean velocities in sections 1 and 2 respectively.

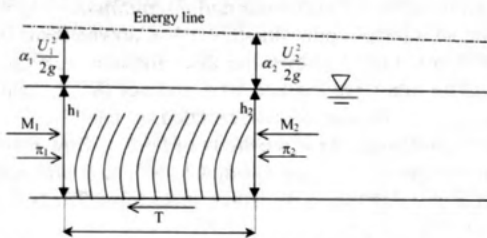


Fig. 4 - Control volume between sections 1 and 2, for determination of flow resistance

In the acceptable hypothesis that wall resistance is negligible with respect to the vegetated bottom (i. e. the hydraulic radius  $R$  is almost equal to the flow depth  $h$ ), the resistance  $T$  is linked to the friction factor  $\lambda$  of Darcy-Weisbach's formula by:

$$T = \tau_0 B \Delta x = \frac{\lambda}{8} \rho U^2 B \Delta x \quad (2)$$

where  $\tau_0$  = the mean resistance per unit area of the bottom,  $B=60$  cm the flume width,  $\Delta x=1$  m the control volume length,  $\rho$  = the water density, and  $U$  the velocity computed in the section with the mean depth  $h_m = (h_1 + h_2)/2$ .

The flow resistance was computed in the continuous situation, in which the flow depth was measured in sections 550 and 650, which correspond to sections 1 and 2 of Fig. 4 respectively. The  $\lambda$  values were then used to determine the functional link:

$$\lambda = f\left(Re; \frac{h_v}{h}\right) \quad (3)$$

where  $Re = U \cdot h/v$  is the Reynolds number ( $v$  = the kinematic viscosity), and  $h_v = 49$  cm the maximum length of the artificial plants. In Eq. 3 the height  $k$  of the inflected plants does not appear, because, for fixed shape and stiffness (negligible) of the experimental plants,  $k$  actually depends on the hydraulic characteristics of the flow ( $h, U, \rho e v$ ) and on the plant length ( $h_v$ ), thus in turn it depends on  $Re$  and  $h_v/h$ . Indeed, suitable tests carried out by us, also considering the ratio  $k/h$  in the  $\lambda$  expression, showed that the latter actually does not affect the  $\lambda$  value.

In practice  $\lambda$  can be expressed as a function only of the particular Reynolds number:

$$Re_v = \frac{U \cdot h_v}{v} \quad (4)$$

Thus, the following expression was achieved:

$$\lambda = 6.07 \cdot 10^5 \cdot Re_v^{-1.24} \quad (5)$$

with a regression coefficient  $r^2 = 0.74$ . The good fit of (5) to the experimental points is shown in Fig. 5.

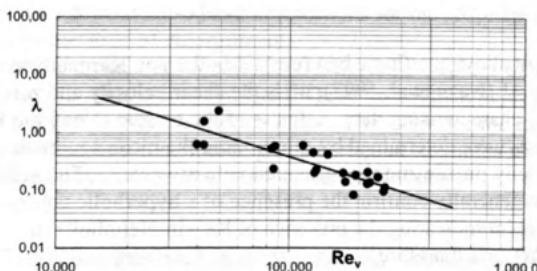


Fig. 5 Fitting of Resistance Law to the experimental points

The practical importance of Eq. 5 is evident: it allows one to calculate the friction factor only knowing the mean flow velocity and maximum leaf length of *Posidonia oceanica* in the computing cell considered. This simple relationship clearly indicates that, for given characteristics of the *Posidonia oceanica* grassland (in particular the leaf length  $h_v$ ), the friction factor  $\lambda$  decreases as the flow velocity  $U$  increases. From a physical viewpoint, this result is attributable to the very considerable flexibility of the leaves, which are erect for low velocities but lie down more and more as  $U$  increases. This implies that, on the one hand, the flow layer blocked by the vegetation is reduced and, on the other hand, the angle of incidence of the flow with the leaves decreases. It should be noted that, even when the leaves are prone, the layer occupied by the vegetation is still thick, involving a large part of the flow. These results are consistent with the conclusions of other researchers who have

studied the hydraulic resistance of flexible vegetation (e. g. Bakry et al., 1992; Järvelä, 2002).

### VELOCITY PROFILES

Velocity profiles were produced for each of the measurement verticals and the Prandtl semi-logarithmic equation (Schlichting 1955) fitted to the upper sector of the profiles. In addition, Reynolds stress trends have been analysed. These profiles typically have three zones: in the first, low velocities are encountered within the vegetation near the bed; at the canopy-water interface and just above it there is a second zone of rapidly increasing velocity; then there is a third zone near the surface where velocity is high but does not vary with depth.

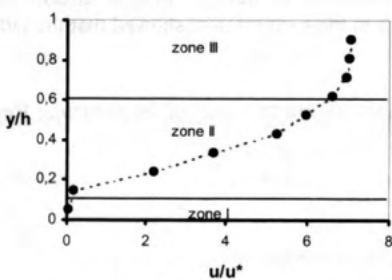


Fig. 6 - Velocity profile

Having plotted the velocity profiles (Fig. 6) for each measurement vertical, the Prandtl semi-logarithmic equation (6) was fitted to the velocity data in the uppermost sector of flow:

$$V_x = \frac{u^*}{\kappa} \ln(z/z_0) \quad (6)$$

where  $z$  is the height above the flume bed (cm),  $\kappa$  is the von Kármán "constant" here assumed equal to 0.41 (Nezu et al. 1997),  $u^*$  is the shear velocity and  $z_0$  is the theoretical "roughness height" characterising the roughness of the bottom (Nepf and Koch 1999). The parameters  $u^*$  and  $z_0$  were determined by minimizing the mean square deviation between the theoretical velocity profile and the measured velocity profile. The velocity profiles of the *fast* experiment generally confirm the presence of a hyperbolic tangent-like profile, with an inflection point indicating the presence of Kelvin-Helmholtz instability (KHI) (Holmes et al. 1998), and therefore vortex activity (Ghisalberti and Nepf 2002).

The velocity profiles upstream of the gap show low velocity values with an average close to zero in the first two decimetres from the bed (where the canopy is more rigid), as found by Nepf and Vivoni (2000). Above this height the velocity field develops a typical rough surface logarithmic profile. Within the vegetation downstream of the gap the velocity profile no longer shows this secondary vortex, and the trend is analogous to that of verticals upstream of the gap.

There is a good fit between the measured velocity in the upper sector and the theoretical velocity profile ( $r^2$  is always higher than 0.95).

The upper part of the mixing layer, below the logarithmic profile is known as the roughness sublayer (Nepf 2004). The roughness height is almost constant upstream of the gap, in the gap it then strongly increases before decreasing downstream, it increases again becoming almost constant downstream of the gap. The shear velocity has an analogous trend along the longitudinal profile.

The *slow* experiment shows two sectors in the velocity profiles with similar behaviour to that of the *fast* case. With respect to the *fast* experiment, slower velocities and a larger lower sector are evident.

Within the gap, an inversion of velocity occurs in the lower flow sector from vertical 600, whereas in the *fast* experiment this inversion was found from 580 onwards indicating the presence of a negative secondary vortex (separation cell). The verticals downstream of the gap show analogous behaviour to those upstream.

Reynolds stress profiles show maxima at the canopy roof where a mixing layer exists. In slower flow the plants are quasi-emergent and flow speeds and Reynolds stress are more uniform.

## CONCLUSIONS

We experimentally examined the hydraulic behaviour of the *Posidonia oceanica*, a plant characteristic of sandy coastal areas in the Mediterranean Sea. The experiments, carried out in a laboratory flume in which the vegetation was artificially reproduced by polyethylene strips, first allowed us to recognize that as flow velocities increased, the low flow region became shallower; and that as water depth increased, the zone of low flow maintained a relatively constant height, while the height of the other zones increased. In applying these results to the flow conditions prevalent in shallow waters, it can be seen that the low velocity flow zone would retain a fairly constant depth, as water velocities do not increase above  $40 \text{ cms}^{-1}$  and the height of the zone is not affected by the water depth. Results confirm the behaviour found in other research, showing two sectors of constant velocity with an interposed transitional zone. Inside the gap, a negative secondary vortex is formed, showing as an inversion of velocity occurring in the lower flow sector.

The zone of very low flow close to the bed encourages sedimentation and reduces the rate of sediment entrainment by the water. This has the ecological effect of stimulating further plant growth and affecting the settlement of benthic fauna. The region of greatest turbulence was found to be at the dynamic boundary between the seagrass canopy and the unobstructed water, which would also have implications for the sediment and ecological processes operating in this kind of environment.

By the application of the momentum equation for each run, the values of the friction factor of the Darcy-Weisbach formula were calculated. These values then made it possible to achieve a monomial expression of the friction factor. The latter, for the experimental areal density of plants, proves to be a function only of a particular Reynolds number, constructed with the mean flow velocity and the *Posidonia oceanica* leaf length.

## REFERENCES

- Bakry, M. F., Gates, T. K. and Khattab, A. F. (1992). "Field-measured hydraulic resistance characteristics in vegetation-infested canals". *J. Irrig. and Drain. Engrg.*, ASCE, 118(2), 256-274.
- Cinelli, F., Pardi, G. & Papi, I. (1995) "Plant biology. La Posidonia Oceanica" (Cinelli, F., Fresi, E., Lorenzi, C. & Mucedola, A.), *Rivista Marittima*, Roma, 21-24.
- Ciraolo, G., Ferrante, F., Ferreri, G. B., Folkard, A. and La Loggia, G. (2001). "Flow resistance of ribbon-like vegetation long and very flexible in shallow water". *Proc. of 3<sup>rd</sup> International Symposium on Environmental Hydraulics*, Dec., Tempe, Arizona USA, CD-ROM.
- Ciraolo, G., and Ferreri, G. B. (2002). "Resistenza al moto di una corrente su un fondo ricoperto da Posidonia oceanica". *Proc. of XXVII Convegno di Idraulica e Costruzioni Idrauliche*, Vol. 3, Sep., Potenza, Italy, pp. 369-376.
- Escartin, J. and Aubrey, D. G. (1995). "Flow structure and dispersion within algal mats". *Estuarine, Coastal and Shelf Sci.*, 40, 451-472.

- Francour, A., Ganteaume, A., and Poulain, M. (1999). "Effects of boat anchoring in *Posidonia oceanica* seagrass beds in the Port-Cros National Park (north-western Mediterranean Sea)." *Aquat. Conserv.*, 9, 391-400.
- Folkard, A. M., Maltese, A., Lombardo, G., Circolo, G. and La Loggia, G. (2003). "Coherent flow structures in gaps within meadows of *Posidonia oceanica*", *Proc. of XXX IAHR Congress, Coastal Environment: processes and integrated management*, Aug., Thessaloniki, Greece, pagg. 595-602.
- Freeman, G. E., Rahmeyer, W., Derrick, D. L. and Copeland, R. R. (1998). "Manning's values for floodplains with shrubs and woody vegetation". *Proc. of USCID Conference on Shared Rivers*, Oct. 28-31, Park City, Utah, U.S. Committee on Irrigation and drainage, Denver, Colorado.
- Holmes, P., Lumley, J.L., and Berkooz, G. (1998). *Turbulence, Coherent Structures, Dynamical Systems and Symmetry*, Cambridge University Press, New York.
- Ikeda, S., and Kanazawa, M. (1996). "Three-dimensional organized vortices above flexible water plants." *J. Hydraul. Eng. - ASCE*, 122(11), 634-640.
- Ghisalberti, M. and Nepf, H. M. (2002). "Mixing layers and coherent structures in vegetated aquatic flows". *J. Geoph. Res.*, 107(C2), 1-11.
- Järvälä, J. (2002). "Flow resistance of flexible and stiff vegetation: a flume study with natural plants". *J. Hydrol.*, 269, 44-54.
- Nasello, C. and Ciraolo, G. (2004). "Misure idrodinamiche nello Stagnone di Marsala." *Proc. XXIX Convegno di Idraulica e costruzioni idrauliche*, Editoriale Bios, Cosenza, Italy, 1(A3), 699-706.
- Nepf, H.M. (2004). "Vegetated flow dynamics." In Fagherazzi, S., Marani, M., and Blum, L.K. (Eds) *The ecogeomorphology of tidal marshes*, Coastal and Estuarine Studies, Volume 59. American Geophysical Union, Washington DC.
- Nepf, H.M., Sullivan, J.A. & Zavistoski, R.A. (1997) A model for diffusion within emergent vegetation. *Limnology and Oceanography* Vol. 42(8): 1735-1745.
- Nepf, H.M., and Koch, E.W. (1999). "Vertical secondary flows in submersed plant-like arrays." *Limnol. Oceanogr.*, 44(4), 1072-1080.
- Nepf, H. M. and Vivoni, E. R. (2000). "Flow structure in depth-limited, vegetated flow". *J. Geoph. Res.*, 105(C12), 28,547-28,557.
- Nezu, I., Kadota, A. and Nakagawa, H. (1997). "Turbulent Structure in Unsteady Depth-Varying Open-Channel Flows." *J. Hydraul. Eng. - ASCE*, 123(9), 752-763.
- Rahmeyer, W., Werth Jr., D. and Freeman, G. (1999). "Improved methods of determining vegetative resistance in floodplains and compound channels". *Proc. of ASCE Conference on Water Resources*, August 8-12, Seattle, Washington, American Society of Civil Engineers, Reston, Virginia.
- Raupach, M. R., Finnigan, J. J. and Brunet, Y. (1996). "Coherent eddies and turbulence in vegetation canopies: The mixing layer analogy". *Boundary Layer Meteorolog.*, 78, 351-382.
- Schlichting, H. (1955). *Boundary layer theory*. Pergamon Press LTD, London.
- Short, F.T. and Wyllie-Echeverria, S. (1996). "Natural and human-induced disturbance of seagrasses." *Environ. Conserv.*, 23, 17-27.

the role of the environment in the formation of algae in coastal waters. The result, as usual, with emphasis on existing research.

#### INTRODUCTION

##### Algal bloom

## BIOGEOCHEMICAL-PHYSICAL INTERACTIONS

The term "biogeochemical-physical interactions" is used here to denote the complex processes which occur between living organisms and their physical environment. The physical environment includes the atmosphere, the water, the soil, and the bottom sediments. The biological environment includes the plants, animals, and microorganisms.

The study of biogeochemical-physical interactions is important because it helps us to understand the relationships between living organisms and their environment. It also helps us to predict how changes in the environment will affect living organisms.

The study of biogeochemical-physical interactions is important because it helps us to understand the relationships between living organisms and their environment. It also helps us to predict how changes in the environment will affect living organisms.

The study of biogeochemical-physical interactions is important because it helps us to understand the relationships between living organisms and their environment. It also helps us to predict how changes in the environment will affect living organisms.

The study of biogeochemical-physical interactions is important because it helps us to understand the relationships between living organisms and their environment. It also helps us to predict how changes in the environment will affect living organisms.

The study of biogeochemical-physical interactions is important because it helps us to understand the relationships between living organisms and their environment. It also helps us to predict how changes in the environment will affect living organisms.

The study of biogeochemical-physical interactions is important because it helps us to understand the relationships between living organisms and their environment. It also helps us to predict how changes in the environment will affect living organisms.

BLÖDINGEOMORPHISME  
WILHELM VON KLEIST

## Modelling the physical structure and the succession of algea in two basins of Lake Mälaren, Sweden, with emphasis on mixing depth

Irina Persson<sup>1</sup> and Hampus Markensten<sup>1,2</sup>

<sup>1</sup>*Limnology/Department of Ecology and Evolution  
Evolutionary Biology Centre  
Uppsala University  
Norbyv. 20  
SE-752 36 Uppsala  
Sweden*

<sup>2</sup>*Department of Public Technology  
Mälardalen University  
Västerås Sweden*

In this study, we are modelling the physics and biology of a shallow (Galten) and a deep (Ekolsn) basin of Lake Mälaren (Sweden's third largest lake) focusing on different mixing depth calculations and the effect on phytoplankton dominance and species succession. Today, Galten and Ekolsn, both eutrophic and of interest for recreation, are regularly suffering from algal blooms in late summer.

We applied the physical lake model PROBE (PROgram for Boundary layers in the Environment) and the algae succession model PROTBAS (PROTech Based Algal Simulations). As input data to the physical lake model, we used a consistent time series of grid data over Sweden based on meteorological stations with a resolution of ( $1 \times 1$ )° squares. The meteorological stations around the lake are weighed together, which provides high quality local data with high temporal resolution. The aim was primarily to analyse the effect on algal dominance from various ways of estimating the mixing depth in the two basins. Mixing depth was calculated in the four following ways: 1) maximum temperature gradient, 2) maximum density gradient, 3) the depth when the temperature changes more than 1 °C /m and 4) the depth where the kinetic energy vanish. The study clearly shows that the two models could successfully be used in sequence. Estimating the mixing depth as when the energy vanish differed from the other methods in terms of being more dynamic, which also had an influence on the phytoplankton.

and does not appear to have had any effect on the results. Thus, it is not clear whether the significant differences between the two models are due to model bias or to the different ways in which the data were used.



Fig. 1. Scatter plot of the relationship between the number of species ( $S$ ) and the number of individuals ( $I$ ) for all the data sets used in this study. The data points are open circles and the solid diagonal line represents the 1:1 relationship.

Although the scatter plot shows a strong positive correlation between the number of species and the number of individuals, the data points do not follow a single linear trend. There is considerable scatter around the 1:1 line, particularly at higher values of  $I$ .

The mean and standard deviation (SD) of the ratio of the number of species to the number of individuals for each data set are given in Table 1. The mean ratios range from 0.00632 to 0.02632, and the SDs range from 0.00041 to 0.00113. The data points for each data set are plotted in Fig. 2, and the mean ratios are shown as open circles. The data points for each data set are plotted in Fig. 2, and the mean ratios are shown as open circles. The data points for each data set are plotted in Fig. 2, and the mean ratios are shown as open circles.

The data points for each data set are plotted in Fig. 2, and the mean ratios are shown as open circles. The data points for each data set are plotted in Fig. 2, and the mean ratios are shown as open circles. The data points for each data set are plotted in Fig. 2, and the mean ratios are shown as open circles.

The data points for each data set are plotted in Fig. 2, and the mean ratios are shown as open circles. The data points for each data set are plotted in Fig. 2, and the mean ratios are shown as open circles. The data points for each data set are plotted in Fig. 2, and the mean ratios are shown as open circles.

The data points for each data set are plotted in Fig. 2, and the mean ratios are shown as open circles. The data points for each data set are plotted in Fig. 2, and the mean ratios are shown as open circles. The data points for each data set are plotted in Fig. 2, and the mean ratios are shown as open circles.

The data points for each data set are plotted in Fig. 2, and the mean ratios are shown as open circles. The data points for each data set are plotted in Fig. 2, and the mean ratios are shown as open circles. The data points for each data set are plotted in Fig. 2, and the mean ratios are shown as open circles.

## EVIDENCE OF THE ROLE OF HORIZONTAL ADVECTION AND SURFACE VERTICAL MIXING IN THE PHYTOPLANKTON DISTRIBUTION IN A STRATIFIED RESERVOIR

T. Serra, J. Vidal, J. Colomer, X. Casamitjana, M. Soler. Department of Physics, University of Girona. Campus Montilivi. 17071-Girona (Spain). e-mail: teresa.serra@udg.es

Determining the ecological consequences of a change in the physical structure in the water column of an aquatic system due to different forces acting on spatial or temporal scales such as wind stress, cooling and heating rates or seiching is a challenge for the control of ecosystem productivity. The time resolution used during the study has important implications on the observed dynamics.

In this study, the competition between horizontal advection, convection and mixing induced by wind shear stress and their roles in the transport of phytoplankton through the water column will be investigated during two different stratified periods of the water column. The suspended particles under study will be the algae populations thriving in the epilimnetic layer of the water column. We will pay attention to whether the different populations present different behaviors or respond equally under the same physical forcing acting on the system.

Sau is a canyon shaped reservoir 18.225 Km long (Figure 1) situated in the central part of the river Ter, which is 200 Km long and has its source in the Pyrenees in the NE of Spain. This reservoir has an elongated geometry with a lacustrine area 3600 m long and a maximum width of 1300 m (Armengol et al., 1999). During the morning the wind usually blows from the main body of the reservoir towards the dam and in the late afternoon and evening the wind reverses its direction and blows from the dam towards the main body of the reservoir. This action of the wind along the main axis of the reservoir leads us to expect the presence of seiches following this axis (Vidal et al., 2005). The stations considered for this study (S1, S2 and S3) are situated at approximately 200 m, 800 m and 1600 m from the dam, respectively (see Figure 1). The depth of the reservoir at station S1 was 39 m and 47 m for the July and September surveys, respectively.

In this study, profiles of the fluorescence of different phytoplankton populations were carried out with an *in situ* submersible five-channel fluorimeter (bbe Moldaenke). This

probe determines four different algae populations previously calibrated in the laboratory. Additionally, the depth is measured using a pressure sensor integrated in the probe and temperature is measured with a sensor beside the transmission window. Measurements of current velocity profiles were carried out with an acoustic Doppler profiler (RDI 600 kHz, Workhorse Sentinel). The ADCP was deployed on the water surface with the beams facing downwards. As a result, we were not able to get information about the water surface velocity (i.e. from 0 to 3 m deep). Continuous data from a moored thermistor string (Aanderaa) were also available. Also, from the meteorological station situated near the dam of the reservoir the air temperature ( $T_a$ , in °C), the relative humidity (RH, in %), the short wave radiation ( $q$ , in  $\text{Wm}^{-2}$ ) and the wind velocity ( $U$ , in  $\text{m s}^{-1}$ ) were obtained. Measurements of fluorescence were taken hourly during a 24-hour cycle at a fixed station (S2, Figure 1) in the Sau reservoir (Catalonia, Spain). This study was carried out during two different stratified conditions of the water column. The first survey was in July 2003 and the second survey was in September of the same year. In July, the field campaign began at 1600 h on the 23<sup>rd</sup> and continued until 1500 h on the 24<sup>th</sup>. In September, the field campaign went from 1200 h on the 24<sup>th</sup> to 1200 h on the 25<sup>th</sup>. For the survey carried out in September, measurements of fluorescence at larger time intervals (~ 4 hours) and at other stations (S1 and S3, see Figure 1) were also taken.

In July, the water column was continuously stratified from the top of the water column downwards. The temperature of the water at the surface was in the 26–28°C range, decreasing to approximately 15 °C at 20 m of depth. Temperature profiles taken in the evening show a slight decrease in temperature of the surface layer. At around 0900 on the second day, this layer is mixed and attains a constant temperature value in the range of 25–26°C. The lowest surface temperature value is reached at the beginning of the morning hours. This mixed surface layer is 1 m thick at 1700 and increases to 4 m at 0630. During the day, solar radiation reestablishes the stratified pattern of the water column with the highest temperature at the surface of the water column decreasing continuously down to the bottom. In September, the temperature gradient is not as continuous as it is in July, and the typical three-layer pattern (epilimnion, metalimnion and hypolimnion) can be appreciated. The epilimnion extends from the surface down to ~15 m of depth with a constant temperature value of ~22°C. The metalimnion goes from 15 m deep to 25 m deep, and from this depth down to the bottom there is the hypolimnion with a constant temperature of ~9°C. In September, a 5 m thick layer is found again at the surface with a constant value of temperature for the profiles from 2130 h (profile not shown) on the first

day until 0500 h on the second day. The lowest values of the temperature at the surface of the lake were found in the morning hours during the second day.

Three different phytoplankton populations were found in the water column during both surveys (July and September): *green algae*, *diatoms* and *cryptophyceae*. In the July survey just a few exemplars of *blue green algae* were found, always with a concentration below 3  $\mu\text{g l}^{-1}$  integrated over the whole water column. *Green algae* were the most abundant and were found from the surface of the water column down to 10 m deep. Vertical profiles of *green algae* show a surface layer with a constant value of chlorophyll ranging from 6 to 12  $\mu\text{g l}^{-1}$ . The depth of this layer changes with time attaining the deepest value ( $\sim 4$  m) at night. At sunrise, the layer shallows and reaches the shallowest depth at noon. Below this layer, the *green algae* population presents a peak of maximum concentration located at a depth that varies with time. This maximum is  $\sim 5$  m deep at 1900 h after which it deepens to  $\sim 6$  m and remains at this depth until morning hours when the population forms a subsurface peak of 12  $\mu\text{g l}^{-1}$  at a depth of  $\sim 2$  m. *Diatoms* are distributed from the surface to a depth of 5 m. During the day diatoms form a subsurface peak at around 2 m deep while at night they are homogeneously distributed in a 4 m deep surface layer. *Cryptophyceae* show a pattern similar to *diatoms*. During the day they form a subsurface peak of 4-6  $\mu\text{g l}^{-1}$  which is situated at a depth of around 2 m. This pattern changes at night where vertical profiles of fluorescence show a constant value of 2  $\mu\text{g l}^{-1}$  in a layer 4 m thick situated at the surface of the water column. In the September survey, *green algae* show similar behavior to that found in July.

If we integrate the concentration of chlorophyll for the three phytoplankton groups over the whole water column, hereafter known as the total concentration of chlorophyll, it can be observed that in July the total concentration of *green algae* increases slightly from 120  $\mu\text{g l}^{-1}$  at the beginning of the survey, attains a maximum of 156  $\mu\text{g l}^{-1}$  at night, and then decreases slightly to 110  $\mu\text{g l}^{-1}$  on the second day (Figure 6a). In the September survey, *green algae* shows the same increase from day to night, but from the night to the second day it remains approximately constant until the end of the survey. In July, *diatoms* increase from a value of 9  $\mu\text{g l}^{-1}$  to a maximum of 40  $\mu\text{g l}^{-1}$  at night (Figure 6b), then decrease again to their initial value on the second day. In September, *diatoms* decrease slightly and continuously from 15  $\mu\text{g l}^{-1}$  on the first day to approximately 5  $\mu\text{g l}^{-1}$  on the second day. In July, the total *cryptophyceae* concentration begins at 5  $\mu\text{g l}^{-1}$  on the first day and then

decreases slightly to  $1 \mu\text{g l}^{-1}$  on the second day (Figure 6c), while in September it decreases from  $15 \mu\text{g l}^{-1}$  and reaches the lowest value of approximately  $5 \mu\text{g l}^{-1}$  at night. From this point onward the population increases strongly, reaching values of  $30 \mu\text{g l}^{-1}$  at 1300 h on the second day (Figure 6c).

Temperature also changes with depth due to wind shear and night cooling. At night the surface layer has a constant temperature value while below this layer the temperature decreases again. During the day, this structure breaks down and the column has a maximum temperature at the surface, decreasing constantly with depth. The depth of the interface where a change in temperature can be found due to night cooling will hereafter be known as the diurnal thermocline. Its depth is drawn in Figure 3a for the July survey and in Figure 3b for the September survey. It deepens from 1 m during the day to 4 m deep at night. During both the July and September surveys the diurnal thermocline begins to deepen at 1600 h and remains at ~4-5 m through the night. At sunrise (~0900 h) it begins to shallow, reaching a depth at 1300 h of 2 m in July and 1 m in September. From the vertical profiles of phytoplankton we can obtain the depth of the interface where each population (*green algae*, *diatoms* and *cryptophyceae*) present a maximum change in the concentration (represented in Figure 3a for the July survey and in Figure 3b for the September survey). The interface of each population deepens at night to around 5 m in both surveys and becomes shallower during day, reaching the same depths in both the July and September surveys. Therefore, the behavior of the interface coincides with the behavior of the diurnal thermocline.

This data set from the Sau reservoir demonstrates the effect of vertical and horizontal movements of the water on the phytoplankton distribution in the column. Both wind shear stress and convection due to cooling contribute to the deepening of the surface layer and also to the formation of a mixed distribution of phytoplankton at the surface. Generally, mixing due to surface cooling dominates at night, while mixing due to the wind shear stress dominates during the day. Horizontal advection due the wind driven current at the surface of the water column also plays an important role in the transport of phytoplankton from other sites of the reservoir, indicating that the phytoplankton is distributed in patches along the reservoir. In addition, the wind excites internal waves or seiches in the reservoir. Seiches will affect the phytoplankton distribution in the water column in the reservoir from surface layers down to deeper layers. In this study, *green algae* reach deep layers in the water column and their distribution is determined by the seiching motion while *diatoms*

and *cryptophyceae*, situated at the top of the water column, are influenced by convection and mixing due to the wind shear stress. All of these processes have been schematized in Figure 4.

Horizontal heterogeneities measured at different stations along the reservoir and due to different habitats explain the variation in the total concentration of phytoplankton at a certain measurement point. Horizontal advection transports water parcels with characteristic phytoplankton composition from one region to another producing changes in the phytoplankton composition at the measured station.

All of these results demonstrate that the phytoplankton dynamics depend on several external factors and in order to understand their behavior it is necessary to determine all the external variables such as the heat balance, the wind velocity and the presence of internal wave oscillations. This study also makes it evident that, since each phytoplankton group selects its preferred position in the water column, the dynamics of each group will depend on the physics of the region where the phytoplankton is located. It is also important to consider high temporal and spatial measurements to complete the description of their dynamics.

#### Acknowledgments

This work has been supported by the Spanish government (MCYT) and the European Union (FEDER) through the CGL2004-02027 project. We would like to thank the Catalan Water Agency Aigües Ter-Llobregat for their support throughout the campaign. We would also like to thank Prof. Joan Armengol for his unconditional support.

#### References

- Armengol, J., Garcia, J.C., Comerma, M., Romero, M., Dolz, J., Roura, M., Han, B.H., Vidal, A. and Simek, K. 1999. Longitudinal processes in canyon type reservoirs: the case of Sau (N.E. Spain). *Theoretical Reservoir Ecology and its Applications*, eds. J.G. Vidal, J., Casamitjana, X., Colomer, J. and Serra, T. 2005. The internal wave field in Sau reservoir: Observation and modeling of a third vertical mode. *Limnology and Oceanography* (in press).

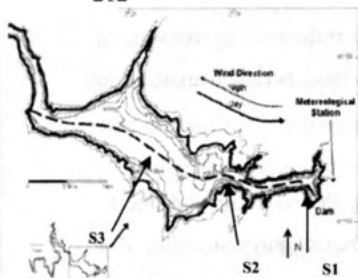


Figure 1

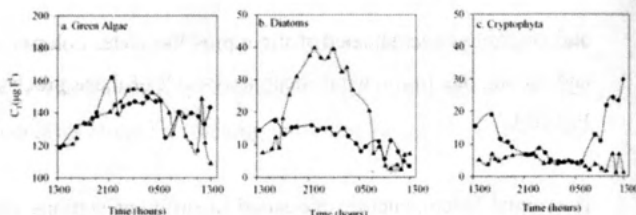


Figure 2

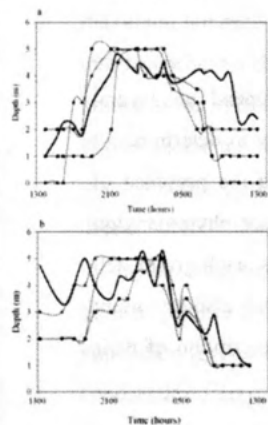


Figure 3

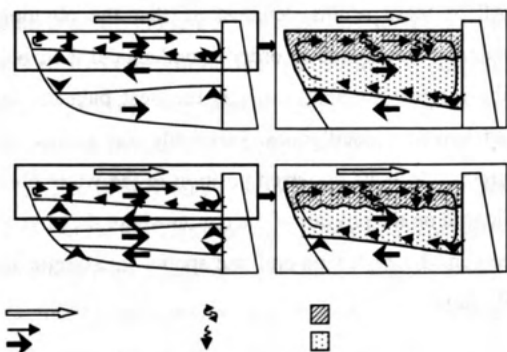


Figure 4

Figure 1. Bathymetric map of the Sau reservoir with the measured stations indicated as S1, S2 and S3. Dashed line represents the main axis of the reservoir and the direction in which the wind velocity and the water currents are projected.

Figure 2. Total concentration of *Green Algae* (▲), *Diatoms* (■) and *Cryptophyceae* (●) for both the July (▲) and September (●) surveys.

Figure 3. Interface depth for *Green Algae* (▲), *Diatoms* (■) and *Cryptophyceae* (●) and thermocline (thick solid line) for the July (a) and September (b) surveys.

Figure 4. Schematic diagram of the seiching, the wind driven current, the mixing due to wind and the surface cooling for the July (a) and September (b) surveys. The extension of green algae, diatoms and cryptophyceae has been also indicated in the enlarged diagrams situated in the right panels of each figure.

## A SYNOPTIC VIEW OF CARBON AND OXYGEN DYNAMICS IN EUROPEAN REGIONAL SEAS: AN APPROACH COUPLING HYDRODYNAMICAL AND BIOGEOCHEMICAL MODELLING AND SATELLITE DATASETS

Laurence Deydier-Stephan<sup>1</sup>, Adolf Stips<sup>1</sup>, Mark Dowell<sup>1</sup> & Wolfram Schrimpf<sup>1</sup>

<sup>1</sup>Inland and Marine Waters Unit, IES, JRC Ispra, Via E.Fermi, 21021 (VA) Ispra, Italy.

e-mail: [laurence.deydier-stephan@jrc.it](mailto:laurence.deydier-stephan@jrc.it)

We present the development of an accurate physical-biogeochemical coupled model for oxygen and carbon cycles in shelf and eutrophicated areas. Following the recent development of eutrophication indices for coastal and marine areas and several recent attempts to implement thorough but simple coupled benthic/pelagic model, we apply the model in highly eutrophicated and sensitive coastal areas of the European seas. We propose a new approach using coupled 3D hydrodynamic model GETM and 1D ecosystem model, additional supplied with primary production data derived from remote sensing. This approach allows us to get a synoptic view in time and space of carbon and dissolved oxygen concentrations for different basins. Our biogeochemical model includes coupled benthic/pelagic processes specifically addressing oxygen quantification in the sediment, as in the benthic and upper layers of the water column for biological and physical processes. This ecosystem model will be gradually transitioned from a simple Particulate Organic Carbon (POC) and Dissolved Oxygen (DO) model to a full NPZD/Sediment model, while being fully coupled with the hydrodynamic model for advection and diffusion processes. We have run the model for the Baltic Sea, for a first application and validation. Results are compared to simulations from other published ecosystem models. The model will be validated along with its application as an eutrophication assessment tool for European regional seas.

### CONCEPTUAL MODELING

Considering the different ecosystems models existing and their actual tendency, it was decided to build upon a simple but quantitative model for eutrophication impact assessment (Vidal *et al.*, 1999), following the DPSIR concept, especially for the oxygen depletion risk, in the coastal shelf areas. Inspired from this concept the focus is first on pressure: physics and nutrients, then on state: higher primary production and production of organic matter, for modeling some of the most visible and worst impact for the ecosystem state: oxygen deficiency. The parameterization of this model is done for a coupled 1D hydrodynamic-biogeochemical model supplied by primary production (PP) derived from remote sensing data. Following some recent developments of ecosystem modeling and eutrophication assessment, as OXYRISK (Djavidnia *et al.*, 2005) and ERGOM (Neumann, 2000; Neumann *et al.*, 2002) a 1D model is developed for Particulate Organic Carbon(POC)/ Dissolved Oxygen (DO) for coastal and marine areas exposed to eutrophication. Furthermore a 'sediment box' is added considering this compartment and its major processes interacting with the pelagic compartments (diagenetic benthic model, Soetaert *et al.*, 1996), but slightly simplified as recommended by Soetaert *et al.* (2000) for carbon and oxygen sources and sinks. The equations are written for each compartment and state variable representing sources and sinks for carbon and oxygen, together with physical processes, such as diffusion (molecular and turbulent), reaeration due to wind stress and bottom shear stress for oxygen dynamics (fig.1). Hence, for each state variable POC and DO, the equations are solved for the mixed layer, pycno, bottom and sediment layers.

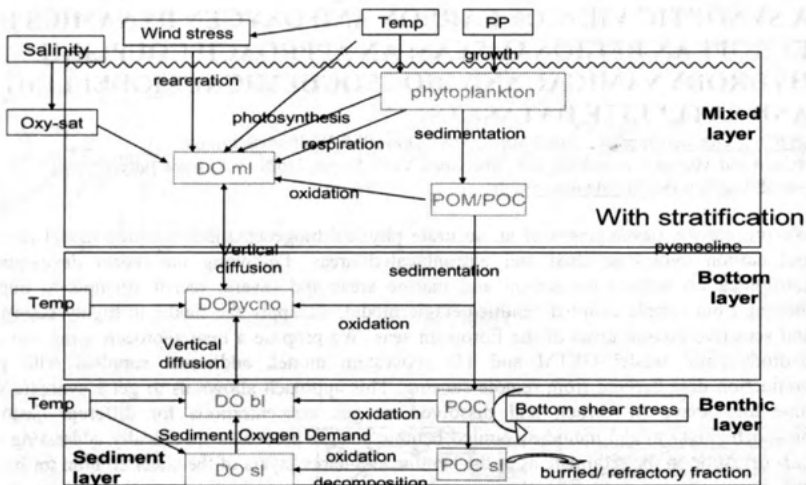


Figure 1: Conceptual sketch of the 1D biogeochemical model with variables (in grey) and processes, considering GETM outputs and remote sensing data as forcing functions (in black).

## MATERIALS & METHODS

### HYDRODYNAMICAL MODEL

The 3D hydrodynamic model used in this study is called GETM / General Estuarine Transport Model and has been developed and validated for the Baltic Sea and North Sea (Burchard & Bolding, 2002, Stips *et al.*, 2004). Meteorological parameters, such as winds, precipitation or evaporation provide the model forcing and the model has a spatial horizontal discrete grid of 5.5 km. Typical variables computed by this model are water temperature, salinity, turbulent diffusivities, mixed layer and bottom layer thickness and bottom shear stress. These results are used as data or forcing functions in the biogeochemical model, together with the wind stress, coming from an ECMWF model. All these outputs are given bi-daily and used after an interpolation to obtain the same time-step and inputs for the biogeochemical model and the whole year run.

### PRIMARY PRODUCTION MODEL

The model of primary production/algorithm used is suitable specifically for coastal waters, using remote sensing data and especially Chl-a, PAR, Kd, SST measurements. This model is integrated over the mixed layer, computed by the hydrodynamic model and is based on a formulation obtained through dimensional analysis by Platt and Sathyendranath (1993). The assignment of the photosynthetic parameters PBmax and Ek is achieved by the combined use of a temperature dependent relationship for the maximum growth rate (Eppley, 1972) and the use of variable formulation to retrieve the C: Chl ratio following the empirical relation of Cloern *et al.*, (1995).

### VALIDATION SITES

In order to verify if this model for the oxygen cycle is valid, the equations and their applicability are verified using *in situ* data in different areas of the Baltic Sea: Great Belt Sea, Kattegat (Fladen, Alborg, Anholt), Bornholm and Arona Basins and Gotland Sea (fig.2).

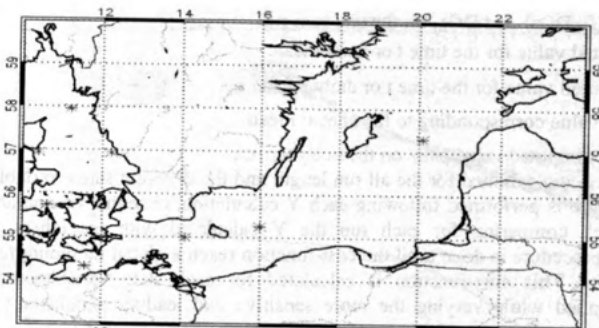


Figure 2: Baltic Sea with stations coordinates

### SENSITIVITY ANALYSIS

Following, the ecosystem theory for building, calibrating and validating an accurate model (Jorgensen, 1992), a sensitivity analysis is compulsory, allowing the calculation of the sensitivity and correlation of the model components. Considering the uncertainty of the model, i.e. the addition of errors in measurements and lack of precision for parameter estimation and the final objective of this model to be applied on a pan-European scale, we performed a global sensitivity analysis, varying the value of each model components considered as a parameter, within the whole range of values found in the literature for biogeochemical models for estuaries, lagoons and shallow seas. The model sensitivity analysis is performed individually, varying each parameter one by one, for 3 sets of initial or optimal values. The sensitivity of the model parameters is evaluated for the different model components contained in our model Friedrichs (2001). This formula is applied not only for fractional increase but also decrease, as the uncertainty evaluation is included in this global sensitivity analysis.

The sensitivity of a certain model component or variable C: DO or POC for mixed layer, pycnocline, bottom and sediment layers, to a given model parameter X: the different parameters showed in table 1, is defined as the fractional change in C due to a fractional change: i in the value of the parameter X.

$$S_{C,X} = \frac{\frac{C_X - C_{X \pm i}}{C_{X \pm i}}}{\frac{X - X_{\pm i}}{X_{\pm i}}}$$

### CALIBRATION

For calibration, we firstly compared the weekly/monthly means, variance distribution and linear correlation coefficient of field/remote sensing data of PP for the first station chosen: Belt Sea.

Then comparisons of in situ/model temperature and salinity distributions and further correlation coefficient calculations are processed for the averaged boxes mixed, pycno and bottom layers, and corresponding pairs of data or sampling date.

Calibration itself is performed following the formula of Jorgensen (1992) on DO mixed, pycno layers and bottom layers, for daily averages but only for the matching days between observed and simulated values.

The cost-function is calculated using the following formula:

$$Y = \left[ \frac{\sum \left( \frac{X_C - X_M}{X_{M,A}} \right)^2}{N} \right]^{1/2}$$

For Y the cost function of  $DO_{ML}$ ,  $DO_{PL}$  and  $DO_{BL}$  on the one year run

$X_C$  = the state variable computed value for the time t or daily mean,

$X_M$  = the corresponding measured value for the time t or daily mean

$X_{M,A}$  = the average measured value corresponding to the annual mean

And N = number of measured-computed value pairs on the one year run

These differences are calculated and summed for the all run length and the different states variables in 1998. An optimization procedure is performed following each Y calculation, changing one parameter value and running the model, comparing for each run the Y calculated with the others. This optimization or minimization procedure is done until the cost-function reach a global minimum for the final model simulation results. This cost-function is calculated for each state variable and the optimization procedure is applied while varying the more sensitive and leading parameter model values, revealed by the sensitivity analysis.

## RESULTS AND DISCUSSION

### ONE-YEAR RUN OF THE MODEL FOR A FIRST-GUESS PARAMETERS VALUES

The values chosen for the parameters, rates and constants come from the literature, or in-situ measurements, either first-guess for the Baltic Sea (table 1).

Table 1: Optimal values for the Belt sea station and the first-guess model run

PARAMETERS	Values	Units
dt	1200	s
Kd sl (oxidation rate in sediment)	0.000000058	s <sup>-1</sup>
Kz sl (sediment/water diffusivity)	0.0000001	m <sup>2</sup> .s <sup>-1</sup>
$\zeta$ (refractory/burried carbon fraction)	0.5	[ $\cdot$ ]
$\Theta_D^{T-20}, \Theta_R^{T-20}, \Theta_R^{T-20}, \Theta_{DS}^{T-20}$	1.047 <sup>T-20</sup> and 1.08 <sup>T-20</sup>	[ $\cdot$ ]
Ksed (sedimentation rate of POC, Ksed=V/h)	0.0000596	s <sup>-1</sup>
tcrit (critical bottom shear stress)	1.0	N.m <sup>-2</sup>
Kphotos (photosynthetic conversion rate)	0.0000115	
K <sub>D</sub> (carbon oxidation rate in water)	0.00000175	s <sup>-1</sup>
Kr (respiration rate in water)	0.00000175	s <sup>-1</sup>

The global sensitivity analysis highlighted the robustness of the model parameters, even when local maxima were detected as for Kd and V (Friedrichs, 2001), the more influenced parameters of the sensitivity analysis on the state variables. Therefore, oxidation rate in water and sinking velocity are considered as the leading control variables (Garcia-Gorriz *et al.*, 2003) of the model, after the physical forcing functions. Considering the sediment compartment, we use the sediment-water diffusion rate: Kz\_sl as the third control variable, in our model, for the further steps of the model evaluation.

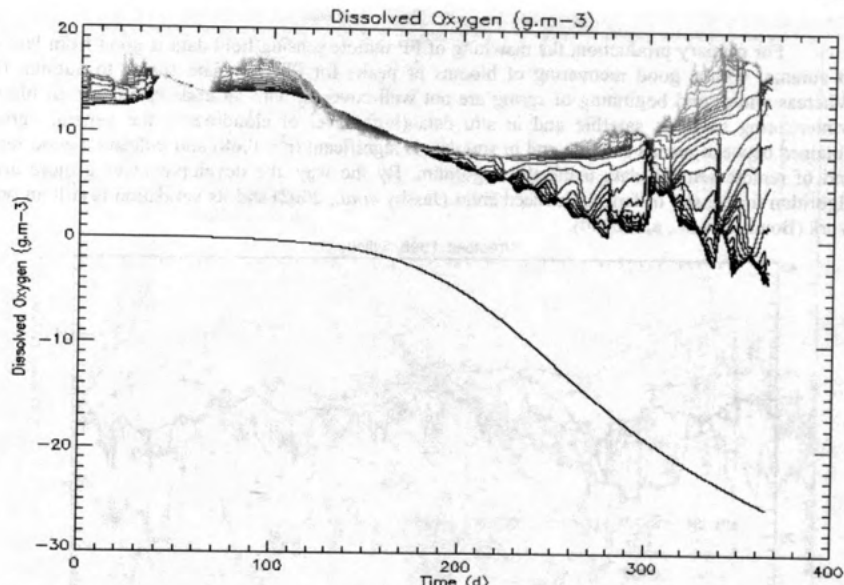


Figure 3: Temporal distribution of DO for all layers (colour scale light to dark grey: surface to the bottom layers) including the sediment layer (black line evolving versus negative concentrations of oxygen), run for Great Belt station, 1998.

The objectives of the sensitivity analysis and first-guess runs are to check the stability and accuracy of the model, before comparison with field measurements. Applying the model in its actual form, we are able to catch and predict hypoxia and anoxia events (fig.3) probably overestimated considering sinking velocity, oxidation rate and water-sediment diffusivities as the main driving ecological variables. For instance, to represent the spring diatoms blooms, sinking velocity is higher, whereas in summer the diffusivity may vary as the amount and fraction of refractory carbon on sediment from low to high.

## CALIBRATION

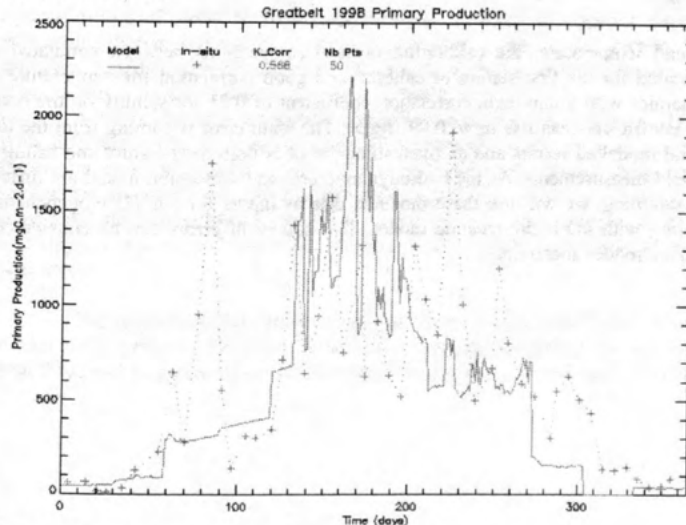


Figure 4: Primary production plots with filed measurements and satellite data

For primary production, the matching of PP remote sensing/field data is good from late spring to autumn, with a good recovering of blooms or peaks for PP from late spring to autumn (fig.4). Whereas winter and beginning of spring are not well covered, with an underestimation of blooms in winter/spring between satellite and in situ data (high level of cloudiness), the general agreement obtained between means satellite and in situ data is significant ( $r^2 = 0.68$ ) and indicate a good recovery and of remote sensing data using this algorithm. By the way, the development of a more accurate algorithm for coastal or land-influenced areas (Jassby *et al.*, 2002) and its validation is still an ongoing work (Bouman *et al.*, a,b, 2000).

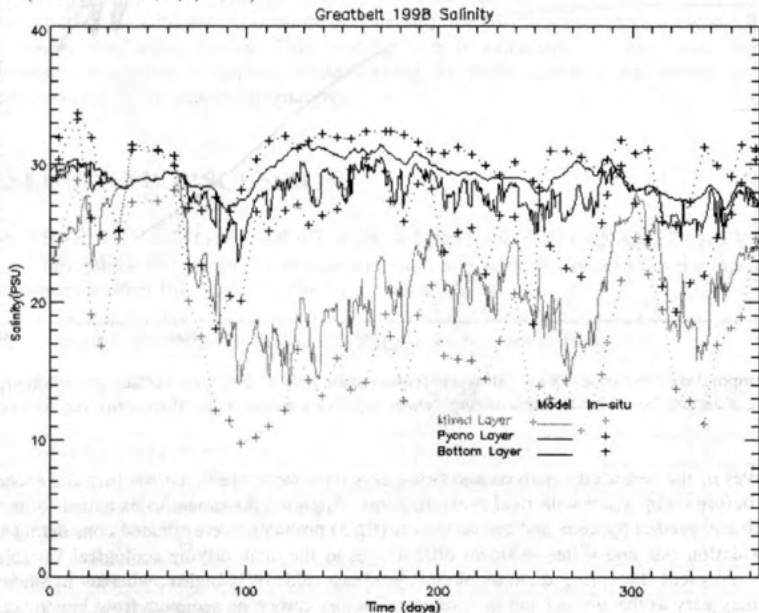


Figure 5: Temperature profile for model and in situ averages in the mixed, pycnocline and bottom layers, for Great Belt station, in 1998.

For salinity and temperature, the calibration or inter-comparisons between simulated and observed values, indicated for the first station of calibration a good correlation for temperature and seasonal cycle as dynamics with a minimum correlation coefficient of 0.71 for salinity on the bottom layers, whereas these coefficients can rise up to 0.99 (fig.5). The main error is coming from the time-lag between *in situ* and modelled results and an overestimation of bottom temperature and salinity in model compared to field measurements. As the hydrodynamic grid and dimension model are different from *in situ* stations sampling, we will use these modeled data as inputs for our 1D biogeochemical model, until its coupling with 3D hydrodynamic model. This source of errors can be considered as minor and included in the model uncertainty.

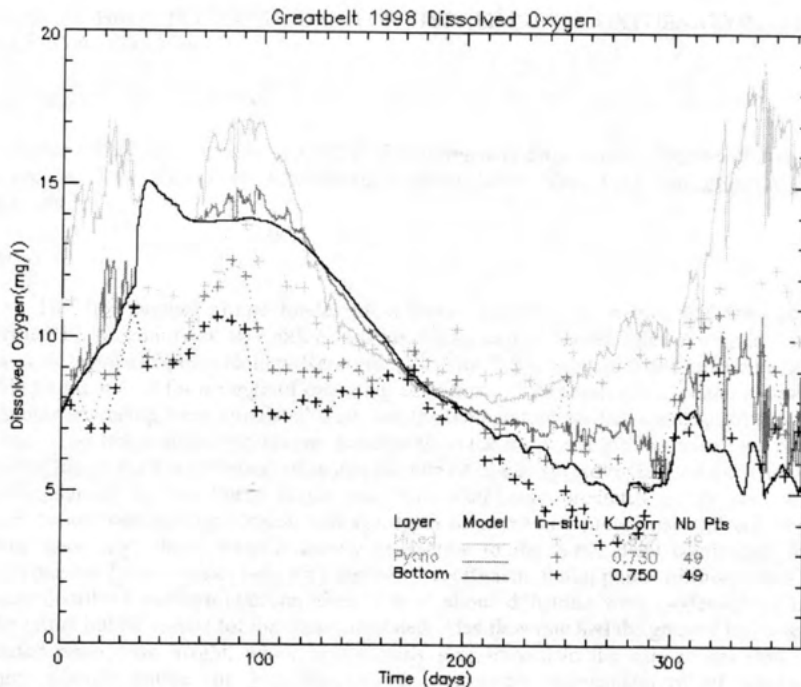


Figure 6: Dissolved Oxygen profiles for model and in situ averages in the mixed, pycnocline and bottom layers, for Great Belt station, in 1998 (linear correlation coefficients calculated for each layer).

For Great Belt station calibration (fig.6), correlation coefficients confirmed the good fitting of the model, at its actual level of complexity even if bottom layer is regularly over/underestimated due to poor field measurements/model results comparison. Another problem is linked to the permanent anoxic layer detected in the Baltic proper and the lack of measurements in the bottom layer for different stations, like Bornholm and Gotland Sea. Anoxia and hypoxia can be detected currently, but for an optimal fitting of model to field measurements, we need to improve slightly the parameterization including different sinking speed and oxidation rate linked to the carbon degradation in water and sediment, together with the model run length, for instance in the sediment compartment and carbon mass, as this is the major source of anoxia in shelves seas.

Actually, the main advantage of this model is its simplicity, as a 1D model it can be coupled with different types of hydrodynamic model, whatever the area of application; but the vertical dimension does not consider the advection or only indirectly through the temperature, salinity, primary production, air-water exchange and diffusivity variations; which constitutes its main drawback. On the other hand, the biogeochemical model remains simple and easy to apply, as it is considering the Carbon and Oxygen in water and sediment and using model outputs and remote sensing data, at the European seas levels.

The application and calibration of the biogeochemical ERGOM 1D model coupled to GETM model are in progress. Hence, a further calibration and validation for the Baltic stations chosen and year 2002 will be presented and discussed together with the model inter-comparison.



## LINEAR BUBBLE PLUME MODEL FOR HYPOLIMNETIC OXYGENATION: FULL-SCALE EVALUATION

V. L. Singleton<sup>1</sup> and J. C. Little<sup>2</sup>

418 Durham Hall, Department of Civil & Environmental Engineering, Virginia Polytechnic Institute and State University, Blacksburg, Virginia 24061-0246, USA., [vickies@vt.edu](mailto:vickies@vt.edu) and [jcl@vt.edu](mailto:jcl@vt.edu)<sup>2</sup>

### Abstract

The first bubble plume model for a linear geometry to include gas transfer was presented by McGinnis et al. (2001). In this work, data collected from a full-scale linear diffuser installed in Spring Hollow Reservoir, Virginia, USA were used to evaluate the linear bubble plume model for a range of operating conditions. The depth of maximum plume rise and plume spreading were simulated well, and the temperature predictions agree closely with the data. The temperature predictions deviated from the measured profiles where the plumes reach the top of the hypolimnion, or where the rate of plume spreading is greatest. Dissolved oxygen addition by the linear plume was somewhat under-predicted by the model. A sensitivity analysis was performed, and the depth of maximum plume rise and equilibrium (neutral buoyancy) depth were relatively insensitive to the entrainment coefficient, initial Froude number (plume water velocity), spreading coefficient, initial plume (diffuser) area, and ambient dissolved nitrogen concentration. Linear plume dynamics were moderately affected by the initial bubble radius for the cases simulated. Gas flow rate had the greatest influence on predicted plume rise height, which was directly proportional to the applied gas flow rate. Oxygen transfer within the hypolimnion was essentially independent of all parameters analyzed except initial bubble radius, decreasing from more than 99 percent to less than 10 percent for air and pure oxygen as the initial radii increased from approximately 1 mm to 2 cm. The results of this work, along with the findings of McGinnis et al. (2004), indicate that plume dynamics and oxygen transfer can successfully be predicted for linear and circular bubble plumes using the discrete-bubble approach of Wüest et al. (1992).

### Introduction

Bubble plumes are used in variety of industrial and environmental applications including oxygenation for wastewater treatment, mixing in chemical reactors, stripping of dissolved gasses (Machina et al. 1992), containment of spills, prevention of ice formation (Fanneløp et al. 1991), and destratification of lakes and reservoirs (Schladow 1992). Bubble plumes are also commonly used for hypolimnetic oxygenation, which preserves stratification of water bodies while adding oxygen to the deepest layer (Wüest et al. 1992, McGinnis et al. 2001). Hypolimnetic anoxia negatively affects water quality downstream of hydropower reservoirs, the drinking-water treatment process, and cold-water fisheries. A bubble plume model to predict oxygen transfer from linear diffuser systems was presented by McGinnis et al. (2001), based on the bubble plume model for a circular diffuser developed earlier by Wüest et al. (1992). However, the linear bubble plume model was not validated by McGinnis et al. (2001) due to a lack of appropriate data. Additionally, model robustness has not been established with data from a full-scale system over a range of operating conditions. Using extensive, high spatial-resolution CTD transect data collected in Spring Hollow Reservoir (SHR), Virginia, USA during diffuser operation in 2003 and 2004, the performance of the linear bubble plume model is evaluated. The motivation for this work includes verification of general model performance prior to application for design purposes and investigation of critical model parameters through implementation of a sensitivity analysis. Also, the accuracy of model predictions, especially with regard to depth of maximum plume rise, should be assessed prior to coupling with lake/reservoir hydrodynamic and water quality models, such as CE-QUAL-W2 (McGinnis et al. 2001). In this paper, the updated linear plume model is

presented, observations and model predictions are compared, and results of a sensitivity analysis are discussed.

#### Linear Bubble Plume Model

The linear bubble plume model is based on eight flux equations that are solved simultaneously to predict water flow rate, oxygen and nitrogen transfer, oxygen and nitrogen concentration, and plume rise height, given diffuser geometry and depth, applied gas flow rate, and initial bubble size. The equations were originally developed by Wüest et al. (1992) for a circular geometry but were modified by McGinnis et al. (2001) for the linear geometry of the system installed in SHR (Tables 1 and 2). The equations that include the spreading coefficient ( $\lambda$ ) were refined for this work to more accurately reflect the geometry of the plume at the ends of the linear diffuser (Tables 1 and 2), which is approximated in plan view as a long rectangle. The width of the plume not occupied by bubbles is assumed to be constant around the rectangular cross-section at a given depth. The entrainment coefficient ( $\alpha$ ) was assumed to be 0.08, and  $\lambda$  was set at 0.85, as reported by Fanneløp et al. (1991) for linear bubble plumes. Further information on equations of state, parameter approximations, and the model solution procedure is provided by Wüest et al. (1992) and McGinnis et al. (2004). To estimate the initial plume water velocity, an equivalent radius was determined based on the initial linear plume area. The Froude number method of Wüest et al. (1992) was employed. A significant contribution by Wüest et al. (1992) is application of a variable buoyancy flux to account for gas dissolution and decompression as the bubbles rise.

#### Application to Spring Hollow Reservoir, Virginia, USA

##### *Field Data Collection*

Field-scale testing was conducted using a linear bubble plume diffuser installed in Spring Hollow Reservoir, Virginia, USA. SHR is a small monomictic, mesotrophic side-stream reservoir that is managed by the Western Virginia Water Authority and serves as one of the principle drinking water sources for Roanoke County. The reservoir has a maximum depth of 65 m and a maximum water surface elevation of 431 m. The approximate surface area and volume are  $0.54 \text{ km}^2$  and  $1.24 \times 10^7 \text{ m}^3$ , respectively. The linear diffuser system was installed in 1997 and can be supplied with compressed air or pure oxygen over a range of gas flow rates (Gantzer 2005).

Three sets of diffuser experiments were conducted when the reservoir was stratified in 2003 and 2004. Tests were performed in 2003 using compressed air (21% O<sub>2</sub>) supplied at a high gas flow rate ( $44 \text{ Nm}^3 \text{ hr}^{-1}$ ) during June 29–July 14 and pure oxygen (97% O<sub>2</sub>) supplied at a low flow rate ( $11 \text{ Nm}^3 \text{ hr}^{-1}$ ) during August 14–26. A third test was conducted in 2004 using pure oxygen but at a higher gas flow rate ( $40 \text{ Nm}^3 \text{ hr}^{-1}$ ) during October 22–November 5. In 2003, the diffuser quickly mixed the rather small hypolimnetic volume during both tests, and the water quality conditions on the dates of data collection (July 2 and August 17 for compressed air and pure oxygen, respectively) were by that time relatively homogeneous as a result of plume-induced mixing. One of the primary objectives of the 2004 experiments was to maximize the plume signature in the hypolimnion and to increase confidence in the linear plume model validation by providing a different set of boundary conditions with which to validate the model. In 2004, the data were therefore collected on October 24, soon after the start of the diffuser operating period. Additionally, the 2004 test was performed later in the stratified season to maximize the ambient oxygen and temperature gradients in the hypolimnion.

The data collected in 2003 and 2004 included numerous high spatial-resolution CTD (conductivity and temperature as a function of depth) (Sea-Bird Model SBE 19plus; 4 Hz sampling rate) profiles measured before, during, and after oxygenation. The CTD profiler was also equipped with a dissolved oxygen (DO) probe. Profiles were obtained laterally across the

diffuser at 0.5 m increments for 0-10 m, 2 m increments for 10-20 m, and 5 m increments for 20-40 m from the centerline of the diffuser (Figure 1). [Note: The diffuser centerline location is shifted to the left in the contour plots for 2004 because the diffuser was repositioned earlier in the year. Also, the operational length of the diffuser was decreased for that year (Table 3).]

Table 1. Key model variables (revised from McGinnis et al. 2001).

Variable	Formula	Units
Entrainment Factor	$E = 2(L + W)\alpha v$	$m^2 s^{-1}$
Plume Water Volume Flux	$Q = LWv$	$m^3 s^{-1}$
Momentum Flux	$M = LWv^2$	$m^4 s^{-2}$
Temperature Flux	$F_T = QT_p$	$^\circ C m^3 s^{-1}$
Dissolved Solids Flux	$F_s = QSp_w$	$kg s^{-1}$
Dissolved O <sub>2</sub> and N <sub>2</sub> Fluxes	$F_{D_i} = QC_i$	$mol s^{-1}$
Gaseous O <sub>2</sub> and N <sub>2</sub> Fluxes	$F_{G_i} = \lambda W(L - W + \lambda W)(v + v_b) y_i$	$mol s^{-1}$

Table 2. Non-linear differential flux equations (revised from McGinnis et al. 2001).

<b>Water Volume Flux</b>	$\frac{dQ}{dz} = E$
Momentum Flux	$\frac{dM}{dz} = \frac{\rho_a - \rho_w}{\rho_p} gLW + \frac{\rho_w - \rho_p}{\rho_p} g\lambda W[L - W(1 - \lambda)]$
Temperature Flux	$\frac{dF_T}{dz} = ET_a$
Salinity Flux	$\frac{dF_s}{dz} = E\rho_a S_a$
Dissolved Gas Flux	$\frac{dF_{D_i}}{dz} = EC_a + \frac{4\pi r^2 N}{v + v_b} K_L (H_i P_i - C_i)$
Gas Flux	$\frac{dF_{G_i}}{dz} = -\frac{4\pi r^2 N}{v + v_b} K_L (H_i P_i - C_i)$

#### Observations and Model Application

To evaluate the linear bubble plume model, predicted plume rise height, spreading, and constituent profiles were compared to experimental observations. Critical model input parameters for the three test conditions (July 2003, August 2003, and October 2004) are shown in Table 3. Bubble size was determined using the correlation developed by McGinnis and Little (2002) for the type of diffuser installed in SHR. The input boundary conditions were obtained from near-field lateral profiles ( $\pm 2$  m and  $\pm 1$  m from plume centerline for 2003 and 2004, respectively) and differed significantly between 2003 and 2004 (Figure 2).

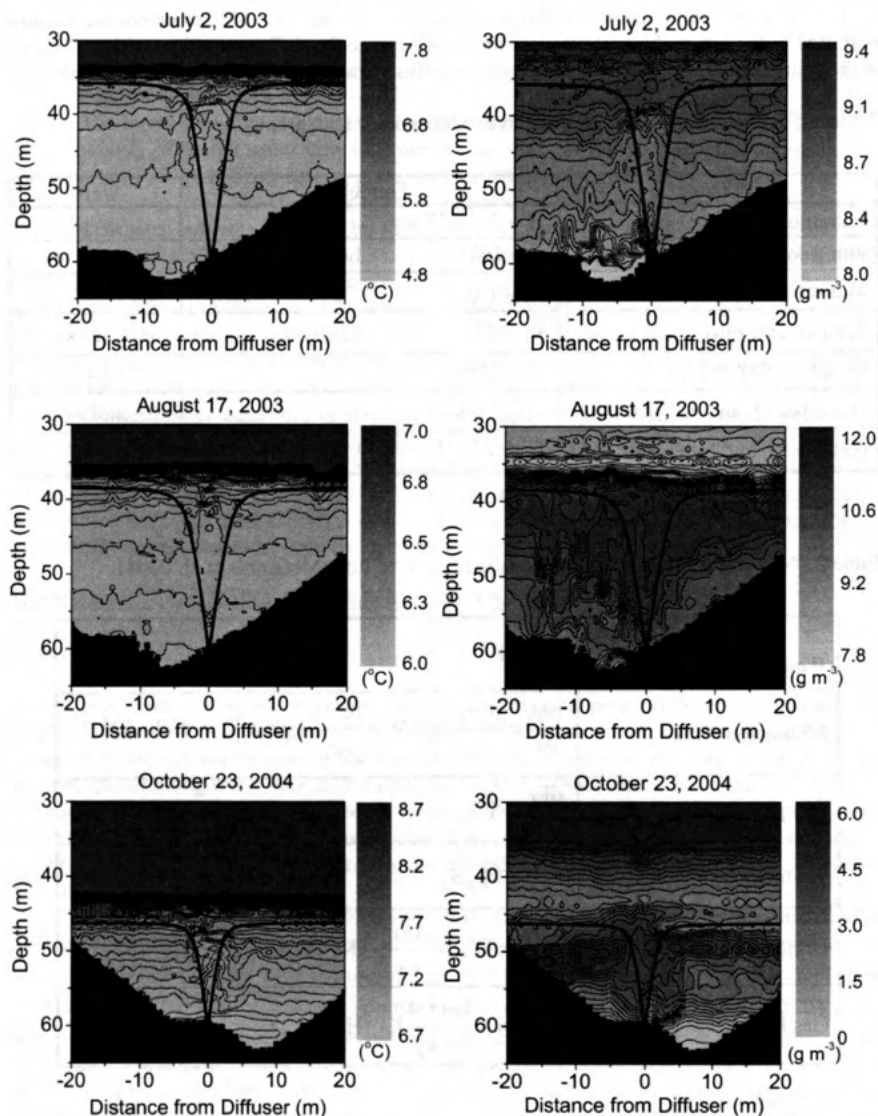


Figure 1. Measured plume temperature ( $^{\circ}\text{C}$ ) (left) and DO ( $\text{g m}^{-3}$ ) (right) contours with linear plume model predictions for diffuser operation with air (July 2003) and pure oxygen (August 2003 and October 2004) in Spring Hollow Reservoir, Virginia, USA. Contours were interpolated from CTD profiles collected at locations indicated by small black squares along the bottom of each plot.

Table 3. Conditions for linear bubble plume model application and sensitivity analysis.

Parameter	July 2003	August 2003	October 2004
O <sub>2</sub> in gas supply (%)	21	97	97
Entrainment coefficient (-)	0.08	0.08	0.08
Spreading coefficient (-)	0.85	0.85	0.85
Operational diffuser length (m)	300	300	250
Initial plume area (m <sup>2</sup> )	55	55	46
Gas flow rate (Nm <sup>3</sup> hr <sup>-1</sup> ) <sup>a</sup>	44	11	40
Bubble radius (m)	$5.7 \times 10^{-4}$	$5.6 \times 10^{-4}$	$5.7 \times 10^{-4}$
Average diffuser depth (m)	60	60	60

<sup>a</sup>1 Nm<sup>3</sup> denotes 1 m<sup>3</sup> of gas at 1 bar and 0 °C

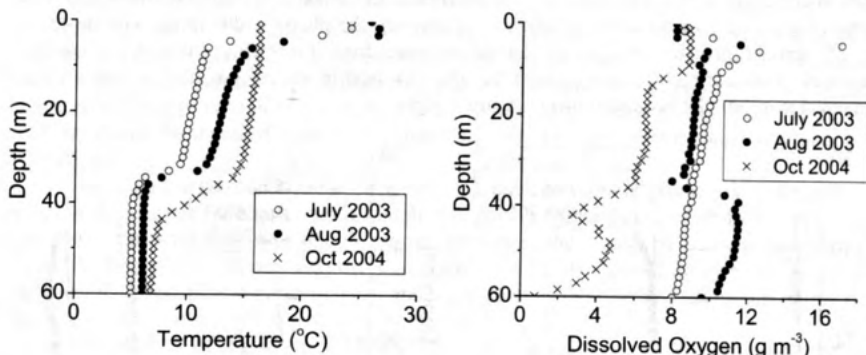


Figure 2. Input boundary conditions for linear plume model evaluation and sensitivity analysis (conductivity profiles not shown.) Data collected during diffuser operation with air (June 2003) and pure oxygen (August 2003 and October 2004) in SHR.

Contour plots of temperature and DO are shown in Figure 1, along with corresponding model predictions for plume diameter as a function of depth and the depth of maximum plume rise. The contour plots show that the plumes in SHR were relatively homogeneous, especially for 2003. This was due to the essentially well-mixed conditions in the hypolimnion as a result of diffuser operation (Figure 1). The structure of the plumes is similar to those observed in weakly stratified conditions by Asaeda and Imberger (1993). Referring to the DO contour for October 23, 2004 (Figure 1), the higher concentrations at lower depths immediately adjacent to both sides of the plume were likely the result of detrained water that falls back past the equilibrium depth due to momentum. This phenomenon was also observed by McGinnis et al. (2004). The depth of maximum plume rise is simulated well by the model over the range of operating conditions (Figure 1). Vertical temperature and DO profiles within the plumes were also predicted by the model (Figure 3). The differences between the July and August 2003 results are primarily due to differences in applied gas flow rate (44 and 11 Nm<sup>3</sup> hr<sup>-1</sup>, respectively) and oxygen fraction of the bubbles. The higher gas, and hence buoyancy, flux for the July diffuser test with compressed air results in a slightly higher depth of maximum plume rise. The model predictions for 2004 differ from those of 2003 because of the differing boundary conditions (Figure 2). McGinnis et al. (2004) also observed that plume properties and model predictions are strongly dependent on near-field boundary conditions, especially temperature. Average measured temperature and DO profiles within the plumes are also presented in Figure 3 for comparison. The temperature predictions deviate from the measured

profiles where the plumes reach the top of the hypolimnion (Figure 3, left), or where the rate of plume spreading is greatest (Figure 1). One reason for this may be that the model assumes that the entrainment coefficient is constant over the height of the plume. In a detailed study of circular plumes, Milgram (1983) found that the entrainment coefficient increased with increasing values of the gas fraction or holdup and with increasing values of a characteristics length that is a function of the 4/5 power of the plume radius and the 1/5 power of the mean bubble rise velocity. Milgram (1983) also reported that the entrainment coefficient for a circular plume decreases with increasing values of the distance between bubbles. As the plume approaches its maximum rise height, the plume width increases rapidly (Figure 1). If linear plumes behave similar to circular plumes, then the entrainment coefficient for linear plumes may also increase as the plume width increases. Another reason for the discrepancy between measured and predicted profiles may be the boundary conditions used in the model simulations. The input boundary profiles selected for the model simulations may not accurately reflect the actual ambient conditions immediately adjacent to the plume along its entire rise height. Measured vertical CTD profiles at the average estimated plume width were averaged and used for boundary conditions. However, the plume width varies with depth, so use of vertical profiles at a single lateral distance from the diffuser is not appropriate. Inaccurate boundary conditions may have also resulted in underprediction of the average measured in-plume DO concentration (Figure 3, right).

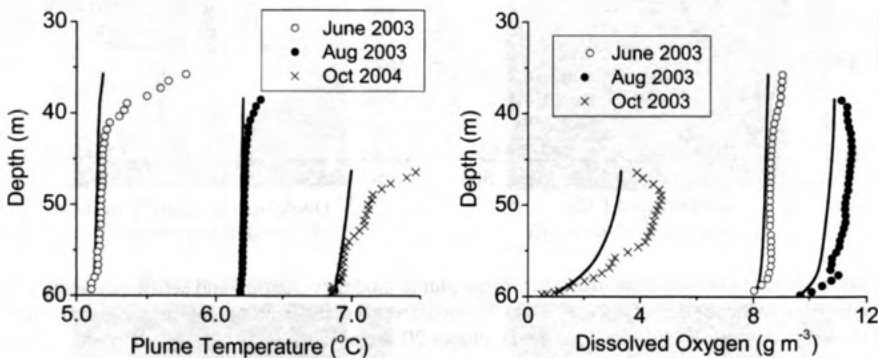


Figure 3. Predictions for linear plume model evaluation. Input boundary conditions and parameters obtained from diffuser system in SHR. Measured average in-plume constituents (symbols) shown on corresponding plots.

#### Sensitivity Analysis

A sensitivity analysis was performed with the linear bubble plume model for each of the three diffuser tests (Table 3). Parameter perturbation was employed, in which model input variables are adjusted to determine their individual effects on model predictions, including depth of maximum plume rise, equilibrium or neutral buoyancy depth, and oxygen transfer efficiency. Knowledge of these plume performance characteristics is especially important during design of hypolimnetic oxygenation systems. The sensitivity analysis method used assumes that each model input parameter is independent. The model variables investigated included  $\alpha$ , initial Froude number,  $\lambda$ , initial plume area, gas flow rate, and initial bubble radius. Currently,  $\alpha$  and  $\lambda$  for the linear plume model are empirical constants derived from laboratory experiments (Fanneløp et al. 1991), and the initial plume water velocity is calculated using a densimetric Froude number (Wüest et al. 1992). The initial plume area, gas flow rate, and, to a lesser extent, initial bubble size can be controlled through oxygenation system and diffuser design. The sensitivity of model predictions to the ambient dissolved nitrogen concentration was also examined for the standard case using compressed air (June 2003). The model

assumes that the background dissolved nitrogen concentration in the hypolimnion is equivalent to the saturated value at atmospheric partial pressure and the average hypolimnetic water temperature.

In general, the depth of maximum plume rise and equilibrium (neutral buoyancy) depth are relatively insensitive to  $\alpha$ ,  $\lambda$ , initial Froude number (plume water velocity), ambient dissolved nitrogen concentration, and values of the initial plume area from about half to twice the actual diffuser area. The depth of maximum plume rise predicted by the circular plume model was not significantly influenced by initial conditions either (Wüest et al. 1992). The plume rise height calculated by the linear bubble plume model is moderately sensitive to the initial bubble radius, but to a lesser extent than the circular bubble plume model (Wüest et al. 1992). The difference may be due to differences between temperature boundary conditions, which caused plume dynamics in SHR to be influenced to a greater degree by the depth of the thermocline. Gas flow rate had the greatest effect on the depth of maximum plume rise, similar to the circular bubble plume model (Wüest et al. 1992). The plume rise height was directly proportional to the gas flow rate, increasing by about 10 m for an increase in gas flow rate from  $10^{-3}$  to  $10^{-1} \text{ Nm}^3 \text{ s}^{-1}$ . Oxygen transfer within the hypolimnion was found to be essentially independent of all parameters analyzed except initial bubble radius, decreasing from more than 99 percent to less than 10 percent for air and pure oxygen as the initial radii increased from approximately 1 mm to 2 cm. (It should be noted that oxygen transfer can continue above the depth of maximum plume rise if the bubbles are not completely dissolved at this depth.)

McGinnis et al. (2004) studied a full-scale circular bubble plume and collected data showing that the bubble core expanded negligibly during plume ascent. This lack of spreading may also occur within a linear bubble plume. However, the sensitivity analysis results of the linear bubble plume model suggest that variations in the spreading coefficient do not significantly affect plume performance parameters such as the depth of maximum plume rise, the equilibrium depth, and oxygen transfer efficiency.

The results of the linear bubble plume model application to SHR revealed that the model was rather insensitive to most of the parameters analyzed including the entrainment coefficient, spreading coefficient, initial plume water velocity, ambient dissolved nitrogen concentration, and initial plume area. The predicted plume rise height and equilibrium depth were somewhat sensitive to the initial bubble size, while the applied gas flow had the greatest effect on plume dynamics. Overall, the linear bubble plume model was found to be less sensitive to input parameters than the circular model, but this insensitivity may be because of the relatively homogeneous boundary conditions present in the hypolimnion of SHR during diffuser testing and data collection.

#### Acknowledgements

We thank Paul Gantzer for field data collection and Dan McGinnis for technical guidance. Financial support was provided by the U. S. National Science Foundation (Grant No. BES 0202034) with supplemental funding from Western Virginia Water Authority.

#### Nomenclature

C	dissolved concentration, $\text{mol m}^{-3}$ .
E	entrainment factor, $\text{m}^2 \text{ s}^{-1}$ .
F <sub>D</sub>	dissolved species flux, $\text{mol s}^{-1}$ .
F <sub>G</sub>	gaseous species flux, $\text{mol s}^{-1}$ .
F <sub>S</sub>	salinity flux, $\text{kg s}^{-1}$ .
F <sub>T</sub>	temperature flux, $^{\circ}\text{C m}^3 \text{ s}^{-1}$ .
g	gravitational acceleration, $\text{m s}^{-2}$ .
H	Henry's coefficient, $\text{mol m}^{-3} \text{ bar}^{-1}$ .
K <sub>L</sub>	mass transfer coefficient, $\text{m s}^{-1}$ .

L	plume length, m.
M	water momentum, $\text{m}^4 \text{s}^{-2}$ .
N	number flux of bubbles, $\text{s}^{-1}$ .
P	pressure, bar.
Q	plume flow rate, $\text{m}^3 \text{s}^{-1}$ .
r	bubble radius, m.
S	salinity, $\text{g kg}^{-1}$ .
T	temperature, $^{\circ}\text{C}$ .
v	velocity, $\text{m s}^{-1}$ .
W	plume width, m.
y	gaseous concentration, $\text{mol m}^{-3}$ .
z	depth, m.

#### Greek letters

$\alpha$	entrainment coefficient, -.
$\lambda$	spreading coefficient, -.
$\rho$	density, $\text{kg m}^{-3}$ .

#### Subscripts

a	ambient water
b	bubble
i	gas species, oxygen or nitrogen
p	plume water and gas mixture
w	plume water

#### References

- Asaeda, T., and J. Imberger. 1993. Structure of bubble plumes in linearly stratified environments. *Journal of Fluid Mechanics* **249**:35-57.
- Fanneløp, T. K., S. Hirschberg, and J. Kueffer. 1991. Surface current and recirculating cells generated by bubble curtains and jets. *Journal of Fluid Mechanics* **229**:629-657.
- Gantzer, P. 2005. Hypolimnetic Oxygenation: Improving Design by Incorporating Diffuser-Induced Oxygen Demand and Eddy Diffusivity. Dissertation Proposal Department of Civil and Environmental Engineering, Virginia Tech, Blacksburg, VA.
- Machina, D. W., J. A. McCorquodale, and J. K. Bewtra. 1992. Numerical and physical modeling of air diffuser plume. *Journal of Environmental Engineering* **118**:253-267.
- McGinnis, D. F., and J. C. Little. 2002. Predicting diffused-bubble oxygen transfer rate using the discrete-bubble model. *Water Research* **36**:4627-4635.
- McGinnis, D. F., J. C. Little, and A. Wuest. 2001. Hypolimnetic oxygenation: Coupling bubble-plume and reservoir models. *in Asian Waterqual 2001, First IWA Asia-Pacific Regional Conference*, Fukuoka, Japan.
- McGinnis, D. F., A. Lorké, A. Wuest, A. Stoeckli, and J. C. Little. 2004. Interaction between a bubble plume and the near-field in a stratified lake. *Water Resources Research* **40**:doi: 10.1029/2004WR003038.
- Milgram, J. H. 1983. Mean flow in round bubble plumes. *Journal of Fluid Mechanics* **133**:345-376.
- Schladow, S. G. 1992. Bubble plume dynamics in a stratified medium and the implications for water quality amelioration in lakes. *Water Resources Research* **28**:313-321.
- Wüest, A., N. H. Brooks, and D. M. Imboden. 1992. Bubble plume modeling for lake restoration. *Water Resources Research* **28**:3235-3250.

## PHYSICAL BACKGROUND OF OXYGEN DEPLETION DEVELOPMENT IN ICE-COVERED LAKES

S. Golosov<sup>1,4)</sup>, E. Schipunova<sup>1)</sup>, O. A. Maher<sup>2)</sup>, A. Terzhevik<sup>3)</sup>, G. Zdorovennova<sup>3)</sup>

<sup>1</sup>Institute of Limnology, Russ. Acad. Sci., 196105 St. Petersburg, Russia; E-mail: sergey\_golosov@mail.ru

<sup>2</sup>Department of Water Resources Engineering, Institute of Technology, Lund University, Sweden; E-mail: osama.maher@tvrl.lth.se

<sup>3</sup>Northern Water Problems Institute, Russ. Acad. Sci., 185030 Petrozavodsk, Russia; E-mail: ark@nwpi.krc.karelia.ru

<sup>4</sup>Institute of Water Ecology and Inland Fishery, D-12561 Berlin, Germany

### *Abstract*

Based on the observational data from four freezing lakes located in Northwestern Russia and North America, the effect of the lake thermal regime on formation, development, and duration of existence of anaerobic zones in ice-covered lakes is estimated. A simple one-dimensional model that describes the formation and development of the dissolved oxygen deficit in shallow ice-covered lakes is suggested. The model reproduces the main features of dissolved oxygen dynamics during the ice-covered period, that is, the vertical structure, the thickness and rate of increase of the anaerobic zone in bottom layers. The model verification was performed with observational data from the shallow ice-covered Lake Vendyurskoe (Karelia, Russia). Results of verification show that the model adequately describes the dissolved oxygen dynamics in winter. The rates of DO consumption by bacterial plankton and by bottom sediments, depending on the heat transfer through the water-sediment interface are calculated. Received results allow predicting appearance of potentially dangerous anaerobic zones in shallow lakes as well as in separate lake areas.

The water quality in freshwater reservoirs in many respects is determined by the saturation of dissolved oxygen (DO). In lakes with high DO concentration, the bacterial destruction of organic matter is accompanied by extraction of carbon dioxide, which is harmless for hydrocarbons, into water. A decrease of the DO concentration or its complete absence leads to the activation of anaerobic processes, which occur with evolving such deoxidized gases as methane ( $\text{CH}_4$ ), hydrogen sulphide ( $\text{H}_2\text{S}$ ), and ammonia ( $\text{NH}_3$ ). Those are capable to not only worsen the water quality, but also to be toxic (especially it concerns  $\text{H}_2\text{S}$ ). The onset and continuous existence of the anaerobic zone in lakes leads to such negative consequences as fish kill, loss of benthic organisms, changes in the trophic chains of water ecosystems, etc.

A DO deficit in shallow lakes occurs in absence of water aeration. Appearance of anaerobic zones in lakes may take place during the open-water period and in winter. The duration of such phenomenon in the former case is rather short as periodic wind mixing provides aeration of the bottom layers. The most dramatic situation may occur in ice-covered lakes located in moderate and high latitudes because the factors defining a DO regime in a shallow ice-covered lake essentially differ from those during the open-water period. First, it is related to main sources of oxygen flow. In winter, the ice cover excludes a gas exchange with atmosphere. Besides, amount of solar radiation penetrating into water becomes negligible that leads to a drastic decrease of photosynthetic intensity. Thus, main sources of oxygen supply practically disappear, and only consumption of oxygen by bacterial plankton in the process of organic matter decomposition together with its absorption by bottom sediments control the DO content in a lake (Hargrave, 1972).

The rate of DO consumption in ice-covered lakes as a rule depends on a set of biological and hydrophysical factors. Usually, the biochemical factors, such as the life activity of the different organisms (including bacterial plankton) within the benthic community, the concentration of the organic matter and DO in the near-bottom zone, are

considered as the main parameters responsible for the appearance of the oxygen depletion in ice-covered lakes (Hutchinson, 1957, Hargrave, 1972, Mathias and Barica, 1980, Cornett and Rigler, 1987). On the other hand, it is well known, that the life activity of the bacterial plankton, which is the main consumer of DO, is strongly dependent on the water temperature (Boyle and Brock, 1973, Welch et al. 1976, Charlton, 1980, Kovaleva et al., 2003). The latter, in turn, is resulting from the complex interactions between the atmosphere, a water column and sediments in lakes, i.e. represents the resulting effect of the physical factors on the problem of the appearance of DO depletion in ice-covered lakes. However, in ice-covered lakes the temperature varies in a very narrow range (from 0 to 4-5°C), and it is commonly assumed that the influence of the temperature under such low values on the bacterial activity is not great.

This study represents an effort to reveal the role of the thermal regime of ice-covered lake in the development of DO winter depletion.

#### *Materials and methods*

Field data collected in different time in three Russian and one American freezing lakes were taken as the empirical material to perform the study. Data from Russian lakes were collected in the Northwestern Russia (Leningradskaya Oblast and Republic of Karelia) during the winter surveys in 1933-34 (Lake Chainoe, maximal depth 9.5 m), in 1963-64 (Lake Krasnoe, maximal depth 14 m) and in 2001-02 (Lake Vendyurskoe, Karelia, maximal depth 12.5 m). The average duration of the ice-covered period in Northwestern Russia is five to six months; the ice may reach one meter of thickness. DO depletion routinely occurs in the chosen lakes and varies in wide range (from 20-60% of saturation to full consumption) not only from year to year, but even between the different areas of lakes. The morphometric parameters of lakes differ rather strongly. The basin of Lake Krasnoe is trough-shaped, whereas the shapes of Lakes Chainoe and Vendyurskoe are irregular. The data from American Lake Allequash were received from the Internet site of the Center for Limnology, University of Wisconsin (<http://limnosun.limnology.wisc.edu>). The depth of the lake is 7 m. The data used in the present paper cover the period from 1982 to 2001. The phenomenon of winter DO depletion is intrinsic to Lake Allequash in the same way as for the Russian lakes. All data from both Russian and American lakes represents the DO and water temperature vertical distributions from top to bottom of the water column, measured in different dates from the beginning to the end of ice-covered periods. The thermal regime of all lakes in consideration is similar, including the under-ice warming of the water column due to heat flux from the sediments. The water temperature varies from 0.1-1.0°C in the beginning of the ice-covered period to 4-5°C in the end.

The data were analysed and processed in terms of the time-dependent relations between the values of the DO deficit and temperature. Obtained functional dependences were used to estimate the rates of the total consumption of DO in lakes subject to the temperature. Finally, the derived results were used in modeling the formation and development of the anoxic conditions in Lake Vendyurskoe. The brief description of the model and discussion of the main results are presented below.

#### *Parameterizations and equations of the model*

In detail, the model of the formation and development of DO depletion in shallow lakes was presented in (Golosov et al., 2004). In this study, just general approach and main regulations of the model will be described.

Equation of the vertical transfer of non-conservative substance can be written as,

$$\frac{\partial C(z,t)}{\partial t} = -\frac{\partial Q}{\partial z} - \gamma [T(z,t)] \cdot C(z,t) \quad (1)$$

where  $C$  is DO concentration;  $t$  is time;  $z$  is depth;  $T(z,t)$  is water temperature,  $\gamma[T(z,t)]$  is total rate of DO consumption,  $[\gamma] = t^{-1}$ .

The model consider the DO vertical distribution within a 'water-sediment' system for two cases, that is, 1) the anoxic zone in a bottom water layer is absent and oxidizing conditions in the upper layer of bottom sediments prevail; and 2) the DO concentration in the bottom layer is close to zero, the oxidized layer in bottom sediments is absent. The vertical DO profile is expressed as,

$$C(z) = \begin{cases} C_s - (C_s - C_D) \cdot f_1\left(\frac{z}{D}\right), & \text{at } 0 \leq z \leq D \text{ and } C_D \neq 0 \\ C_D \cdot [1 - f_2\left(\frac{z}{\delta}\right)], & \text{at } D \leq z \leq \delta \text{ and } C_D \neq 0 \\ C_s \cdot [1 - f_3\left(\frac{z}{H}\right)] & \text{at } 0 \leq z \leq H \leq D \text{ and } C_D = 0 \end{cases} \quad (2)$$

Here,  $D$  is depth of location,  $C_s$  concentration of DO at the "water-ice" boundary,  $C_D$  near-bottom DO concentration,  $\delta$  is the lower boundary of the oxidized layer in sediments and  $H$  is the upper boundary of the anoxic zone,  $f_1(\xi_1)$ ,  $f_2(\xi_2)$ ,  $f_3(\xi_3)$  are dimensionless functions of the dimensionless depths  $\xi_1 = z/D$ ;  $\xi_2 = z/\delta$ ;  $\xi_3 = z/H$ . The functions are monotonic and determined in the respective intervals from 0 to  $D$ , from  $D$  to  $\delta$  and from 0 to  $H$  as,

$$f_1(0) = f_2(0) = f_3(0) = 0, \quad f_1(1) = f_2(1) = f_3(1) = 1 \quad (3)$$

These functions describe the vertical distribution of DO in a water column, in the upper layer of sediments, and in a water column in the case of oxygen depletion ( $C_D = 0$ ).

Integrating (1) from  $z = 0$  to  $z = D$  and from  $z = D$  to  $z = \delta$  and taking into account (2), two ordinary differential equations, linking surface and bottom DO concentrations, the thickness of the upper oxidized layer of bottom sediments, the oxygen flux through the water-sediment interface and bacterial oxygen consumption, can be received,

$$\frac{dC_s}{dt} \cdot D \cdot (1 - \alpha_1) + \frac{dC_D}{dt} \cdot D \cdot \alpha_1 - \frac{d\alpha_1}{dt} \cdot D \cdot (C_s - C_D) = Q_{CS} - Q_{CD} - \int_0^D \gamma[T(z,t)] C(z) dz \quad (4)$$

$$\frac{dC_D}{dt} \cdot (\delta - D) \cdot (1 - \alpha_2) + \frac{d(\delta - D)}{dt} \cdot C_D \cdot (1 - \alpha_2) = Q_{CD} - \gamma_2 \cdot C_D \cdot (\delta - D) \cdot (1 - \alpha_2) \quad (5)$$

Here,  $Q_{CS}$  and  $Q_{CD}$  are oxygen fluxes through the lower surface of ice and through the bottom, respectively;  $\gamma_1$  and  $\gamma_2$  are the rates of oxygen consumption in the water column and in the oxidized layer of sediments (empirical parameters of the model);  $\alpha_1 = \int_0^1 f_1(\xi_1) d\xi_1$

and  $\alpha_2 = \int_0^1 f_2(\xi_2) d\xi_2$  are values of integrals of dimensionless functions.

Equation (4) can be simplified taking into account that the oxygen flux  $Q_{CS}$  during the ice-covered period is negligibly small, and temporal variability of the surface concentration is less than that in bottom layers for one order of magnitude.

Thus, the first term in (4) can be neglected, and  $C_s$  can be considered as constant. Equations (4-5) describe the development of the vertical DO distribution in a water column and in the upper oxidized layer of bottom sediments until  $C_D$  and  $\delta$  are not equal to zero.

The system includes five unknown parameters, *viz.* the oxygen flux through the water-sediment interface  $Q_{CD}$ , the near-bottom concentration  $C_D$ , the thickness of the oxidized layer of bottom sediments ( $\delta \cdot D$ ) and parameters  $\alpha_1$  and  $\alpha_2$ . To close the system, functions  $f_1(\xi_1)$  and  $f_2(\xi_2)$  should be defined, and the equation to calculating  $Q_{CD}$  to be formulated.

To define the shape of  $f_1(\xi_1)$ , let us use the following procedure. The expression for  $Q_{CD}$  can be written as,

$$Q_{CD} = -\chi_C \frac{\partial C}{\partial z} \quad (6)$$

where  $\chi_C$  is molecular DO diffusivity in water. Taking into account (2), the vertical DO gradient at  $z = D$  can be written as,

$$\frac{dC}{dz} = -\frac{(C_s - C_D)}{D} \frac{df_1}{d\xi_1} \quad (7)$$

or

$$\frac{df_1}{d\xi_1} = \frac{Q_{CD} \cdot D}{\chi_C \cdot (C_s - C_D)} = A \quad \text{at } \xi_1 = 1 \quad (8)$$

Thus, (9) represents the non-stationary boundary condition to defining the shape of function  $f_1(\xi_1)$  that describes temporal variability of the vertical DO profile. As it was shown above, the DO concentration at the water-ice boundary changes during the ice-covered period slightly. Hence, the vertical DO flux in this area is also negligibly small. In terms of the parameterization (2), this means that derivative of function  $f_1(\xi_1)$  at  $\xi_1 = 0$  is also equal to zero [ $f_1'(0) = 0$ ]. Thus, to define the function shape, we have four boundary conditions that allow producing  $f_1(\xi_1)$  as the third-power polynomial with variable coefficients,

$$f_1(\xi_1) = (3 - A) \cdot \xi_1^2 + (A - 2) \cdot \xi_1^3 \quad (9)$$

The corresponding integral of  $f_1(\xi_1)$  is,

$$\alpha_1 = \frac{6 - A}{12} \quad (10)$$

To define the shape of  $f_2(\xi_2)$ , let us consider the peculiarities of the vertical DO distribution in the upper oxidized layer of bottom sediments. At its upper boundary, the DO concentration is close to  $C_D$ . At the lower boundary, the concentration is equal to zero. Besides, at the lower boundary the oxygen flux is absent. In such case we have two boundary conditions (3) and one additional [ $f_2'(1) = 0$ ] to define the shape of the function. This allows producing  $f_2(\xi_2)$  as the second-power polynomial with constant coefficients,

$$f_2(\xi_2) = 2 \cdot \xi_2 - \xi_2^2 \quad (11)$$

The corresponding integral  $\alpha_2$  of the function equals to  $2/3$ .

In the situation when the dissolved oxygen in the near-bottom layer is fully consumed by bacterial plankton, the vertical profile is described by the third formula in (2). Integrating (1) from  $z = 0$  to  $z = H$  and taking into account (2), the equation to calculating the temporal variability of the anoxic layer thickness can be received,

$$\frac{dH}{dt} = -\gamma [T(z, t)] \cdot H \quad (12)$$

To define the form of functional dependence of the DO consumption on depth and temperature the following parameterization is assumed in the model,

$$\gamma [T(z, t)] = \left[ \gamma_{\min} + (\gamma_{\max} - \gamma_{\min}) \cdot f_4 \left( \frac{z}{D} \right) \right] \cdot f_5 \left( \frac{T}{T_{\max}} \right) \quad \text{at } 0 \leq z \leq D \quad (13)$$

where

$$f_4\left(\frac{z}{D}\right) = \left(\frac{z}{D}\right)^2, \quad f_5\left(\frac{T}{T_{\max}}\right) = \left(\frac{T}{T_{\max}}\right)^2 \quad (14)$$

Here,  $\gamma_{\min}$  and  $\gamma_{\max}$  are the minimal and the maximal values of DO consumption in a lake during the ice-cover period,  $T_{\max}$  is the maximal value of the water temperature for the same period,  $f_4$  and  $f_5$  are dimensionless functions describing the variability of the rate of DO consumption in dependence on depth and temperature. Usually, the minimal and maximal values of DO consumption correspond to the lower boundary of ice and to the upper layer of sediments respectively. The value of the maximal temperature is close to 4°C, i.e. to the temperature of the maximal density of fresh water.

The model (4), (5), (9), (11), (12) and (13) describes all main stages of the vertical distribution of dissolved oxygen in the 'water-sediment' system during the ice-covered period.

#### *Empirical verification of the model parameterizations*

The suggested model comprises four dimensionless functions of different dimensionless arguments which should be derived from the field data (function  $f_3$  should not to be defined, because the corresponding integral of this function disappears at the deriving of the equation (12)). The observational data in mentioned above lakes were used to define the shapes of the functions.

Fig. 1a represents the measured and calculated vertical DO profiles in the water column of Lake Vendyurskoe corresponding to different dates of the winter 2001-02. Results of calculations (Fig. 1) show that parameterization (9) describes the temporal variability of the vertical DO profile, from the ice cover formation to the end of its existence, fairly well. This means that the representation of the water DO profile in the form of (9) is quite acceptable.

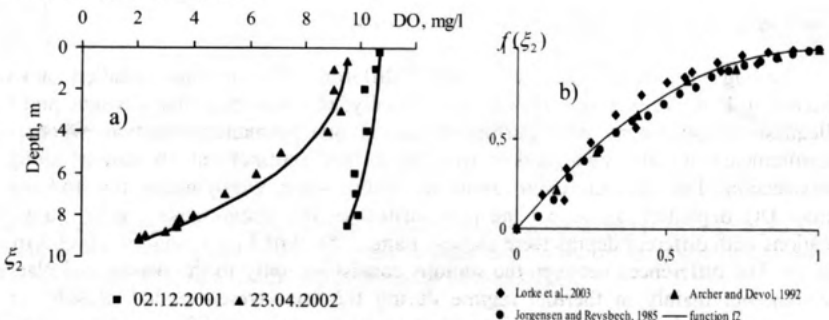


Fig. 1(a, b) Results of the verification of the model parameterisations against the field data.

Results of the verification of the polynomial parameterisation (11) of the vertical DO distribution within the upper oxidized layer of the sediments are presented in Fig. 1b. Unfortunately, authors do not possess own observational data on the vertical distribution of DO in sediments, which can be received only with use of special microprofilers. Therefore, polynomial (11) is defined from the data of natural and laboratory studies performed by the other investigators (Archer and Devol, 1992; Jorgenson and Revsbech 1985; Lorke et al., 2003). Agreement between the empirical data and the polynomial representation shown in Fig. 1b can be considered as remarkable.

Finally, the Fig. 2 represents the dependence of DO consumption on the depth and temperature.

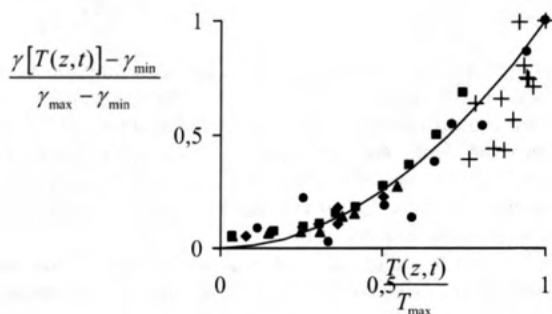


Fig. 2 Functional dependence of the rate of DO consumption on dimensionless temperature. Cruciform symbols correspond to the data from the American Lake Allequash, the other symbols stand for the observational data from Russian lakes mentioned above; the line marks the approximation of the observational data by the quadratic polynomial (13).

In addition to the good agreement between measured data and its polynomial approximation, one more point should be noted. Lake Allequash is located at 46°N, and by the definition is warmer than the Russian lakes, which are located at 60°N (Krasnoe and Chainoe) and at 67°N (Vendyurskoe). The rate of DO consumption in American lakes is considerably higher than that in Russian lakes. All data from Lake Allequash lies in the upper right corner of the diagram. Thus, the parameterization (13) is acceptably describing the dependence of DO consumption on depth and temperature as well as the other parameterizations of the model.

#### *Results of numerical runs of the model and discussion*

Among aforementioned field data from different lakes the most detailed data were obtained in Lake Vendyurskoe in 2001-02. Actually, in Lakes Krasnoe, Chainoe and Lake Allequash measurements were performed just at one permanent location, whereas the measurements in Lake Vendyurskoe were performed routinely at 16 stations along the cross-section. That was the main reason to choose Lake Vendyurskoe for studying the winter DO depletion. To reveal the peculiarities of the phenomenon under study, two locations with different depths were chosen, namely St. 9 of 11.5 m and St. 16 of 5 m (see Fig. 3). The differences between the stations consist not only in the depths and places of location, but mainly in thermal regime during the ice-covered period. Results of the thermal surveys show that the intensity of under ice warming is different at these stations. Thus, the near-bottom temperature in St. 16 varies from 0.9°C in the middle of November (beginning of ice formation) to 2.5 °C in the middle of April (the end of ice-covered period). The corresponding variability of temperature in St. 9 covers the range from 1.2°C to 3.6°C.

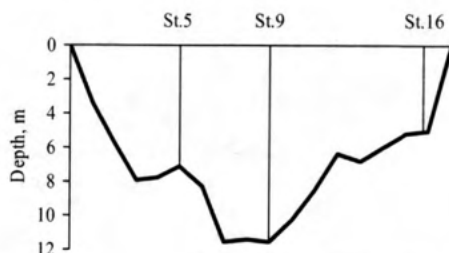


Fig.3. Schematic representation of the cross-section along the Lake Vendyurskoe and location of the stations chosen.

The differences between the stations consist not only in the depths and places of location, but mainly in thermal regime during the ice-covered period. Results of the thermal surveys show that the intensity of under ice warming is different at these stations. Thus, the near-bottom temperature in St. 16 varies from 0.9°C in the middle of November (beginning of ice formation) to 2.5 °C in the middle of April (the end of ice-covered period). The corresponding variability of temperature in St.9 covers the range from 1.2°C to 3.6°C.

The effect of the temperature on the formation of DO depletion was studied in a set of the model runs. Firstly, the model calculated the DO deficit and the thickness of the anoxic zone using the real temperature conditions observed during the surveys. Results of these runs are presented in Fig. 4.

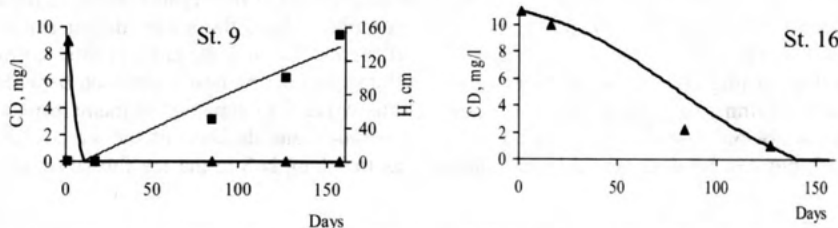


Fig. 4. Temporal dynamics of DO concentration and thickness of the anoxic zone in St. 9 and St. 16 during the winter 2001-02. Triangles and squares are the measured values of DO and H respectively. Thick and thin lines are the results of calculations.

The distance between both stations does not exceed one kilometer, but the oxygen conditions differ strikingly. The storage of DO in bottom layers at the deeper station became negligible no longer than in a half of month after the ice formation, whereas at St. 16 the more or less essential deficit of DO appeared just in the middle of April. At St. 9, the completely anoxic zone started developing after full DO consumption and reached the thickness of 1.5 m in the end of the winter. At the St. 16, the anoxic zone did not appear at all. It should be noted, that the model runs differ from each other only by the courses of temperature.

The following runs of the model were intended to reveal the effect of the shift of thermal regime on the formation of DO depletion. The under ice DO regime for St. 9 was calculated using the temperature measured at the "cold" St. 16, and vice versa, the "warm" winter conditions for St. 16 were simulated with temperature data obtained at the St. 9. Results of simulations are presented in Fig. 5.

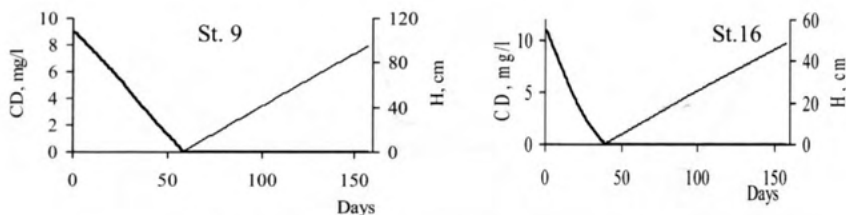


Fig.5 Results of numerical experiments. Thick lines mark the temporal variability of DO; thin ones mark the development of anoxic zone thickness (H).

The model experiments show a rather strong dependence between the DO and thermal regimes of lakes (or their separate areas). Under conditions of "cold" winter, the full consumption of DO at deep St. 9 has been developed in two months after the ice period began. Respectively, the anoxic zone started to develop later comparing to the "cold" case and reached essentially lower thickness in the end of winter. These results were quite expected. More dramatic situation took place in shallow St. 16. The shift in temperature entailed serious worsening in DO regime. The fully anoxic zone is observed already in 40 days after the ice formation. The rate of its development reached  $0.5 \text{ cm} \cdot \text{d}^{-1}$ . It is not as high as at St. 9, but notice that in the case of "cold" winter there was no anoxic zone at this station at all.

The results of numerical experiments performed in the present study allow formulating some conclusions on the nature and the reasons of the winter DO depletion in shallow ice-covered lakes. In lakes, where the concentration of the organic matter is not a limiting factor (the cases of mesotrophic and eutrophic lakes), the winter deficit can be formed due to peculiarities of the winter thermal regime. In turn, the latter is affected by warming/cooling during the previous summer/autumn and by the heat interaction between a water column and sediments. So, it means that the winter DO depletion in many respects depends not only on the biochemical processes in lakes and duration of the ice-covered period, but can be determined by the physical factors long before the ice formation in a lake.

*Acknowledgements* The present study is supported by European Commission (project INTAS -01-2132), the Swedish Institute (VISBY Programme), Åke och Greta Lisshed Foundation, Sweden, the Russian Academy of Sciences, and the German Foundation of the Basic Research (DFG, Project KI-853/3-1). The support is gratefully acknowledged. Authors express their admiration and gratitude to the field research team of the Northern Water Problems Institute for their heroic efforts at collecting field data during winter field campaigns.

#### References

- Archer D., and A. Devol. 1992. Benthic oxygen fluxes on the Washington shelf and slope: A comparison of in situ microelectrode and chamber flux measurements. *Limnol. Oceanogr.* **37**: 614-629.
- Boyle C. and T. Brock. 1973. Bacterial decomposition processes in Lake Wingra sediments during winter. *Limnol. Oceanogr.* **18**(4): 628-634.
- Charlton M. 1980. Hypolimnion oxygen consumption in lakes: discussion of productivity and morphometry effects. *Can. J. Fish. Aquat. Sci.* **37**: 1531-1539.

- Cornett R and F. Rigler 1987. Vertical transport of oxygen into the hypolimnion of lakes. *Can. J. Fish. Aquat. Sci.* **44**: 852-858.
- Golosov, S., A. Terzhevik, O.A. Maher, E. Shipunova, and G. Zdorovennova, 2004, Modelling seasonal dynamics of dissolved oxygen in a shallow stratified lake. In L. Bengtsson and O.A. Maher, Eds, Proc. 8<sup>th</sup> Workshop on Physical Processes in Natural Waters, Lund, 153-164.
- Hargrave B. 1972. A comparison of sediment oxygen uptake, hypolimnetic oxygen deficit and primary production in Lake Esrom, Denmark. *Vehr. Int. Ver. Limnol.* **18**: 134-139.
- Hutchinson, G. 1957. *A treatise on limnology*. Vol I. J. Wiley and Son, Inc., NY, 1015 p.
- Jorgensen B., and N. Revsbech. 1985. Diffusive boundary layers and the oxygen uptake of sediments and detritus. *Limnol. Oceanogr.* **30**: 111-122.
- Kovaleva N., V. Medientz, E. Gazetov. 2003. Influence of temperature and oxygen content on the intensity of the organic matter decay in Black Sea. *Gidrobiologicheskiy Zhurnal* (J. of Hydrobiology). **39**(4): 34-40. (in Russian)
- Lorke A., B. Muller, M. Maerki, A. Wuest. 2003. Breathing sediments: The control of diffusive transport across the sediment-water interface by periodic boundary-layer turbulence. *Limnol. Oceanogr.* **48**(6):2077-2085.
- Mathias J. and J. Barica 1980. Factors controlling oxygen depletion in ice-covered lakes. *Can. J. Fish. Aquat. Sci.* **37**: 185-194.
- Welch H., P. Dillon, A. Sreedharan. 1976. Factors affecting winter respiration in Ontario lakes. *J. Fish. Res. Board Can.* **33**: 1809-1815.



## MIXING AND COLD WATER

— 2 —

Brugge (Belg.) 1937. 10. 27.

## WARM DISCHARGES INTO COLD LAKES

Anthony Kay

Department of Mathematical Sciences, Loughborough University,  
Loughborough, Leicestershire, LE11 3TU

A.Kay@Lboro.ac.uk

### ABSTRACT

Discharges of cooling water from power stations are typically 10°C warmer than the receiving water. If the outfall is near a lake bed, the warm water is expected to rise to the surface, while being cooled by turbulent entrainment of lake water. It will then spread out over the lake surface as a gravity current, cooling further by entrainment. Thus the ecology of the lake bed will not be affected, except in the immediate vicinity of the outfall.

However, suppose the lake is at or close to 0°C. Because fresh water has its maximum density at 4°C, a discharge at 10°C only needs to cool to 8°C in order to become denser than its surroundings. If this happens while the plume of warm water is rising from the bed, it may never reach the surface, but will return to the bed as a "fountain". Even if it does reach the surface and form a gravity current, this current may be arrested when it loses buoyancy; a plume will then descend to the bed from the head of the arrested current. Either way, the bed will be affected by water that may be as warm as 8°C.

Theoretical models of these phenomena depend crucially on the parametrisation of entrainment. For vertical plumes, the entrainment assumption of Morton, Taylor & Turner is well established. However, for gravity currents, it is not clear how entrainment should best be modelled; indeed, some experimental results appear to be in conflict with each other. Nevertheless, we present theoretical analyses of both types of flow, showing how the behaviour of warm plumes and gravity currents in cold water depends on initial conditions of temperature and volume flux.

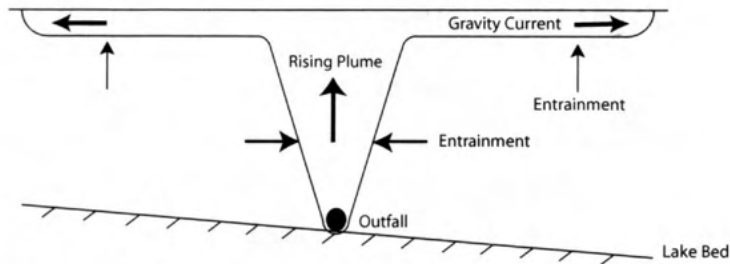


Figure 1: Behaviour of warm water discharge from an outfall in a lake warmer than 4°C: the plume and surface gravity current of warm water remain positively buoyant while entraining lake water

## INTRODUCTION

Power stations discharge cooling water at temperatures approximately 10°C higher than it is taken in (Macqueen, 1979). The discharged water is therefore less dense than the receiving water. If it is released near the bed of a lake, it will rise to the surface as a buoyant plume and will then spread out across the lake surface as a light gravity current. In both these stages it will be diluted by turbulent entrainment of lake water, so that its temperature will gradually cool towards the ambient lake temperature. This scenario is shown in Figure 1, from which it is apparent that the ecology of the lake bed should be unaffected by the warm water.

However, suppose the lake is below the temperature of maximum density, approximately 4°C in fresh water: as a specific example, we consider a discharge at 10°C into a lake at 0°C. Mixing between the warm discharge water and the cold receiving water can then produce water which is denser than either component, the so-called cabbeling phenomenon (e.g. Foster (1972)). This will occur when the mixing has cooled the discharge to below 8°C in our example. If this temperature of zero buoyancy (at which the discharge and ambient water have the same density) is reached before the rising plume reaches the lake surface, a "fountain" will form as shown in Figure 2(a), with the denser mixed water returning towards the lake bed around the central rising plume. However, if the plume reaches the lake surface still warmer than 8°C, it can start spreading out across the surface; however, further mixing, which is most intense just behind the head of a gravity current (Hacker *et al.*, 1996), will produce increasing volumes of water below 8°C. This will eventually cause the head of the gravity current to be arrested, and a plume of dense, but warm (compared to the ambient) water will then descend to the lake bed: see Figure 2(b). In either of these scenarios, the end result is that regions of the lake bed may experience temperatures up to 8°C warmer

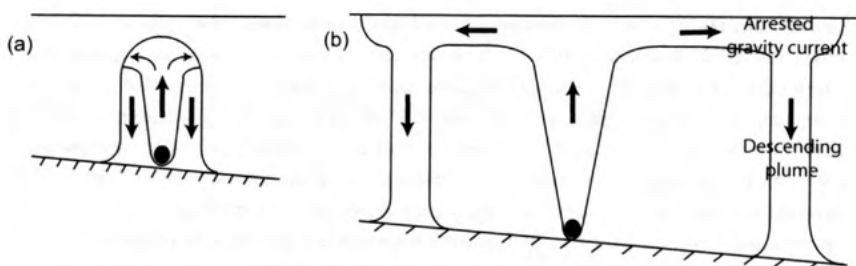


Figure 2: Possible behaviours of warm water discharge from an outfall in a lake cooler than 4°C: (a) the warm water loses buoyancy in the plume stage, and returns to the lake bed as a "fountain", or (b) the zero-buoyancy condition is reached in the gravity current stage, at which point the warm water descends to the bed as a plume from the head of the gravity current

than the natural lake temperatures. This has been observed in Lake Michigan by Hoglund and Spigarelli (1972), who measured a rise of 5.2°C from a natural ambient temperature of 0.5°C and discussed the biological implications of such a temperature rise. These authors only measured temperatures at a few locations in the vicinity of a power station outfall; we are not aware of any field observations of the flow in this situation, and the only laboratory simulations of the phenomenon appear to be those of Marmoush *et al.* (1984), who used a lock-exchange experiment to study a warm gravity current in water below the temperature of maximum density.

The object of the present work is to develop a theoretical analysis of the initial rising plume and the gravity current. [The eventual descending plume (see Figure 2(b)) may be modelled similarly to the rising plume, with the main feature of interest being that the downward buoyancy force increases as the plume entrains ambient water, until it has cooled to the temperature of maximum density; this is contrary to the normal expectation that entrainment decreases the buoyancy.] Fundamental to our models are parametrisations of entrainment, the physical process which is responsible for the most interesting features of both stages. For vertical turbulent plumes, the entrainment assumption of Morton *et al.* (1956), in which the entrainment velocity is assumed proportional to the mean vertical velocity in the plume, is well established. In contrast, there is no commonly used formula to describe entrainment into gravity currents; we shall use the formulae derived by Hallworth *et al.* (1996) using dimensional analysis supported by laboratory measurements.

Our analysis is two-dimensional throughout, so it could be supposed to apply to a discharge from a long diffuser. A discharge from a single outlet would require an axisymmetric analysis, but the main features are likely to be similar. We suppose

throughout that the lake is isothermal, with numerical results being given for a discharge at 10°C into a lake at 0°C. This can be considered as a worst-case scenario. Most lakes of moderate depth which freeze over in Winter are inverse stratified: the temperature increases with depth, from 0°C at the surface to a maximum which may be close to 4°C at the bed. By supposing an isothermal lake, we are over-estimating the temperature contrast between a rising plume and the ambient, hence over-estimating the rate at which entrainment will cool the plume, and so finding a lower bound on the height to which a plume can rise before losing buoyancy. Similarly for a descending plume from the head of an arrested gravity current, this assumption would over-estimate its density contrast with the ambient, so yielding an upper bound on the velocity with which it impinges on the bed as well as on its temperature difference with the lake water at the bed.

### THE RISING PLUME

We consider a plume of half-width  $b$ , vertical velocity  $w$  and temperature  $T$ , each of which vary with height  $z$ , in a lake of uniform ambient temperature  $T_\infty$ . Lake water is entrained into the plume at velocity

$$v_e = \alpha w \quad (1)$$

where the entrainment constant  $\alpha$  will be taken to have the value 0.1 in all calculations below (Turner, 1973). The Boussinesq approximation then allows us to express conservation of mass as an equation for volume flux,

$$\frac{d}{dz}(bw) = \alpha w, \quad (2)$$

and conservation of thermal energy is expressed in an equation for temperature flux:

$$\frac{d}{dz}(bwT) = \alpha w T_\infty. \quad (3)$$

Because  $T_\infty$  is uniform, the thermal flux

$$F = 2bw(T - T_\infty) \quad (4)$$

is conserved.

The plume's momentum flux varies due to buoyancy forces, resulting from the density difference between the plume and the ambient:

$$\frac{d}{dz}(bw^2) = gb \frac{\rho_\infty - \rho}{\rho_m}. \quad (5)$$

The densities of the plume and the ambient may be calculated in terms of the respective temperatures using a quadratic relationship

$$\rho = \rho_m - \beta(T - T_m)^2, \quad (6)$$

which is a good fit to experimental data for temperatures up to 10°C (Oosthuizen & Paul, 1996): here  $T_m \approx 4^\circ\text{C}$  is the temperature of maximum density for fresh water and  $\rho_m = 1.000 \times 10^3 \text{ kg.m}^{-3}$  is the density at that temperature, while the constant  $\beta$  has the value  $8.0 \times 10^{-3} \text{ kg.m}^{-3}(\text{°C})^{-2}$ . This equation of state may be used to express the buoyancy force in (5) in terms of temperatures, which may in turn be eliminated in favour of volume flux  $bw$  using (4). Given initial conditions of width, velocity and temperature at the source of the plume (e.g. the power station outfall), the thermal flux  $F$  can be calculated and a simple numerical integration of the equations for volume flux and momentum flux can then be done to yield the width, velocity and temperature as functions of height.

The results presented graphically below are in terms of dimensionless variables defined as follows. A temperature scale for the flow is the difference between the temperature of maximum density and the temperature of the ambient, so our dimensionless temperature is

$$\theta = \frac{T - T_\infty}{T_m - T_\infty}; \quad (7)$$

thus  $\theta = 2$  at the temperature of zero buoyancy, with the plume being denser than the ambient when  $\theta > 2$  and lighter when  $\theta < 2$ ; for a discharge at 10°C into a lake at 0°C, we have  $\theta_s = 2.5$  (where the subscript  $s$  on any variable indicates source conditions). The source half-width  $b_s$  provides a length scale for height and half-width. A scale for the buoyancy force is

$$g_m = \frac{g\beta(T_m - T_\infty)^2}{\rho_m}, \quad (8)$$

so that dimensionless velocity can be defined as a Froude number

$$\phi = \frac{w}{(g_m b_s)^{1/2}}. \quad (9)$$

For a power station discharge, the temperature and volume flux are fixed by the cooling water requirements, so the Froude number at the outfall is the only parameter within the designer's control. Macqueen (1979) quotes a volume flux of  $25 \text{ m}^3.\text{s}^{-1}$  and a maximum discharge velocity of  $2 \text{ m.s}^{-1}$ ; to comply with the 2-dimensional geometry of our model, we suppose (arbitrarily) a diffuser of length 100 m, so that the source width is 0.125 m. Since  $g_m \approx 1.3 \times 10^{-3} \text{ m.s}^{-2}$  for the given temperature conditions, this yields the source Froude number as  $\phi_s \approx 50$ ; a broader source or a lower velocity would give a lower value of  $\phi_s$ .

The maximum height  $z_f$  attained by the plume is the height at which the velocity falls to zero (assuming a sufficiently deep body of water); this, and the dimensionless temperature  $\theta_f$  at  $z = z_f$ , are shown in Figure 3. Not surprisingly, increasing the source velocity (i.e. Froude number) for a given source width allows the plume to reach a greater height. It can be shown that for large  $\phi_s$ ,

$$\frac{z_f}{b_s} \sim k\alpha^{-1/3}\phi_s^{4/3} \quad \text{or} \quad z_f \sim k\alpha^{-1/3}g_m^{-2/3}w_s^{4/3}b_s^{1/3}, \quad (10)$$

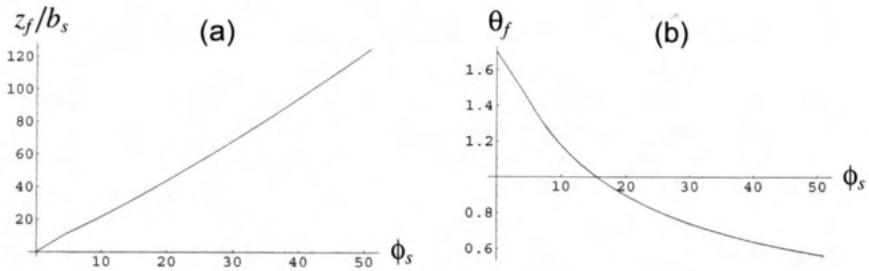


Figure 3: (a) Maximum height (scaled with source width) and (b) dimensionless temperature at the maximum height, plotted as functions of source Froude number for a plume discharged with temperature  $\theta_s = 2.5$

where the numerical factor  $k$  is found to be approximately 0.24. We may suppose that  $z_f$  is the maximum depth of water in which a plume can reach the surface and then spread out as a gravity current (the desirable outcome), so in our example with  $\phi_s = 50$  and  $b_s = 0.125$  m, Figure 3 yields  $z_f \approx 120b_s = 15$  m. However, the plume-top temperatures (Figure 3(b)) are well below the temperature of zero buoyancy ( $\theta = 2$ ), indicating that the momentum of a plume can carry it a considerable distance against adverse buoyancy forces; but if a plume reaches the surface denser than the ambient, it will be unable to spread across the surface as a gravity current. Thus we argue that the height  $z_n$  at which the temperature of zero buoyancy is reached gives the maximum depth of water that will prevent a "fountain" forming. This is plotted in Figure 4, where we see that  $z_n \sim 2.8b_s$  for large  $\phi_s$  (where this numerical value depends only on the dimensionless source temperature and the entrainment constant). The implications for outfall design are clear: avoiding the fountain effect requires the outfall width to be as large as possible and the exit velocity to be just within the large- $\phi_s$  regime. The difference in behaviour between  $z_n$  and  $z_f$  is because the former depends purely on the source momentum flux in the large- $\phi_s$  regime, whereas the latter is mainly determined by the erosion of that momentum flux by adverse buoyancy forces.

## THE GRAVITY CURRENT

A surface gravity current, either spreading out from the top of a rising plume or from a surface discharge of warm water, would in most cases of practical relevance be a steady phenomenon. Unfortunately a theory of entrainment into gravity currents only appears to be available for currents from sudden releases, in particular the lock-

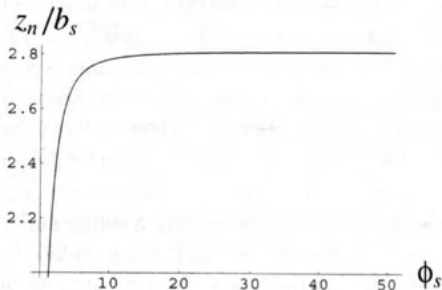


Figure 4: Height at which plume attains zero buoyancy, plotted as a function of source Froude number for a plume discharged with temperature  $\theta_s = 2.5$

exchange set-up. Hallworth *et al.* (1996) assumed that entrainment is into the head of the gravity current, and defined an entrainment ratio

$$E \equiv \frac{\text{volume of entrained ambient fluid in head}}{\text{volume of original current fluid in head}}. \quad (11)$$

They derived a formula for  $E$  as a function of horizontal distance travelled, involving several empirical constants:  $\alpha$  and  $k$  respectively parametrise entrainment of ambient fluid and loss of fluid from the head to the tail of the gravity current, while  $S$  is a shape factor for the head. From their experiments, they found

$$\alpha = 0.019, k = 0.203, S = 0.55; \quad (12)$$

for a gravity current along a free surface, and

$$\alpha = 0.065, k = 0.142, S = 0.71. \quad (13)$$

for a gravity current along a smooth, rigid boundary (e.g. representing flow under an ice cover).

We assume that a gravity current comes to rest when it has entrained sufficient lake water for its temperature to drop to the temperature of zero buoyancy. If its initial temperature is  $T_0$ , this occurs when the entrainment ratio is

$$E = \frac{T_0 + T_\infty - 2T_m}{2T_m - 2T_\infty} \quad (14)$$

Using the Hallworth *et al.* (1996) formula for  $E$  as a function of distance, we can then calculate the distance  $x_n$  travelled before the zero-buoyancy condition is reached:

$$x_n = \frac{2\sqrt{A_s}}{S(k-\alpha)} \left\{ 1 - \left( \frac{T_0 - T_\infty}{2(T_m - T_\infty)} \right)^{-(k-\alpha)/2\alpha} \right\} \quad (15)$$

where  $A_s$  is the cross-section area of the current (in the longitudinal-vertical plane) at the stage where entrainment starts. Note that the index  $(k-\alpha)/2\alpha$  has the contrasting numerical values 4.84 in free-surface flow and 0.592 under a rigid lid, due mainly to the much greater entrainment under a rigid lid; this in turn results from overturning motions caused by the no-slip condition at a rigid surface (Simpson, 1997). For a release at  $10^\circ\text{C}$  into a lake at  $0^\circ\text{C}$ , we obtain  $x_n = 13.8\sqrt{A_s}$  at a free surface but  $x_n = 2.4\sqrt{A_s}$  under an ice cover. Although these results apply to lock-exchange releases, we may hope that they do at least give a rough indication of the distance travelled by a steady gravity current, with  $\sqrt{A_s}$  being replaced by some length scale representative of the near-field of the source. In particular, we note that an ice cover may greatly reduce the distance that such a gravity current can propagate.

## References

- Foster, T.D. 1972 An analysis of the cabbeling instability in sea water. *J. Phys. Oceanogr.* **2**, 294 – 301.
- Hacker, J., Linden, P.F. & Dalziel, S.B. 1996 Mixing in lock-release gravity currents. *Dyn. Atmos. Oceans* **24**, 183 – 195.
- Hallworth, M.A., Huppert, H.E., Phillips, J.C. & Sparks, R.S.J. 1996 Entrainment into two-dimensional and axisymmetric turbulent gravity currents. *J. Fluid Mech.* **308**, 289 – 311.
- Hoglund, B. & Spigarelli, S.A. 1972 Studies of the sinking plume phenomenon. *Proc. 15th Conf. Great Lakes Res*, pp. 614 – 624.
- Macqueen, J.F. 1979 Turbulence and cooling water discharges from power stations. In: C.J. Harris (ed.), *Mathematical Modelling of Turbulent Diffusion in the Environment*, 379 – 437.
- Marmoush, Y.R., Smith, A.A. & Hamblin, P.F. 1984 Pilot experiments on thermal bar in lock exchange flow. *J. Energy Engng.* **110**, 215 – 227.
- Morton, B.R., Taylor, G.I. & Turner, J.S. 1956 Turbulent gravitational convection from maintained and instantaneous sources. *Proc. R. Soc. Lond. A* **234**, 1 – 23.
- Oosthuizen, P.H. and Paul, J.T. 1996 A numerical study of the steady state freezing of water in an open rectangular cavity. *Int. J. Num. Meth. Heat Fluid Flow* **6**, 3 – 16.
- Simpson, J.E. 1997 *Gravity Currents in the Environment and the Laboratory*, 2nd Edn. Cambridge University Press.
- Turner, J.S. 1973 *Buoyancy Effects in Fluids*. Cambridge University Press.

## COLD-WATER EVENTS IN THE MIXED LAYER OF LAKE GENEVA

### B. Ozen

*Laboratoire d'hydraulique environnementale, EPFL, S-18, CH-1015, Lausanne, Switzerland  
baris.ozen@epfl.ch*

### S. A. Thorpe

*School of Ocean Sciences, University of Bangor, Menai Bridge, Bangor, United Kingdom  
oss413@bangor.ac.uk*

### U. Lemmin

*Laboratoire d'hydraulique environnementale, EPFL, S-18, CH-1015, Lausanne, Switzerland  
ulrich.lemmin@epfl.ch*

### T. R. Osborn

*Department of Earth and Planetary Science, The Johns Hopkins University, Baltimore, Maryland  
osborn@jhu.edu*

### Abstract

Measurements of temperature, velocity, and microscale velocity shear were made from the research submarine, F. A. Forel, in the near-surface mixed layer of Lake Geneva in conditions of moderate winds of 6–8 m s<sup>-1</sup> and of net heating at the water surface. The submarine carried arrays of thermistors and a turbulence package, including airfoil shear probes whose data were used to estimate the rate of dissipation of turbulent kinetic energy per unit mass. Measurements revealed large-scale structures, coherent over the 2.38 m vertical extent sampled by a vertical array of thermistors, consisting of filaments tilted in the wind direction. They are typically about 1.5 m wide, decreasing in width in the upward direction, and are horizontally separated by typically about 25 m in the downwind direction. Originating from the upper thermocline, they are characterized by their relatively low temperature and low rates of dissipation of turbulent kinetic energy with respect to the mixed layer, and by an upward vertical velocity of a few cm s<sup>-1</sup>.

### 1. Introduction

The understanding of processes that contribute to the vertical transfer of momentum, heat and gases within the near-surface mixed layer of oceans and lakes, into and from the thermocline, and between the water and the atmosphere has increased in the last decades, largely due to new methods of observation.

Processes associated with Langmuir circulation and with the instability of the mean shear flow within the layer or with thermal convection are identified to be mainly responsible for the vertical transfer of heat from the surface at depths greater than the depth where turbulence generated by surface wave breaking may dominate mixing. These processes may be identified by the presence of large-scale coherent

structures in the thermal or velocity field, for example by temperature anomalies and vertical velocities in the case of Langmuir circulation, temperature ramps or microfronts in the case of processes related to the mean shear, and plumes in convective conditions. Studies of the structure of the temperature field within Langmuir circulation are described by Thorpe and Hall (1982) and Thorpe et al. (2003). Temperature ramps are investigated by Thorpe and Hall (1977, 1982) and Thorpe and Osborn (2005), and convective plumes by Thorpe et al. (1999).

The processes by which water is entrained into the mixed layer from the underlying thermocline are, at best, poorly known. According to laboratory experiments by Strang and Fernando (2001), Kelvin-Helmholtz or Holmboe instability may be important. Which type of instability dominates is dependent on the magnitude of a bulk Richardson characterizing the flow and stratification at the base of a turbulent upper layer.

Our objective here is to describe observations made from a moving platform in the mixed layer of a lake that provide evidence of the entrainment into the mixed layer of cold water filaments from the underlying thermocline, structures that appear not to have been identified in previous observations.

## 2. Site and Observational Setup

Observations were carried out in Lake Geneva from the submarine F. A. Forel operated at a site close to the northern shore of the Lake, off the port of Ouchy,

Lausanne. The bathymetry of the lake is shown in Fig. 1a with an inset of the observation site in Fig. 1b.

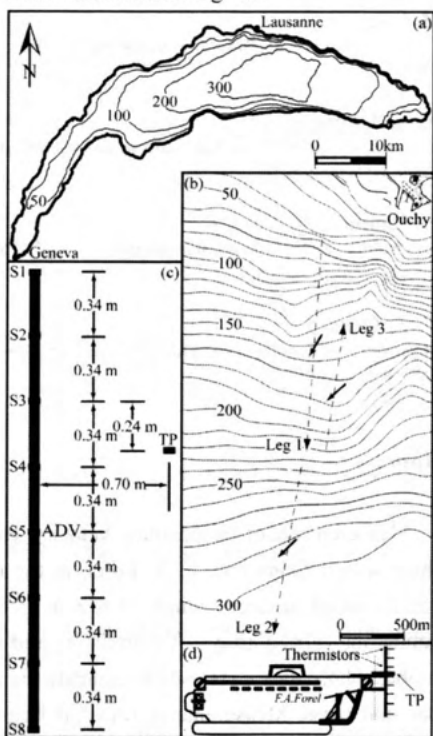


**Fig. 1:** (a) Bathymetric map of Lake Geneva with an inset of the observation site (b). The depth contours are in meters. Tracks of the submarine corresponding to the legs are indicated. Small arrows on the tracks indicate mean direction of the wind during the legs. (c) Relative positions of the sensors viewed from ahead of the submarine. The thermistors are labeled S1-S8. TP shows the location of the turbulence package. (d) Sketch, not to scale, of the F. A. Forel, showing relative positions of the sensors on the bow.

For the present study, the F. A. Forel (Thorpe et al., 1999) was equipped with an array of high-precision fast response thermistors, an acoustic Doppler velocimeter (ADV), and a turbulence package. The thermistors provided measurements of temperature, with a resolution of 1 mK at a frequency of 10 Hz, which are used to obtain information about

Leg	Depth (m)	Course Direction (°)	Cruise Speed (m s <sup>-1</sup> )	Wind Speed (m s <sup>-1</sup> )	Wind Direction (°)
1	4.4 ± 0.33	184		6.1	40
2	6.5 ± 0.30	189	0.43 ± 0.02	6.3	45
3	5.3 ± 0.44	8		6.0	48

**Table 1:** Navigational and meteorological data averaged over the legs. Unavoidably occurred variations in the submarine movement are indicated by the deviations. Meteorological data were obtained from the nearest meteorological station of the Swiss Meteorological Network.

the vertical field of temperature that the submarine is passing through. The ADV made velocity measurements in the range of ± 1 m s<sup>-1</sup> with 1% accuracy at the same sampling frequency as the thermistors. The turbulence package (Thorpe et al., 2003), included two airfoil probes (Osborn and Crawford, 1980) for sensing the vertical and horizontal velocity shear from which the rate of dissipation of turbulent kinetic energy per unit mass,  $\varepsilon$ , is estimated. Fig. 1c and d show relative positions of all measuring instruments. A pressure transducer, two accelerometers, and a compass on the submarine supplemented the above mentioned instruments providing measurements of depth, pitch, roll, and heading at frequencies of 10 Hz with resolutions of 0.1 m and 1°, respectively.

Data were obtained on 01 November 2001, with three legs run at uniform speed and constant depth. Tracks of the submarine are shown in Fig. 1b and a summary of the navigational and meteorological data, averaged over the legs, is given in Table 1.

The mixed layer thickness at the site was determined to be about 10 m from a preliminary dive of the submarine. The net heat flux into the lake through the water surface was about 170 W m<sup>-2</sup>. The mean thermal compensation depth (Woods, 1980),  $Z_{tc}$ , above which there is a net cooling of the water, was about 0.6 m. The

significant wave height,  $H_s$ , estimated from visual observations, was about 0.3–0.4 m. The mean depths at which observations were carried out remained thus large compared to  $Z_{tc}$  and  $H_s$ .

### 3. Conditional Analysis

Temperature data have a negative skewness and show many instances when the temperature descends rapidly to values below the local average, suggesting the presence of filaments of water being entrained from the upper thermocline. An analysis is carried out using conditional sampling in order to investigate the structure of these cold-water events, and their effect on the dissipation of TKE and the water motion. Identification of the cold-water events is made using temperature data recorded by one of the thermistors selected as reference. Each thermistor record is averaged over 1 s intervals and detrended by removing a running mean over a period of 1 min. To provide a basis for event identification a threshold level is chosen as

$$T' = \bar{T}' - C\sigma_T \quad (1)$$

where  $T'$  is the detrended temperature at the reference thermistor,  $\sigma_T$  is the standard deviation of the detrended record, the overbar denotes a temporal average, and the constant  $C$  is taken to be equal to 1.5.

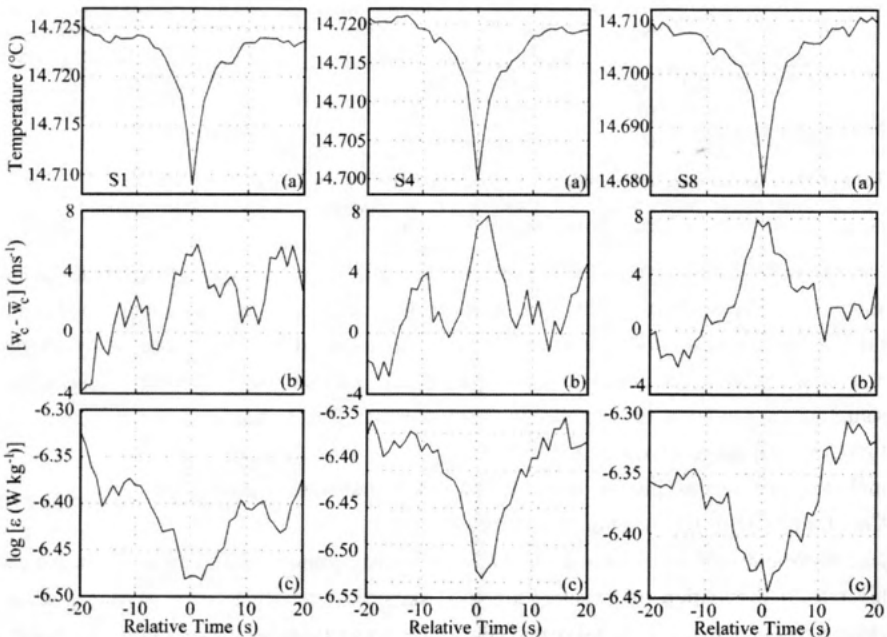


**Fig. 2:** Average time sections of the measured values through conditionally sampled cold-water events in legs 1, 2, and 3. Panels show (a) the temperature recorded by the reference thermistor, (b) the vertical velocity, and (c) the rate of dissipation. The reference thermistor used to identify the events is, from left to the right, S1, S4, and S8, respectively.

Instances when the temperature recorded by the reference thermistor remains below this threshold level are recognized as cold-water events. The times of passage of the minimum values during these events are selected as times of the events. Intervals centered on the times of events are extracted from the data, and averaged together to obtain average time sections of these quantities across events at the reference thermistor.

Fig. 2 shows average time sections of the temperature recorded by the reference thermistors, here chosen as S1, S4, and S8, together with the vertical velocity of the water corrected for the vertical motion of the submarine, and the rate of dissipation, across event in legs 1–3.

The temperature recorded at the reference thermistors S1, S4, and S8 decreases on the average by about 16, 20, and 21 mK, respectively, at times of events. The rate of dissipation shows a pronounced minimum, reaching values about 50% lower than the mean at the mean depth of the submarine. At the same time, the vertical velocity of water increases indicating an upward movement. These variations are consistent with upward transport of cold water with relatively low turbulence levels from below the observation depth.

Fig. 3 shows average time sections of the temperature across events in legs 1–3, and gives further information about the nature of the cold-water events.

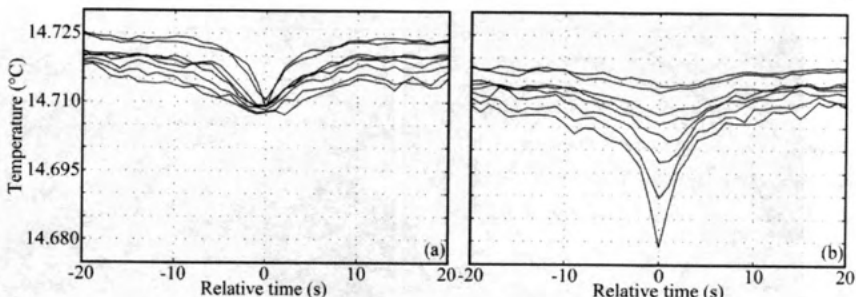


**Fig. 3:** Average time sections of the temperature recorded by the vertical array of thermistors through cold-water events in legs 1, 2, and 3. The events are identified using (a) thermistor S1, and (b) thermistor S8, as references. The temperatures are, top to bottom, from the thermistor S1 to S8 on the vertical array. Legs 1 and 2 are to the south; time is reversed while analyzing the data from leg 3, which was made in the northerly direction, in order to preserve the tilted temperature structure.

Selection of S1 as the reference thermistor reveals a temperature decrease that is replicated in all thermistors of the array without much reduction in strength, but with minima values that tend towards earlier times, indicating that the mean event has a tilted structure (Fig. 3a). When the lowest thermistor, S8, is selected as the reference, the cold-water signal is weakly detected at the top thermistor, although a trend towards an increase at the time of the temperature minima is visible at the lower thermistors (Fig. 3b). The difference between these two conditional sets of temperatures is consistent with cold-water events that are produced by filamentary structures moving upwards from levels below the submarine, but which may not span the totality of the array.

The temperature anomaly in the events of Fig. 3a is about 20 mK. The mean temperature gradient in the mixed layer, estimated from measurements during preliminary submarine dives is about 1.7 mK m<sup>-1</sup>. This implies that a vertical scale of about 12 m may be associated with the temperature anomalies: the source of the cold water is therefore in the upper

thermocline below the mixed layer, since the submarine operates only about 3.3 m above the base of the mixed layer. The mean distance between events is about 25 m but with a large standard deviation of 30 m. Their mean width (the mean distance moved by the submarine when the temperature remained less than the threshold value) is about 1.6 m ± 1 m at the observation depths.

#### 4. Correlation, coherence and phase of temperature data

Cross-correlation coefficients with time lags,  $\tau$ , between pairs of thermistors at relative positions  $A$  and  $B$  ( $X_{AB}$ ) are calculated using 1 s averaged temperature records in order to investigate the structure of the temperature field in the mixed layer.

The time-lagged cross-correlation values allow two-dimensional diagrams to be constructed in  $z-x$  plane, where  $x$  is directed along the submarine path in the travel direction and  $z$  is vertically upwards. Distances in  $x$  direction are derived using Taylor's frozen field hypothesis and the mean submarine speed.

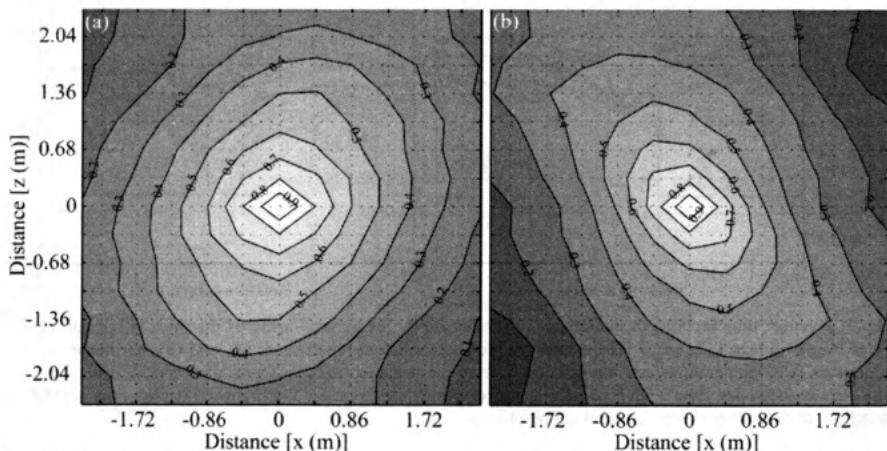


**Fig. 4:** Contour plots of the cross-correlation coefficients in the x-z plane during legs 1 and 3. Correlation distances are measured using the thermistor S1 as one of the locations. (a) and (b) show isocontours during leg 1 and 3, respectively.

Fig. 4 shows the constant  $X_{AB}$  surfaces in the z-x plane for legs 1 and 3, obtained using correlations between S1 and the other thermistors down the array. Both diagrams show roughly elliptical correlation contours tilted at about  $60^\circ$  to the horizontal. Coherent structures are tilted in opposite directions, consistent with the direction of the legs relative to the wind direction (Leg 3 is in a direction opposite to that of the first leg, and upwind).

The mean structure of the temperature field is also investigated using coherence and phase differences of temperature data recorded at 10 Hz. The coherence decreases as the vertical separation of thermistors increases. Using the Taylor frozen field hypothesis and the mean submarine speed, coherence of sensors separated at 0.34, 0.68 and 1.02 m is found to be significant ( $> 0.6$ ) at frequencies corresponding to horizontal distances of about 4.8 m, 8.1 m, and 15.5 m, respectively, in legs 1 and 3.

The phase differences between vertically separated pairs of thermistors in these two

legs, made in opposite directions, differ in sign for frequencies where the temperature data are found to be coherent, implying that coherent structures are tilted in the downwind direction. A measure for the inclination of the structures to the horizontal is obtained using the phase differences and the mean submarine speed. This angle is found to be about  $78^\circ$ , somewhat greater than the tilt angles found by correlation techniques.

## 5. Conclusion

Observations made from the F. A. Forel operating in the mixed layer of Lake Geneva allowed us to identify large-scale coherent structures, events in which the relatively cold water, originating in the thermocline, is transferred vertically upwards and entrained into the mixed layer.

A sketch of the cold-water events identified in the mixed layer is shown in Fig. 5. They consist of filaments, tilted in a sense consistent with the mean wind-driven

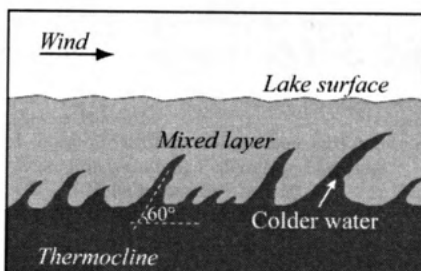


Fig. 5: Sketch showing the cold-water filaments in the mixed layer.

shear in the mixed layer, across which both the temperature and the rate of dissipation decrease are less than in the ambient water. They are characterized by a vertical motion at speeds of about  $5 \text{ cm s}^{-1}$  in the upward direction.

The filaments have similar tilt angles to those reported for temperature ramps in the Loch Ness by Thorpe and Hall (1980). This suggests that the two structures may be part of a single process. No connection has however been established. The thin tilted structures strongly resemble those seen in visualizations of the disturbed density field resulting from Holmboe instability, but without a definite linkage to their source it is impossible to be certain.

Further investigations with thermistors and velocimeters, capable of sampling the upper thermocline and the mixed layer at the same time, would be worthwhile to identify the presence and structure of the mixing processes, and to better understand the dynamics of this presently undersampled region of entrainment into the mixed layer.

## References

- Osborn, T. R. and W. R. Crawford, 1980: An airfoil probe for measuring turbulent velocity fluctuations in water. *Air-Sea Interaction; Instruments and Methods*, F. Dobson, L. House and R. Davis, Eds., Plenum, 801 pp.
- Strang, E. J. and H. J. S. Fernando, 2001: Entrainment and mixing in stratified shear flows. *J. Fluid Mech.*, **428**, 349-386.
- Thorpe, S. A. and A. J. Hall, 1977: Mixing in upper layer of a lake during heating cycle. *Nature*, **265**, 719-722.
- Thorpe, S. A. and A. J. Hall, 1980: The mixing layer of Loch Ness. *J. Fluid Mech.*, **101**, 687-703.
- Thorpe, S. A. and A. J. Hall, 1982: Observations of the thermal structure of Langmuir circulation. *J. Fluid Mech.*, **114**, 237-250.
- Thorpe, S. A. and T. R. Osborn, 2005: Skewness of spatial gradients of turbulent dissipation rate in the mixed layer. *J. Phys. Oceanogr.* (Under review).
- Thorpe, S. A., U. Lemmin, C. Perrinjaquet, and I. Fer, 1999: Observations of the thermal structure of a lake using a submarine. *Limnol. Oceanogr.*, **44**, 1575-1582.
- Thorpe, S. A., T. R. Osborn, J. F. E. Jackson, R. G. Lueck, and A. J. Hall, 2003: Measurements of turbulence in the upper-ocean mixing layer using Autosub. *J. Phys. Oceanogr.*, **33**, 122-145.
- Woods, J. D., 1980: Diurnal and seasonal variation of convection in the wind-mixed layer of the ocean. *Quart. J. Roy. Meteor. Soc.*, **106**, 379-394.

und schreibt sie mit dem Namen des Verfassers, der sie geschrieben hat.

Die Schriftstellerin schreibt die Schriftstellerin, die sie geschrieben hat.

Die Schriftstellerin schreibt die Schriftstellerin, die sie geschrieben hat.

Die Schriftstellerin schreibt die Schriftstellerin, die sie geschrieben hat.

Die Schriftstellerin schreibt die Schriftstellerin, die sie geschrieben hat.

Die Schriftstellerin schreibt die Schriftstellerin, die sie geschrieben hat.

Die Schriftstellerin schreibt die Schriftstellerin, die sie geschrieben hat.

Die Schriftstellerin schreibt die Schriftstellerin, die sie geschrieben hat.

Die Schriftstellerin schreibt die Schriftstellerin, die sie geschrieben hat.

Die Schriftstellerin schreibt die Schriftstellerin, die sie geschrieben hat.

Die Schriftstellerin schreibt die Schriftstellerin, die sie geschrieben hat.

Die Schriftstellerin schreibt die Schriftstellerin, die sie geschrieben hat.

Die Schriftstellerin schreibt die Schriftstellerin, die sie geschrieben hat.

Die Schriftstellerin schreibt die Schriftstellerin, die sie geschrieben hat.

Die Schriftstellerin schreibt die Schriftstellerin, die sie geschrieben hat.

Die Schriftstellerin schreibt die Schriftstellerin, die sie geschrieben hat.

Die Schriftstellerin schreibt die Schriftstellerin, die sie geschrieben hat.

Die Schriftstellerin schreibt die Schriftstellerin, die sie geschrieben hat.

# VERTICAL SLICE TOMOGRAPHY EXPERIMENT IN LAKE GENEVA: OBSERVING THE WINTER COOLING

Xavier Falourd

Laboratoire d'Electromagnétisme et d'Acoustique  
 École Polytechnique Fédérale de Lausanne  
 CH - 1015 Lausanne Switzerland  
 Email: xavier.falourd@epfl.ch

Physical limnology in Lake of Geneva tries to identify the dominant processes of transport and mixing which influence the water quality of the lake. Based on ocean acoustic tomography, an acoustic experiment is performed in Lake of Geneva so as to define future developments for 3D lake tomography. In Lake Acoustic Tomography, acoustic sources and receivers are strategically distributed around a lacustrine basin and they simultaneously emit and receive coded signals. By measuring sound travel times in two directions between vertical arrays of hydrophones, it is expected to infer the vertical thermal stratification and large scale dynamics using tomography inversions techniques. A first vertical slice tomographic experiment was carried out during the winter 2003-2004 in the main part of Lake of Geneva using two vertical arrays of emitters and receivers between Lausanne and Amphion. Based on the modelling of sound propagation in an inhomogeneous moving medium and its systematic comparison with experimental data, it is shown that the qualification of the major processes controlling hydrodynamics (thermal stratification, internal waves) is possible by the analysis of sound travel times between two sites close to the banks during the cooling season.

## 1 Introduction

It is established that the supply of high quality drinking water will be of great importance in the near future. The large deep lakes playing a paramount part for this provisioning, strategies for their long-term management must be elaborated. The development of the concepts and suitable tools requires a better comprehension of the transport and the mixing of the water masses. Physical limnology tries to identify these processes by quasi-continuous observations from moored instrumentation and by numerical modelling. Its goal is to explain the forces generating internal waves, and to understand the role of the episodic events and their impact on the lake. Since most measurements are carried out from boats (temperature profiles) and/or with a network of moored instruments (current profilers, chains of thermistors), only local properties are measured. Therefore, the environmental management of the lakes thus requires to have a method of observation to qualify large scale processes using permanent networks for forecasting applications.

Based on ocean acoustic tomography principles [8] [2] [10], an acoustic experiment is performed in the Lake of Geneva so as to define future developments for limnological phenomena observations, ie to investigate the dynamics of physical processes in lakes.

Due to the relation between sound speed and water temperature, the sound travel time is a direct measure of the average temperature between the source and the receiver. By measuring the travel times of sound pulses over extended periods of time, it is anticipated that basin-scale measurements of lake temperatures can be obtained because of the accurate path-integral relations between the travel time data and the unknown temperature (or sound speed) variations: this is known as solving the forward problem of tomography. The inverse solution is often constructed as a minimum mean-square-error estimate with (a priori) specified solutions and noise variances of observed time series.

In Lake Acoustic Tomography (LAT), acoustic sources and receivers are strategically distributed around a lacustrine basin. One or more of each can be combined in a system and they simultaneously emit and receive coded signals. By measuring sound travel times in two directions between vertical arrays of hydrophones, placed at the boundary of the lake, we expect to infer the vertical thermal stratification and large scale dynamics of the lake using tomography inversions techniques. However, differently from open-ocean applications, bottom limited and range-dependent propagation conditions actually present challenges for the tomographic purpose. The paper presents the results of an experimentation carried out during the winter 2003-2004 in the lake of Geneva in order to observe the winter cooling. Some results are briefly presented giving different aspects of the research engaged [3].

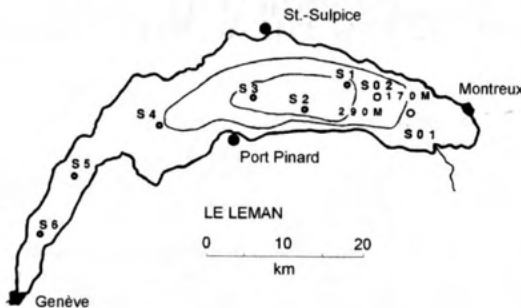


Figure 1: Situation of stations s1 to s6, s01 and s02.

## 2 Annual cycle of the thermal stratification

As the field of temperature characterizes the propagation of the sound, its evolution during an annual cycle must be analyzed so as to get a prior information useful for the determination of the tomographic instrumentation. In order to make a synthesis of the forward problem, one representative model of the vertical stratification is defined. The two major processes involved in the water column dynamics of the lake during the annual cycle are the heat flux and the field of wind.

In order to develop a model, the study starts from the data base established partly between the years 1987 and 1991 on the request of the International Commission for the Protection of the Lake of Geneva (CIPEL) [7] [6]. This one is composed of 93 temperature profiles taken at six predefined locations covering the three principal zones of the lake; namely the Small Lake, the Great Lake and the High Lake (Fig. 1). Fig. 2 illustrates the evolution of the temperature between January 1, 1987 and January 1, 1992 at locations s1 to s3 after averaging and interpolating the three fields  $\mathbf{T}_{s1}$ ,  $\mathbf{T}_{s2}$  and  $\mathbf{T}_{s3}$  composed of profiles taken simultaneously. The model rests on the reduction of the field of temperature situated in the Great Lake in a daily field of temperature  $\mathbf{T}$  of dimension  $365 \times 300$ . The principle is to define the intrinsic parameters of the stratification that make it possible to obtain characteristic sound speed profiles.

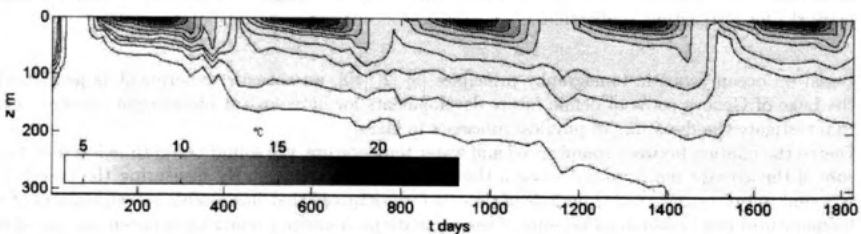


Figure 2: Evolution of the average field of temperature from stations s1 to s3 (Great Lake) between 01-01-1987 and 01-01-1992.

From the methods of decomposition of a field by the principal components analysis [9] [12] [4], we infer to evaluate the major processes characterizing the thermal stratification of the Great Lake. It is obvious that one must expect to find significant processes in relation with heat flux and seasonal wind effects on water dynamics. The field of temperature is reduced of its average value for each depth and its covariance matrix is defined by  $R_T = \mathbf{T}^\top \mathbf{T}$ . Principal components describing the field of temperature  $\mathbf{T}$  are calculated by the resolution of the eigenvalue problem according to  $R_T C = C \Lambda$  where  $\Lambda$  is the diagonal matrix containing the eigenvalues  $\lambda_j$  of  $R_T$ . The matrix  $C$  is composed of the eigenvectors  $\vec{c}_j$  of  $R_T$  corresponding to the eigenvalues  $\lambda_j$ . It is possible to rebuild the field considering the  $J$  principal components  $\vec{c}_j$  and their time series  $\vec{a}_j$ :  $\mathbf{T}(-) = \sum_{j=1}^J \vec{a}_j \vec{c}_j$ .

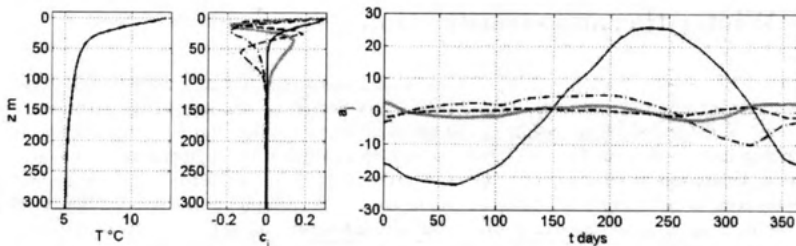


Figure 3: Left: annual temperature profile; middle: principal components  $c_1$  to  $c_4$ ; right: their respective time series during an annual cycle (January 1 to December 31).

The model  $\mathbf{T}(-)$  is built by summation of the  $J$  relative fields of temperature  $\mathbf{T}_j$ , associated with each principal component  $c_j$ , to the mean temperature profile which is directly in agreement with the parameters  $\phi$ ,  $T_{0,a}$  and  $T_{z,a}$  defined by M. Straskraba [11]. Finally, the thermal stratification  $\mathbf{T}(-)$  described by the four principal components define more than 99 % of the field  $\mathbf{T}$  (Table 1, Fig. 3).

Table 1: PCA results

PC n°	1	2	3	4
ratio (%)	92.43	6.49	0.83	0.20

Fig. 4 illustrates the three relative fields  $\mathbf{T}_1$ ,  $\mathbf{T}_2$  and  $\mathbf{T}_{3+4}$ . The impact of  $c_1$  concentrates primarily on the first 25 meters of water describing the heat flux action on upper water masses. Its time series  $a_1$  is proportional to the temperature evolution during the annual cycle on the surface  $T_0$  given by Straskraba [11].  $c_2$  acts mostly between October and January, period of mixing of the upper water masses due to the wind forcing.  $c_3$  and  $c_4$  are not directly interpreted here but may qualify the thermocline development when added. From these four principal components, a calendar representative of the temperature profiles is established as a prior information to evaluate the thermal stratification of the Great Lake constituting an useful information when investigating the inverse problem [8].

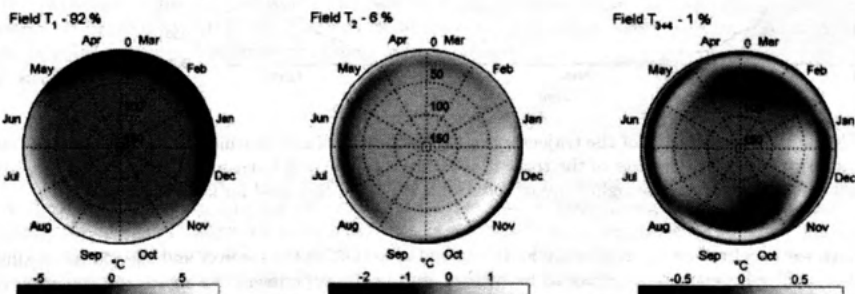


Figure 4: Polar diagrams representing fields of temperature  $\mathbf{T}_1$ ,  $\mathbf{T}_2$  and  $\mathbf{T}_{3+4}$  (resp. left to right). Diagrams describe the temperature field in the first 150 meters of water, with in radial axis the depth and in angle the annual cycle

Since the thermal stratification is weak and that internal waves provoke large tilts of the thermocline due to wind forcing during the cooling season, the study is focused on the winter period which constitutes the simplest scenario for detecting large scale hydrodynamical processes by acoustic tomography.

### 3 Winter thermal stratification

In winter, the solar radiation can be so weak, that the losses dominate the total heat budget of the lake during all day: the heat flux goes from the lake towards the atmosphere. The temperature of the lake surface decreases, as the height of the quasi-isothermal epilimnion,  $h_e$ , increases; hence for one rigorous winter, winter cooling can involve a homogenization of the temperature on the whole water column. Under this water mass, one finds a stratified structure composed of the thermocline and the hypolimnion. So as to evaluate the action of the cooling of the upper water masses and the descent of the thermocline, we propose a simple model qualifying the vertical profile of temperature. The thermal state of the water column is modelled by two different functions defining the upper and lower water masses,  $T(z) = T_u(z) + T_b(z)$  where  $T_u$  qualify the epilimnion and  $T_b$  the structure composed by the thermocline and the hypolimnion. It is supposed that during the cooling the gradient of temperature in the thermocline is constant. Once the cooling defined, we attempt to observe its influence on the propagation between two sites close to the banks.

### 4 Cooling and ray diagram

A common way to study the sound propagation is based on ray theory: the sound propagation is described by rays ie the paths followed by the wavefronts between the source and the receiver. Each ray is defined by its travel time and others geometric parameters (angle of incidence, maximum and minimum depth, ...). In order to observe the influence of the cooling on the acoustic propagation, a whole set of rays is calculated covering a complete cooling of the water column for a given instrumental configuration and with range independent sound speed profiles. Simulations are made using the 2D-ray tracing software PRAMM 2.4. Both emitters and receivers, in the nearshore of Lausanne and Amphion, are supposed to be fixed at 30 m above the bottom of the lake at 45 m depth and at a distance of 13.175 km.

The resolution of the direct problem consists of the determination of the rays to be compared with experimental identified ones. These rays are composed of refracted - refracted rays (R-R), refracted - surface reflected rays (R-SR), refracted - bottom reflected rays (R-BR) and surface reflected - bottom reflected rays (SR-BR) (Fig. 5).

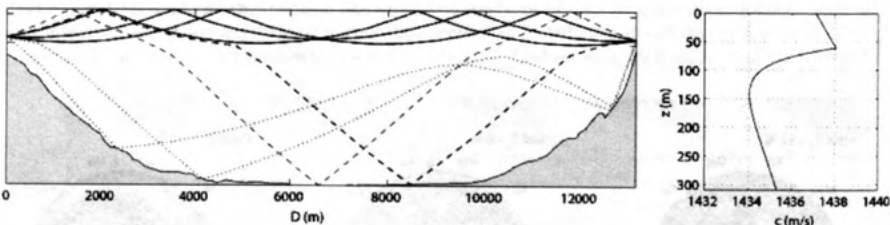


Figure 5: Representation of the trajectory of the rays for a winter stratification (contracted representation). On left: trajectories of the three types of rays on the axis Lausanne - Amphion (R-SR, R-BR dot, SR-BR dash); on right: one of the sound speed profiles used for simulation.

Each ray is defined by its travel time  $\tau$ , its angle of arrival  $\theta_r$  on the receiver and  $z_m$  and its maximum depth. These parameters having to be defined during the experiment, we figure the evolution of  $\tau$  and  $z_m$  during the winter cooling denoted by the increase of  $h_e$  (Fig. 6).

One notices that two groups of rays (R-R, R-SR) are dissociated in time (and angle [-5°, 5°], not described here) facilitating their experimental identification using a vertical array of receivers. Some R-SR rays denote an increase of their travel times and some appears as the epilimnion grows. It should be noticed that these rays, without any reflection on the bottom of the lake, qualify the hydrodynamical state of the epilimnion. Regarding their maximal depths, it is remarkable that they are detected once the transducers are within the epilimnion. A set of simulations reveals that the full description of the cooling of the epilimnion requires to fix transducers beneath the surface when considering these well discriminated rays.

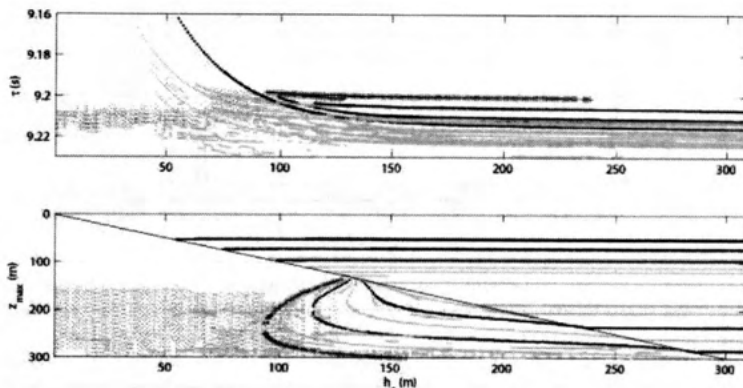


Figure 6: Groups of rays during cooling: R-R (black +), R-SR (black ·), R-BR (gray :) and SR-BR (gray ·). Top: travel times  $\tau$ ; bottom: maximum depth of the rays  $z_m$  and the line  $z = h_e$ .

Some SR-BR rays with similar characteristics are detected during the cooling presenting a remarkable decrease of their travel times with quasi-constant high angles of incidence. These rays are thus complemented too and their path explores the whole water column. Consequently some rays of the two groups R-SR and SR-BR are of interest for the tomographic purpose. It is then possible to define a strategy of observation for the experimental qualification of the thermal stratification of the lake.

## 5 Acoustic Set Up

An experiment was conducted during the winter 2003/2004 to validate the feasibility of lake acoustic tomography. The tomographic set up is composed by two linear arrays of four hydrophones and one emitter laid around the Great Lake, defining the small axis. Both emitters and receivers are connected to permanent shore stations composed of amplifiers and GPS-controlled computers by reinforced cable of length up to 1000 m. Emitted sounds are linear frequency modulated signals in the 10-30 kHz band, but only the 10-16 kHz band is considered due to undesirable noise. Measurements at pulse rate of twelve per hour, controlled by GPS clocks, are carried out so as to observe the thermal stratification. A comparison of the structure of the emitted and the received signals allows the identification of rays. Let us denote  $e(t)$  the emitted signal, the received signal is modelled as the noisy output of a linear system. It is given by  $r(t) = (e * h)(t) + \nu(t)$  where  $\nu(t)$  is a gaussian additive noise and  $h(t)$  is the lake impulse response. The received signal can be expressed:

$$r(t) = \sum_{p=1}^P \alpha_p e(t - \tau_p) + \nu(t), \quad (1)$$

where  $\alpha_p$  and  $\tau_p$  are respectively the attenuation and the arrival time associated to the  $p^{th}$  path, and  $P$  is the number of paths. The one shot analysis, derived from a classical cross-correlation method [1], validate the model (1) where estimated parameters  $\hat{\alpha}_p, \hat{\tau}_p$  have to be extracted (Fig. 7). Multi-shot analysis allows to observe the low evolution of the lake impulse response showing distinctive traces representing stable rays (Fig. 8). From this figure, different evolutions in time and in amplitude of the detected rays can be observed describing the dynamics of the water masses between December 18, 2003 and February 25, 2004.

Comparing simulated results to experimental ones, it is remarkable that evolutions of some detected rays from R-SR and SR-BR groups present a good agreement, thus constituting a first validation of the action of the cooling on the propagation. In order to validate the tomographic purpose, we consider the temperature of the lake surface  $T_1$  as an indicator of the cooling: some couples of travel times of the first R-SR ray and their related temperature  $T_1$  are compared with simulations. The not-well defined parameters of the experiment such as the distance and the depths of sources and receivers are

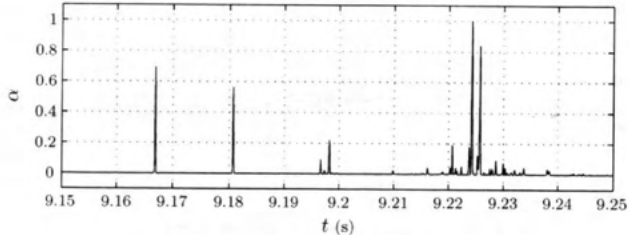


Figure 7: One-shot analysis on December 24, 2003 00.25 (Amphion → Lausanne). Peaks are associated with rays being characterized by their amplitudes  $\hat{\alpha}$  and their travel times  $\hat{\tau}$ .

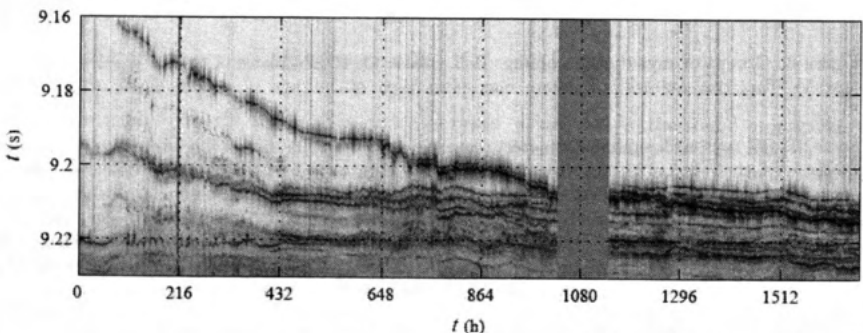


Figure 8: Multi-shot analysis between December 18, 2003 and February 25, 2004 (Amphion → Lausanne). Detected rays are identified by the dark points.

reintroduced in the modelling; finally a set of new parameters (very similar to initial ones) enables to fit the model of the cooling to experimental data (Fig. 9). However a better comparison would consider the evolution of the travel times with the total heat budget, this one permanently decreasing during this period. Nevertheless, simulated and experimental results confirm the contribution of the tomographic purpose to observe long term processes of the winter cooling. Moreover periodical fluctuations observed in the multi-shot analysis, reveal some characteristics of internal waves, thus requiring to consider range dependent sound speed profiles for a better comprehension of the dynamics of the Great Lake.

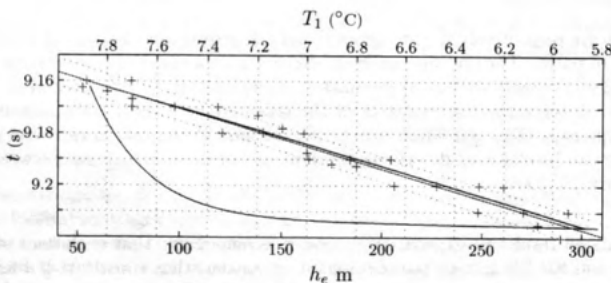


Figure 9: Comparison of experimental and simulated data for the first R-SR detected ray. In gray, experimental points  $(\tau_1, T_1)$ ; black line, travel times according to the surface temperature extract from the model of cooling; curved gray line, travel times according to the height of the epilimnion.

## 6 Internal waves

Since winter temperature profiles can be easily evaluated because of their two layers structure, the winter cooling represents the simplest scenario for the identification of the rays. However the previous simulations do not consider large scale movements characterizing the dynamics of the lake of Geneva, limiting the interpretation of the detected rays in a one-shot analysis. The qualification of the action of these dynamics on the propagation of the sound thus requires to implement a model based on range dependent sound speed profiles.

The wind generates surface waves but also internal waves contributing to the development of currents [5]. When the field of wind has a constant direction but a fluctuating speed, the lake responds directly to these fluctuations. To illustrate the influence of water movements on the acoustic propagation, we carry out an assumption of the thermocline tilt on the axis Lausanne-Amphion which is modelled by a variation of the various sound speed profiles in several sites. A cycle of an oscillation is qualified by a sinusoidal variation of the height of the epilimnion: sound speed profiles are then range and time dependant. Nevertheless, currents induced by the movement are not introduced in this modelling.

We focus the modelling so as to understand the observed cyclic fluctuations of the two first detected rays (R-SR and SR-BR) on December 24, 2003 between 01.00 and 15.00 (Fig. 10, left). The first detected ray R-SR oscillates with a period of 13.7 hours approximately defining a travel times fluctuation of 2100  $\mu$ s. The second group, SR-BR, crossing the whole water column, has the same period and an amplitude of 4200  $\mu$ s. Like it was observed on the weather data, these fluctuations are directly associated to the thermocline tilt after an event of continuous and strong wind during the previous days. In addition, one notes in this measurement the increase of the travel times being in accord with the cooling of the epilimnion. In order to validate these observations, an evaluation of the quantification of these phenomena is carried out by ray tracing using the software package PRAMM 3.0.

The simulated cooling and thermocline tilt is defined by an increase of the height of the epilimnion starting at  $h_e = 60$  m with an increment of 10 cm per angular variation  $\delta\Theta$  figuring a whole oscillation. Finally the height reached is 63.2 m. Fig. 10 (right) exhibits the fluctuations of the two group of rays R-SR and SR-BR identified during the experiment. Amplitudes of travel times fluctuations are in the same order of magnitude than those observed in the experiment data and would be in relation with Poincaré waves. From this successful observation, one can say that during the winter cooling, it is necessary to engage range and time dependant modelling so as to fit experimental data. Starting from these two well defined rays, one would consider the others rays, not taken into account in the present paper, to fit the real thermal stratification considering currents associated with the oscillation of the water masses.

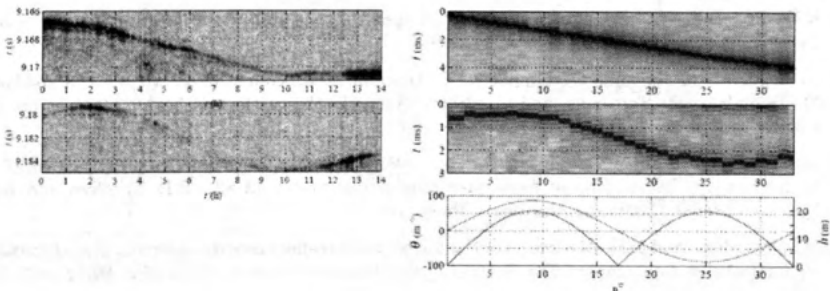


Figure 10: Left: detection of the first two groups of rays of the type R-SR (top) and SR-BR (bottom) on December 24, 2003 between 01.00 and 15.00. Right : Simulation of detection during the thermocline tilt and the cooling for  $h = 20$  m and  $\delta z = 3.2$  m. Top, effect on a ray R-SR (réf. with 9,1655 s); in the medium, on a ray SR-BR (réf. 9,1885 s); in bottom,  $\theta$  in millidegree and  $h$  in m during a cycle.

## 7 Conclusion

The analysis of travel time fluctuations, derived from classical cross-correlation method, shows the high variability of the propagation path induced by internal waves and other currents within the Great Lake during the experimentation. We have found in the acoustic data, indications for basin scale phenomena (Poincaré waves) and winter cooling of the water masses, clearly illustrated by well discriminated rays. Nevertheless, it reveals that one shot analysis is not well defined during the winter cooling since large fluctuations of the travel times are directly correlated to internal waves. The analysis of the dynamic of the cooling expect to integrate a multi-shot analysis, since experimental data are in relation with the two different parameters governing the lake: heat budget and wind forcing. Therefore it would be of interest to develop a modelling based on acoustic propagation coupled to lake hydrodynamics.

## Acknowledgment

The author would like to thank the Swiss National Science Foundation for supporting this research.

## References

- [1] G.C. Carter. *Coherence and time delay estimation*. IEEE Press, 1992.
- [2] Y. Desaubies. Tomographie acoustique de l'océan. *Onzième Colloque GRETSI*, Nice, pages 1C–5C, 1987.
- [3] X. Falourd. *Tomographie acoustique du Léman*. Number 3171. PhD thesis, Ecole Polytechnique Fédérale de Lausanne, 2004.
- [4] T. Folegot, C. Bodennec, and Y. Stephan. Effet des ondes internes en golfe de gascogne: la campagne intimate'98. *5èmes Journées d'Acoustique Sous-Marine*, Brest, (15), 2000.
- [5] W.H. Graf. Waves on and in lake of geneva. *Proc. XXII Congress IAHR; in Topics in Lake and Reservoir Hydraulics*, pages 1–49, 1987.
- [6] U. Lemmin, C. Perrinjaquet, and W.H. Graf. Etude de la variation saisonnière des phénomènes de mélange dans l'hypolimnion du léman. campagne 1987. *Rapport de la Comission internationale pour la protection des eaux du Léman contre la pollution (CIPEL)*, campagne 1987, pages 85–95, 1988.
- [7] J. Michalski and U. Lemmin. Dynamics of vertical mixing in the hypolimnion of a deep lake: Lake geneva. *Limnology and Oceanography*, 40(4):809–816, 1995.
- [8] W. Munk, P. Worcester, and C.Wunsch. *Ocean Acoustic Tomography*. Cambridge University Press, 1995.
- [9] R.W. Preisendorfer. *Principal component analysis in meteorology and oceanography*. Elsevier, Developments in atmospheric science 17, 1988.
- [10] U. Send, G. Krahnmann, D. Mauuary, Y. Desaubies, F. Gaillard, T. Terre, J. Papadakis, M. Taroudakis, E. Skarsoulis, and C. Millot. Acoustic observations of heat content across the mediterranean sea. *NATURE*, 385:615–617, 1997.
- [11] M. Straskraba. "The effects of physical variables on freshwater production: analysis based on models" in *The functioning of freshwater ecosystems.*, pages 13–83. E.D. Le Cren and R.H. Lowe-McConnell, Cambridge University Press, 1980.
- [12] M.I Taroudakis and M.G. Markaki. On the use of matched-field processing and hybrid algorithms for vertical slice tomography. *The Journal of the Acoustical Society of America*, 102(2):885–895, 1997.

# EFFECTS OF CATCHMENT ALTERATIONS ON INTERNAL PROCESSES IN LAKE BRIENZ

An analysis of nutrients, suspended particles, turbidity, lake-internal hydraulics and productivity  
 David Finger, Lorenz Jaun, Catherine Hoyle, Peter Bossard, Martin Schmid & Alfred Wüest  
 Applied Aquatic Ecology, EAWAG, CH-6047 Kastanienbaum, Switzerland

## Abstract

Since the 1980's a continuous decline of the local lake whitefish (*Coregonidae*) population has been observed in Lake Brienz (Brienzsee) [Müller, 2003]. Previous investigations indicate that human interferences (construction of hydropower dams and sewage treatment plants) in the catchment of the lake may have changed the quality of the inflowing water and the run-off dynamics of the River Aare, the major inflow to the lake. It is speculated, that those human interferences might have reduced the primary production and jeopardize the entire ecology of Lake Brienz.

The presented project consists of three work programs: the first work program describes the boundary conditions in the catchments of Lake Brienz before and after the construction of hydropower dams. In the second work program the light attenuation, which limits primary production was assessed using spectrophotometers. In the third work program the phosphorus budget is described and quantified. In the last work program in-situ primary production is simulated considering the findings of the three proceeding work programs.

## Introduction

Lake Brienz is situated about 70 km southeast of Berne ( $7^{\circ} 53' / 8^{\circ} 3'$  E,  $46^{\circ} 41' / 46^{\circ} 45'$  N), in the front ranges of the Swiss Alps (at 564 m asl). With a volume of  $5.2 \text{ km}^3$ , a surface area of  $30 \text{ km}^2$ , and a maximal depth of 261 m, Lake Brienz is a typical representative of the peri-alpine lakes in Switzerland. Its simple basin was eroded of the Mesozoic rocks by fluvial and glacial forces [Sturm and Matter, 1978]. The two major inflows, the River Aare and the River Lütschine (Figure 1), enter the lake at the opposite longitudinal ends. These two rivers transport annually over 250'000 tons of suspended materials into the lake and dominate the sedimentation (Table 1), which is almost entirely clastic. In the deltas of these two inflowing rivers a few minor submerged channels have been identified.

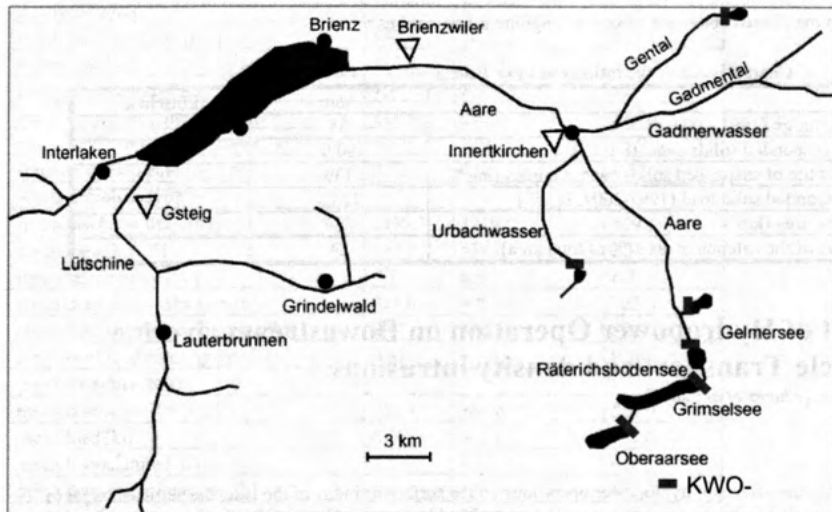


**Figure 1:** Overview of the catchment of Lake Brienz including six of the nine hydropower dams operated by KWO

The stupendous particle load of Lake Brienz has its origin in the headwaters of the two rivers: the glaciers of the *Bernese Oberland*. At Gsteig (Figure 1) the Lütschine drains a catchment area of 379 km<sup>2</sup>, of which 17.4 % are covered by glaciers [LHG-BWG, 2005]. Unlike the Lütschine, whose hydraulic regime remained in its natural state, the hydrology of the Aare is characterized by a complex damming system, operated by the *Kraftwerk Oberhasli AG* (KWO). In fact, over 60% of the annual discharge at Brienzwiler (Figure 1) is stored in reservoirs and released when electricity consumption is high (KWO data). The Aare drains an area of 554 km<sup>2</sup> (at Brienzwiler), of which about 21 % are covered by glaciers [LHG-BWG, 2005]. About 1/3 of the total Aare discharge originates from the most important glaciers, the Unter- and Oberaargletscher, which supply the KWO dam system.

Since the 1980's a continuous decline of the local lake whitefish (*Coregonus fatioi*) population has been observed in Lake Brienz [Müller, 2003]. During the same time period local fishermen have repeatedly claimed that the turbidity in the lake's surface water increased [naturaqua, 1993; Schudel and Ochsenbein, 1995; Siegenthaler et al., 1996]. Such an increase of turbidity in the surface layers of the lake would reduce the penetration depth of daylight into the lake water. As a direct consequence the primary production of algae would be diminished, which again would have a negative effect on the zooplankton population and on the whole food chain. A drastic collapse (of over 90%) of the fish yield in the year 1999 coincided with the almost total disappearance of daphnia (*daphniidae*), the local water flea population. The investigations indicate that the lake whitefish were suffering of undernourishment [Müller, 2003]. This unfortunate event demonstrates the fragility of the Lake Brienz ecosystem.

A key parameter in the ecosystem system of Lake Brienz is the primary production, as it provides the basis of the food chain. The drastic disappearance of the daphnia population in 1999 indicates that primary production might react very sensitive to external alterations in the catchment of the lake. In the present project two major hypotheses are identified as possible causes for the hampered primary production:

- Increase of the surface turbidity in the lake, and
- Reduction of nutrients input to the lake

In a first step the physical boundary conditions and the particle budget of the lake are being assessed. By assessing suspended particle loads and determining the intrusion depth of the two rivers effects of hydropower operations on the surface particle content in the lake can be determined. In a second step the light attenuation in the lake due to the different optical active substances is quantified by means of in situ and lab light spectro-photometry. In a third step the phosphorus balance of Lake Brienz is presented. Lake Brienz is in fact ultra-oligothrophic and bio-available phosphorus never amounts to more than 1 µg l<sup>-1</sup> throughout the year. The study concludes with actually measured C-assimilation in the lake. Effects of the hydropower operation mentioned above are subject of ongoing investigations.

**Table 1:** Characteristic of the Inflows to Lake Brienz

Property	Aare	Lütschine
Mean discharge (1991-2004, m <sup>3</sup> s <sup>-1</sup> )	35	19
Average suspended solids conc. (mg l <sup>-1</sup> )	80.0	110.6
90%- quantile of suspended solids conc. samples (mg l <sup>-1</sup> )	139	283
Mean suspended solid load (1997-2004, kt yr <sup>-1</sup> )	128.5	173.6
Catchment area (km <sup>2</sup> )	554	379
Glaciation of the catchment area (% of total area)	21	17

## Effect of Hydropower Operation on Downstream riverine Particle Transport and density intrusions

Reference: [Finger et al., 2005]

### Methods

To quantify the effects of hydropower operations on the surface turbidity of the lake, the particle budget of Lake Brienz during the last seven years was assessed and hypothetical budgets for the natural situation (without hydropower activities in the catchments) were numerically simulated. The vertical turbidity dynamics were assessed by means of CTD profiles (profiles of conductivity, temperature, pH, dissolved oxygen and light transmission) which have been conducted since 1997. The measured light transmission was experimentally calibrated to suspended solids in the lake water (CL), which allowed a reconstruction of vertical distribution of CL back to 1997. Water samples and discharge in the major inflows were used to estimate the suspended particle loads entering the lake. Using the equation of state (density equation) the intrusion depth of the inflows and the suspended particle load entering the epilimnion of the lake were

estimated. During 2003 and 2004 *in-situ* sedimentation rates in 50 m and 250 m depth were measured using traps in order to compare sedimentation with the estimated suspended particle input.

Finally, to estimate the impacts of hydropower activities, a situation without water retention in the catchments was simulated. For this purpose, simulations of discharge- and temperature- regime were conducted in companion studies [Moosmann, 2005; Sägesser and Weingartner, 2005]. Relying on the simulated discharges of an undammed Aare, the pre-dam suspended particle load was reconstructed using a rating curve technique [Cohn et al., 1989; Crawford, 1991]. Based on the seven years of simulated particle budget under dammed and undammed situation, the impacts of anthropogenic water retention in the catchments on surface turbidity in the lake were assessed and variations due to year specific meteorological conditions were determined.

#### *Summary of the Results*

Table 2 summarizes the differences between the suspended load input dynamics of the two rivers and the reconstructed pre-dam situation based on the eight years of simulations. In an average year, the Aare River transports 26 % less load than the Lütschine. However, since the Lütschine water plunges twice as frequently to the deep water of the lake as the Aare, the mean load to the epilimnion from the Aare is 44% higher than from the Lütschine. Deep water intrusions by the Aare are slightly more frequent in the reconstructed pre-dam situation, but lower salinity and 2 °C warmer water temperatures hinder a deep water intrusion dynamics comparable to the Lütschine. Since cabbeling instability leads to deep water intrusions of both rivers during winter months, the intrusion dynamics driven by suspended solids differ mainly during the warm months April to October.

**Table 2:** Summary of intrusion dynamics of the two rivers and the pre-dam situation

	Aare	pre-dam Aare	Lütschine
<b>entire year</b>			
mean discharge 106 [m <sup>3</sup> yr <sup>-1</sup> ]*	1173.9	1138.2	620.5
mean load [kt yr <sup>-1</sup> ]	128.5	357.6	173.6
mean temperature [°C]	5.9	6.7	5.7
mean deep water intrusion [h yr <sup>-1</sup> ]	1271.0	1331.0	3029.0
mean load entering epilimnion [kt yr <sup>-1</sup> ]	92.9	232.8	64.7
fraction of load entering Epi [-]	0.72	0.65	0.37
<b>April-October</b>			
mean discharge 106 [m <sup>3</sup> ]	942.6	1023.2	543.4
mean load [kt]	114.8	353.4	170.7
mean temperature [°C]	7.1	8.7	7.0
mean deep water intrusion [h]	118.5	205.5	446.0
mean load entering epilimnion [kt]	86.4	229.7	63.9
fraction of load entering Epi [-]	0.75	0.65	0.37
<b>April-October 1999</b>			
mean discharge 106 [m <sup>3</sup> ]	1135.3	1210.0	629.1
mean load [kt]	162.2	538.0	224.4
mean temperature [°C]	6.7	8.6	6.7
mean deep water intrusion [h]	211.0	408.0	725.0
mean load entering epilimnion [kt]	99.5	313.5	58.8
fraction of load entering Epi [-]	0.61	0.58	0.26
<b>April-October 2003</b>			
mean discharge 106 [m <sup>3</sup> ]	915.4	984.8	534.0
mean load [kt]	61.6	343.2	241.0
mean temperature [°C]	7.3	8.2	6.8
mean deep water intrusion [h]	0.0	187.2	612.0
mean load entering epilimnion [kt]	61.6	253.0	101.5
fraction of load entering Epi [-]	1.00	0.74	0.42

\*Note : difference between mean discharge of the Aare and the pre-dam Aare is due to errors in the hydrological model of the Aare

About 90 % of the annual load of the Aare enters Lake Brienz between April and October; the summer load in the Lütschine accounts for over 98 % of the annual load. Furthermore, during summer deepwater intrusions in the Lütschine are about four times more frequent than in the Aare. This pattern does not change significantly during years characterized by high water events such as 1999 (extreme snowfall during winter 1998/1999 led to devastating flooding in spring 1999). However, in case of extreme heat waves, as was the case during summer 2003 [Schär *et al.*, 2004], the importance of the Lütschine increases. During the summer 2003, 62 % of the total input entering the epilimnion could be attributed to the Lütschine. Simulations of the pre-dam situation depict a doubling of the deep water intrusion frequency of the Aare. Nevertheless, the pre-dam Aare transports a 2.5 times higher load into the epilimnion. This circumstance remains valid throughout the abnormal years like 1999 and 2003.

Hence, considering the perceptions of local fishermen, an assessment of the characteristics of the suspended load is essential. The retention in the reservoirs selectively removes the larger particles and shifts a part of the input of small particles from summer to winter. About 10 % (or about 13.7 kt yr<sup>-1</sup>) of the annual Aare load enters the lake during circulation phase in the winter. This load originates primarily from the reservoirs upstream and hence is composed of particle size smaller than 7 µm. Hence, sedimentation velocity of less than 0.01 mm s<sup>-1</sup> (based on the Stokes relation) and increased turbulence due to the winter circulation lead to a distribution in the entire lake.

## Light regime

Reference: [Jaun, 2005]

### Methods

As explained in section 3 the annual suspended particle load in the Aare River has been halved by the construction of the dams. Hence, surface turbidity in Lake Brienz could only have increased due to an increased input of fine particles into the surface layers of the lake. It is therefore essential to assess the light attenuation due to inorganic suspended particles in order to draw further conclusion concerning the primary production in the lake.

There are two major processes which contribute to vertical light attenuation in natural waters: Light scattering and light absorption. While pure water, suspended organic matter and dissolved substances primarily adsorb light, inorganic suspended particles merely scatter the light rays. Scattering of light rays prolongs the path of the light ray before reaching a certain water depth. Consequently absorption due to water and its compounds increases. In order to quantify these processes in lake Brienz, inherent (measurements with an artificial light source in the lab) and apparent (*in situ*) light attenuation were determined for the potentially active light spectrum using a spectrophotometer U2000 (Hitachi, Japan) for the lab measurements and two radiometers for *in-situ* measurements (Geophysical & Environmental Research, USA).

During five samplings (August, October, November, December 2004 and March 2005) inherent and apparent light attenuation were determined simultaneously to water sampling. The collected water samples were subsequently analyzed for suspended particle concentration, particle size distributions, particular organic carbon, dissolved organic carbon and chlorophyll a. The simultaneous determination of inherent light attenuation and water properties allows an identification of the agent of the light attenuation. Hence, the evolution of light attenuation due to organic and inorganic matter in Lake Brienz was assessed.

### Results

Inherent and apparent light attenuation in Lake Brienz both correlate well with suspended particulate matter. Furthermore 95 % of the inherent light attenuation can be attributed to scattering due to inorganic particles. As theoretical calculations according to the anomalous diffraction theory of van de Hulst (1957) [Spinrad, 1986] indicate, 80% of the inherent scattering is caused by particle sizes smaller than 4µm in diameter. In spectral light attenuation the contribution of suspended matter (400 - 550 nm wavelengths) and water (550 - 700 nm) can clearly be distinguished. However for primary production it is not the spectral light intensity which is important, but the amount of light quanta at a specific depth measured with a broadband PAR radiometer. Correlations between the vertical attenuation coefficient of light quanta measurements and suspended solids correlate adequately, allowing the reconstruction of light attenuation at known particle concentrations.

## Phosphorus balance

Reference: [Hoyle *et al.*, 2005]

### Methods

Like in most Swiss lakes, over the past three decades a decrease in phosphorus (P) (the primary production limiting nutrient) input has been observed in Lake Brienz due to the establishment of sewage treatment plants and water protection laws in the early seventies. Today Lake Brienz is in an ultra-oligotrophic state with mean phosphorus concentration below  $1 \mu\text{g l}^{-1}$  during spring circulation. Total phosphorus concentrations in the two rivers can however reach values above  $30 \mu\text{g l}^{-1}$ . Most of this phosphorus is bound to inorganic suspended particles and hence not bioavailable. Hence in order to assess the phosphorus balance it is important to distinguish between bioavailable phosphate (SRP), organic phosphorus (which can become bioavailable once mineralized) and inorganic particulate phosphorus (which will never be bioavailable). Phosphorus (P) input was estimated using two different methods: rating curve technique relying on a QC-correlation (discharge vs. concentration) and Land use method which estimated P-erosion into the rivers based on land use data and point source P originating from sewage treatment plants [Prasuhn and Mohni, 2003]. The sedimentation of P was determined by sequential extraction (which allows to determine the content of different types of phosphorus) of sediment material collected in two sediment traps at the center of the lake. Water samples collected throughout 2003 were analyzed for different P-fractions as well, in order to determine the actual P-content in the lake. Furthermore, P-fractions were determined in a sediment core in order to reconstruct the history of P-sedimentation (?) during the past century.

### Results

Major P-fluxes in Lake Brienz are illustrated in figure 2. According to this P-balance, Lake Brienz is in a steady state. About 97 % of the 200 tons P entering the system settle out as particulate P.

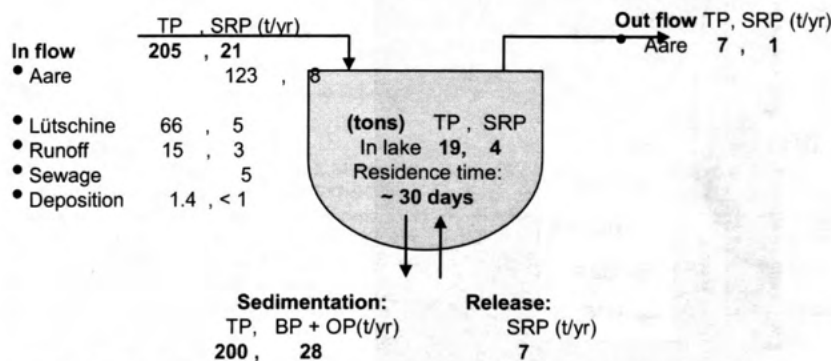


Figure 2: Phosphorus balance in Lake Brienz: TP: total phosphorus; SRP: bioavailable phosphorus;

Essential for the primary production is the bio available load which represents only about  $21 - 28 \text{ t yr}^{-1}$ . Consequently the average concentration of bioavailable P throughout the year lies at  $0.85 \mu\text{g l}^{-1}$ . Hence, conditions for primary production are very limited. P-content in sediment cores indicate an eutrophication phase during the late eighties. However P content before the 1970's was similar to present contents.

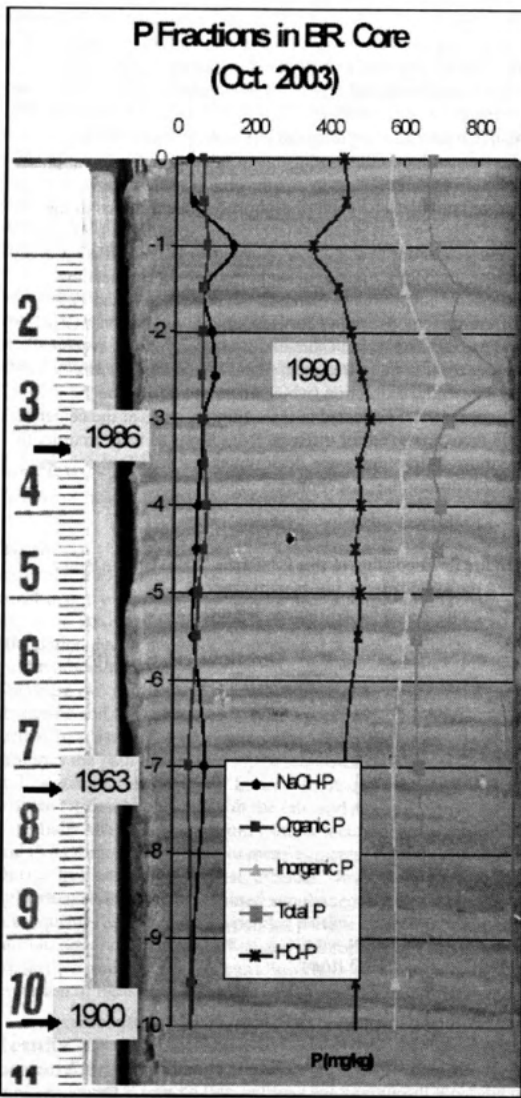


Figure 3: P-content in a sediment core depicting eutrophication phase during the early nineties.

## Primary Production

### Methods

Primary production in the lake was determined in monthly monitoring campaigns starting in December 2003 until June 2005. Sampling in the upper 35m water column was conducted at the center of the lake and the following measurements were performed: (1) Determination of C-Assimilation (using the <sup>14</sup>C-Raditracер-Acid Bubbling Method); (2) pH and alkalinity measurements (3) Chlorophyll a measurements; (4) Light attenuation of PAR; (5) Temperature and conductivity

For each measuring campaign a PI relation was established, which allows a prediction of the C-assimilation based on the global radiation measured simultaneously at the surface of the lake. Hence, continuous C-assimilation was estimated by adequately interpolating the parameters of the PI relation and global radiation

measured by the MeteoSwiss in Interlaken. Furthermore, monthly PAR profiles conducted in the framework of a national monitoring program since 1999 were used to determine light availability for the preceding years.

## Results

Figure 4 illustrates preliminary results of simulated average C-Assimilation in Lake Brienz since 1999. Since the method do not account for phosphorus limitation, the presented values have to be considered with precaution. Modeling approach and configuration are still in development.

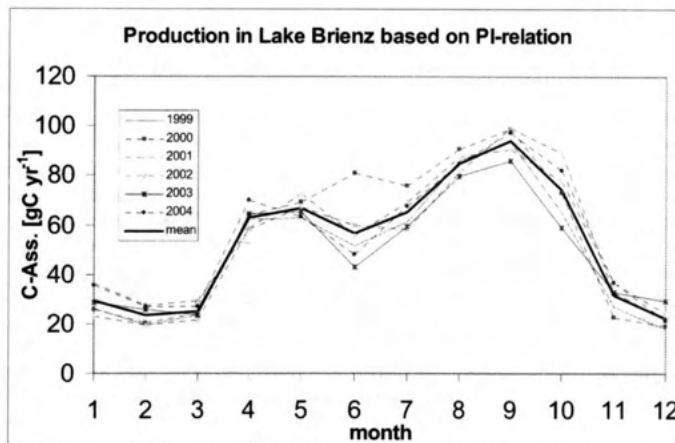


Figure 4: Monthly C-Assimilation in Lake Brienz for the years 1999 to 2004

## References

- Cohn, T.A., L.L. Delong, E.J. Gilroy, R.M. Hirsch, and D.K. Wells (1989), Estimating constituent loads, *Water Resources Research*, 25(5), 937-942.
- Crawford, C.G. (1991), Estimation of suspended-sediment rating curves and mean suspended-sediment Loads, *Journal of Hydrology*, 129(1-4), 331-348.
- Finger, D., M. Schmid, and A. Wüest (2005), Effect of hydropower operation on downstream riverine particle transport and density intrusion into a peri-alpine lake, *in preparation*.
- Hoyle, C., D. Finger, B. Müller, and A. Wüest (2005), Phosphorus cycling in Lake Brienz, *in preparation*.
- Jaun, L., Light attenuation in Lake Brienz, Master thesis, ETH Zurich, 2005.
- LHG-BWG 2005, *Hydrological Yearbook of Switzerland*, Bern.
- Moosmann, L., Rekonstruktion des Temperaturregimes der Aare ohne Kraftwerkeinfluss, EAWAG, Kastanienbaum, 2005.
- Müller, R., Populationsdynamische Untersuchungen an den Felchen des Brienzsees, EAWAG, Kastanienbaum, 2003.
- naturaqua, Trübung Brienzsee, Amt für Gewässerschutz und Abfallwirtschaft des Kantons Bern, 1993.
- Prasuhn, V., and R. Mohni, GIS-gestützte Abschätzung der Phosphor- und Stickstoffeinträge aus diffusen Quellen in die Gewässer des Kantons Bern, Amt für Gewässerschutz & Abfallwirtschaft Kanton Bern, 2003
- Sägesser, M., and R. Weingartner, Veränderung der Hydrologie der Aare, in *Institute of Geography*, Institute of Geography - University of Bern, Bern, 2005.
- Schär, C., P.L. Vidale, D. Luthi, C. Frei, C. Haberli, M.A. Liniger, and C. Appenzeller (2004), The role of increasing temperature variability in European summer heatwaves, *Nature*, 427(6972), 332-336.
- Schudel, B., and U. Ochsenebein, Brienzsee - Weniger Schwebstoffe und trotzdem trüber?, Gewässer- und Bodenschutzzlabor des Kantons Berns (GBL), 1995.
- Siegenthaler, C., M. Sturm, H. Suter, and A. Wüest, Das Verhalten von Schwebstoffen im Brienzsee, EAWAG, Dübendorf, 1996.
- Spinrad, R.W. (1986), A calibration diagram of specific beam attenuation, *Journal of Geophysical Research-Oceans*, 91(C6), 7761-7764.
- Sturm, M., and A. Matter (1978), Turbidites and varves in Lake Brienz (Switzerland): deposition of clastic detritus by density currents, *Spec. Publs int. Ass. Sediment.*, 2, 147 - 168.

ad un certo punto si è voluto fare una sorta di "censimento" della popolazione europea, e si è scoperto che non c'era nessuno. E' stato quindi deciso di far nascere dei bambini, e si è fatto inviare da ogni parte del mondo dei "genitori" che hanno dato vita a dei bambini. I bambini sono cresciuti e sono diventati grandi, e adesso sono tutti insieme in Europa. Ma non solo sono insieme, sono anche tutti fratelli e sorelle. E' per questo che la Europa è un grande famiglia.

## CONVECTIVE DYNAMICS ABOVE THE UPPER INTERFACE OF A WARM AND SALTY FLUIDIZED BED LOCATED AT THE BOTTOM OF A LAKE

Xavier Sánchez and Elena Roget

*Physics Department and Institute of the Environment*

*University of Girona*

*Campus de Montilivi, PII, 17071-Girona, Catalonia, Spain*

*xavier.sanchez@udg.es; elena.roget@udg.es*

### 1. - Introduction

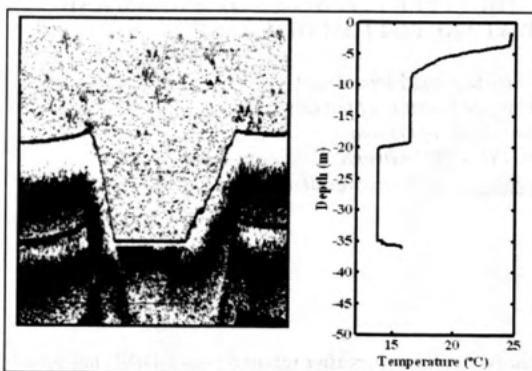
Double-Diffusive Convection with a Diffusive Regime (hereafter referred to as DDDR) has been studied and observed in nature for a long time and in recent years many works stated the importance of DDDR in heat transport within natural aquatic systems (Kelley, Fernando, Gargett, Tanny and Özsoy, 2003). DDDR in lakes has also been widely documented with examples such as Hoare (1966) at Lake Vanda (Antarctica) and Newman (1976) at Lake Kivu (Rwanda), or in more recent works like Schmid, Lorke, Dinkel, Tanyileke, and Wüest (2004) at Lake Nyos (Cameroon). However, only a few of these works are based on microstructure measurements (for example, Padman and Dillon, 1989; Robertson, Padman and Levine, 1995) and even in these cases fluxes could not be determined directly. In this paper, starting from microstructure temperature, fine-scale turbidity and precision conductivity data, we go on to accurately describe the staircase pattern we measured in Lake Banyoles (Catalonia, Spain) and determine the heat flux at both the diffusive interfaces and within the turbulent convective layer.

The most accepted and used flux models for DDDR are based on the well-known 4/3 flux law (Turner, 1973), although their physical bases have been widely questioned (Fernando, 1989a; Fernando, 1989b; Kelley, 1990). Using our data, recorded in a very low stability regime (density ratio  $R_\rho \approx 1.1$ ), we will discuss this issue.

### 2.- Description of the studied case

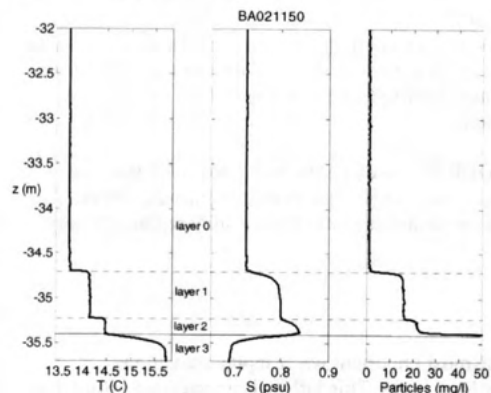
At Lake Banyoles, which is of karstic origin, the most important water inputs are various underground sources coming from the Pyrenees Mountains. This inflow is warmer and saltier than hypolimnetic water and it carries sediments in suspension. At the bottom of the sub-basins where the flow enters the lake, a warm fluidized bed with a sharp upper interface of particle concentration, salinity and temperature is formed (Casamitjana and Roget, 1988). At the upper interface of this fluidized bed, particle concentration plus salinity (decreasing upwards) have the opposite effects of temperature (also decreasing upwards) on the vertical density distribution, and the corresponding density ratio is slightly greater than one. This condition, plus the fact that particle and salt diffusivities are lower than thermal diffusivity, determines the existence of a DDDR. That is, the upper interface of the fluidized bed is step-like for the three scalar fields, with well-mixed turbulent convective layers separated by diffusive interfaces.

Figure 1 shows details of the basin of Lake Banyoles where the data analyzed here were recorded. In Fig. 1-left there is an echo sounding of the basin where the fluidized bed and its clear upper interface at 35 m of depth can be observed inside the conic region at the bottom. The temperature profile of the whole column during the campaign is shown in Fig. 1-right. The existence of the second thermocline at about 20 m of depth greatly isolates the region below it from the rest of the lake.



**Figure 1:** Echo sounding image of the basin studied (left) and temperature profile of the campaign (right).

Data analyzed here come from 13 consecutive profiles recorded within a time interval of one and a half hours. These profiles were recorded with a free-falling MSS profiler (Prandke and Stips, 1998) and show a nice stable staircase pattern. Details of the staircase can be seen in Figure 2 where we present one of these profiles.



**Figure 2:** One of the profiles of Temperature, Salinity and Particle Concentration. The salinity seems to be reduced inside the fluidized bed but this is due to the effect of particle concentration on conductivity.

In the following parts of this paper we will refer to the different regions in accordance with the numbers of this figure; that is, region 0 corresponds to the hypolimnion, the convective layers are regions 1 and 2, and region 3 is that of the fluidized bed. Sharp diffusive interfaces can be clearly observed between regions 0-1, 1-2 and 2-3. As discussed previously, all variables in this plot increased downwards with the exception of salinity in zone 3. That was due to the effect of a high concentration of particles on the conductivity signal from which salinity is computed. Because of the relatively large time response of the conductivity sensor to temperature, the salinity steps look smoother than those of temperature and particle concentration.

Stability conditions of this system can be evaluated from the smoother profiles of T, S and C with the density ratio,  $R_\rho = (\beta dS/dz + \gamma dC/dz) / (\alpha dT/dz)$ , where  $\beta$  is the saline contraction coefficient,  $\gamma$  the particle concentration contraction coefficient,  $\alpha$  the thermal expansion coefficient and  $dT/dz = -\Delta T/D$ ,  $dS/dz = -\Delta S/D$  and  $dC/dz = -\Delta C/D$ , with the increments corresponding to the sharp interfaces and D to the corresponding lower convective layer.

Considering all the measured profiles, for the upper interface we obtain

$$(\beta \Delta S_{0-1} / \alpha \Delta T_{0-1}) = 0.97 \pm 0.02, \quad (\gamma \Delta C_{0-1} / \alpha \Delta T_{0-1}) = 0.15 \pm 0.01 \text{ and so } R_\rho^{0-1} = 1.12 \pm 0.03$$

identifying a DDD regime with very low stability conditions (Kelley, Fernando, Gargett, Tanny, and Özsoy, 2003). In Table 1 the individual density ratios and their components are presented.

For the lower interface, conductivity and turbidity sensors were saturated before reaching the value of the well-mixed region, so available data will underestimate the density ratio.

$\Delta T_{01}$ (C)	$\Delta C_{01}$ (mg/l)	$\Delta S_{01}$ (psu)	$R_\rho$
0.42	14.8	0.073	1.13
0.43	14.4	0.074	1.10
0.42	14.5	0.074	1.12
0.40	13.9	0.072	1.15
0.42	14.5	0.073	1.11
0.40	13.8	0.071	1.15
0.41	14.4	0.072	1.11
0.43	15.5	0.074	1.11
0.44	14.4	0.074	1.07
0.45	13.3	0.075	1.07
0.42	14.8	0.072	1.11
0.40	14.9	0.073	1.18
0.40	13.3	0.071	1.14
$0.42 \pm 0.02$	$14.4 \pm 0.6$	$0.073 \pm 0.001$	$1.12 \pm 0.03$

**Table 1:** Increments of  $T$ ,  $C$  and  $S$  at the diffusive interface 0-1. The last row contains the mean value and the error.

### 3.- Diffusive interfaces

As stated by Howard (1966), thermal interfaces evolve in a diffusive way, increasing in size, until instability appears and convective structures are generated and propagated into the adjacent layer above. Instabilities of the diffusive interface are governed by the interfacial Rayleigh number,

which is defined as  $Ra_\delta = g\alpha(\Delta T/2)\delta_T^3/\nu\kappa_T$ , where  $\Delta T/2$  is the temperature increment between the diffusive kernel and the mixed layer (half the temperature increment at the interface) and  $\delta_T = -\Delta T/2(dT/dz)_{int\, erf}$  is the size of the diffusive front (half the interface size),  $(dT/dz)_{int\, erf}$

being the temperature gradient at the diffusive kernel. Linear stability theory predicts a value of the order of 1000 as the maximum and critical value for the Rayleigh number (Turner, 1973). The cumulative distribution function for the  $Ra_\delta$  computed at interfaces 0-1 and 1-2 for the whole set of profiles is represented in Figure 3. We can see that the maximum value is about 10,000 and that 89% of the values are under 3000. Median and mean interfacial Rayleigh numbers are 1000 and 2300, respectively.

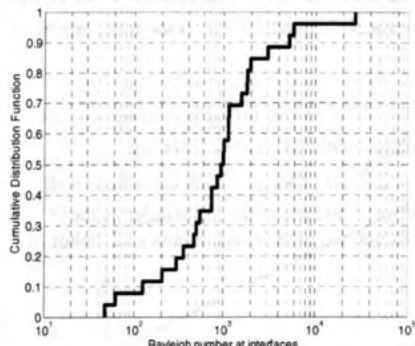


**Figure 3:** Cumulative distribution function for Rayleigh numbers at interfaces 0-1 and 1-2.

Following this analysis, and corroborated by visual inspection of the interfaces, we can assume that the thermal fluxes,  $F_T$ , at the diffusive interfaces can be obtained using the thermal gradient method (Burmeister, 1993), that is,  $F_T = -\kappa_T (\partial T / \partial z)_{\text{interface}}$  where  $\kappa_T \approx 10^{-7} \text{ m}^2/\text{s}$  is the molecular thermal diffusivity and  $(\partial T / \partial z)_{\text{interface}}$  is computed like the maximum value of the derivative. Doing so, results at the three interfaces are:  $F_{T0-1} = (4 \pm 2) \cdot 10^{-6} \text{ C.m/s}$ ,  $F_{T1-2} = (3 \pm 2) \cdot 10^{-6} \text{ C.m/s}$  and  $F_{T2-3} = (4 \pm 1) \cdot 10^{-6} \text{ C.m/s}$ . Because the heat flux through the 3 consecutive interfaces can be considered to be equal within the error range, we can conclude that the studied step-like structure was in a stationary state or very close to it, with a mean thermal flux  $F_T = (4 \pm 2) \cdot 10^{-6} \text{ C.m/s}$  and the corresponding heat flux  $F_Q = (17 \pm 8) \text{ W/m}^2$ .

#### 4.- Turbulence at the convective layer

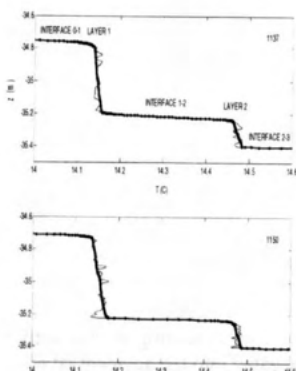


**Figure 4:** Two profiles with convective layers, 1 and 2. Microstructure temperature signal (solid) and monotonized profile (dotted).

Alternatively, temperature flux can also be computed based on the microstructure data within the convective layers. Details of microstructure temperature signals within these layers for different profiles are shown in Figure 4 (solid line) together with the corresponding monotonized profile (dotted lines).

One-dimensional power spectra for temperature variance have been obtained for the two layers based on the mean spectra for individual profiles and represented in Figure 5. From these spectra, the temperature variance dissipation rate,  $\chi$ , can be obtained integrating the spectra (Hinze, 1975). Then, the turbulent temperature flux can be obtained under stationary and local equilibrium conditions from  $w' T' = -\chi / [2(\partial T / \partial z)]$ , where  $T'$  are the temperature fluctuations,  $w'$  the vertical velocity fluctuation,  $\bar{T}' w'$  the turbulent temperature vertical flux and  $\partial T / \partial z$  is the mean trend inside the layer (Kanta and Clayson, 2000).

In our case we found  $\chi_1 = 3 \cdot 10^{-7} \text{ C}^2/\text{s}$ ,  $\chi_2 = 6 \cdot 10^{-7} \text{ C}^2/\text{s}$ , and  $(\partial \bar{T} / \partial z)_1 = -0.04 \text{ C/m}$ ,  $(\partial \bar{T} / \partial z)_2 = -0.13 \text{ C/m}$ , so the thermal fluxes within each turbulent convective layer are  $F_T^{\text{layer}1} \equiv \bar{w'} \bar{T}' = 3.8 \cdot 10^{-6} \text{ Cm/s}$  and  $F_T^{\text{layer}2} \equiv \bar{w'} \bar{T}' = 2.3 \cdot 10^{-6} \text{ Cm/s}$ , which agree very well with those calculated at the diffusive interfaces in Section 3 and are of the same order as those calculated from mean flow variables in other works (Roget, Colomer, Casamitjana and Llebot, 1993).

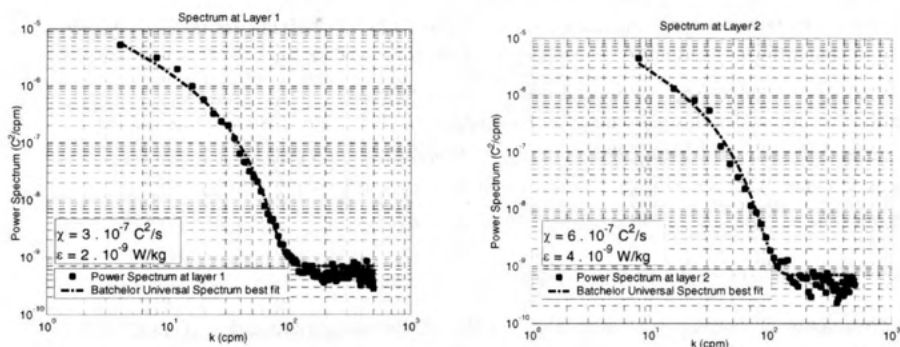


**Figure 5:** Mean Spectrum at layer 1 and 2 and best fit to Batchelor model (Kelley et al. 2003)

Finally the turbulence kinetic energy dissipation rate,  $\varepsilon$ , can also be obtained based on classical universal turbulent temperature spectral models which depend on both  $\chi$  and  $\varepsilon$  (Batchelor, 1959). So, if  $\chi$  is known, then  $\varepsilon$  can be determined by finding the best fit of the experimental spectra to the theoretical one. In Figure 5, together with the experimental spectra for each layer, we also present the best fit to the universal Batchelor spectra. Best fits have been obtained following the approach of Ruddick, Anis and Thomson (2000) and corresponding to  $\varepsilon_1' = 2 \cdot 10^{-9}$  W/kg (or  $m^2/s^3$ ) and  $\varepsilon_2 = 4 \cdot 10^{-9}$  W/kg. Note that according to the balance equation for the turbulent kinetic energy, when shear production can be disregarded and stationarity and local equilibrium assumed, the total buoyancy flux, which in our case is  $b' = g\alpha\overline{T'w'} - g\beta'\overline{S'w'} - g\gamma\overline{C'w'}$ , equals  $\varepsilon$ .

## 5. Testing Flux laws

Although we have been able to experimentally determine the fluxes, fine scale and microstructure measurements are usually not available so models have been developed with the idea of determining the fluxes from mean variables. Generally, heat flux models are based on the relationship  $Nu = C \cdot Ra_D^p$ , where  $Ra_D$  is the layer Rayleigh number,  $Nu = F_T D / \kappa_T \Delta T$  is the Nussel number (a non-dimensional flux) and  $C$  is either considered a constant or a function of the density ratio.

In our case, at layers 1 and 2 we have  $Ra_{D1} = (5 \pm 1) \cdot 10^8$ ,  $Ra_{D2} = (1.6 \pm 0.6) \cdot 10^7$

and  $Nu_{D1}^{exp} = 40 \pm 10$ ,  $Nu_{D2}^{exp} = 11 \pm 6$ , as represented in Fig. 7. Accordingly, our experimental results do not corroborate the generally well accepted  $4/3$  law (in which  $p=1/3$ ), with the most usually parameterizations of  $C$  as a function of the density ratio. This may be because analytical forms of  $C(R_\rho)$  are fit to experimental data and for  $R_\rho \rightarrow 1$  few data are available, and what are available are very dispersed, varying over one order of magnitude (see Fig. 5).

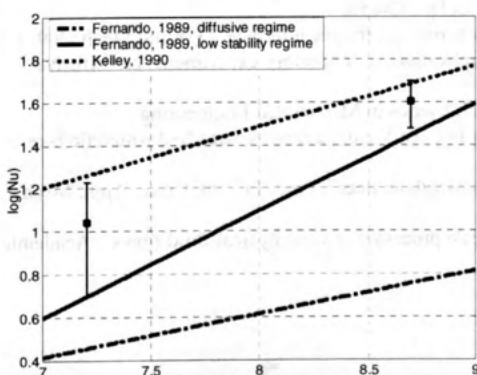


**Figure 7:** Flux laws and experimental data with bar error for the two-step, mean values over 13 profiles. We are between Kelley, 1990 and Fernando, 1989 for low-stability regimes.

Alternatively, however, we found that our data supports Kelly's (1990) law for thermal convection (not double diffusion) reasonably well where  $Nu = (0,164 \pm 0,004)$ .  $Ra^{0,284 \pm 0,001}$  which for the studied layers predicts  $Nu_1^{teor} = 48$  and  $Nu_2^{teor} = 18$  (See Fig. 7).

Further, we found that fluxes predicted by Fernando's law (Fernando, 1989) for low-stability regimes  $Nu = 4.7 \cdot 10^{-4} \cdot (Ra_D \cdot Pr)^{1/2}$  ( $Nu_1^{teor} = 28$  and  $Nu_2^{teor} = 5$ ) are close to our measurements. That is not the case, however, for his parameterization for diffusive regimes  $Nu = 7 \cdot 10^{-2} \cdot (Ra_D \cdot Pr)^{1/5}$ . ( $Nu_1^{teor} = 6$  and  $Nu_2^{teor} = 3$ ).

## SUMMARY AND CONCLUSIONS

Microstructure measurements taken in a low-stability, double-diffusivity regime (density ratio  $R_\rho \approx 1,1$ ) with two convective layers have been analyzed and used to test existing models/parameterizations of fluxes. Detailed analysis of Rayleigh numbers at the interfaces show that they are mainly lower or closer to the critical number: maximum value is about 10,000 and that 89% of the values are under 3000. Median and mean interfacial Rayleigh numbers are 1000 and 2300, respectively.

Fluxes have been determined by two different methods: a) the thermal gradient method at the diffusive interfaces; and b) from microstructure temperature variance and the monotonous temperature background gradient at the convective layers. Agreement between the two methods is excellent and they are in accordance with an estimation of the buoyancy flux obtained from mean characteristics of the system (not discussed here).

A comparison of these experimental fluxes to classical heat flux laws shows that predictions are not in agreement with our measurements perhaps because analytical forms of  $C(R_\rho)$  are fit to experimental data and for,  $R_\rho \rightarrow 1$  few data are available, and what are available are very dispersed, varying over one order of magnitude. We found, however, relatively good agreement with results predicted by Kelley's method for thermal convection without stabilizing fields and for Fernando's model for low stability conditions.

## ACKNOWLEDGMENTS

This work has been supported by grant GL2004-02007/HID of the Spanish Government. We are very grateful to Gemma Rustullet, Núria Cabezas, Elena Recas, Dr. Farmers Corrales and Dr. Pere Sarquella of the Chemical Engineering Group of the University of Girona and to Marianna Soler of the Physics Department for their support in the laboratory work, helping to calibrate the turbidity sensor, and for their patience.

## REFERENCES.

- Batchelor, G.K., 1959. "Small scale variation of convected quantities like temperature in turbulent field. Part 1. General discussion and the case of small conductivity". *J. Fluid Mech.* 5, 113.
- Burmeister, L.C., 1993. "Convective heat transfer". John Wiley & Sons. 619 pp.
- Casamitjana, X., Roget, E., 1993. Resuspension of sediment by focused groundwater in Lake Banyoles. *Limnology and Oceanography*, 38(3), 643-656.
- Fernando, H.J.S., 1989a. "Buoyancy transfer across a diffusive interface". *J. Fluid Mech.* 209, 1-34.
- Fernando, H.J.S., 1989b. "Oceanographic implications of laboratory experiments on diffusive interfaces". *J. Phys. Oceanogr.* 19, 1707.
- Hinze, J.O., 1975. "Turbulence". Mc-Graw-Hill series in Mechanical Engineering.
- Hoare, R.A., 1966. "Problem of heat transfer in Lake Vanda, a density stratified Antarctic lake". *Nature*, 10, 787-789.
- Howard, L.N., 1966. "Convection at high Rayleigh number", Proc. 11<sup>th</sup> Int. Cong. Appl. Mech. Berlin, Springer.
- Kanta, L.H. and Clayson, C. 2000. "Small scale processes in Geophysical fluid flows". Academic Press. 883 p.

- Kelley, D.E., 1990. "Fluxes through diffusive staircases : A new formulation". Journal of Geophysical Research 95, 3365.
- Kelley, D.E.; Fernando, H.J.S.; Gargett, A.E.; Tanny, J.; Özsoy, E., 2003. "The diffusive regime of double-diffusive convection". Progress in Oceanography, 56, 461.
- Newman, F.C., 1976. "Temperature steps in Lake Kivu: A bottom heated saline lake". J. Phys. Oceanogr. 6, 157.
- Padman, L.; Dillon, T.M., 1989. "Termal microstructure and internal waves in the Canada Basin diffusive staircase". Deep-Sea Research 36, 531.
- Prandke, H. and Stips, A. , 1998. "Test measurements with an operacional microstructure turbulence profiler: detection limit of dissipations rates". Aquatic Sciences 60, 191.
- Robertson, R.; Padman, L.; Levine, M.D., 1995. "Fine structure, microstructure, and vertical mixing processes in the upper ocean in the western Weddell Sea". Journal of Geophysical Research 100, 18517.
- Roget, E., Colomer, J., Casamitjana, X. Llebot, J. E., 1993. Bottom currents induced by baroclinic forcing in lake Banyoles (Spain), *Aquat. Sci.* 55(3), 206- 227.
- Ruddick, B.; Anis, A.; Thomson, K., 2000. "Maximum likelihood spectral fitting: the Batchelor spectrum". J. Atmos. Oceanic Technol. 17, 1541.
- Schmid, M.; Lorke, A.; Dinkel, C.; Tanyileke, G.; Wüest, A., 2004. "Double-diffusive convection in lake Nyos, Camerun". Deep-Sea Research I 51, 1097.
- Turner, J.S., 1973. "Buoyancy effects in fluids", Cambridge University Press.

Brooks  
Cope  
Moor  
Hawkins, L. M. 1922-  
Parson, Agnes  
Keay, J. R. and Chapman, S.  
1922-1931 p.

## MIXING PROCESSES IN LAKE VAN (TURKEY)

Heike Kaden<sup>(1)</sup>, Frank Peeters<sup>(1)</sup>, Andreas Lorke<sup>(1)</sup>, Rolf Kipfer<sup>(2,3)</sup>,  
Matthias Brennwald<sup>(2)</sup>, Yama Tomonaga<sup>(2)</sup>

- (<sup>1</sup>) Environmental Physics, Limnological Institute, University of Constance, 78464 Constance, Germany (Heike.Kaden@uni-konstanz.de, Frank.Peeters@uni-konstanz.de, andreas.lorke@uni-konstanz.de)
- (<sup>2</sup>) Dept. of Water Resources and Drinking Water, Swiss Federal Institute for Environmental Science and Technology (EAWAG), 8600 Dübendorf, Switzerland (rolf.kipfer@eawag.ch, matthias.brennwald@eawag.ch, tomonaga@eawag.ch)
- (<sup>3</sup>) Isotope Geology, Swiss Federal Institute of Technology (ETHZ), 8092 Zürich, Switzerland

Lake Van is a saline (~ 21 g/kg) closed basin lake located in the East Anatolian Highlands of Turkey at an altitude of 1650 m a.s.l. It is the largest lake in Turkey (3522 km<sup>2</sup>) and the world's largest and deepest (455 m) soda lake with a pH of 9.75. Since the late 1980's the lake level increased by several meters (Kadioglu et al. 1997). Tracer studies in 1989 and 1990 suggested that deep-water exchange in Lake Van was very rapid with renewal rates on the order of one to two years (Kipfer et al. 1994). This study investigates whether the freshwater influx associated with the lake level rise since the 1990's had an effect on water column stratification and vertical mixing dynamics.

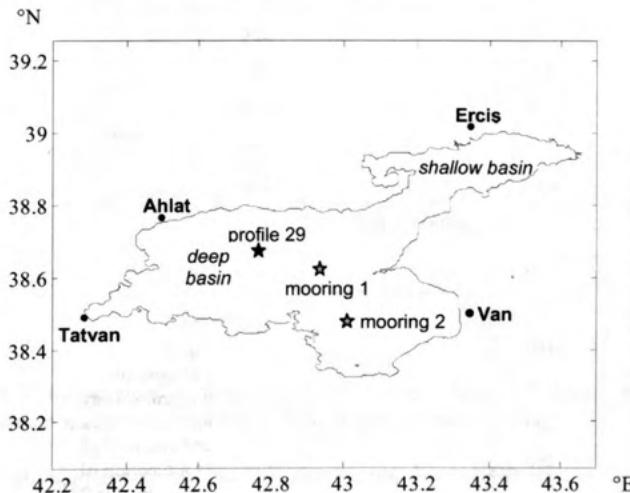


Fig. 1:  
Map of Lake Van  
with the position  
of profile 29 and  
the mooring  
(38°39.299' N and  
42°45.986 E).

During a field campaign in May 2005 CTD-profiles (conductivity, temperature, depth) were measured with an Idronaut ocean seven 330 CTD probe at 66 stations distributed all over the lake (Fig. 1). In addition to the standard CTD sensors, the Idronaut probe was equipped with sensors for dissolved oxygen, light transmissivity, pH, and chlorophyll fluorescence. Two moorings consisting of 22 thermistors (TR-1050, RBR Ltd., Canada and

Minilog, Vemco Ltd., Canada) and two current metres (Aanderaa Instruments, Norway) were installed for a time period of 9 days. Furthermore, water samples were collected for tracer analysis of He,  $^3\text{H}$ , SF<sub>6</sub>, CFC-12 and noble gases (profile 20: 38°34.401' N, 42°46.293' E and profile 29: 38°39.299' N, 42°45.986' E).

Figure 2 shows data from the CTD-probe collected at the main basin of Lake Van (profile 29, see Fig. 1). Potential temperature decreases from the surface down to 30 m depth with the main thermocline located between 10 and 30 m. Between 30 m and 80 m depth temperature increases but below 80 m temperature decreases again with increasing depth thus forming a local temperature maximum at 80 m depth. A similar temperature maximum at intermediate depths was observed in all CTD-profiles reaching down to depths below 100 m. Salinity was calculated from conductivity, temperature and pressure using the UNESCO formula for sea water (UNESCO, 1981b) without accounting for the ionic composition of Lake Van water. Hence the true absolute values of salinity may differ significantly from the salinity values in Fig. 2. However, the relative variation of salinity should be represented reasonably well. Salinity is lowest near the lake surface and increases with increasing depth. Therefore, it can be assumed that salinity stabilizes the water column. The salinity gradient apparently is sufficiently large to compensate the

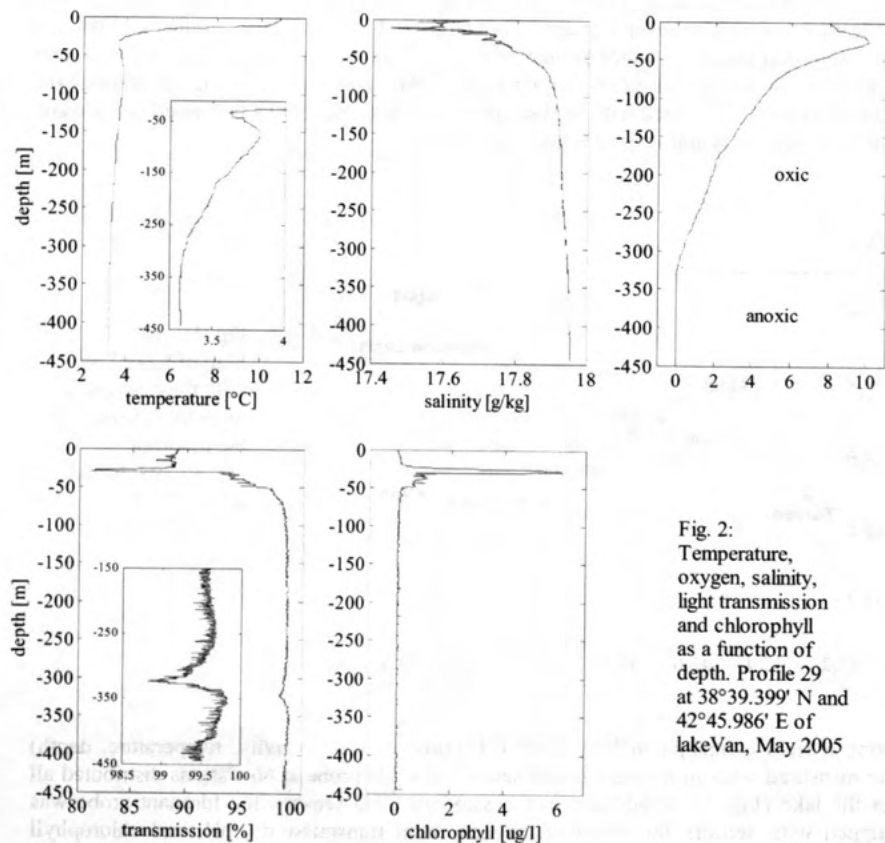


Fig. 2:  
Temperature,  
oxygen, salinity,  
light transmission  
and chlorophyll  
as a function of  
depth. Profile 29  
at 38°39.399' N and  
42°45.986' E of  
lakeVan, May 2005

destabilizing effect of temperature in the depth range between 30 m and 80 m depth. Within the lake lowest salinity values were observed in the shallow north-eastern basin whereas highest values were found in the deep water of the main basin. The maximum difference in salinity within the basin reached up to 2.3 g/kg.

Dissolved oxygen was in atmospheric equilibrium at the lake surface. Oxygen levels are maximal at about 25 m depth. Below this maximum dissolved O<sub>2</sub> decreases down to 0 mg/l at a depth around 320 m and below. The O<sub>2</sub>-profile indicates an anoxic layer in the deepest 100 m of the water column. This is in contrast to observations from 1990 where dissolved oxygen determined by Winkler titration was 2.39 mg/l at 320 m depth and 0.53 mg/l at 440 m depth (Reimer et al., 1994) (Fig. 3).

Light transmission has a minimum at about 30 m which corresponds to a deep chlorophyll maximum and a broad peak in dissolved oxygen. Apparently algal biomass is responsible for this feature in the light transmission, chlorophyll fluorescence and oxygen profiles. The vertical distribution of light transmission has a peak at about 320 m depth, which corresponds to the depth of the transition between oxic and anoxic conditions. We suggest that reduction processes of manganese and / or iron triggered by bacterial activity are responsible for the reduced light transmission at this depth.

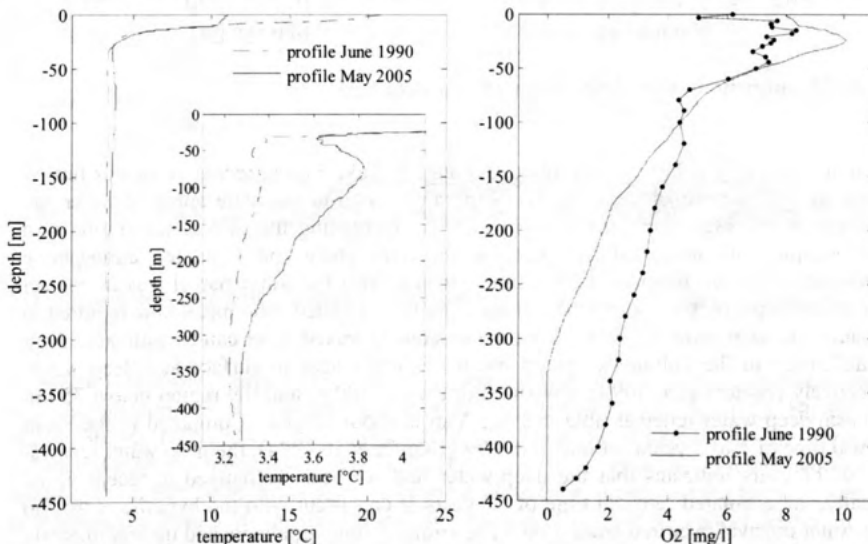


Fig.3: Comparison of temperature and oxygen data from June 1990 (Kipfer et al., 1994; Reimer et al., 1994) and May 2005 (profile 29, see Fig. 1).

In comparison to the measurements from June 1990 temperature increased below the thermocline and oxygen values are shifted to lower values below 150 m depths in 2005 (Fig. 3). In 1990 the lake contained oxygen down to maximum depth whereas in 2005 the deep water below 320 m depth is anoxic. These differences between 2005 and 1990 can be explained by a change in mixing conditions, i.e. by fast vertical mixing in 1990 and slower vertical mixing in recent years. Today, the strong salinity gradient in the upper 100 m most likely prevents mixing down to larger depths. The density difference corresponding to a salinity difference of 0.2 g/kg at about 4°C cannot be compensated by cooling. Hence, seasonal cooling probably does not result in significant mixing below 100 m.

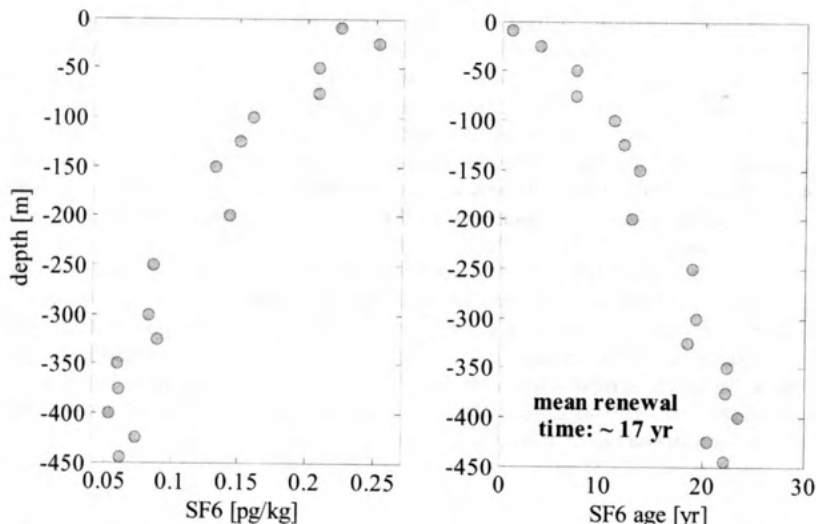


Fig. 4: SF<sub>6</sub> concentrations and SF<sub>6</sub> water ages at station 29.

The hypothesis of a reduced deep-water exchange in Lake Van in recent years was further proved by SF<sub>6</sub> tracer analysis (Fig. 4). SF<sub>6</sub> can be used to calculate apparent water age from which exchange rates can be estimated. By comparing the SF<sub>6</sub> concentration in a water sample with historical SF<sub>6</sub> data in the atmosphere and assuming atmospheric equilibrium at in-situ temperature the time elapsed since the water parcel was in contact with the atmosphere, the apparent water age, can be calculated. The mean time required to exchange the deep water by water from the seasonally mixed layer can be estimated from the difference in the volume-weighted mean SF<sub>6</sub> water ages in surface and deep water, respectively (Peeters et al. 1999). Considering the top 100 m and the region below 350 m the mean deep water renewal time in Lake Van is about 17 year. Compared to the mean renewal time of 1 to 2 years estimated in 1990 (Kipfer et al. 1994), the deep water renewal time of 17 years indicates that the deep-water had not been exchanged in recent years. Actually, the estimated renewal time of 17 years is consistent with the hypothesis that no deep-water renewal occurred since 1990. The strong salinity gradients and the intermediate temperature maximum observed in 2005 also suggest that vertical mixing is rather weak. The hypothesis that vertical exchange has been significantly reduced in recent years is further supported by the data on dissolved oxygen from 1990 and 2005 indicating a strong decline of the oxygen levels in the deep water (Fig. 3). Reduced vertical mixing implies a reduced transport of dissolved oxygen to the deep water and thus the development of anoxic conditions. In summary, climatic change causing a rise of lake level resulted in an increased stratification due to an increase in vertical salinity gradients. Thus convective processes responsible for deep water renewal in Lake Van are suppressed and deep-water residence times increased substantially leading to anoxic conditions in the bottom 100 m of Lake Van.

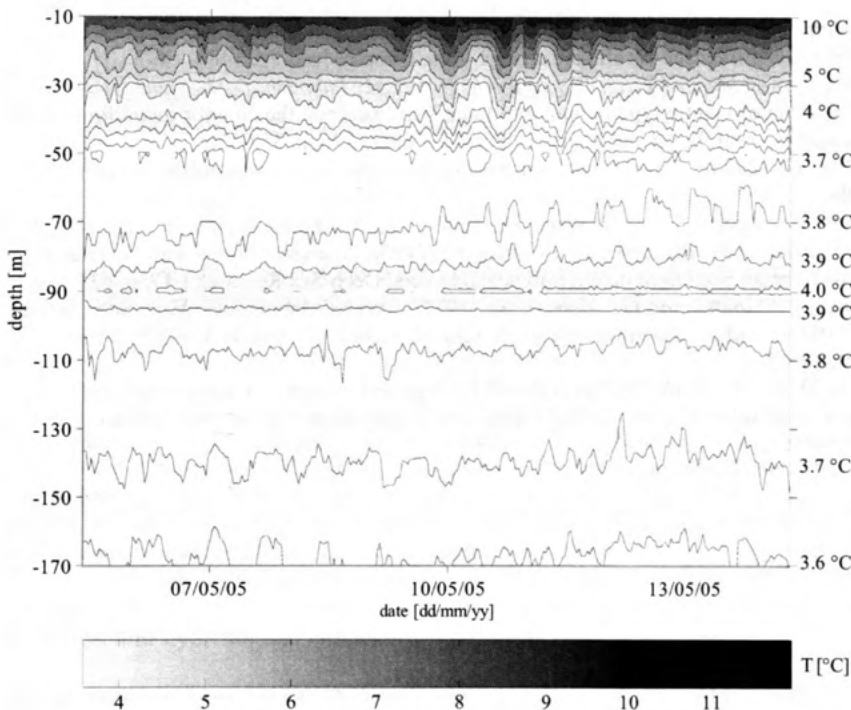


Fig. 5: Isotherms calculated from the temperature measured by the moored thermistors.

In addition to the investigation of the long term vertical exchange, short term dynamics was studied using 16 thermistors moored at different depth (7, 10, 13, 20, 25, 30, 40, 50, 60, 70, 80, 90, 100, 125, 150, 175 m) at  $38^{\circ}28.172'N$  and  $43^{\circ}01.086'E$  (Fig. 1). Isotherms calculated from the temperature time series (Fig. 5) show the decrease of temperature with depth in the upper 50 m, the maximum at about 80 to 90 m depth, and the further decrease in temperature below 90 m towards the lake bottom. The most prominent feature in the time series are regular oscillations of the isotherms. The period of these oscillations is about 17 hours which is somewhat shorter than the inertial wave period of 19.24 hours. The current velocities at 10 m and 100 m depths, measured by the moored current meters, rotate clockwise with the same period. The phase of the oscillations in the currents at 10 m is shifted by about 5 hours to the currents at 100 m depth. This suggests that the observed oscillations cannot be due to inertial wave motion but rather that a Poincare-like internal wave is responsible for the clockwise rotation. A more detailed investigation of the internal wave dynamics requires longer time series of temperature and current velocities which will be collected by new moorings installed in Lake Van.

**References:**

- Kadioglu, M., Sen, Z., and Batur, E. (1997): The greatest soda-water lake in the world and how it is influenced by climate change, *Ann. Geophysicae*, 15, 1489–1497
- Kipfer, R., Aeschbach-Hertig, W., Baur, H., Hofer, M., Imboden, D.M., Signer, P. (1994): Injection of mantle type helium into Lake Van (Turkey): the clue for quantifying deep water renewal, *Earth and Planetary Science Letters* 125, p. 357-370
- Lemcke, G. (1996): Paläoklimarekonstruktion am Van See (Ostanatolien, Türkei), PhD thesis, ETH Zurich
- Peeters, F., Kipfer, R., Achermann, D., Hofer, M., Aeschbach-Hertig, W., Beyerle, U., Imboden, D.M., Rozanski, K., Fröhlich, K. (1999): Analysis of deep-water exchange in the Caspian Sea based on environmental tracers, *Deep-Sea Research I* 47, p. 621-654
- Reimer, A., Landmann, G., Kempe, S. (1994).: Wasserchemie des Van Sees, seiner Zuflüsse und der Porenwässer, in: Abschlußbericht DFG Projekt Wo 395/2-1 bis 2-4, chapter 5
- UNESCO, ICES, SCOR, IAPSO (1981b): Background papers and supporting data on the practical salinity scale 1878, Unesco technical papers in marine science, Nr.37, UNESCO

# Suspended sediment controlling the path of the Mulde flood waters through Lake Goitsche

Bertram Boehrer and Martin Schultze

Umweltforschungszentrum Leipzig-Halle GmbH, Brückstraße 3a, D-39114 Magdeburg,  
[Bertram.Boehrer@ufz.de](mailto:Bertram.Boehrer@ufz.de), [Martin.Schultze@ufz.de](mailto:Martin.Schultze@ufz.de)

## Abstract

After heavy rains, Mulde River (Central Germany) came up with extremely high water in August 2002. Eventually a dam of a side channel broke, and the floods found their way into Mining Lake

Goitsche. The flood waters first entered the most eastern subbasin "Döbern" and only later they also impacted on the other subbasins of the Lake, however less severely. Due to the suspended material the flood waters were dense enough to overcome the summer stratification and sank to the deepest location of the first basin. Most of the suspended material got deposited in this basin. As a consequence the density decreased and in the succeeding basins the flood waters could not intrude into the deep water. Hence the hypolimnia of the second and third basin were not directly impacted by the flood waters, and remained stable until the winter circulation later in the year.

## Location and hydrological situation

Lake Goitssche is located in Central Germany about 100km south west of Berlin (see Figure 1). The lake basin originates from lignite mining, and regular filling with river water from the nearby river Mulde was implemented in the years 1999 to 2002 until a water level of 71.5m was reached. Over the succeeding years, legal agreements were to be signed before the water level could be raised to the final water level of 75m above sea. In direct vicinity of Lake Goitsche, the bed of river Mulde is located. The river bed is separated from the lake by a dam before traversing the Mulde reservoir. Upstream of the Mulde reservoir a small side channel is connected to the river course.

As a consequence of a 5b-weather situation, when in summer warm and moist air masses are advected from the Mediterranean into Central Europe, extremely heavy rains fell in Czech Republic and the nearby areas of the neighbouring countries. The catchment area of the River Mulde was one of the most badly affected. Hence the water levels rose to maxima that had never been documented in history before.

With the floods going down the river, also the water level in the small side channel rose. In addition, upstream of the location of interest, water had found its way behind the Mulde dam and approached the small side channel from the outside. Eventually the dam of this side channel broke and opened the path for Mulde waters to enter the area next to Lake Goitsche. The soil got drenched and became mobile. A mixture of water and suspended soil moved towards the lake and entered it. Within a few hours a new river bed of several hundred meter length 200 meters width and 4 meters depth had formed. The solid material had been transported into the lake. A rough estimate indicated that about 1 million cubic meters of soil had been moved by 100 million cubic meters of water (see Boehrer and Schultze 2005).

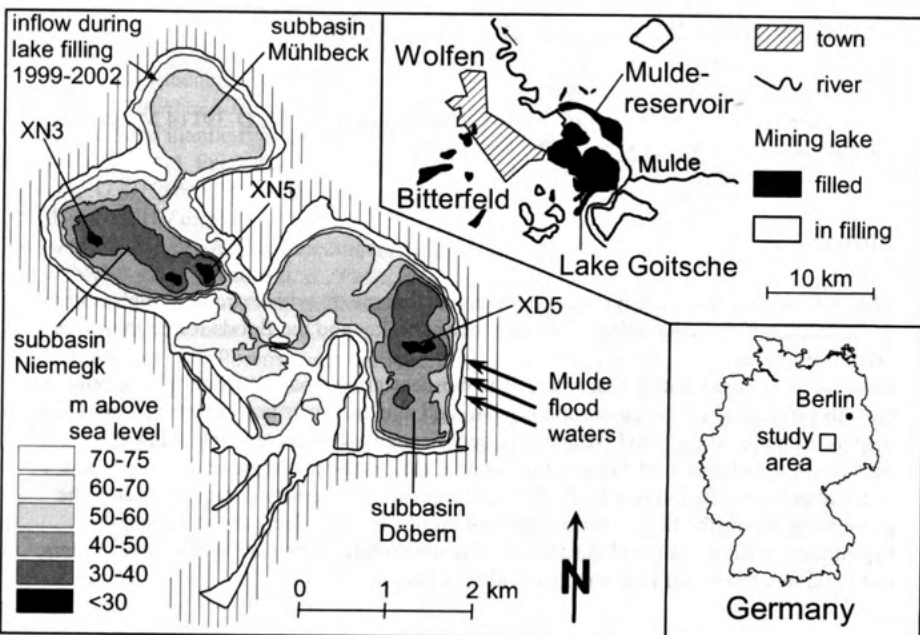


Figure 1: Contour map of Lake Goitsche showing the location of the measuring stations and the regular Mulde river course the location where Mulde river water was intentionally introduced and where the floods forced their way into the lake. (from Boehrer and Schultze 2005)

### Path through Lake Goitsche

The suspended material contributed to the density of the flood waters, which entered Lake Goitsche. On the average, one percent of the volume was made up by suspended material, increasing the density of the waters far beyond the density of the much colder hypolimnion water of the subbasin "Döbern". As a consequence, the flood waters flowed on the lake bed to the deepest location. (see Figure 2, 2<sup>nd</sup> panel).

Under the quieter conditions of the lake environment, the suspended material started to settle, and the continuously inflowing floodwaters replaced the hypolimnion and epilimnion of the subbasin Döbern before it crossed the separating sill to subbasins Niemegk and Mühlbeck. On the base of salinity and temperature, it was estimated that subbasin Döbern contained a mixture of 90% floodwaters and 10% previous hypolimnion water, when the river discharge had dropped again (Figure 2, 3<sup>rd</sup> panel).

By the time the floodwaters could cross the sill, they had lost most of its suspended material. The density then was lower than the hypolimnion water in subbasins Niemegk and Mühlbeck. Thus the flood waters traversed subbasins Niemegk and Mühlbeck in the epilimnion, without affecting the hypolimnia directly (Figure 2, 4<sup>th</sup> panel).

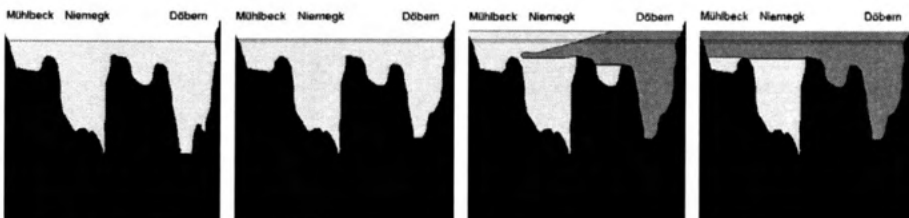


Figure 2: Sequence of four snapshots of longitudinal transects through Lake Goitsche showing the path of intruding Mulde flood waters through the separate subbasins in August 2002. black = bottom contour of the lake, dark grey = flood waters heavily loaded with suspended matter or deposited material, grey = waters with high portion of Mulde flood waters, faint grey = original lake water. (from Boehrer and Schultze 2005)

## Consequences

The path of the Mulde flood waters determined where the suspended material was deposited, and what quantity of dissolved substances, such as heavy metals or nutrients, got imported into the separate subbasins. The knowledge of this path is crucial for the correct interpretation of the ecological consequences originating from Mulde flood waters in Lake Goitsche.

## References

- Boehrer and Schultze (2005): Path of the 2002 Mulde flood through Lake Goitsche, Germany. Verh. Internat. Verein. Limnol. 29 (in press)

the first time, and the author has been unable to find any reference to it in any of the literature on the subject. It is described as follows:

The plant is a small, annual, erect, glabrous herb, 15-20 cm. tall, with a slender, smooth stem, which bears a few scattered, minute, appressed hairs near the base. The leaves are opposite, sessile, linear-lanceolate, acute at the apex, 10-15 mm. long, 2-3 mm. wide, with a few scattered, minute, appressed hairs on the upper surface. The flowers are numerous, axillary, in whorls of 4, 5, or 6, each whorl subtended by a small, linear bract. The flower stalks are slender, smooth, and puberulous only near the base. The flowers are white, 5-petaled, 5-6 mm. in diameter, with a short, slender pedicel. The fruit is a slender, smooth, linear capsule, 10-12 mm. long, 2-3 mm. wide, with a short, slender style.

The author has examined a specimen of this plant from the herbarium of the Missouri Botanical Garden, and has determined it to be a new species, which he has named *Monnieria*.